

DISSERTATION

Validated novel pipelines to study linear and non-linear
between-site functional brain interaction with application in
Parkinsonian gait

Validierte neue Pipelines zur Untersuchung linearer und
nichtlinearer inter-regionaler funktioneller Hirninteraktionen mit
Anwendung auf Parkinson-typischen Gang

zur Erlangung des akademischen Grades
Doctor of Philosophy (PhD)

vorgelegt der Medizinischen Fakultät
Charité – Universitätsmedizin Berlin

von

Franziska Pellegrini

Erstbetreuung: Prof. Dr. rer. nat. Stefan Haufe

Datum der Promotion: 20. Juni 2025

Table of Contents

Index of figures.....	iii
Index of abbreviations	iv
Abstract	vi
1 Introduction	1
1.1 Parkinson's Disease	1
1.2 Electroencephalography.....	3
1.3 Functional connectivity	3
1.4 Signal mixing	4
1.5 FC analysis.....	6
1.6 Research questions.....	6
2 Methods	8
2.1 Simulations.....	8
2.1.1 Data generation.....	9
2.1.2 Analysis pipeline	9
2.1.3 Evaluation	14
2.2 Minimal exploratory analysis of function connectivity in motor imagery	15
2.2.1 Linear functional connectivity in left vs. right motor imagery.....	16
2.2.2 Phase-amplitude coupling using bispectral metrics	16
2.3 Functional connectivity in walking patients with Parkinson's Disease.....	17
2.3.1 Subjects and experimental design	17
2.3.2 Positron emission tomography	17
2.3.3 Kinematic measures.....	17
2.3.4 Electroencephalography	18
2.3.5 Statistical evaluation	19
2.4 ROIconnect toolbox.....	19

3 Results	21
3.1 Linear phase-phase coupling	21
3.2 Phase-amplitude coupling	22
3.3 Exploratory analysis of functional connectivity in motor imagery	23
3.4 Functional connectivity in walking patients with Parkinson's Disease.....	24
4 Discussion.....	27
4.1 Summary of the results	27
4.2 Insights from the simulations	28
4.3 The functional connectome during gait in Parkinson's Disease	29
4.4 Limitations	30
4.5 Implications for clinical application	32
5 Conclusion	32
References	34
Statutory declaration	48
Declaration of contribution to publications	49
Excerpt from journal summary list.....	50
Publications	51
Curriculum vitae	165
List of publications.....	167
Acknowledgements	168

Index of figures

Figure 1. Structure of the linear functional connectivity simulation.	10
Figure 2. Structure of the phase-amplitude coupling simulation.	13
Figure 3. Performance of linear functional connectivity (FC) pipelines in their ability to detect inter-regional ground-truth interactions.	20
Figure 4. Comparison of different phase–amplitude coupling (PAC) metrics.....	22
Figure 5. Results of the exploratory analysis of functional connectivity (FC) in left- and right-hand motor imagery (Mti) tasks.	24
Figure 6. Phase-amplitude coupling (PAC) between the left and right postcentral and precentral cortices during motor imagery of moving the right hand.	25
Figure 7. Kinematic and functional connectivity (FC) patterns in walking patients with Parkinson's Disease.....	26

Index of abbreviations

BEM	Boundary Element Method
BOI	Band Of Interest
COH	Coherence
DICS	Dynamic Imaging of Coherent Sources
EEG	Electroencephalography
eLORETA	exact Low-Resolution Electromagnetic Tomography
ECoG	Electrocorticography
EMG	Electromyography
FC	Functional Connectivity
FDR	False Discovery Rate
FO	Fast Oscillation
GC	Granger Causality
gFPR	global False Positive Rate
ICA	Independent Component Analysis
iCOH	imaginary Coherency
IFOF	Inferior Fronto-Occipital Fasciculus
IMU	Inertial Measurement Unit
LCMV	Linearly Constraint Minimum Variance
LFP	Local Field Potential
LME	Linear Mixed-Effect Model
MEG	Magnetoencephalography
MI	(mean-vector length) Modulation Index
MIC	Maximized Imaginary Coherency
MIM	Multivariate Interaction Measure
MRI	Magnetic Resonance Tomography
Mtl	Motor Imagery
PCA	Principal Component Analysis
PD	Parkinson's Disease
PET	Positron Emission Tomography
PR	Percentile Rank
ROI	Region Of Interest
RQ	Research Question

SMA	Supplementary Motor Area
SNR	Signal-to-Noise Ratio
SO	Slow Oscillation
SUV	Standardized Uptake Value
SVD	Singular Value Decomposition
TRGC	Time-Reversed Granger Causality
UPDRS-III	Unified Parkinson's Disease Rating Scale motor part

Abstract

Over the past years, the focus in the field of functional neuroimaging has shifted to evaluating the patterns of interaction between distinct and specialized brain regions, as interactions contain more information than the mere localization of brain activity.

Locomotion is a complex process which relies on the well-coordinated interplay between distributed brain areas. In patients with Parkinson's disease, this interplay may be disturbed and the gait impaired. One aim of this thesis is, therefore, to characterize cortical interaction patterns within the locomotor network of walking patients with Parkinson's Disease.

Typical workflows for analyzing inter-regional functional connectivity (FC) from magneto- and electroencephalography (M/EEG) recordings involve several sequential processing steps. At each step, researchers are presented with numerous processing methods to choose from, and each decision they make has the potential to significantly impact the outcome of the analysis and its interpretation. In the first two studies that contributed to this thesis, we addressed this problem by evaluating the validity and reliability of various FC analysis pipelines using systematic simulations.

The first study compares pipelines that analyze directed and undirected linear FC between predefined brain regions. It shows that the best results are achieved by a pipeline that uses Linearly Constrained Minimum Variance (LCMV) to reconstruct sources, aggregates time series within regions using a fixed number of the strongest principal components, and utilizes robust multivariate FC metrics.

Building on this pipeline, the second study expands the scope to the analysis of phase-amplitude coupling (PAC). It demonstrates the potential of a recently introduced method, the anti-symmetrized bispectrum (ASB), to explore PAC between different sites in mixed-signal scenarios. The results of this study provide evidence that the ASB effectively avoids identifying spurious between-site PAC in mixed-signal scenarios while consistently detecting true bivariate interactions of interest.

Finally, in the concluding study, we employed the recommended pipeline to examine directed FC within the cortical locomotor network of walking patients with Parkinson's Disease. The study identifies a decreased information flow from the supplementary motor area to sensory and motor regions, along with increased FC to visuomotor areas. Furthermore, we observed correlations between FC and gait performance, highlighting the relationship between FC and disease severity in Parkinson's Disease.

Additionally, to ensure that our recommendations are readily available to a wide range of practitioners, we introduce the ROIconnect plugin, an open source for the EEGLAB toolbox that implements the methods and pipelines for linear FC and PAC estimation that this thesis recommends.

Zusammenfassung

In den letzten Jahren hat sich auf dem Gebiet der funktionellen neuronalen Bildgebung der Schwerpunkt auf die Auswertung von Interaktionen zwischen spezialisierten Hirnregionen verlagert, da Interaktionen informativer als die bloße Lokalisierung der Hirnaktivität sind.

Fortbewegung ist ein komplexer Prozess, der auf dem gut koordinierten Zusammenspiel zwischen verteilten Hirnarealen beruht. Bei Patienten mit Morbus Parkinson kann dieses Zusammenspiel gestört und der Gang beeinträchtigt sein. Ziel dieser Arbeit ist es, die kortikalen Interaktionsmuster im Bewegungsnetzwerk von gehenden Parkinson-Patienten zu charakterisieren.

Die Analyse der interregionalen funktionellen Konnektivität (FK) aus Magneto- und Elektroenzephalographie-Aufzeichnungen (M/EEG) umfasst mehrere aufeinander folgende Verarbeitungsschritte. Bei jedem Schritt stehen Forschenden zahlreiche Methoden zur Auswahl. Jede Entscheidung, die sie treffen, kann das Ergebnis der Analyse und deren Interpretation erheblich beeinflussen. In dieser Dissertation befasse ich mich mit diesem Problem, indem ich die Gültigkeit und Zuverlässigkeit verschiedener FK-Analysepipelines mithilfe systematischer Simulationen bewerte.

Die erste Studie vergleicht Pipelines, die gerichtete und ungerichtete lineare FK zwischen vordefinierten Gehirnregionen analysieren. Sie zeigt, dass Pipelines, die eine LCMV-Quellenrekonstruktion, die Aggregation von Zeitreihen innerhalb von Regionen unter Verwendung einer festen Anzahl der stärksten Hauptkomponenten und die Verwendung robuster multivariater FK-Metriken umfassen, die besten Ergebnisse erzielen.

In der zweiten Studie wird der Anwendungsbereich auf die Analyse der Phasen-Amplituden-Kopplung (PAK) ausgeweitet. Sie demonstriert das Potenzial einer kürzlich eingeführten Methode, des antisymmetrischen Bispektrums (ASB), um PAK zwischen Regionen in Mixed-Signal-Szenarien zu untersuchen. Die Ergebnisse dieser Studie belegen, dass das ASB die Identifizierung von unechter interregionaler PAK in Szenarien

mit gemischten Signalen wirksam vermeidet und gleichzeitig echte bivariate Wechselwirkungen konsequent verlässlich aufdeckt.

In der letzten Studie wird die empfohlene Pipeline eingesetzt, um Veränderungen in der gerichteten FK innerhalb des kortikalen motorischen Netzwerks während des Gehens bei Patienten mit Parkinson-Krankheit zu untersuchen. Die Studie zeigt einen verringerten Informationsfluss vom supplementär-motorischen Areal zu sensorischen und motorischen Regionen sowie eine erhöhte FK zu visuomotorischen Arealen. Darüber hinaus werden Korrelationen zwischen der FK und der Gangbeeinträchtigung festgestellt, was den Zusammenhang zwischen FK und dem Schweregrad der Erkrankung bei Morbus Parkinson verdeutlicht.

Außerdem stelle ich das ROIconnect-Plugin vor, ein frei verfügbares Tool für die EEGLAB-Toolbox. Dieses Plugin enthält die empfohlenen Methoden und Pipelines für die lineare FK- und PAK-Schätzung, die in dieser Arbeit diskutiert und vorgestellt werden.

1 Introduction

Pathological neural communication is a hallmark feature in various neurological diseases, including Parkinson's Disease (PD; Tessitore et al., 2019). In PD, complex cognitive processes such as gait are impacted (Mirelman et al., 2019). Understanding the connections that facilitate communication between brain structures is crucial, as it sheds light on the collaborative efforts of these structures in executing cognitive tasks and provides insights into the underlying neural mechanisms. Despite the significance of connectomes, the computational tools required for their analysis are not fully developed. This thesis aims to advance tools to analyze connectomes in neurological diseases such as PD. The developed tools are applied to investigate the altered neural communication in PD, with the overarching objective of providing valuable insights for improved diagnosis and treatment strategies.

1.1 Parkinson's Disease

PD is a neurodegenerative movement disorder that affects the dopaminergic system in the brain (Bergman et al., 1990). The diagnosis is based on three cardinal motor symptoms (Postuma et al., 2015): bradykinesia (slowness of movements), in combination with either rest tremor (trembling of a fully resting limb), rigidity (muscle stiffness), or both.

Features of electrophysiological recordings, such as magneto- or electro-encephalography (M/EEG) or local field potentials (LFP), have been extensively studied in context of PD (e.g., Soikkeli et al., 1991). The enhanced power of beta band activity recorded by depth electrodes from the subthalamic nuclei, integral parts of the basal ganglia, stands out as the most stable biomarker in PD (Hammond et al., 2007; Kühn et al., 2006, 2008). Studies indicate that interventions such as levodopa treatment and deep brain stimulation (DBS) can effectively reduce beta activity in the STN, leading to clinically observed improvements of motor symptoms (e.g., Kühn et al., 2006, 2008).

Gait impairments are a common phenomenon in PD (Galna et al., 2015; Schoneburg et al., 2013). They are reflected in changes in step length and variability and freezing of gait. Gait impairments result from a dysfunction of the cortical motor network, which includes premotor, sensorimotor, and visuomotor cortical areas (Peterson et al., 2014). However, direct studies of cortical network dynamics during actual locomotion, especially in non-

medicated PD patients, are still lacking. Thus, it is unknown how movement information flows within this network in the absence of striatal dopamine, and which integration processes are most important for gait in this context.

Brain connectivity analysis is crucial for unraveling the pathomechanisms of PD, as it enables the localization and quantification of disruptions in brain communication. The investigation of connectivity is especially interesting in complex processes like locomotion. Healthy locomotion relies on well-coordinated movements of different body parts to achieve forward motion and maintain postural balance. This requires dynamic interplay between brain areas that integrate premotor, sensorimotor, and visuomotor information (MacKinnon, 2018). It has been suggested that the cerebral cortex plays a crucial role in modulating repetitive movement patterns (Clancy et al., 2019). That is, connectivity changes within the locomotor network condition the generation of these patterns at the spinal level (Takakusaki, 2017). This in turn means that the cortical locomotor network can compensate for subcortical pathological changes through adaptive adjustments (Tosserams et al., 2022). A deeper understanding of cortical control of locomotion could improve the treatment of gait disorders. Further, connectivity features have the potential to serve as a biomarker for the diagnosis and treatment of PD.

Numerous studies rely on connectivity measures that may be considered unreliable (e.g., Silberstein et al., 2005), thereby imposing limitations on the interpretation of the derived biomarkers. The primary focus of this thesis is to provide dependable estimation methods of various types of brain interactions. By addressing the challenges posed by potentially unreliable measures, this approach aims to enhance the robustness and accuracy of the derived markers, contributing to a more trustworthy understanding of neurological processes. This thesis focuses on non-invasive recordings like EEG, which play a crucial role in characterizing pathological brain activity. Non-invasive methods not only facilitate the observation and understanding of pathological brain activity but also enable the generation and testing of hypotheses about the disease. Non-invasive biomarkers are easily obtainable, making it practical to routinely screen large populations of individuals at risk. Furthermore, non-invasive biomarkers may be suitable for controlling adaptive DBS treatment of PD.

1.2 Electroencephalography

The current generated by a single neuron is too small to produce a detectable electric or magnetic field outside of the scalp (Nunez & Srinivasan, 2006). However, when many neurons in a patch of the cortex fire together, their spatially structured postsynaptic potentials add up to produce a measurable signal that can be detected non-invasively with M/EEG (Cohen, 2017; Nunez & Srinivasan, 2006). These signals are generated primarily in pyramidal neurons of the cortex, which are modeled as dipoles for analysis of M/EEG data. Dipoles are characterized by their location, orientation, and current intensity, and determine the measurements at the level of the M/EEG sensor.

The high temporal resolution of M/EEG allows measurement of neuronal activity with a high sampling frequency. This allows a unique insight into the fast dynamics of human brain functions. Thus, it enables the observation of the synchronization of fast oscillatory signals (Berger, 1929), which is an important mechanism for functional communication between different brain regions (Fries, 2005). The amplitudes and frequencies of these signals vary from one mental state to another, and the distinction between them is based on their biological significance (Buzsáki, 2006).

1.3 Functional connectivity

In recent years, there have been more and more studies that have gone beyond the localization of neuronal activity and have instead focused on the interaction between brain regions (J.-M. Schoffelen & Gross, 2019). With the goal of better understanding cognitive processes and behavior, brain connectivity has been studied using modern imaging techniques. The field is divided into two research streams: anatomical connectivity and FC. While anatomical connectivity studies the physical connections between units in the brain, FC studies the statistical dependencies between time series. FC is particularly interesting because it may reflect the mechanism of communication between groups of neurons (Fries, 2005). There are many types of FC. This thesis focuses on linear phase–phase and (non-linear) phase–amplitude coupling (PAC; Jirsa & Müller, 2013).

Linear phase–phase coupling measures the phase relationships between different signals (Bastos & Schoffelen, 2016). Specifically, it measures the consistency of phase differences between signals over time points. Metrics that examine phase–phase connectivity can be divided into two categories: First, there are metrics, like coherence

(COH; Nunez & Srinivasan, 2006), that capture undirected, or symmetric, interactions. In contrast, metrics like Granger Causality (GC; Bressler & Seth, 2011; Granger, 1969) also provide an indication of the direction of the interaction and thus provide information about which region influences the other. The latter are based on the idea that causality shows itself in temporal precedence from cause to effect.

PAC is a phenomenon in which the amplitude of a fast oscillation (FO) correlates with the phase of a slow oscillation (SO; e.g., Canolty et al., 2006). It is thought to facilitate the coordination of neural activities across spatial and temporal scales for cognitive processes such as memory, attention, and learning (Canolty & Knight, 2010). Studies have shown that PAC may be pathologically elevated in patients with movement disorders (de Hemptinne et al., 2013; Yin et al., 2022).

PAC can occur within a single signal (within-site; e.g., Florin & Baillet, 2015) or between signals originating from different locations (between-site; e.g., Nandi et al., 2019; Voytek & Knight, 2015). Some studies have suggested that between-site PAC is a mechanism for long-distance communication (Jirsa & Müller, 2013) and acts as a gating mechanism that allows different networks to work in parallel (van der Meij et al., 2012).

Conventional techniques (e.g., Canolty et al., 2006; Tort et al., 2010) for measuring PAC consist of bandpass filtering the original signal, extracting the amplitude of the FO, and evaluating the relationship between the phase of the SO and the envelope of the FO. Recent studies (Kovach et al., 2018; Zandvoort & Nolte, 2021) have suggested a close relationship between the cross-bispectrum and PAC, allowing to use the cross-bispectrum to measure PAC. A major advantage of the bispectrum is that it does not depend on filter parameters in the preprocessing step, and effectively suppresses Gaussian noise (Nikias & Pan, 1988).

1.4 Signal mixing

It is challenging to estimate FC in M/EEG because the signals are prone to signal mixing, which can lead to inaccurate estimates (Haufe et al., 2013; Nolte et al., 2004). Signal mixing occurs for several reasons: First, using a shared reference when recording electrophysiological signals can lead to artificially high correlations between signals from different sites (Bastos & Schoffelen, 2016). Second, volume conduction effects can arise when signals are measured with M/EEG (Schaworonkow & Nikulin, 2022). Here,

electrical signals propagate from a source to nearby electrodes or sensors, resulting in artificially high correlations between measurements. A solution is to localize the original signal sources in the brain and estimate the original signal. However, when this estimation is imperfect, signals from one brain source contaminate signals from another source (Schoffelen & Gross, 2009). This source leakage is a third reason for signal mixing.

Signal mixing can give rise to an artificially enhanced linear phase-phase FC (Schoffelen & Gross, 2019). These false positive connections manifest as apparent FC between brain regions, despite the absence of a genuine functional relationship between them.

When measuring PAC within a single site, signal mixing is not an issue. However, when examining PAC between sites, spurious coupling may be detected due to the presence of within-site PAC in a seed region that propagates to other regions (Pellegrini, Nguyen, et al., 2023). If only the lower frequencies spread to a potential target region, spurious between-site PAC may be observed between the phase measured at the target region and the amplitude of the high-frequency component in the seed region. If the entire frequency spectrum spreads to potential target regions, there is an additional risk of detecting spurious between-site PAC between the phase of the seed region and the amplitude of the target region. Consequently, when investigating PAC between different sites, we need to rule out the possibility that observed coupling does not arise from a within-site PAC that is spread to other measurement locations through some form of signal mixing.

The effects of signal mixing can be reduced by reconstructing the latent sources of measured signals. In M/EEG, the source activity in the brain can be estimated from the measurements recorded at the sensors on the scalp (Baillet et al., 2001). This estimation entails inferring the activity at numerous points within the brain based on a limited number of sensor measurements (e.g., 5000 sources vs. 64 sensors). The forward problem addresses the question of what would be measured at the sensors given a specific source activity and brain anatomy with varying conductivities between sources and sensors. It has a unique solution. In contrast, the inverse problem is ill-posed due to the vast number of sources surpassing the number of sensors (Baillet et al., 2001). Consequently, algorithms designed to solve the inverse problem impose constraints. E.g., ‘exact’ low resolution electromagnetic tomography (eLORETA; Pascual-Marqui et al., 2011) uses a weighted minimum norm criterion, while beamformers like linearly constrained minimum

variance (LCMV; Van Veen et al., 1997) and dynamic imaging of coherent sources (DICS; Gross et al., 2001) assume independence between different sources. In Study 1 (Pellegrini, Delorme, et al., 2023), we investigate the influence of the inverse solution on the accuracy of detecting FC. Due to the ill-posed nature of the problem, none of the inverse solutions can perfectly reconstruct the sources. Consequently, it is likely that some residual source leakage remains, which complicates the estimation of FC at the source level.

To address this challenge, *robust* FC metrics have been developed (e.g., Haufe et al., 2013; Nolte et al., 2004, 2008). Robust FC metrics capitalize on the fact that spurious interactions resulting from signal mixing occur instantaneously, while genuine physiological interactions exhibit a non-zero time delay. Thus, robust FC metrics selectively capture statistical dependencies characterized by a non-zero-time delay, and effectively suppress contributions with a zero-delay. There exists a range of robust FC metrics for linear phase-phase FC, like the imaginary part of coherency (iCOH; Nolte et al., 2004) or time-reversed Granger Causality (TRGC; Haufe et al., 2012). However, in the case of between-site PAC, there is no consensus on a robust metric yet.

1.5 FC analysis

A pipeline for analyzing inter-regional FC from M/EEG involves three key building blocks: Firstly, it includes the source reconstruction using algorithms such as eLORETA, LCMV, or DICS. Secondly, the multivariate patterns can be summarized into lower-dimensional patterns within regions of interest (ROIs), e.g., by selecting a representative source or using principal component analysis (PCA; Hillebrand et al., 2012). Finally, FC estimation is achieved by employing measures like, iCOH. These building blocks can be combined in diverse ways, creating numerous possible pipelines (see also Kapralov et al., 2023).

1.6 Research questions

Previous studies have indicated that the cortical locomotor network plays a key role in PD gait disturbances (Tard et al., 2015). Dynamic interactions among distributed cortical areas are crucial for integrating frontal, sensorimotor, and visuomotor information during gait to meet environmental needs (Mirelman et al., 2019). However, we currently lack

understanding cortical network dynamics during actual locomotion, particularly in unmedicated PD patients.

Research question (RQ) 1: How does locomotor information flow within the cortical network in unmedicated PD patients during walking?

Employing a multimodal approach, I focus on studying FC in a non-invasive setting, utilizing robust metrics for assessing FC to ensure reliability. My emphasis is on the beta band. First, I hypothesize a different FC pattern in the cortical motor network during walking compared to resting. Second, I hypothesize that FC during walking is correlated with gait characteristics such as stride duration.

Analyzing cortico-cortical FC from M/EEG is not trivial. Previous simulation studies have focused on assessing specific components of analysis pipelines. Studies have evaluated the accuracy of various inverse solutions (e.g., Allouch et al., 2022; Anzolin et al., 2019; Hashemi et al., 2021), compared different FC metrics (e.g., Haufe et al., 2012, 2013), or tested approaches to reduce signal dimensionality within ROIs (see, e.g., Basti et al., 2020). Others have focused on comparing results from full FC analyses in real data without the benefit of knowing the ground truth (Mahjoory et al., 2017). Despite the promise shown in these studies, the evaluation of complete data analysis pipelines, rather than individual steps, is still lacking. The lack of consensus on the most accurate and effective methods can lead to inconsistent results, hindering the progress of FC research. Therefore, there is a need to systematically validate entire analysis pipelines:

RQ 2: Which analysis pipelines detect inter-regional linear FC reliably?

With the ancillary research questions: What source localization technique is most suitable for detecting inter-regional FC? How should time series be aggregated within ROIs? Which metric is most reliable in detecting inter-regional FC? How does the performance of detecting ground-truth interactions vary depending on crucial data parameters like signal-to-noise ratio (SNR), the number of ground-truth interactions, noise composition, and the length of the interaction delay? I hypothesize that robust metrics will detect FC better than non-robust metrics. Further, I hypothesize that DICS, as a frequency-resolved beamformer, will lead to poor detection of directed FC, since it does not preserve the time structure of the signals.

An interesting continuation of FC studies in PD involves investigating non-linear FC, such as PAC. Previous investigations have found within-site PAC in PD patients, which was correlated with behavior (Gong et al., 2021). A highly interesting and novel direction is the investigation of PAC between different brain structures. This expansion of the existing portfolio of brain interactions holds the potential to enhance our understanding of neural communication mechanisms beyond linear FC (van der Meij et al., 2012). However, challenges arise due to biases introduced by volume conduction effects in conventional measurement methods for between-region PAC: traditional measures of PAC may be highly sensitive to signal mixing, leading to false positives and biased results. Thus, a robust between-site PAC measure is needed. A promising direction is the anti-symmetrized bispectrum (ASB; Chella et al., 2014), having demonstrated its ability to measure non-linear interactions while mitigating mixing effects and suppressing Gaussian noise. However, it is not yet clear whether it can be used for between-site PAC measurements.

RQ3: Can the ASB reliably measure between-site PAC without being affected by signal mixing?

I hypothesize that the ASB method can effectively measure between-site PAC without being affected by biases induced by signal mixing.

2 Methods

2.1 Simulations

When analyzing real brain data, ground-truth information flow patterns are unknown. Consequently, testing the accuracy of analysis pipelines on real data is not feasible. To evaluate the performance of a pipeline, the straightforward approach is to use simulation data. In the following sections, I describe the workflow of simulation Study 1 (Pellegrini, Delorme, et al., 2023) and 2 (Pellegrini, Nguyen, et al., 2023). Since they are closely related and build upon each other, I describe them here jointly. Thus, all descriptions apply to both studies unless indicated otherwise. MATLAB code to reproduce the results of Study 1 and 2 is available online ¹.

¹ <https://github.com/fpellegrini/FCsim> and <https://github.com/fpellegrini/PAC>

2.1.1 Data generation

In the first step, we simulated ground-truth neuronal data, that is, a set of time series with known ground-truth functional connections. For Study 1, which investigates linear phase-to-phase coupling, we simulated the ground-truth signal as white noise filtered in the alpha band. A unidirectional interaction was modeled by copying the time series and introducing a small time delay. For Study 2, which investigates PAC, we investigated two settings: one with a true between-site PAC interaction, and one with a within-site PAC signal which spread to other locations. To generate the between-site interaction, we generated a SO in the alpha band (10 Hz), and a FO in the gamma band (60 Hz), whose amplitude was modulated by the phase of the SO. To generate the within-site PAC signal, we generated the SO and FO, and then merged them into one signal. In all simulations, these ground-truth signals were then mixed with a pink background noise.

In addition to the interacting ground-truth signal, we generated non-interacting sources called brain noise. These time series consisted only of random pink noise, without any signal or interaction.

We used a three-dimensional source model (Mazziotta et al., 1995) of the brain, with each source belonging to one of the 68 ROIs of the Desikan-Killiany atlas (Desikan et al., 2006). In each ROI, we placed one time series, some interacting and some containing only brain noise. Subsequently, we projected the interacting and non-interacting source activity to a sensor space with 97 sensors by using a leadfield, generated from the ICBM template head model (Mazziotta et al., 1995). At the sensor level, we generated white noise for each sensor, and then mixed the signal, brain noise, and sensor noise with a specified SNR. Finally, a 1 Hz high-pass filter was applied.

2.1.2 Analysis pipeline

The analysis pipelines consisted of three main steps: source reconstruction, dimensionality reduction within ROIs, and FC estimation. In Study 1, we tested a whole range of approaches that are used commonly in the literature (see Figure 1; e.g., Babiloni et al., 2018; Gomez-Rodriguez et al., 2010; Kapralov et al., 2023; Perinelli et al., 2022; Schoffelen et al., 2017).

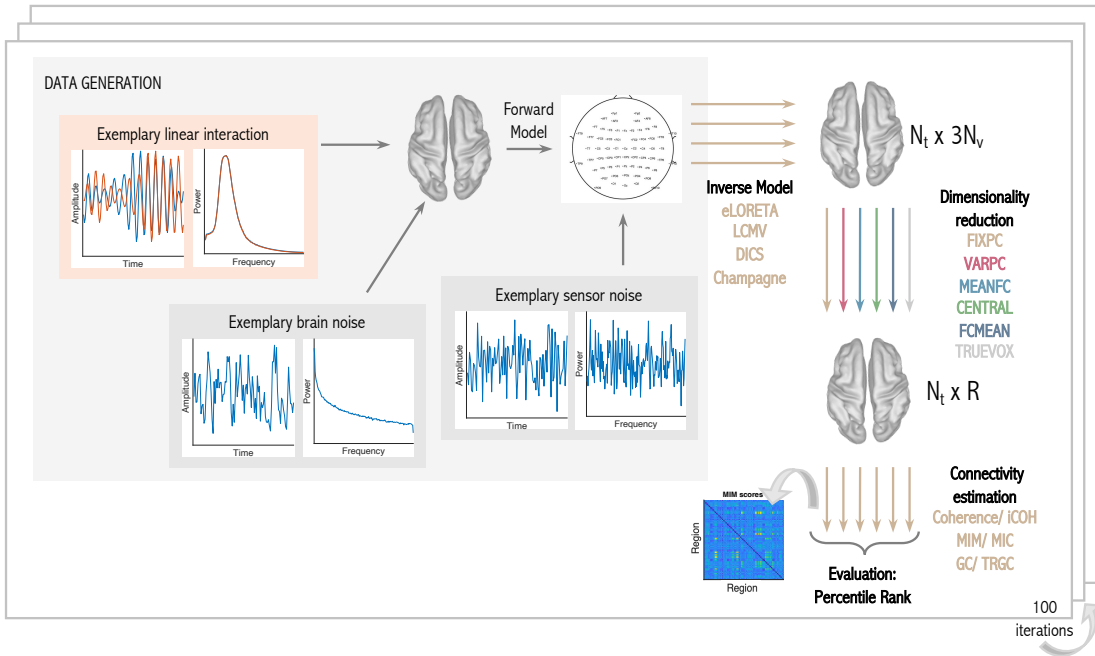


Figure 1. Structure of the linear functional connectivity simulation.

Every experiment consisted of five consecutive steps: (1) Data generation. (2) Source projection using an inverse model. (3) Dimensionality reduction within regions. (4) Functional connectivity estimation. (5) Performance evaluation. Every experiment was carried out 100 times. Modified from (Pellegrini, Delorme, et al., 2023).

Source projection

In Study 1, we tested four inverse methods: eLORETA (Pascual-Marqui et al., 2011), LCMV (Van Veen et al., 1997), DICS (Gross et al., 2001), and Champagne (Wipf et al., 2010). In short, eLORETA optimizes the estimation by ensuring spatially smooth current density distributions. LCMV and DICS are both beamformers, maximizing the contribution of sources of interest while minimizing the contribution from all other sources by amplifying the activity from the sources of interest with unit gain. While LCMV acts on the broad-band signal, DICS provides a spectrally resolved source estimate. The Champagne algorithm utilizes a hierarchical sparse Bayesian inference approach. It applies a zero-mean Gaussian prior independently to each voxel representing a potential source of neural activity. This allows for more precise localization of the underlying sources while promoting sparsity and reducing noise in the estimation.

Aggregation within regions

By projecting the sensor activity to source level, we obtained three time series for each estimated source, representing the activity in the three spatial dimensions of a current dipole. In the next pipeline step, we aggregated all time series within a ROI. One approach to this is to apply a PCA and select the strongest PCs, which account for most of the variance within a region, for further processing. In Study 1, we tested the selection of fixed numbers of PCs (FIXPC pipelines), as well as variable number of PCs for every region, depending on how much variance they account for (VARPC pipelines). We also tested a pipeline that selects the central source of every region for further processing (CENTRAL pipeline), a pipeline that first calculates the FC score for every source combination of two regions and subsequently averages all scores (FCMEAN pipeline), a pipeline that averages the time series and subsequently calculates the FC score (MEANFC pipeline), and a baseline pipeline whose FC score is based on the activity at the ground-truth source location (TRUEVOX pipeline).

In Study 2, we built on the insights gained in Study 1 and employed a pipeline consisting of LCMV source projection and PCA dimensionality reduction to one PC for every region (see Figure 2).

Functional connectivity measurement

In Study 1, we evaluated six different metrics for their ability to correctly measure linear FC: coherence (Nolte et al., 2004; Nunez & others, 1997), iCOH (Nolte et al., 2004), the multivariate interaction measure (MIM) and the maximized imaginary coherency (MIC; Ewald et al., 2012), GC (Bressler & Seth, 2011; Granger, 1969), and TRGC (Haufe et al., 2012; Winkler et al., 2016). In the following I give a short overview of these metrics.

Complex-valued coherency C between two (multivariate) Fourier-transformed time series $x(f, e) \in \mathbb{C}^K$ and $y(f, e) \in \mathbb{C}^L$ at frequency f and epoch e , is defined as:

$$C_{xy}(f) = \frac{s_{xy}(f)}{(s_{xx}(f) s_{yy}(f))^{1/2}} \in \mathbb{C}^{K \times L}, \text{ where}$$

$S_{xy} = \langle x(f, e) y^*(f, e) \rangle_e \in \mathbb{C}^{K \times L}$ denotes the cross-spectrum, with $.*$ representing the complex conjugation and $\langle . \rangle$ denoting the expectation value which is approximated by averaging over epochs e . COH, iCOH, MIM and MIC are based on coherency. Its absolute value, COH, indicates the stability of the phase difference. COH is sensitive to both zero-

delay and non-zero-delay synchronizations, which can be problematic in M/EEG measurements. In contrast, iCOH, the absolute value of the imaginary part of coherency, is a more robust measure of FC, effectively filtering out spurious zero-delay synchronizations caused by factors such as volume conduction or source leakage. MIM and MIC build on iCOH but capture interactions between multiple time series. That is, they are designed to maximize the iCOH between two sets of multivariate time series in such a way that the iCOH between the resulting projected signals is maximized. GC is a method to determine the directional interactions between time series by evaluating their predictability. In short, if the past information of one time series A can improve the prediction of another time series B better than using the past information of time series A alone, then GC can infer that A is Granger-causal for B. This approach not only detects the presence of a connection between time series, but also estimates its direction. GC, like COH, can produce erroneous results due to signal mixing. TRGC overcomes this limitation by testing the temporal order of the time series. That is, TRGC estimates the directed information flow twice, once on the original time series and once on a time-reversed version of the time series. If the effect is not an artifact due to signal mixing, GC will be reduced or reversed when the temporal order of the time series is reversed.

In Study 2, we tested approaches for reliable between-region PAC detection: three approaches related to the mean vector length modulation index (MI), and two approaches based on the cross-bispectrum. The MI (Canolty et al., 2006) is computed by first calculating the phase $\varphi_s(t)$ at time point t of a low-frequency signal using the Hilbert transform, and calculating the amplitude envelope $a_f(t)$ of a high-frequency signal using the absolute value of its Hilbert transform. The MI is the temporal average of the complex values obtained by multiplying the amplitude envelope by the complex exponential of the phase angle: $MI = \left| \frac{1}{N_t} \sum_{t=1}^{N_t} z_t \right| \in \mathbb{R}$, with $z(t) = a_f(t)e^{i\varphi_s(t)}$, $t = 1, \dots, N_t$, with N_t denoting the number of time points, and $| \cdot |$ denoting the absolute value.

The MI method is not robust to signal mixing. In Study 2, we investigated whether it can be robustified by an orthogonalization of the time series. We used the multivariate symmetric orthogonalization technique (Colclough et al., 2015) on ROI time series for this purpose, which is based on the Löwdin method and can be solved using singular value decomposition (SVD).

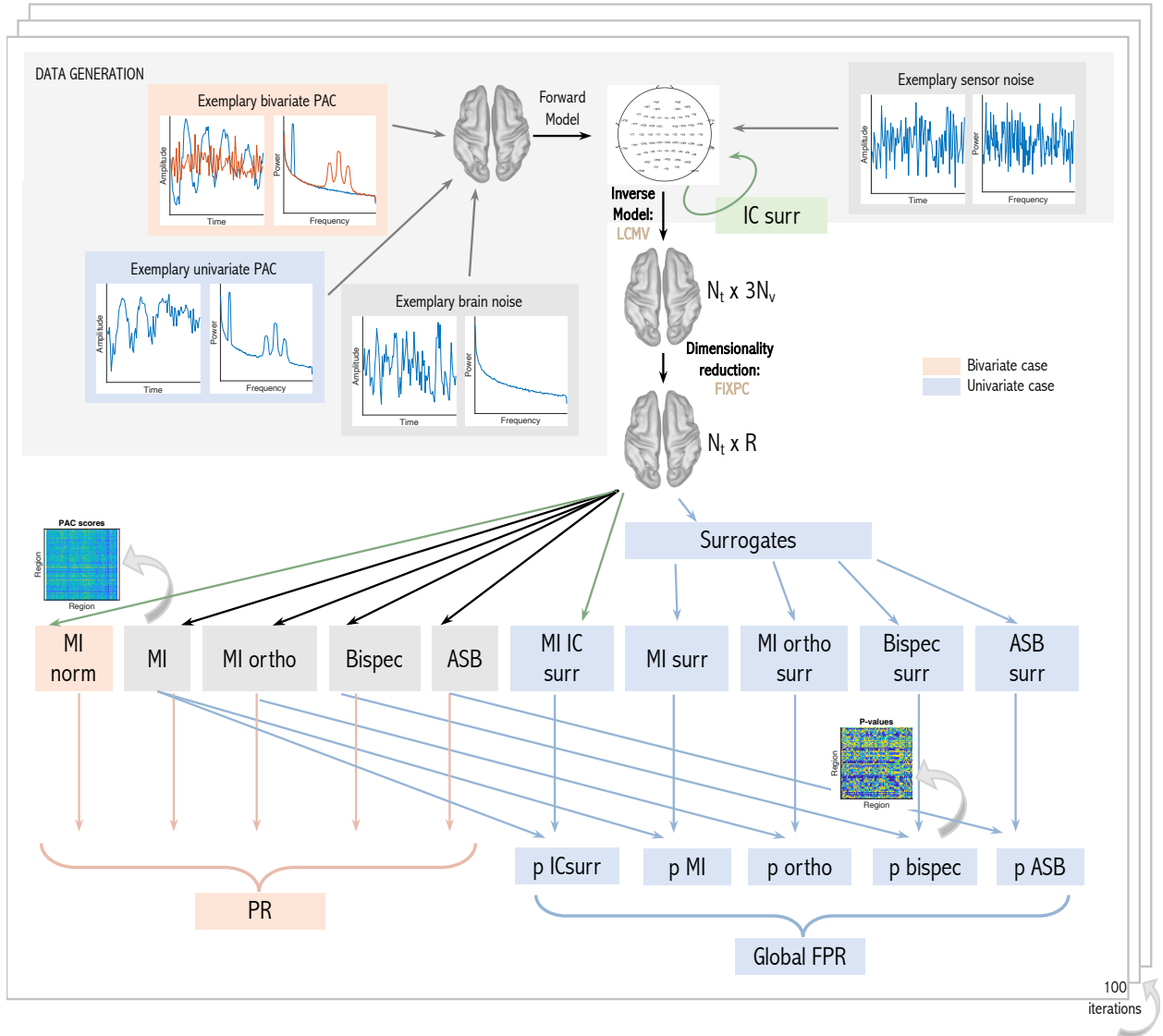


Figure 2. Structure of the phase-amplitude coupling simulation.

Every experiment consisted of the following steps: data generation, source reconstruction, dimensionality reduction with a principal component analysis, and calculation of inter-regional PAC scores. In the bivariate case, PAC detection performance is evaluated with the percentile rank (PR). In the univariate case, null distributions are generated from surrogate data (surr) and a *p*-value for every region combination is calculated. From this, we calculate the global false positive rate (global FPR). Modified from (Pellegrini, Nguyen, et al., 2023).

Another potential approach to control for signal mixing is to compare the MI to a null distribution generated from shuffled independent components (Shahbazi et al., 2010). First, an independent component analysis (ICA; e.g., Bell & Sejnowski, 1995) is run on the time series matrix, and applied to unmix the sensor data to ICs. Next, the order of epochs of the two IC time series is permuted. The IC surrogates are then projected back to the original space, and the MI is calculated from these surrogate data.

Recent studies (Kovach et al., 2018; Zandvoort & Nolte, 2021) suggested that the cross-bispectrum can also be used to measure PAC. Indeed, it has been shown that a specific subtype of the bispectrum, namely the cross-bispectrum between two channels, evaluated at two frequencies, is closely related to the MI for specific filter settings (Kovach et al., 2018; Zandvoort & Nolte, 2021). To calculate the bispectrum between two time series, the data are first epoched and Fourier-transformed using a symmetric Hanning window. The bispectrum is then calculated from the Fourier estimate between the two channels k and m at two different frequencies f_1 and f_2 , and averaged over the epochs:

$$B_{k,m,m}(f_1, f_2) = \frac{1}{N_e} \sum_e^{N_e} x_{k,e}(f_1) x_{m,e}(f_2) x^*_{m,e}(f_1 + f_2) \in \mathbb{C}.$$

As the MI, the bispectrum can be affected by signal mixing. In Chella et al. (2014), it has been suggested that the bispectrum can be robustified by an anti-symmetrization. Anti-symmetrization is achieved by subtracting the bispectrum between the channels m , k , and m from the bispectrum between k , m , and m :

$$B_{[k,m,m]}(f_1, f_2) = B_{k,m,m}(f_1, f_2) - B_{m,k,m}(f_1, f_2).$$

In Study 2, we tested for the first time whether the ASB can also be used to achieve a robust estimate for between-site PAC.

2.1.3 Evaluation

For all bivariate interactions, including the simulated linear phase-phase interactions in Study 1, and the bivariate phase-amplitude interactions described in Study 2, we employed the percentile rank (PR) metric for evaluating the detection performance. In short, the PR gives the percentage of FC scores of all region combinations that are less high than the FC score of the ground-truth region combination.

Additionally, we evaluated global false positive rate (gFPR) of all pipelines in the univariate case. We used an epoch-permutation approach to obtain a null distribution and statistically assessed significant between-region interactions (see Figure 2). The gFPR was then defined as the number of significant PAC interactions divided by the total number of PAC scores.

2.2 Minimal exploratory analysis of function connectivity in motor imagery

Motor imagery (Mtl) involves mentally simulating movement and has been shown to elicit neural activity measurable by EEG in primary sensory and motor areas (Neuper et al., 2005). It is very likely that Mtl may also be reflected in higher FC from and to these areas, making Mtl an ideal use case for showcasing our recommended pipeline's applicability. Further, it is possible that PAC may arise during Mtl, indicating cognitive integration and communication processes in movement planning. Investigating the occurrence of between-region PAC or within-region PAC adds further depth to understanding the underlying neural processes.

Here, I present an exploratory analysis² of FC during Mtl tasks (published as part of Study 1 and 2). The data used in this analysis come from the Berlin arm of the VitalBCI study (Blankertz et al., 2010; Sannelli et al., 2019) involving 39 participants who performed an experiment where they imagined movements with either their left or right hand (Mtl Calibration set 1-3). In each trial, a visual stimulus presenting a fixation cross accompanied by an arrow indicating the task (left or right Mtl) was presented. After 4 seconds, the stimulus disappeared, and the screen remained black for 2 seconds. Each participant completed 75 trials for each Mtl condition. During the experiment, EEG data were recorded using a 119-channel whole-head EEG system with a sampling rate of 1000 Hz. However, for our analyses, we used a subset of 90 channels.

We selected 26 subjects based on previous studies that confirmed effective separation of left and right Mtl conditions using statistical and machine learning techniques (referred to as 'Category I' in Sannelli et al., 2019).

We filtered the EEG data using a high-pass filter of 1 Hz, and a low-pass filter of 45 Hz, all implemented as zero-phase forward and reverse second-order digital high-pass Butterworth filters. The data were subsequently downsampled to 100 Hz. We visually inspected the power spectrum and the topographical distribution of alpha power to identify and reject channels affected by artifacts (an average of 1.19 channels per participant, ranging from zero to five), followed by a spherical scalp spline interpolation.

Next, we computed a leadfield using the Colin27 5003 Standard-10-5-Cap339 template head model. The data were segmented into epochs ranging from 1 to 3 seconds post-

² Code available under <https://github.com/fpellegini/MotorImag>

stimulus presentation, and the left and right Mtl trials were separated for further analysis. To compute the LCMV source projection filter and apply it to the sensor data, we utilized the *pop_roi_activity* function of our new ROIconnect plugin³ for EEGLAB.

2.2.1 Linear functional connectivity in left vs. right motor imagery

For Study 1, we estimated inter-regional linear FC based on the three strongest PCs of each region. The MIM values were averaged across frequencies ranging from 8 to 13 Hz. To simplify the MIM matrix we summed up the MIM estimates for each region (netMIM).

We evaluated the statistical significance of the netMIM for each region independently for the two Mtl conditions by using a permutation test. The *p*-values of the subjects were aggregated using Stouffer's method (Dowding & Haufe, 2018). Finally, we applied false-discovery rate (FDR)-correction (α -level = 0.05) to account for multiple comparisons. Additionally, we examined the statistical differences between the netMIM scores for the left- and right-hand Mtl conditions using paired t-tests for each region.

2.2.2 Phase-amplitude coupling using bispectral metrics

In Study 2, we computed within-region and between-region PAC between the left and right precentral and post-central cortices. We estimated PAC once using the bispectrum without anti-symmetrization and once using the ASB to demonstrate the different behavior of the two metrics. We considered phase frequencies ranging from 1 to 12 Hz and amplitude frequencies ranging from 1 to 50 Hz with a resolution of 1 Hz. It is important to note that Fourier coefficients can only be accurately inferred up to the Nyquist frequency of 50 Hz, and the third term of the bispectrum includes the sum of the phase and amplitude frequencies. Thus, our analyses were constrained to frequency combinations where the sum of the phase and amplitude frequency is lower than the Nyquist frequency. To prevent interference between FOs and SOs, we limited our analysis to FOs with frequencies at least three times higher than the corresponding SO, avoiding confounds with harmonics. To assess the statistical significance of the observed PAC scores, we again applied a permutation test. To aggregate the resulting *p*-values across subjects, we again utilized Stouffer's method (Dowding and Haufe, 2018).

³ <https://github.com/sccn/roiconnect>

2.3 Functional connectivity in walking patients with Parkinson's Disease

Study 3 (Pellegrini, Pozzi, et al., 2023) aimed at characterizing directed FC in the motor network of walking patients with PD. My contribution lied in the analysis of the recorded EEG, including the individual head modeling, electromyography (EMG), and inertial unit measurement (IMU) data, and writing the first draft of the paper. That is, all credits for data recording and experimental design go to my colleagues Dr. Chiara Palmisano and Prof. Ioannis Isaias. For the sake of completeness, I will still describe the data acquisition and experimental design here briefly.

2.3.1 Subjects and experimental design

We included ten patients with PD (five females) who did not have any other diseases or impairments, with an average age of 60 ± 7 years, and disease duration of 9 ± 7 years. Patients were required to be able to walk for at least three minutes without assistance and were assessed while in the OFF-medication and OFF-stimulation states. Disease severity was assessed using Unified Parkinson's Disease Rating Scale motor part (UPDRS-III; Martínez-Martín et al., 1994) and the disease stage was assessed using the Hoehn and Yahr scale (Bhidayasiri & Tarsy, 2012). One patient was removed from the analysis due to high artifact levels in their EEG data.

The experiment had two conditions: resting and walking. During the resting condition, participants stood still with their eyes open, while during the walking condition, participants walked barefoot at their self-selected speed along an ellipsoidal path.

2.3.2 Positron emission tomography

Fluorodeoxyglucose-positron emission tomography (FDG-PET) scans were performed once after 10 min of resting and once after 10 min of walking. The PET images were processed using statistical parametric mapping (SPM8) and the standardized uptake value ratio (SUV) was calculated. A pairwise t-test was performed for each region to estimate the change of activity between the resting and walking recording. The regions that showed a significant activity increase were selected as ROIs for the EEG power and FC analyses.

2.3.3 Kinematic measures

The kinematics of lower limbs were recorded throughout the walking period using EMG and IMU. Heel strike and toe-off events were detected from the angular velocity profiles

measured with respect to the medio-lateral axis by the IMU. Swing duration was calculated as the duration between successive toe-off and heel strike events. Stride duration was calculated as the time difference between two successive heel strikes. In three subjects, IMU recordings were not possible, and gait events were predicted from EMG activity following the protocol that we published in Haufe et al. (2023).

2.3.4 Electroencephalography

Preprocessing

EEG data were collected using a 64-channel EEG device (MOVE, Brain Products). The data were resampled to 125 Hz and filtered using a lowpass filter at 45 Hz, and a highpass filter at 1 Hz. Artifactual channels and segments were identified using automated artifact rejection (Kothe & Makeig, 2013) and manual inspection. Artifactual channels were replaced with spherical spline interpolation. We removed eye movement artifacts using regression of the time series of two electrodes closest to the eyes to all other channels. Since walking imposes major movement artifacts on EEG data (Kline et al., 2015), we applied artifact subspace reconstruction (Kothe & Makeig, 2013) to further clean the data. Then, ICA was applied, and eye, heart, and muscle ICs were visually detected and rejected. Artifactual segments were excluded for ICA but retained for subsequent analyses to ensure the continuity of the data. Finally, the EEG data were re-referenced to a common-average reference.

Individual head models

Individual volume conductor models were constructed for eight out of nine participants to account for their different head anatomies. For one participant without available structural magnetic resonance imaging (MRI), the ICBM-152 template (Mazziotta et al., 1995) was used. MRI and EEG channel positions were co-registered using fiducial points. The source model consisted of 2000 locations evenly spaced and placed on the cortex surface. The leadfields were constructed based on exact channel positions and individual anatomies derived from structural MRI data. The MRI data were segmented into grey matter and white matter, and personalized head models were constructed with the boundary element method (BEM) with three layers (scalp, outer skull, inner skull). Based on our insights from Study 1, we used a personalized LCMV filter to project the channel

time series to the source locations. Sources were labelled using the automated anatomical labelling atlas (Tzourio-Mazoyer et al., 2002).

Power and functional connectivity estimation

We cut each trial into intervals of one-minute length to avoid a bias in the FC measures (Vinck et al., 2010). Power and FC were calculated for every interval and treated as different samples for linear mixed-effects (LME) modeling. We chose the pipeline that achieved the best performance in the simulations in Study 1. That is, we employed PCA within every region, selected the three strongest PCs for further processing, and finally calculated directed FC using the multivariate version of TRGC (Barnett & Seth, 2014; Haufe et al., 2012). Power was calculated using the Welch method for every source and averaged within regions. Power and FC scores were averaged within two personalized frequency bands of interest (BOIs): a low-frequency band containing theta and alpha rhythms, and the beta band.

2.3.5 Statistical evaluation

We used LMEs to compare power and FC between resting and walking conditions and to investigate the relationship between gait impairment and power/FC. In both analyses, we included the subject number and hemisphere as random and fixed factors, respectively. We used Pearson's correlation to assess the relationship between disease severity, measured by the UPDRS-III score, and kinematic scores. FDR-correction was used to correct for multiple comparisons.

2.4 ROIconnect toolbox

Based on the results of Study 1 and 2, we implemented the recommended pipelines in the EEGLAB toolbox, now available as a plugin called ROIconnect⁴. The plugin includes functionalities for analyzing and visualizing spectral power, inter-regional linear phase-phase FC, and PAC in EEG source space. A detailed description of the toolbox's functionality can be found in Study 1 and 2.

⁴ <https://github.com/sccn/roiconnect>

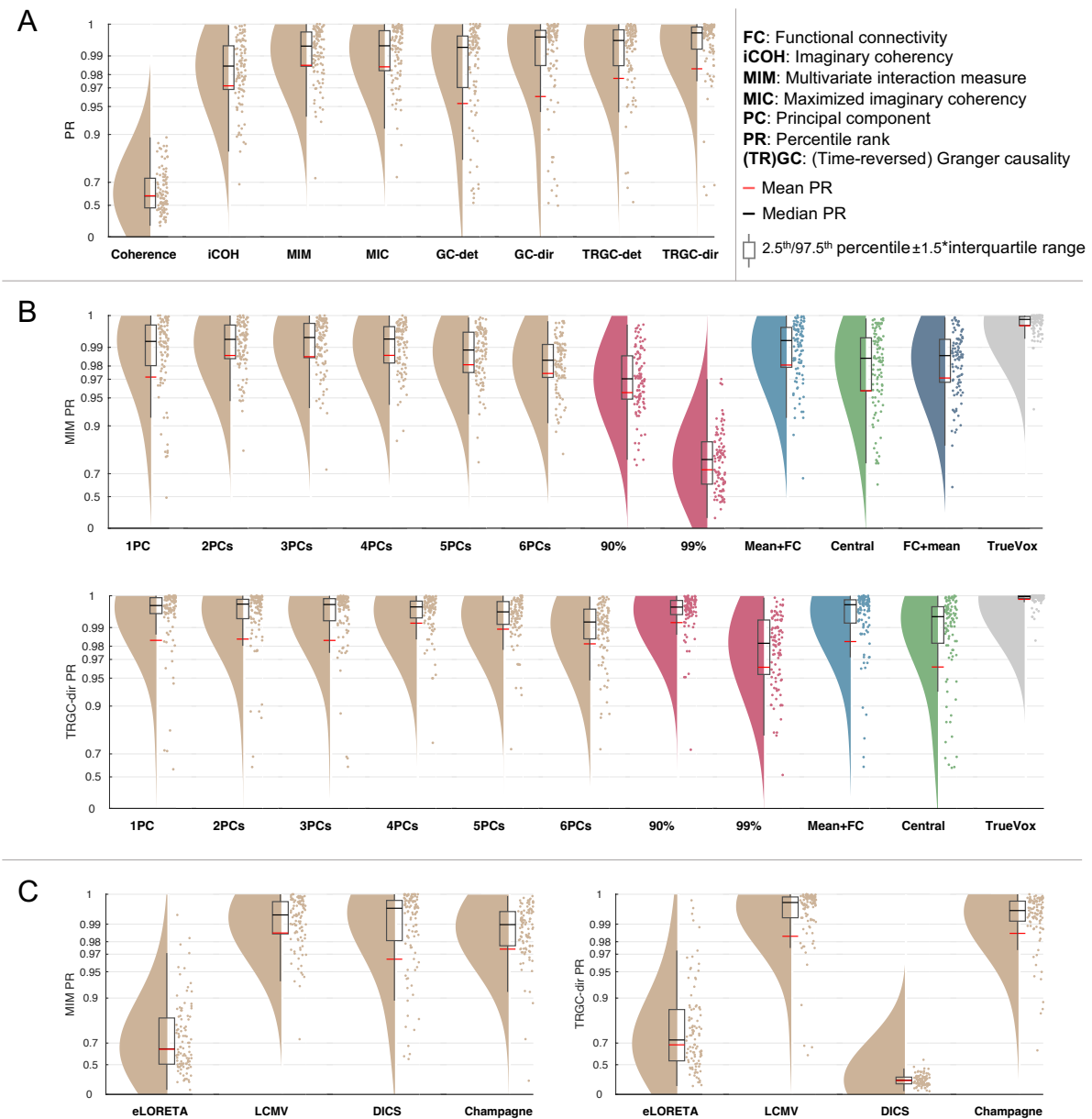


Figure 3. Performance of linear functional connectivity (FC) pipelines in their ability to detect inter-regional ground-truth interactions.

A) Comparison of FC metrics. B) Comparison of pipelines with different types of data aggregation within regions. Top: Undirected FC reconstruction performance achieved using the multivariate interaction measure (MIM). Bottom: Directed FC reconstruction performance achieved using time-reversed Granger causality (TRGC). C) Comparison of inverse solutions. Left: Undirected FC reconstruction performance achieved using the MIM. Right: Directed FC reconstruction performance achieved using TRGC. Modified from (Pellegrini, Delorme, et al., 2023).

3 Results

3.1 Linear phase-phase coupling

In Study 1, we tested the performance of COH, iCOH, MIC, MIM, GC, and TRGC on their ability to detect ground-truth FC. Unless indicated otherwise, we used the following default values: the LCMV inverse solution, SNR = 3.5 dB, brain noise-to-signal noise ratio = 0 dB, two ground-truth interactions, a time delay randomly chosen between 50 and 200 msec, and one generated source per region.

The results show that MIM, MIC, and TRGC most reliably detect ground-truth FC (Figure 3A). COH and GC were less reliable in detecting ground-truth interactions ($p_{COH, MIM} < 10^{-4}$; $p_{GC, TRGC} < 10^{-4}$).

An important step in the analysis of inter-regional FC is the type of dimensionality reduction within regions. In the next experiment, we compared different approaches to aggregate neural activity within regions (Figure 3B). The results show that FIXPC pipelines generally perform better than most other pipelines for MIM. Within the FIXPC pipelines, the pipelines with two, three, or four PCs perform best. The VARPC pipelines, which select a different number of PCs for each region, perform significantly worse ($p_{VARPC, FIXPC3} < 10^{-4}$). The result is similar for directional estimation with TRGC. However, VARPC90 achieves competitive performance here as well.

The next experiment (Figure 3C) tested the effect of the type of inverse solution on pipeline performance. The beamformer solutions and Champagne outperformed eLORETA in detecting undirected FC (all $p < 10^{-4}$). LCMV had a slight advantage over Champagne in this regard ($p_{Champagne, LCMV} = 0.0013$). In determining directionality, LCMV provided accurate estimates, while DICS hindered detecting ground-truth interaction direction ($p_{DICS, LCMV} < 10^{-4}$) and eLORETA had lower overall performance ($p_{eLORETA, LCMV} < 10^{-4}$).

Note that in Study 1, we additionally present the influence of different types and strengths of the SNR, the number of ground-truth interactions, and the magnitude of the time delay on the accuracy of FC estimates.

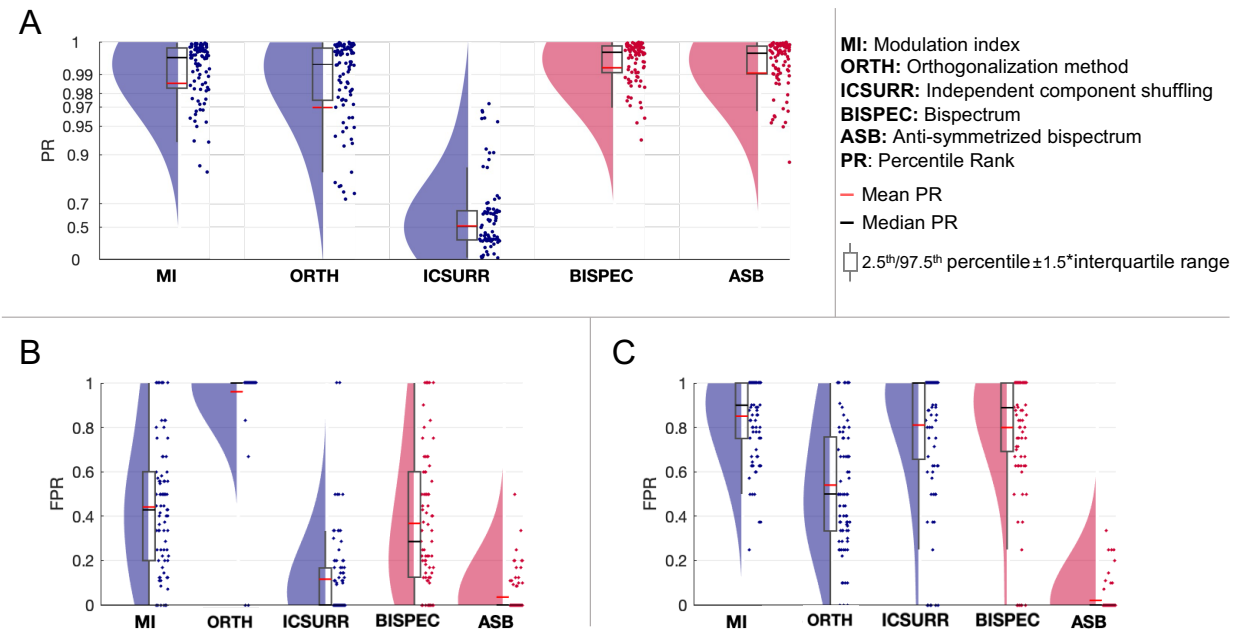


Figure 4. Comparison of different phase–amplitude coupling (PAC) metrics.

A) Performance of detecting ground-truth between-region PAC, measured by the percentile rank. B+C) Ability to avoid detecting spurious between-region PAC, measured by the global false positive rate (gFPR). B) gFPR of detecting PAC between low-frequency phase of ground-truth seed regions and high-frequency amplitude of neighboring regions. C) gFPR of detecting PAC between high-frequency amplitude of ground-truth seed regions and low-frequency phase of neighboring regions. Modified from (Pellegrini, Nguyen, et al., 2023).

3.2 Phase-amplitude coupling

Study 2 evaluated the performance of different PAC metrics in detecting between-region PAC interactions. We found that bispectral metrics perform better than MI-based metrics, with the ASB performing similarly well as the bispectrum without antisymmetrization (Figure 4A). Interestingly, both MI extensions, MI+orthogonalization and IC shuffling, perform worse than the original MI.

In a second experiment, we evaluated the ability of the metrics to avoid measuring spurious between-region PAC in the univariate setting. The ASB detects the fewest false positives between the phase of the seed region containing the univariate PAC and the amplitude of neighboring regions, whereas the MI and bispectrum without antisymmetrization fail to remove the effect of source leakage and detect more false positives (Figure 4B). The pattern is similar for PAC detection between the amplitude of the ground-truth seed region containing univariate PAC and the phase of the neighboring regions, with ASB still yielding the fewest false positives (Figure 4C).

Note that in Study 2, we additionally present the influence of SNR, and the number of ground-truth interactions on the accuracy of bivariate PAC detection, as well as the results of spurious between-region PAC detection in the univariate case for non-neighboring regions.

3.3 Exploratory analysis of functional connectivity in motor imagery

In Studies 1 and 2, we estimated linear FC and PAC from EEG data recorded during a Mtl experiment. In Figure 5A and B, we show the $-\log_{10} p$ -values resulting from a test of the net MIM scores per region against a null distribution. Here we already see a slight lateralization in netFC, depending on the condition of right vs. left Mtl. In Figure 5C, we present results from a direct comparison between the two conditions. Here, the lateralization of the netFC becomes clearly visible.

In Figure 6, we present the results of the analysis of PAC between the left and right pre- and post-central cortices during right-hand Mtl. For Figure 6A we used the bispectrum without anti-symmetrization to estimate PAC. Here we observe significant within-region PAC as well as between-region PAC, primarily involving the phase of low-frequency oscillations and the amplitude of beta and gamma oscillations.

In Figure 6B, we present the results obtained using the ASB. We do not observe any significant univariate PAC in any of the four regions. Furthermore, a notable difference is evident when comparing the PAC between regions within the same hemisphere in Figure 6A compared to Figure 6B. The effects observed with the uncorrected bispectrum seem to be influenced by spurious between-region PAC, likely originating from signal spread between the pre- and post-central cortices within the same hemisphere. This effect appears to be successfully eliminated by antisymmetrization.

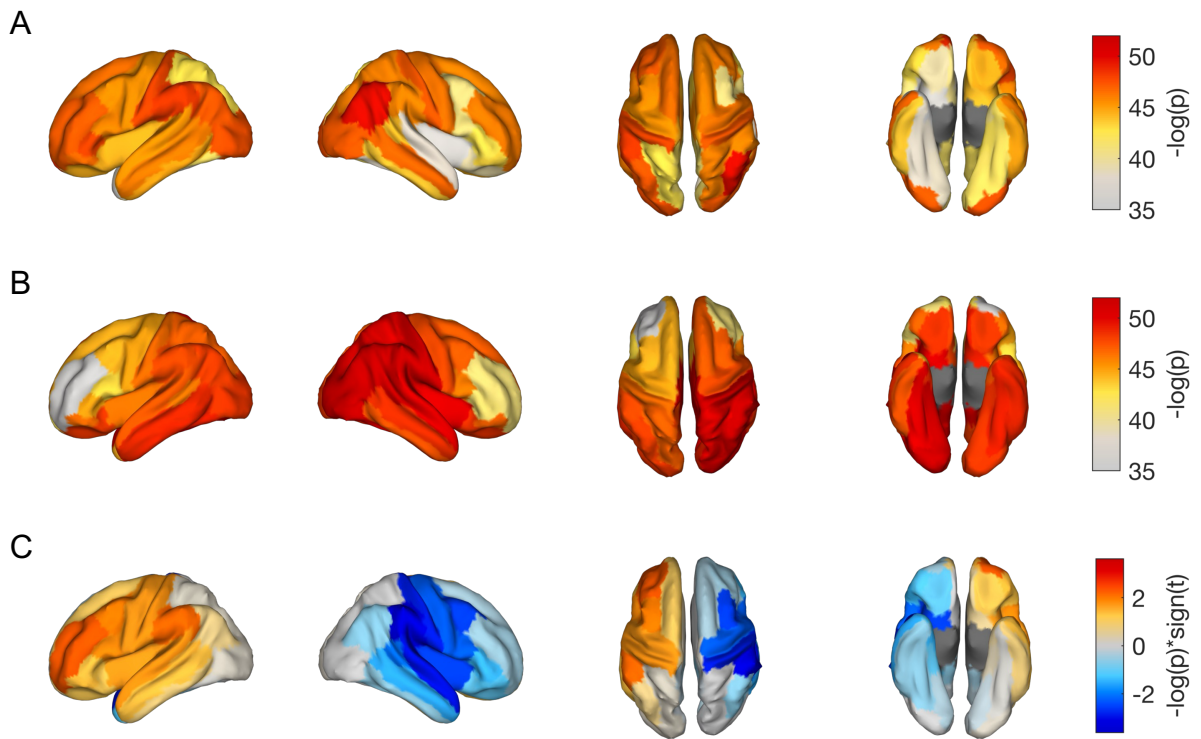


Figure 5. Results of the exploratory analysis of functional connectivity (FC) in left- and right-hand motor imagery (Mtl) tasks.

A) Statistical significance of the netMIM scores during left Mtl ($-\log_{10} p$ -values). B) Statistical significance of the netMIM scores during right Mtl ($-\log_{10} p$ -values). C) Comparison of netMIM scores in left- vs. right-hand Mtl tasks ($-\log_{10} p$ -values, multiplied with the sign of the t-statistic). Positive values indicate higher FC in the left-hand Mtl trials. From (Pellegrini, Delorme, et al., 2023).

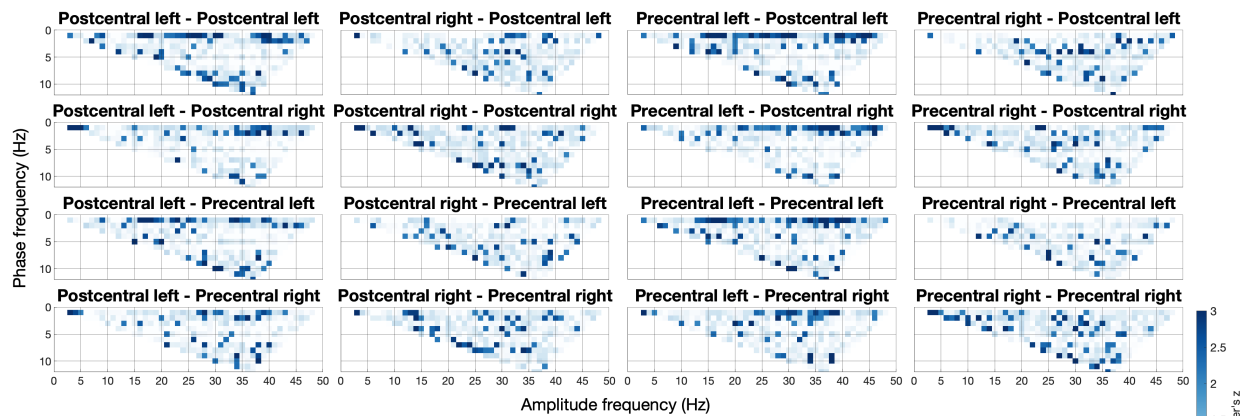
3.4 Functional connectivity in walking patients with Parkinson's Disease

We found a positive correlation between stride duration and UPDRS-III motor score ($p = 0.017$, coeff = 0.800, Figure 7B), but no significant correlations for swing duration. Therefore, stride duration was chosen for further analysis.

We investigated changes in brain metabolic activity during walking compared to the resting condition. Our findings reveal a distributed pattern of metabolic activation in the frontal, parietal, and occipital cortical areas during unperturbed overground walking. Specifically, increased metabolic activity was observed in the supplementary motor area (SMA), paracentral lobule, postcentral gyrus, superior parietal lobule, precuneus, superior occipital gyrus, middle occipital gyrus, cuneus, calcarine fissure and surrounding cortex, and lingual gyrus. At the subcortical level, we observed activation in the thalamus and

cerebellum, while no activation was found in the basal ganglia nuclei. Notably, no hypoactive brain regions were identified.

A



B

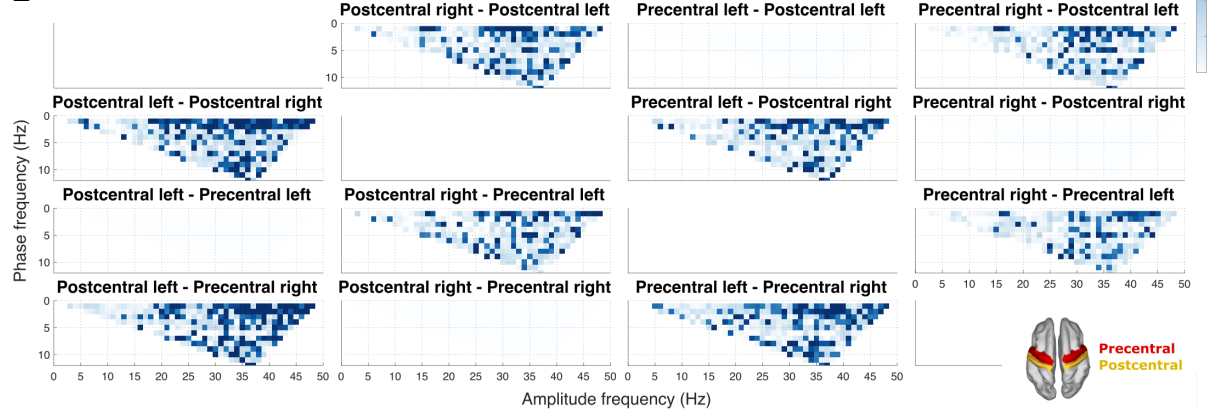


Figure 6. Phase-amplitude coupling (PAC) between the left and right postcentral and precentral cortices during motor imagery of moving the right hand.

A) Results of the PAC analysis assessed by the bispectrum without anti-symmetrization. B) Results of the PAC analysis assessed by the anti-symmetrized bispectrum. Displayed are z-scores resulting from Stouffer's method of combining subject-level p -values. In both figures, statistical significance ($p < 0.05$) is indicated by color opacity. From (Pellegrini, Nguyen, et al., 2023).

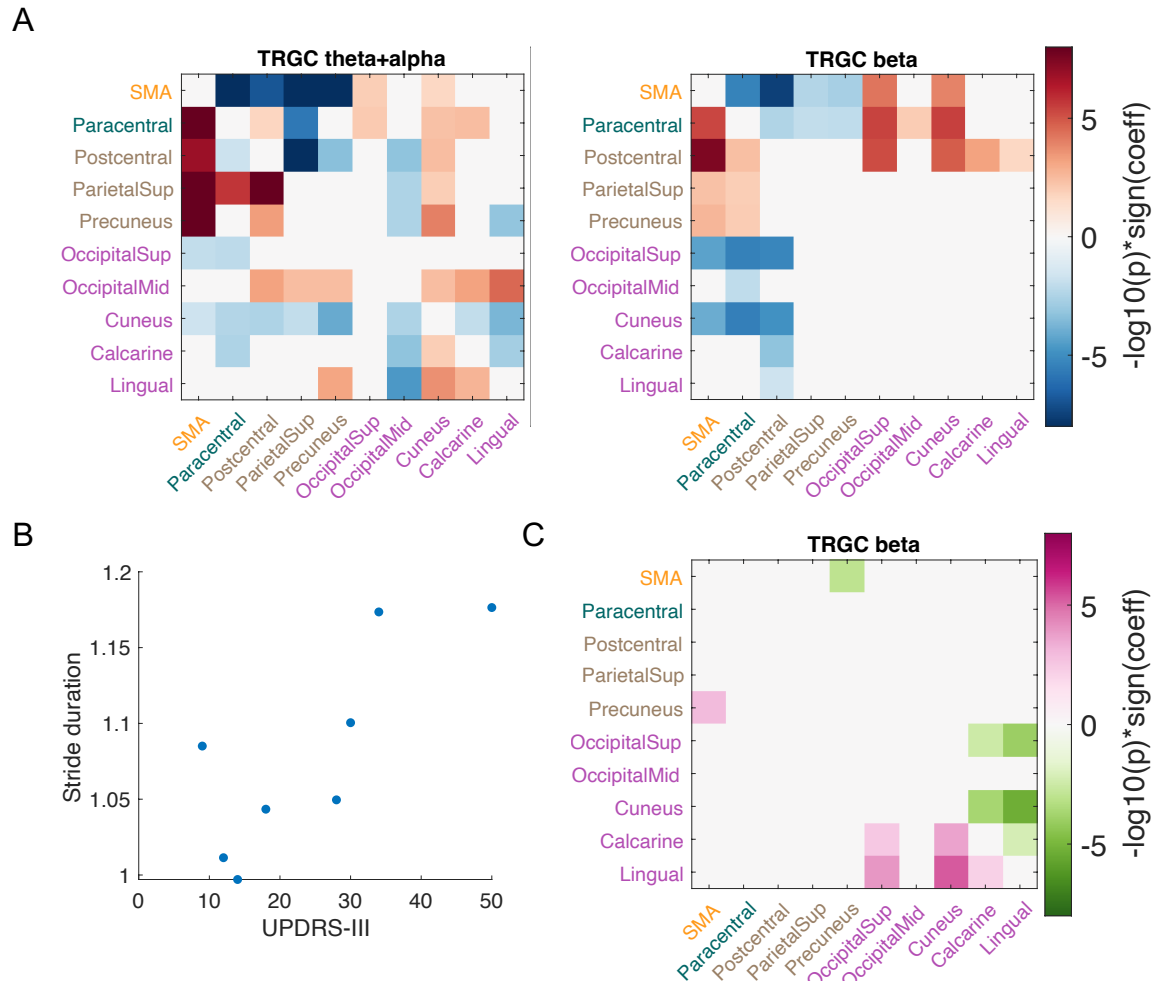


Figure 7. Kinematic and functional connectivity (FC) patterns in walking patients with Parkinson's Disease.

A) Comparison of EEG markers between resting and walking conditions in the theta+alpha and beta bands. Shown are signed $\log_{10} p$ -values. Changes in directed FC were estimated by time-reversed Granger causality. Red colors either indicate more information flow from the ROI on the Y-axis to the ROI on the X-axis in walking compared to resting, or less information flow from the ROI shown on the X-axis to the ROI shown on the Y-axis. B) Correlation between stride duration and UPDRS-III score ($p = 0.017$, Pearson's correlation coefficient = 0.800). Dots represent single subjects. C) Correlation between stride duration and TRGC during walking (signed $\log_{10} p$ -values). Pink colors indicate a positive correlation between stride duration and the net information flow from a region plotted on the Y-axis to a region plotted on the X-axis, while red colors indicate a negative correlation. In all subfigures, signed $\log_{10} p$ -values that were not significant after FDR-correction were set to zero. Modified from (Pellegrini, Pozzi, et al., 2023).

We investigated the dynamics of cortical network activity during walking, focusing on metabolically activated areas (Figure 7A). EEG power analysis showed increased activity in the theta+alpha and beta frequency bands across all regions during walking compared to standing. Directed FC analysis revealed distinct patterns among frontal, parietal, and occipital areas. Specifically, in the beta band, reduced information flow was observed

from the SMA to sensory and motor areas, while connectivity to visuomotor areas increased. The paracentral lobule exhibited a stronger information flow to SMA and visuomotor areas while demonstrating weaker connectivity to sensory parietal areas. Visuomotor areas exhibited decreased FC, while the lingual gyrus and medial occipital lobule showed mild decoupling. Similar patterns were observed in the low-frequency band.

Next, we assessed the correlation of cortical network dynamics during walking with gait performance measured through the stride duration. We explored the relationship between EEG power and gait kinematics, revealing a general negative correlation between stride duration and EEG power. Subsequently, we focused on FC and found that only changes in the beta frequency band were correlated with motor performance. Notably, FC between the SMA, precuneus, and visuomotor areas exhibited associations with gait kinematics. Specifically, a higher information flow from the SMA to the precuneus corresponded to shorter stride duration, indicating faster gait (Figure 7C). Likewise, increased information flow from visuomotor areas to the lingual gyrus correlated with shorter stride duration, indicating better gait performance. Conversely, a higher information flow from visual areas to the cuneus was associated with longer stride duration, indicative of a hypokinetic gait.

4 Discussion

4.1 Summary of the results

In the studies of this dissertation, we investigated methods for analyzing EEG data, exploring metrics for linear phase-phase FC (Study 1) and PAC (Study 2), and providing insights into underlying neural processes of pathological locomotion in PD (Study 3). Study 1 compared data analysis pipelines for extracting linear FC between predefined brain regions from simulated EEG data. The results show that it is beneficial to use a pipeline consisting of LCMV source reconstruction, aggregate time series within regions using a fixed number of strongest PCs, and use robust connectivity metrics like MIM for undirected or TRGC for directed FC estimation. Study 2 developed and tested a novel metric, the ASB-PAC, in its ability to assess between-site PAC in mixed-signal settings. We found evidence that the ASB-PAC can avoid the detection of spurious between-site PAC in mixed-signal settings while detecting ground-truth between-site interactions reliably. Finally, Study 3 used the suggested pipeline to investigate alterations in FC in

the cortical locomotor network during walking. We identified reduced information flow from the SMA to sensory and motor areas but increased FC to visuomotor areas, with correlations between SMA connectivity and gait performance.

4.2 Insights from the simulations

The choice of the regularization parameter in inverse solutions affects source reconstruction accuracy (Hashemi et al., 2021). While this is less important for beamformers, careful selection is necessary for full inverse solutions like Champagne and eLORETA. Therefore, we used a spatial cross-validation method that automatically sets the parameter based on the data (Habermehl et al., 2014; Hashemi et al., 2021). We found that DICS performs poorly in determining directionality compared to LCMV due to inconsistencies across frequencies. For directed or cross-frequency FC analyses, we therefore recommend to avoid using DICS.

Studies 1 and 2 clearly revealed that robust FC metrics outperform non-robust metrics in detecting genuine neuronal interactions. COH, in particular, is heavily influenced by the volume conduction effect. TRGC performs well for investigating interaction direction and detection but has longer computation times compared to MIM. NetGC without time reversal showed comparable performance to TRGC, indicating that netGC values already provide some robustness against volume conduction artifacts. This has already been shown previously (Winkler et al., 2016). In general, we recommend using robust FC metrics such as iCOH, MIM/MIC, or TRGC.

Regarding aggregation within regions, employing an SVD/PCA and selecting a fixed number of components for further processing yielded better results than selecting a variable number of components in each ROI. When investigating this, we found that the final connectivity score of the VARPC pipelines for MIM and MIC was positively correlated with the number of voxels in the respective ROIs, indicating a bias depending on ROI size. This bias likely arises due to the degrees of freedom in fitting MIM/MIC, which scale linearly with the number of voxels within a ROI. This may lead to overfitting and an overestimation of MIM/MIC. However, such behavior was not observed for TRGC, likely because potential biases in signal dimensionalities cancel out by the time reversal and by using the quotient of full and reduced model.

In Study 2, neither orthogonalization nor the IC surrogate method improved the original MI metric for detecting between-region PAC. However, these methods have not been designed for disentangling univariate PAC from bivariate PAC. ICA, by design, consistently fails to separate the two Gaussian sources and thus permuting ICs does not create an appropriate null distribution. Employing spatio-spectral decomposition (Nikulin et al., 2011) instead of ICA could improve the performance.

The ASB, which was shown to perform best for disentangling within-site from between-site PAC, involves subtracting an interaction term, B_{mkm} , from the original bispectral estimate of PAC, B_{kmm} . B_{mkm} does not have an interpretation as PAC itself and is unlikely to occur in the real brain. Instead, it likely arises predominantly due to mixing effects in the presence of true within-site PAC. By removing B_{mkm} , we can enhance the robustness of the analysis without significantly discarding genuine neuronal activity.

4.3 The functional connectome during gait in Parkinson's Disease

In Study 3, we demonstrated a reduction in SMA connectivity with sensorimotor areas during walking in PD patients, which may be connected to gait impairments. This fits well with the current state of research showing that the SMA's interaction with somatosensory cortical areas is crucial for integrating motor programs with somatosensory information for postural control (Takakusaki, 2013). Further, a dysfunction of the SMA is linked to gait impairment in PD (Tessitore et al., 2019).

Visuomotor processing plays a crucial role in gait control in PD (Martens & Almeida, 2012). In line with this, our study found a decrease of FC between visuomotor areas, and both premotor and sensorimotor cortices. Especially noteworthy is the correlation between FC from the cuneus and lingual gyrus to other visual areas and stride duration. While increased FC from the visual areas to the lingual gyrus was related to faster walking, increased FC from visual areas to the cuneus was related to hypokinetic gait. While the direct involvement of the cuneus and lingual gyrus in locomotor control is yet to be fully understood, their FC patterns and associations with gait performances suggest their relevance in PD-related gait impairments.

Our exploratory analysis points to two main functional roadblocks in PD: impaired information flow from the cuneus to the SMA, hindering visuomotor integration, and reduced flow from the SMA to sensorimotor areas, affecting the forwarding of locomotor

programs. To compensate, increased information flow to the lingual gyrus may serve as a rescue strategy for processing and forwarding locomotor information. This rerouting may be supported by the anatomical connections of the inferior fronto-occipital fasciculus (IFOF). The IFOF has been shown to connect the cuneus and lingual gyrus to the frontal lobe (Palejwala et al., 2021) and lesions in the IFOF have been associated with worsening gait performances (Kvickström et al., 2011).

The correlation of FC changes with gait performances was observed in the beta frequency band, highlighting its relevance in motor control. Further research is needed to explore subcortical pathways and the impact of treatments like dopaminergic therapy and neuromodulation on the locomotor information pathway.

4.4 Limitations

Simulations certainly have their limitations. The tradeoff between realism and simplicity of data is a crucial factor to consider when designing them. Simulation studies have inherent limitations due to unverifiable assumptions. In Studies 1 and 2, we made several assumptions regarding linear dynamics, fixed time delay, interaction in certain frequency bands, the number of interactions, SNR, and stationarity of signals and noise. Additionally, the simulated environment focused on dominant point-like sources, and potentially overestimated the beamformer performance. Also, the assumption of few interacting sources against a non-interacting background may not hold for real-world FC analyses. While some of these parameters were systematically varied to assess pipeline performance, the realism of parameter choices can be questioned. Future simulation studies should aim to increase the realism of generated pseudo-EEG signals. This can be achieved by incorporating typical EEG artifacts and utilizing biologically inspired models based on known anatomical connections.

Studies 1 and 2 explore various processing pipelines, FC metrics, and data parameters. However, they are not exhaustive, and other parameters may influence FC detection. Previous works (see Pellegrini et al., 2023 for an overview) have highlighted the impact of parameters like channel density, location of interacting sources, data length, referencing, co-registration, and quality of head models on FC detection. Numerous other inverse solutions and dimensionality reduction techniques exist, which were not investigated in these studies. Neither did we examine the effect of the number of epochs

and epoch length, which have been shown to introduce biases in certain connectivity metrics. Vinck et al., (2010) recommend using a fixed number of epochs throughout an experiment, especially when comparing different groups or experimental conditions. We have accounted for this issue in the implementation in the ROIconnect toolbox, and in Study 3.

In our studies, we did not address the phenomenon of so-called ‘ghost interactions’ (Palva et al., 2018). These refer to spurious FC between non-interacting brain regions caused by signal spread from nearby interacting regions. These effects may be small, but significant in case of high SNR and sample sizes. Future work should take a further step and conduct systematic assessments of statistical maps obtained from connectomes, using our findings as a basis for analysis.

Also Study 3 has several limitations. First, our sample size was rather small, due to the study's multimodal design. Second, the lack of a control group restricts the generalizability of our findings. However, it is important to note that this study specifically focused on PD patients due to the relevance of gait impairments in this population. Third, the recorded EEG data were affected by gait-related artifacts due to movement of cables and muscular activity during walking. Both these artifacts, and neural activity of interest are correlated with the gait events. We aimed at cleaning the data thoroughly by employing the artifact subspace reconstruction method (Kothe & Makeig, 2013), which is designed for highly artifactual data. However, the cleaning procedure was likely imperfect. Therefore, we restricted our analyses to the continuous data stream and refrained from analyzing gait-locked neural activity. Lastly, we limited our analyses to cortical EEG signals. While the cerebellum is known to play a significant role in the locomotor network, the extent to which the EEG signal captures its contributions is still debated. Therefore, we opted to exclude the cerebellum from our analysis, even though it showed an activation in the PET in walking. The same limitation applies to the thalamus.

4.5 Implications for clinical application

We have implemented our recommended pipelines for analyzing FC in EEG data in a new open-source plugin called ROIconnect⁵. This plugin provides an easy-to-use interface for researchers, enabling them to apply robust measures of FC without needing to implement the methods themselves. By making this plugin available to the broader research community, we hope to facilitate future investigations of the complex mechanisms underlying brain function and dysfunction.

Further, we presented an openly accessible simulation framework⁶ in Study 1 and 2, that allows the community to easily replace individual pipeline steps and simulate data following a plug-and-play principle. Future studies are encouraged to test different aspects of the pipelines, utilize alternative data, and investigate additional FC metrics.

In Study 3, we presented an exploratory analysis of FC patterns in walking patients with PD. Based on the results, we present a framework incorporating new suggestions on the interplay between visuomotor areas and the motor network. This new framework must be confirmed by future studies. A deeper understanding of pathological changes of FC in PD may lead to enhanced therapy, e.g., with DBS, which has been associated with an impact on long-range synchronization (de Hemptinne et al., 2013).

5 Conclusion

The estimation of inter-regional FC from EEG is an interesting, yet challenging problem. In the studies that contributed to this thesis, we showed that many commonly used analysis pipelines do not reliably estimate ground-truth FC but detect many false positives due to signal mixing. This may have heavy implications for medical and neuroscientific research aiming at characterizing healthy and pathological FC. We identified analysis pipelines that are robust to the signal mixing problem and showcased how they can be applied to explore FC in walking patients with PD. Finally, to make the recommended pipelines easily accessible to a broader bandwidth of researchers, we implemented them as a plugin to the commonly used open-source GUI-based EEGLAB toolbox. Taken

⁵ <https://github.com/sccn/roiconnect>

⁶ <https://github.com/fpellegrini/FCsim> and <https://github.com/fpellegrini/PAC>

together, the work presented in this thesis sets the foundation for future studies to advance knowledge about the human connectome.

References

- Allouch, S., Duprez, J., Khalil, M., Hassan, M., Modolo, J., & Kabbara, A. (2022). Methods Used to Estimate EEG Source-Space Networks: A Comparative Simulation-Based Study. *2022 44th Annual International Conference of the IEEE Engineering in Medicine and Biology Society (EMBC)*, 3590–3593. <https://doi.org/10.1109/EMBC48229.2022.9871047>
- Anzolin, A., Presti, P., Van De Steen, F., Astolfi, L., Haufe, S., & Marinazzo, D. (2019). Quantifying the Effect of Demixing Approaches on Directed Connectivity Estimated Between Reconstructed EEG Sources. *Brain Topography*. <https://doi.org/10.1007/s10548-019-00705-z>
- Babiloni, C., Del Percio, C., Lizio, R., Noce, G., Lopez, S., Soricelli, A., Ferri, R., Pascarelli, M. T., Catania, V., Nobili, F., Arnaldi, D., Famà, F., Orzi, F., Buttinelli, C., Giubilei, F., Bonanni, L., Franciotti, R., Onofrj, M., Stirpe, P., Fuhr, P., Gschwandtner, U., Ransmayr, G., Garn, H., Fraioli, L., Pievani, M., D'Antonio, F., De Lena, C., Güntekin, B., Hanoglu, L., Basar, E., Yener, G., Emek-Savas, D. D., Triggiani, A. I., Taylor, J. P., De Pandis, M. F., Vacca, L., Frisoni, G. B., & Stocchi, F. (2018). Functional cortical source connectivity of resting state electroencephalographic alpha rhythms shows similar abnormalities in patients with mild cognitive impairment due to Alzheimer's and Parkinson's diseases. *Clinical Neurophysiology: Official Journal of the International Federation of Clinical Neurophysiology*, 129(4), 766–782. <https://doi.org/10.1016/j.clinph.2018.01.009>
- Baillet, S., Mosher, J. C., & Leahy, R. M. (2001). Electromagnetic brain mapping. *IEEE Signal Processing Magazine*, 18(6), 14–30. <https://doi.org/10.1109/79.962275>

- Barnett, L., & Seth, A. K. (2014). The MVGC multivariate Granger causality toolbox: A new approach to Granger-causal inference. *Journal of Neuroscience Methods*, 223, 50–68. <https://doi.org/10.1016/j.jneumeth.2013.10.018>
- Basti, A., Nili, H., Hauk, O., Marzetti, L., & Henson, R. N. (2020). Multi-dimensional connectivity: A conceptual and mathematical review. *NeuroImage*, 221, 117179. <https://doi.org/10.1016/j.neuroimage.2020.117179>
- Bastos, A. M., & Schoffelen, J.-M. (2016). A Tutorial Review of Functional Connectivity Analysis Methods and Their Interpretational Pitfalls. *Frontiers in Systems Neuroscience*, 9. <https://doi.org/10.3389/fnsys.2015.00175>
- Bell, A. J., & Sejnowski, T. J. (1995). An Information-Maximization Approach to Blind Separation and Blind Deconvolution. *Neural Computation*, 7(6), 1129–1159. <https://doi.org/10.1162/neco.1995.7.6.1129>
- Berger, H. (1929). Über das Elektrenkephalogramm des Menschen. *Archiv für Psychiatrie und Nervenkrankheiten*, 87(1), 527–570. <https://doi.org/10.1007/BF01797193>
- Bergman, H., Wichmann, T., & DeLong, M. R. (1990). Reversal of Experimental Parkinsonism by Lesions of the Subthalamic Nucleus. *Science*, 249(4975), 1436–1438. <https://doi.org/10.1126/science.2402638>
- Bhidayasiri, R., & Tarsy, D. (2012). Parkinson's Disease: Hoehn and Yahr Scale. In R. Bhidayasiri & D. Tarsy, *Movement Disorders: A Video Atlas* (pp. 4–5). Humana Press. https://doi.org/10.1007/978-1-60327-426-5_2
- Blankertz, B., Sannelli, C., Halder, S., Hammer, E. M., Kübler, A., Müller, K.-R., Gabriel Curio, & Dickhaus, T. (2010). Neurophysiological Predictor of SMR-Based BCI Performance. *NeuroImage*, 51(4), 1303–1309.
- Bressler, S. L., & Seth, A. K. (2011). Wiener–Granger Causality: A well established methodology. *NeuroImage*, 58(2), 323–329.

- Buzsáki, G. (2006). *Rhythms of the brain*. Oxford University Press.
- Canolty, R. T., Edwards, E., Dalal, S. S., Soltani, M., Nagarajan, S. S., Kirsch, H. E., Berger, M. S., Barbaro, N. M., & Knight, R. T. (2006). High Gamma Power Is Phase-Locked to Theta Oscillations in Human Neocortex. *Science*, 313(5793), 1626–1628. <https://doi.org/10.1126/science.1128115>
- Canolty, R. T., & Knight, R. T. (2010). The functional role of cross-frequency coupling. *Trends in Cognitive Sciences*, 14(11), 506–515. <https://doi.org/10.1016/j.tics.2010.09.001>
- Chella, F., Marzetti, L., Pizzella, V., Zappasodi, F., & Nolte, G. (2014). Third order spectral analysis robust to mixing artifacts for mapping cross-frequency interactions in EEG/MEG. *NeuroImage*, 91, 146–161. <https://doi.org/10.1016/j.neuroimage.2013.12.064>
- Clancy, K. B., Orsolic, I., & Mrsic-Flogel, T. D. (2019). Locomotion-dependent remapping of distributed cortical networks. *Nature Neuroscience*, 22(5), 778–786. <https://doi.org/10.1038/s41593-019-0357-8>
- Cohen, M. X. (2017). Where Does EEG Come From and What Does It Mean? *Trends in Neurosciences*, 40(4), 208–218. <https://doi.org/10.1016/j.tins.2017.02.004>
- Colclough, G. L., Brookes, M. J., Smith, S. M., & Woolrich, M. W. (2015). A symmetric multivariate leakage correction for MEG connectomes. *NeuroImage*, 117, 439–448. <https://doi.org/10.1016/j.neuroimage.2015.03.071>
- de Hemptinne, C., Ryapolova-Webb, E. S., Air, E. L., Garcia, P. A., Miller, K. J., Ojemann, J. G., Ostrem, J. L., Galifianakis, N. B., & Starr, P. A. (2013). Exaggerated phase–amplitude coupling in the primary motor cortex in Parkinson disease. *Proceedings of the National Academy of Sciences*, 110(12), 4780–4785. <https://doi.org/10.1073/pnas.1214546110>

- Desikan, R. S., Ségonne, F., Fischl, B., Quinn, B. T., Dickerson, B. C., Blacker, D., Buckner, R. L., Dale, A. M., Maguire, R. P., Hyman, B. T., Albert, M. S., & Killiany, R. J. (2006). An automated labeling system for subdividing the human cerebral cortex on MRI scans into gyral based regions of interest. *Neuroimage*, 31(3), 968–980.
- Dowding, I., & Haufe, S. (2018). Powerful Statistical Inference for Nested Data Using Sufficient Summary Statistics. *Frontiers in Human Neuroscience*, 12, 103. <https://doi.org/10.3389/fnhum.2018.00103>
- Ewald, A., Marzetti, L., Zappasodi, F., Meinecke, F. C., & Nolte, G. (2012). Estimating true brain connectivity from EEG/MEG data invariant to linear and static transformations in sensor space. *NeuroImage*, 60(1), 476–488. <https://doi.org/10.1016/j.neuroimage.2011.11.084>
- Florin, E., & Baillet, S. (2015). The brain's resting-state activity is shaped by synchronized cross-frequency coupling of neural oscillations. *Neuroimage*, 111, 26–35.
- Fries, P. (2005). A mechanism for cognitive dynamics: Neuronal communication through neuronal coherence. *Trends in Cognitive Sciences*, 9(10), 474–480. <https://doi.org/10.1016/j.tics.2005.08.011>
- Galna, B., Lord, S., Burn, D. J., & Rochester, L. (2015). Progression of gait dysfunction in incident Parkinson's disease: Impact of medication and phenotype. *Movement Disorders*, 30(3), 359–367. <https://doi.org/10.1002/mds.26110>
- Gomez-Rodriguez, M., J.Leskovec, & A.Krause. (2010). Inferring Networks of Diffusion and Influence. *KDD*.
- Gong, R., Wegscheider, M., Mühlberg, C., Gast, R., Fricke, C., Rumpf, J.-J., Nikulin, V. V., Knösche, T. R., & Classen, J. (2021). Spatiotemporal features of β-γ phase-

- amplitude coupling in Parkinson's disease derived from scalp EEG. *Brain*, 144(2), 487–503. <https://doi.org/10.1093/brain/awaa400>
- Granger, C. W. J. (1969). Investigating Causal Relations by Econometric Models and Cross-spectral Methods. *Econometrica*, 37(3), 424–438.
- Gross, J., Kujala, J., Hamalainen, M., Timmermann, L., Schnitzler, A., & Salmelin, R. (2001). Dynamic imaging of coherent sources: Studying neural interactions in the human brain. *Proceedings of the National Academy of Sciences*, 98(2), 694–699. <https://doi.org/10.1073/pnas.98.2.694>
- Habermehl, C., Steinbrink, J., Müller, K.-R., & Haufe, S. (2014). Optimizing the regularization for image reconstruction of cerebral diffuse optical tomography. *Journal of Biomedical Optics*, 19(9), 096006–096006.
- Hammond, C. H., Bergman, H. D., & Brown, P. (2007). Pathological synchronization in Parkinson's disease: Networks, models and treatments. *Trends in Neurosciences*, 30, 357–364. <https://doi.org/10.1016/j.tins.2007.05.004>
- Hashemi, A., Cai, C., Kutyniok, G., Müller, K.-R., Nagarajan, S. S., & Haufe, S. (2021). Unification of sparse Bayesian learning algorithms for electromagnetic brain imaging with the majorization minimization framework. *NeuroImage*, 239, 118309. <https://doi.org/10.1016/j.neuroimage.2021.118309>
- Haufe, S., Isaias, I. U., Pellegrini, F., & Palmisano, C. (2023). Gait Event Prediction Using Surface Electromyography in Parkinsonian Patients. *Bioengineering*, 10(2), 212. <https://doi.org/10.3390/bioengineering10020212>
- Haufe, S., Nikulin, V. V., Müller, K.-R., & Nolte, G. (2013). A critical assessment of connectivity measures for EEG data: A simulation study. *NeuroImage*, 64, 120–133. <https://doi.org/10.1016/j.neuroimage.2012.09.036>

- Haufe, S., Nikulin, V. V., & Nolte, G. (2012). Alleviating the Influence of Weak Data Asymmetries on Granger-Causal Analyses. In F. Theis, A. Cichocki, A. Yeredor, & M. Zibulevsky (Eds.), *Latent Variable Analysis and Signal Separation* (Vol. 7191, pp. 25–33). Springer Berlin Heidelberg. https://doi.org/10.1007/978-3-642-28551-6_4
- Hillebrand, A., Barnes, G. R., Bosboom, J. L., Berendse, H. W., & Stam, C. J. (2012). Frequency-dependent functional connectivity within resting-state networks: An atlas-based MEG beamformer solution. *NeuroImage*, 59(4), 3909–3921. <https://doi.org/10.1016/j.neuroimage.2011.11.005>
- Jirsa, V., & Müller, V. (2013). Cross-frequency coupling in real and virtual brain networks. *Frontiers in Computational Neuroscience*, 7, 78.
- Kapralov, N., Jamshidi Idaji, M., Stephani, T., Studenova, A., Vidaurre, C., Ros, T., Villringer, A., & Nikulin, V. (2023). *Sensorimotor brain-computer interface performance depends on signal-to-noise ratio but not connectivity of the mu rhythm in a multiverse analysis of longitudinal data* [Preprint]. Neuroscience. <https://doi.org/10.1101/2023.09.30.558407>
- Kline, J. E., Huang, H. J., Snyder, K. L., & Ferris, D. P. (2015). Isolating gait-related movement artifacts in electroencephalography during human walking. *Journal of Neural Engineering*, 12(4), 046022. <https://doi.org/10.1088/1741-2560/12/4/046022>
- Kothe, C. A., & Makeig, S. (2013). BCILAB: A platform for brain–computer interface development. *Journal of Neural Engineering*, 10(5), 056014. <https://doi.org/10.1088/1741-2560/10/5/056014>

- Kovach, C. K., Oya, H., & Kawasaki, H. (2018). The bispectrum and its relationship to phase-amplitude coupling. *NeuroImage*, 173, 518–539. <https://doi.org/10.1016/j.neuroimage.2018.02.033>
- Kühn, A. A., Kempf, F., Brücke, C., Doyle, L. G., Martinez-Torres, I., Pogosyan, A., Trittenberg, T., Kupsch, A., Schneider, G.-H., Hariz, M. I., Vandenberghe, W., Nuttin, B., & Brown, P. (2008). High-frequency stimulation of the subthalamic nucleus suppresses oscillatory β activity in patients with Parkinson's disease in parallel with improvement in motor performance. *The Journal of Neuroscience*, 28(24), 6165–6173.
- Kühn, A. A., Kupsch, A., Schneider, G.-H., & Brown, P. (2006). Reduction in subthalamic 8–35 Hz oscillatory activity correlates with clinical improvement in Parkinson's disease. *European Journal of Neuroscience*, 23(7), 1956–1960.
- Kvickström, P., Eriksson, B., Van Westen, D., Lätt, J., Elfgrén, C., & Nilsson, C. (2011). Selective frontal neurodegeneration of the inferior fronto-occipital fasciculus in progressive supranuclear palsy (PSP) demonstrated by diffusion tensor tractography. *BMC Neurology*, 11(1), 13. <https://doi.org/10.1186/1471-2377-11-13>
- MacKinnon, C. D. (2018). Sensorimotor anatomy of gait, balance, and falls. In *Handbook of Clinical Neurology* (Vol. 159, pp. 3–26). Elsevier. <https://doi.org/10.1016/B978-0-444-63916-5.00001-X>
- Mahjoory, K., Nikulin, V. V., Botrel, L., Linkenkaer-Hansen, K., Fato, M. M., & Haufe, S. (2017). Consistency of EEG source localization and connectivity estimates. *NeuroImage*, 152, 590–601. <https://doi.org/10.1016/j.neuroimage.2017.02.076>
- Martens, K. A. E., & Almeida, Q. J. (2012). Dissociating between sensory and perceptual deficits in PD: More than simply a motor deficit. *Movement Disorders*, 27(3), 387–392. <https://doi.org/10.1002/mds.24042>

- Martínez-Martín, P., Gil-Nagel, A., Gracia, L. M., Gómez, J. B., Martínez-Sarriés, J., Bermejo, F., & The Cooperative Multicentric Group. (1994). Unified Parkinson's disease rating scale characteristics and structure. *Movement Disorders*, 9(1), 76–83. <https://doi.org/10.1002/mds.870090112>
- Mazziotta, J. C., Toga, A. W., Evans, A., Fox, P., & Lancaster, J. (1995). A probabilistic atlas of the human brain: Theory and rationale for its development. The International Consortium for Brain Mapping (ICBM). *NeuroImage*, 2(2), 89–101.
- Mirelman, A., Bonato, P., Camicioli, R., Ellis, T. D., Giladi, N., Hamilton, J. L., Hass, C. J., Hausdorff, J. M., Pelosin, E., & Almeida, Q. J. (2019). Gait impairments in Parkinson's disease. *The Lancet Neurology*, 18(7), 697–708. [https://doi.org/10.1016/S1474-4422\(19\)30044-4](https://doi.org/10.1016/S1474-4422(19)30044-4)
- Nandi, B., Swiatek, P., Kocsis, B., & Ding, M. (2019). Inferring the direction of rhythmic neural transmission via inter-regional phase-amplitude coupling (ir-PAC). *Scientific Reports*, 9(1), 6933. <https://doi.org/10.1038/s41598-019-43272-w>
- Neuper, C., Scherer, R., Reiner, M., & Pfurtscheller, G. (2005). Imagery of motor actions: Differential effects of kinesthetic and visual–motor mode of imagery in single-trial EEG. *Cognitive Brain Research*, 25(3), 668–677. <https://doi.org/10.1016/j.cogbrainres.2005.08.014>
- Nikias, C. L., & Pan, R. (1988). Time delay estimation in unknown Gaussian spatially correlated noise. *IEEE Transactions on Acoustics, Speech, and Signal Processing*, 36(11), 1706–1714. <https://doi.org/10.1109/29.9008>
- Nikulin, V. V., Nolte, G., & Curio, G. (2011). A novel method for reliable and fast extraction of neuronal EEG/MEG oscillations on the basis of spatio-spectral decomposition. *NeuroImage*, 55, 1528–1535.

- Nolte, G., Bai, O., Wheaton, L., Mari, Z., Vorbach, S., & Hallett, M. (2004). Identifying true brain interaction from EEG data using the imaginary part of coherency. *Clinical Neurophysiology*, 115(10), 2292–2307.
<https://doi.org/10.1016/j.clinph.2004.04.029>
- Nolte, G., Ziehe, A., Nikulin, V. V., Schlögl, A., Krämer, N., Brismar, T., & Müller, K.-R. (2008). Robustly Estimating the Flow Direction of Information in Complex Physical Systems. *Physical Review Letters*, 100(23).
<https://doi.org/10.1103/PhysRevLett.100.234101>
- Nunez, P. L., Srinivasan, R., Westdorp, A. F., Wijesinghe, R. S., Tucker, D. M., Silberstein, R. B., & Cadusch, P. J. (1997). EEG coherency: I: statistics, reference electrode, volume conduction, Laplacians, cortical imaging, and interpretation at multiple scales. *Electroencephalography and Clinical Neurophysiology*, 103(5), 499–515.
- Nunez, P. L., & Srinivasan, R. (2006). *Electric fields of the brain: The neurophysics of EEG* (2nd ed). Oxford University Press.
- Palejwala, A. H., Dadario, N. B., Young, I. M., O'Connor, K., Briggs, R. G., Conner, A. K., O'Donoghue, D. L., & Sughrue, M. E. (2021). Anatomy and White Matter Connections of the Lingual Gyrus and Cuneus. *World Neurosurgery*, 151, e426–e437. <https://doi.org/10.1016/j.wneu.2021.04.050>
- Palva, J. M., Wang, S. H., Palva, S., Zhigalov, A., Monto, S., Brookes, M. J., Schoffelen, J.-M., & Jerbi, K. (2018). Ghost interactions in MEG/EEG source space: A note of caution on inter-areal coupling measures. *NeuroImage*, 173, 632–643.
<https://doi.org/10.1016/j.neuroimage.2018.02.032>
- Pascual-Marqui, R. D., Lehmann, D., Koukkou, M., Kochi, K., Anderer, P., Saletu, B., Tanaka, H., Hirata, K., John, E. R., Prichep, L., Biscay-Lirio, R., & Kinoshita, T. (2011). Assessing interactions in the brain with exact low-resolution

electromagnetic tomography. *Philosophical Transactions of the Royal Society A: Mathematical, Physical and Engineering Sciences*, 369(1952), 3768–3784.
<https://doi.org/10.1098/rsta.2011.0081>

Pellegrini, F., Delorme, A., Nikulin, V., & Haufe, S. (2023). Identifying good practices for detecting inter-regional linear functional connectivity from EEG. *NeuroImage*, 120218. <https://doi.org/10.1016/j.neuroimage.2023.120218>

Pellegrini, F., Nguyen, T. D., Herrera, T., Nikulin, V., Nolte, G., & Haufe, S. (2023). *Distinguishing between- from within-site phase-amplitude coupling using antisymmetrized bispectra* [Preprint]. Neuroscience. <https://doi.org/10.1101/2023.10.26.564193>

Pellegrini, F., Pozzi, N. G., Palmisano, C., Marotta, G., Buck, A., Haufe, S., & Isaias, I. U. (2023). *Cortical networks of parkinsonian gait: A metabolic and functional connectivity study* [Preprint]. Neurology. <https://doi.org/10.1101/2023.10.09.23296653>

Perinelli, A., Asseconti, S., Tagliabue, C. F., & Mazza, V. (2022). Power shift and connectivity changes in healthy aging during resting-state EEG. *NeuroImage*, 256, 119247. <https://doi.org/10.1016/j.neuroimage.2022.119247>

Peterson, D. S., Pickett, K. A., Duncan, R., Perlmuter, J., & Earhart, G. M. (2014). Gait-Related Brain Activity in People with Parkinson Disease with Freezing of Gait. *PLoS ONE*, 9(3), e90634. <https://doi.org/10.1371/journal.pone.0090634>

Postuma, R. B., Berg, D., Stern, M., Poewe, W., Olanow, C. W., Oertel, W., Obeso, J., Marek, K., Litvan, I., Lang, A. E., Halliday, G., Goetz, C. G., Gasser, T., Dubois, B., Chan, P., Bloem, B. R., Adler, C. H., & Deuschl, G. (2015). MDS clinical diagnostic criteria for Parkinson's disease: MDS-PD Clinical Diagnostic Criteria. *Movement Disorders*, 30(12), 1591–1601. <https://doi.org/10.1002/mds.26424>

- Sannelli, C., Vidaurre, C., Müller, K.-R., & Blankertz, B. (2019). A large scale screening study with a SMR-based BCI: Categorization of BCI users and differences in their SMR activity. *PLOS ONE*, 14(1), e0207351. <https://doi.org/10.1371/journal.pone.0207351>
- Schaworonkow, N., & Nikulin, V. V. (2022). Is sensor space analysis good enough? Spatial patterns as a tool for assessing spatial mixing of EEG/MEG rhythms. *NeuroImage*, 253, 119093. <https://doi.org/10.1016/j.neuroimage.2022.119093>
- Schoffelen, J. M., Hulten, A., Lam, N., Marquand, A. F., Udden, J., & Hagoort, P. (2017). Frequency-specific directed interactions in the human brain network for language. *Proc. Natl. Acad. Sci. U.S.A.*, 114(30), 8083–8088.
- Schoffelen, J.-M., & Gross, J. (2009). Source connectivity analysis with MEG and EEG. *Human Brain Mapping*, 30(6), 1857–1865. <https://doi.org/10.1002/hbm.20745>
- Schoffelen, J.-M., & Gross, J. (2019). Studying Dynamic Neural Interactions with MEG. In S. Supek & C. J. Aine (Eds.), *Magnetoencephalography: From Signals to Dynamic Cortical Networks* (pp. 519–541). Springer International Publishing. https://doi.org/10.1007/978-3-030-00087-5_18
- Schoneburg, B., Mancini, M., Horak, F., & Nutt, J. G. (2013). Framework for understanding balance dysfunction in Parkinson's disease: Balance in PD. *Movement Disorders*, 28(11), 1474–1482. <https://doi.org/10.1002/mds.25613>
- Shahbazi, F., Ewald, A., Ziehe, A., & Nolte, G. (2010). Constructing Surrogate Data to Control for Artifacts of Volume Conduction for Functional Connectivity Measures. In S. Supek & A. Sušac (Eds.), *17th International Conference on Biomagnetism Advances in Biomagnetism – Biomag2010* (pp. 207–210). Springer. https://doi.org/10.1007/978-3-642-12197-5_46

- Silberstein, P., Pogosyan, A., Kühn, A. A., Hotton, G., Tisch, S., Kupsch, A., Dowsey-Limousin, P., Hariz, M. I., & Brown, P. (2005). Cortico-cortical coupling in Parkinson's disease and its modulation by therapy. *Brain*, 128(6), 1277–1291. <https://doi.org/10.1093/brain/awh480>
- Soikkeli, R., Partanen, J., Soininen, H., Pääkkönen, A., & Riekkinen, P. (1991). Slowing of EEG in Parkinson's disease. *Electroencephalography and Clinical Neurophysiology*, 79(3), 159–165. [https://doi.org/10.1016/0013-4694\(91\)90134-P](https://doi.org/10.1016/0013-4694(91)90134-P)
- Takakusaki, K. (2013). Neurophysiology of gait: From the spinal cord to the frontal lobe: Neurophysiology of Gait. *Movement Disorders*, 28(11), 1483–1491. <https://doi.org/10.1002/mds.25669>
- Takakusaki, K. (2017). Functional Neuroanatomy for Posture and Gait Control. *Journal of Movement Disorders*, 10(1), 1–17. <https://doi.org/10.14802/jmd.16062>
- Tard, C., Delval, A., Devos, D., Lopes, R., Lenfant, P., Dujardin, K., Hossein-Foucher, C., Semah, F., Duhamel, A., Defebvre, L., Le Jeune, F., & Moreau, C. (2015). Brain metabolic abnormalities during gait with freezing in Parkinson's disease. *Neuroscience*, 307, 281–301. <https://doi.org/10.1016/j.neuroscience.2015.08.063>
- Tessitore, A., Cirillo, M., & De Micco, R. (2019). Functional Connectivity Signatures of Parkinson's Disease. *Journal of Parkinson's Disease*, 9(4), 637–652. <https://doi.org/10.3233/JPD-191592>
- Tort, A. B. L., Komorowski, R., Eichenbaum, H., & Kopell, N. (2010). Measuring Phase-Amplitude Coupling Between Neuronal Oscillations of Different Frequencies. *Journal of Neurophysiology*, 104(2), 1195–1210. <https://doi.org/10.1152/jn.00106.2010>

- Tosserams, A., Weerdesteyn, V., Bal, T., Bloem, B. R., Solis-Escalante, T., & Nonnekes, J. (2022). Cortical Correlates of Gait Compensation Strategies in Parkinson Disease. *Annals of Neurology*, 91(3), 329–341. <https://doi.org/10.1002/ana.26306>
- Tzourio-Mazoyer, N., Landeau, B., Papathanassiou, D., Crivello, F., Etard, O., Delcroix, N., Mazoyer, B., & Joliot, M. (2002). Automated Anatomical Labeling of Activations in SPM Using a Macroscopic Anatomical Parcellation of the MNI MRI Single-Subject Brain. *NeuroImage*, 15(1), 273–289. <https://doi.org/10.1006/nimg.2001.0978>
- van der Meij, R., Kahana, M., & Maris, E. (2012). Phase-Amplitude Coupling in Human Electrocorticography Is Spatially Distributed and Phase Diverse. *The Journal of Neuroscience*, 32(1), 111–123. <https://doi.org/10.1523/JNEUROSCI.4816-11.2012>
- Van Veen, B. D., Van Drongelen, W., Yuchtman, M., & Suzuki, A. (1997). Localization of brain electrical activity via linearly constrained minimum variance spatial filtering. *IEEE Transactions on Biomedical Engineering*, 44(9), 867–880. <https://doi.org/10.1109/10.623056>
- Vinck, M., van Wingerden, M., Womelsdorf, T., Fries, P., & Pennartz, C. M. A. (2010). The pairwise phase consistency: A bias-free measure of rhythmic neuronal synchronization. *NeuroImage*, 51(1), 112–122. <https://doi.org/10.1016/j.neuroimage.2010.01.073>
- Voytek, B., & Knight, R. T. (2015). Dynamic network communication as a unifying neural basis for cognition, development, aging, and disease. *Biological Psychiatry*, 77(12), 1089–1097. <https://doi.org/10.1016/j.biopsych.2015.04.016>

- Winkler, I., Panknin, D., Bartz, D., Müller, K.-R., & Haufe, S. (2016). Validity of time reversal for testing Granger causality. *IEEE Transactions on Signal Processing*, 64(11), 2746–2760. <https://doi.org/10.1109/TSP.2016.2531628>
- Wipf, D. P., Owen, J. P., Attias, H. T., Sekihara, K., & Nagarajan, S. S. (2010). Robust Bayesian estimation of the location, orientation, and time course of multiple correlated neural sources using MEG. *NeuroImage*, 49(1), 641–655. <https://doi.org/10.1016/j.neuroimage.2009.06.083>
- Yin, Z., Zhu, G., Liu, Y., Zhao, B., Liu, D., Bai, Y., Zhang, Q., Shi, L., Feng, T., Yang, A., Liu, H., Meng, F., Neumann, W. J., Kühn, A. A., Jiang, Y., & Zhang, J. (2022). Cortical phase-amplitude coupling is key to the occurrence and treatment of freezing of gait. *Brain*, 145(7), 2407–2421. <https://doi.org/10.1093/brain/awac121>
- Zandvoort, C. S., & Nolte, G. (2021). Defining the filter parameters for phase-amplitude coupling from a bispectral point of view. *Journal of Neuroscience Methods*, 350, 109032. <https://doi.org/10.1016/j.jneumeth.2020.109032>

Statutory declaration

„Ich, Franziska Pellegrini versichere an Eides statt durch meine eigenhändige Unterschrift, dass ich die vorgelegte Dissertation mit dem Thema: “Validated novel pipelines to study linear and non-linear between-site functional brain interaction with application in Parkinsonian gait” / “Validierte neue Pipelines zur Untersuchung linearer und nichtlinearer inter-regionaler funktioneller Hirninteraktionen mit Anwendung auf Parkinson-typischen Gang” selbstständig und ohne nicht offengelegte Hilfe Dritter verfasst und keine anderen als die angegebenen Quellen und Hilfsmittel genutzt habe.

Alle Stellen, die wörtlich oder dem Sinne nach auf Publikationen oder Vorträgen anderer Autoren/innen beruhen, sind als solche in korrekter Zitierung kenntlich gemacht. Die Abschnitte zu Methodik (insbesondere praktische Arbeiten, Laborbestimmungen, statistische Aufarbeitung) und Resultaten (insbesondere Abbildungen, Graphiken und Tabellen) werden von mir verantwortet.

Ich versichere ferner, dass ich die in Zusammenarbeit mit anderen Personen generierten Daten, Datenauswertungen und Schlussfolgerungen korrekt gekennzeichnet und meinen eigenen Beitrag sowie die Beiträge anderer Personen korrekt kenntlich gemacht habe (siehe Anteilserklärung). Texte oder Textteile, die gemeinsam mit anderen erstellt oder verwendet wurden, habe ich korrekt kenntlich gemacht.

Meine Anteile an etwaigen Publikationen zu dieser Dissertation entsprechen denen, die in der untenstehenden gemeinsamen Erklärung mit dem/der Erstbetreuer/in, angegeben sind. Für sämtliche im Rahmen der Dissertation entstandenen Publikationen wurden die Richtlinien des ICMJE (International Committee of Medical Journal Editors) zur Autorenschaft eingehalten. Ich erkläre ferner, dass ich mich zur Einhaltung der Satzung der Charité – Universitätsmedizin Berlin zur Sicherung Guter Wissenschaftlicher Praxis verpflichte.

Weiterhin versichere ich, dass ich diese Dissertation weder in gleicher noch in ähnlicher Form bereits an einer anderen Fakultät eingereicht habe.

Die Bedeutung dieser eidesstattlichen Versicherung und die strafrechtlichen Folgen einer unwahren eidesstattlichen Versicherung (§§156, 161 des Strafgesetzbuches) sind mir bekannt und bewusst.“

Datum

Unterschrift

Declaration of contribution to publications

Franziska Pellegrini contributed the following to the below listed publications:

Publication 1:

Franziska Pellegrini, Arnaud Delorme, Vadim Nikulin, Stefan Haufe, Identifying good practices for detecting inter-regional linear functional connectivity from EEG, NeuroImage, 2023.

Contribution: I worked out the methodological approach of the simulation together with my supervisor Prof. Stefan Haufe. Further, I wrote the code for all simulations and for the analysis of the motor imagery real data example, I created all figures and tables of the publication, wrote the original draft, and conducted all analyses for the revision. I developed the ROIconnect toolbox together with Prof. Stefan Haufe, Prof. Arnaud Delorme, and Tien Dung Nguyen.

Publication 2:

Franziska Pellegrini, Tien Dung Nguyen, Taliana Herrera, Vadim Nikulin, Guido Nolte, Stefan Haufe, Distinguishing between- from within-site phase-amplitude coupling using antisymmetrized bispectra, bioRxiv, 2023.

Contribution: I worked out the methodological approach of the simulation together with my supervisor Prof. Stefan Haufe. Further, I wrote the code for the two-channel simulations together with Taliana Herrera. I wrote the code for the whole-brain simulations and for the analysis of the motor imagery real data example. I created all figures and tables of the publication, and wrote the original draft. Further, I developed the updated version of the ROIconnect toolbox together with Tien Dung Nguyen, Prof. Stefan Haufe, and Prof. Arnaud Delorme.

Publication 3:

Franziska Pellegrini, Nicoló G. Pozzi, Chiara Palmisano, Giorgio Marotta, Andreas Buck, Stefan Haufe, Ioannis U. Isaias, Cortical networks of parkinsonian gait: a metabolic and functional connectivity study, medRxiv, 2023.

Contribution: I computed the individual head models, preprocessed and analyzed the recorded EEG, EMG, and IMU data, designed and conducted the statistical analysis together with Prof. Stefan Haufe, wrote the first draft of the paper, and created the figures 2, 4, and 5.

Signature, date, and stamp of first supervising university professor / lecturer

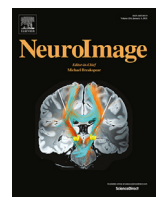
Signature of doctoral candidate

Excerpt from journal summary list

Journal Data Filtered By: **Selected JCR Year: 2021** Selected Editions: SCIE,SSCI
 Selected Categories: "**NEUROIMAGING**" Selected Category Scheme: WoS
Gesamtanzahl: 14 Journale

Rank	Full Journal Title	Total Cites	Journal Impact Factor	Eigenfaktor
1	Journal of NeuroInterventional Surgery	9,929	8.572	0.01850
2	NEUROIMAGE	131,266	7.400	0.10055
3	HUMAN BRAIN MAPPING	29,646	5.399	0.03211
4	AMERICAN JOURNAL OF NEURORADIOLOGY	29,851	4.966	0.02313
5	NeuroImage-Clinical	14,307	4.891	0.02775
6	JOURNAL OF NEURORADIOLOGY	1,789	4.600	0.00198
7	Brain Imaging and Behavior	5,231	3.224	0.00963
8	NEURORADIOLOGY	7,350	2.995	0.00608
9	NEUROIMAGING CLINICS OF NORTH AMERICA	1,810	2.624	0.00165
10	PSYCHIATRY RESEARCH-NEUROIMAGING	6,533	2.493	0.00448
11	JOURNAL OF NEUROIMAGING	3,013	2.324	0.00326
12	CLINICAL EEG AND NEUROSCIENCE	1,528	2.046	0.00131
13	STEREOTACTIC AND FUNCTIONAL NEUROSURGERY	2,241	1.643	0.00178
14	KLINISCHE NEUROPHYSIOLOGIE	77	0.633	0.00003

Copyright © 2022 Clarivate Analytics



Identifying good practices for detecting inter-regional linear functional connectivity from EEG



Franziska Pellegrini^{a,b,*}, Arnaud Delorme^c, Vadim Nikulin^d, Stefan Haufe^{e,f,a,b,1}

^a Charité-Universitätsmedizin Berlin, Charitéplatz 1, Berlin, 10117, Germany

^b Bernstein Center for Computational Neuroscience, Philippstraße 13, Berlin, 10117, Germany

^c Swartz Center for Computational Neuroscience, 9500 Gilman Dr, La Jolla, California, 92903-0559, United States

^d Department of Neurology, Max Planck Institute for Human Cognitive and Brain Sciences Leipzig, Stephanstraße 1a, Leipzig, 04103, Germany

^e Technische Universität Berlin, Straße des 17. Juni 135, Berlin, 10623, Germany

^f Physikalisch-Technische Bundesanstalt Braunschweig und Berlin, Abbestraße 2–12, Berlin, 10587, Germany

ARTICLE INFO

Keywords:

Electroencephalography
Inter-regional functional connectivity
Simulation
Source reconstruction
Linearly-constrained minimum variance beamforming
Multivariate interaction measure
Time-reversed granger causality

ABSTRACT

Aggregating voxel-level statistical dependencies between multivariate time series is an important intermediate step when characterising functional connectivity (FC) between larger brain regions. However, there are numerous ways in which voxel-level data can be aggregated into inter-regional FC, and the advantages of each of these approaches are currently unclear.

In this study we generate ground-truth data and compare the performances of various pipelines that estimate directed and undirected linear phase-to-phase FC between regions. We test the ability of several existing and novel FC analysis pipelines to identify the true regions within which connectivity was simulated. We test various inverse modelling algorithms, strategies to aggregate time series within regions, and connectivity metrics. Furthermore, we investigate the influence of the number of interactions, the signal-to-noise ratio, the noise mix, the interaction time delay, and the number of active sources per region on the ability of detecting phase-to-phase FC.

Throughout all simulated scenarios, lowest performance is obtained with pipelines involving the absolute value of coherency. Further, the combination of dynamic imaging of coherent sources (DICS) beamforming with directed FC metrics that aggregate information across multiple frequencies leads to unsatisfactory results. Pipelines that show promising results with our simulated pseudo-EEG data involve the following steps: (1) Source projection using the linearly-constrained minimum variance (LCMV) beamformer. (2) Principal component analysis (PCA) using the same fixed number of components within every region. (3) Calculation of the multivariate interaction measure (MIM) for every region pair to assess undirected phase-to-phase FC, or calculation of time-reversed Granger Causality (TRGC) to assess directed phase-to-phase FC. We formulate recommendations based on these results that may increase the validity of future experimental connectivity studies.

We further introduce the free ROIconnect plugin for the EEGLAB toolbox that includes the recommended methods and pipelines that are presented here. We show an exemplary application of the best performing pipeline to the analysis of EEG data recorded during motor imagery.

1. Introduction

In recent years, the field of functional neuroimaging has seen a shift from the mere localization of brain activity towards assessing interaction patterns between functionally segregated and specialized brain regions (Friston, 2011; Schoffelen and Gross, 2019). Functional connectivity (FC), in contrast to structural connectivity, expresses a statistical dependency between two or more neuronal time series. It has been proposed

that FC reflects inter-areal brain communication (Fries, 2015). Moreover, empirical FC estimates have been linked to various cognitive functions (Schoffelen and Gross, 2019) and show pathological alterations in many neurological diseases like Parkinson's Disease, Alzheimer's Disease, and epilepsy (Van Diessen et al., 2015).

Electroencephalography (EEG) and Magnetoencephalography (MEG) are suitable tools for recording neural activity non-invasively with high temporal resolution. Pipelines for analysing inter-regional

* Corresponding author.

E-mail address: franziska.pellegrini@charite.de (F. Pellegrini).

¹ Principal corresponding author.

FC from M/EEG recordings typically consist of a series of processing steps: artifact cleaning, source projection, aggregation of signals within regions of interests (ROIs), and, finally, FC estimation. At each step, researchers can choose between a huge selection of processing methods, where every decision has the potential to crucially affect the final result of an analysis and its interpretation (Colclough et al., 2016; Mahjoory et al., 2017; Wang et al., 2014). This not only complicates the comparison of results from different FC studies, it also raises the question: which pipelines are suitable for reliable source-level FC detection from M/EEG?

In the absence of a robust ground truth on information flow patterns in the human brain, computer simulations are a straightforward way to address such questions (Ewald et al., 2012). Indeed, numerous works have aimed to validate parts or aspects of M/EEG FC methodologies by employing simulated activity. Several studies have focused on assessing the accuracy of different inverse solutions (Allouch et al., 2022; Anzolin et al., 2019; Bradley et al., 2016; Castaño Candamil et al., 2015; Grova et al., 2006; Halder et al., 2019; Hasemi et al., 2021; Haufe et al., 2008; 2011; Hincapié et al., 2017; Jaiswal et al., 2020). Others have tested the performance of different FC metrics (Allouch et al., 2022; Anzolin et al., 2019; Astolfi et al., 2007; Haufe et al., 2013; Silverhuth et al., 2012; Sommariva et al., 2019); however, not always on source-reconstructed data exhibiting realistic levels of source leakage.

Many studies aim at aggregating FC within physiologically defined ROIs (Basti et al., 2020; Idaji et al., 2021; Palva et al., 2010; 2011; Schoffelen et al., 2017; Supp et al., 2007). This approach has various advantages. First, it is computationally more tractable (both memory- and time-wise) than the computation of FC between many pairs of individual sources, and it can avoid numerical instabilities for FC metrics that require full-rank signals. Second, interpreting or even visualizing FC between thousands of separate sources is almost impossible. Third, statistical testing is far easier due to a much reduced number of multiple comparisons. And, forth, across-subject statistical analyses are eased by working on a standardized set of regions rather than in individual anatomical spaces lacking a common set of source locations.

There have been various suggestions on how to reduce the signal dimensionality within ROIs. While some approaches focus on selecting one source for each ROI that best represents the activity of all sources in it (Ghumare et al., 2018; Hillebrand et al., 2012; Perinelli et al., 2022), others involve some kind of averaging or weighted averaging over all source time series of a ROI (Korhonen et al., 2014; Palva et al., 2010; 2011). This approach can be made more general by using the strongest principal component (PC) of all sources of a ROI as a representative time series of that ROI (Basti et al., 2020; Ghumare et al., 2018; Hillebrand et al., 2012; Rubega et al., 2019; Supp et al., 2007). The assumption behind this is that the projection of the data that captures the highest amount of variance within a ROI (its strongest PCs) also reflects the connectivity structure of that ROI best. While most works use only the first PC per region, the use of multiple components has also been suggested (e.g. Schoffelen et al., 2017). For this approach, the subsequent FC estimation is usually calculated between pairs of multivariate time series. Another approach, used for example in Schoffelen et al. (2017), is to apply a multivariate FC metric (here, a multivariate extension of Granger causality, Barrett et al., 2010) to the first C PCs of each pair of ROIs. Comparable undirected metrics are the multivariate interaction measure (MIM) and the maximized imaginary coherency (MIC) (Basti et al., 2020; Ewald et al., 2012), which are currently already in use for source-to-source FC estimation (e.g. D'Andrea et al., 2019). These are promising approaches towards more reliable FC estimation. But their virtue in the context of inter-regional FC estimation is still unclear. Moreover, a comprehensive approach evaluating entire data analysis pipelines rather than individual steps is still lacking (see Haufe and Ewald, 2019; Mahjoory et al., 2017).

Consequently, this work addresses the following questions: First, which pipelines are promising candidates for inferring phase-to-phase FC? Second, which pipelines are promising candidates for inferring the

directionality of an interaction? And, most importantly, which pipelines are not suitable to detect FC from data that is corrupted by signal mixing? In addition, we investigate how the number of PCs per ROI affects FC estimation. Finally, we evaluate how the performance of detecting ground-truth interactions varies depending on crucial data parameters like the signal-to-noise ratio (SNR), the number of ground-truth interactions, the noise composition, and the length of the interaction delay. All pipelines are tested within an EEG signal simulation framework that builds on our prior work (Haufe and Ewald, 2019). Note that we focus here on 1:1-phase-to-phase coupling with non-zero time delay, which is the most commonly studied type of FC. Other coupling types including phase-amplitude, amplitude-amplitude, phase-frequency, frequency-frequency, and amplitude-frequency coupling (e.g., Jirsa and Müller, 2013) are not studied here. Further note that we do not intend to propose a realistic model of EEG data or the whole brain. Rather, we aim to identify metrics and pipelines that can accurately reconstruct ROI-level functional connectivity (FC) in the presence of signal mixing, which heavily affects popular metrics used to infer directed and undirected linear FC. That is, we don't address the question of whether networks estimated using FC metrics provide an accurate depiction of actual brain networks.

The best-performing methods and pipelines identified in this study are implemented in the free ROIconnect plugin for the EEGLAB toolbox. We describe the functionality of ROIconnect and apply it to investigate EEG phase-to-phase FC during left and right hand motor imagery.

2. Methods

2.1. Data generation

We generate time series at a sampling rate of 100 Hz with a recording length of three minutes ($N_t = 100 \cdot 60 \cdot 3 = 18000$ samples). For spectral analyses, we epoch the data into $N_e = 90$ segments of $T = 200$ samples (2 seconds) length.

Ground-truth activity of interacting sources (c.f. Fig. 1a) is generated as random white noise filtered in the alpha band (8 to 12 Hz). Throughout, we use zero-phase forward and reverse second-order digital band-pass Butterworth filters. The interaction between two regions is modeled as unidirectional from the sending region to the receiving region. This is ensured by defining the activity at the receiving region to be an exact copy of the activity at the sending region with a certain time delay (see Section 3). Additionally, pink (1/f scaled) background noise is added to the sending and receiving regions independently. More specifically, both the ground-truth signal and the pink background noise are first normalized to have unit-norm in the interacting frequency band. To this end, every interacting ground-truth signal time series $\mathbf{g}_x \in \mathbb{R}^{N_t}$ at region x is divided by its ℓ_2 -norm: $\mathbf{g}_{xn} = \frac{\mathbf{g}_x}{\|\mathbf{g}_x\|_{\ell_2}}$. Every pink background noise time series $\mathbf{p}_x \in \mathbb{R}^{N_t}$ is filtered in the interacting frequency band to obtain $\mathbf{p}_{x8-12Hz} \in \mathbb{R}^{N_t}$. The unfiltered noise time series is then divided by the ℓ_2 -norm of its filtered version: $\mathbf{p}_{xn} = \frac{\mathbf{p}_x}{\|\mathbf{p}_{x8-12Hz}\|_{\ell_2}}$. Subsequently, a weighted sum of the normalized signal time series and the normalized noise time series is calculated:

$$\mathbf{s}_x = \theta \mathbf{g}_{xn} + (1 - \theta) \mathbf{p}_{xn} \in \mathbb{R}^{N_t} \quad (1)$$

The result is called the (interacting) signal (Fig. 1b). The parameter θ takes values between 0 and 1 and defines the source-level SNR in decibel (dB): $SNR_\theta = 20 * log_{10}(\frac{\theta}{1-\theta})$. The source-level SNR is set to 3.5 dB ($\theta=0.6$). The transposed column vectors of all $2N_I$ signal time series \mathbf{s} form the signal sources $\tilde{\mathbf{J}}_I \in \mathbb{R}^{2N_I \times N_t}$, with N_I region pairs containing the $2N_I$ interacting signals.

In contrast, activity of a non-interacting source at region y $\mathbf{b}_y \in \mathbb{R}^{N_t}$ – referred to as brain noise (Fig. 1c) – is generated using random pink noise only without additional activity in the alpha band. The transposed column vectors of all $R - 2N_I$ brain noise time series \mathbf{b} form the brain noise sources $\tilde{\mathbf{J}}_b \in \mathbb{R}^{R-2N_I \times N_t}$, with R denoting the number of regions.

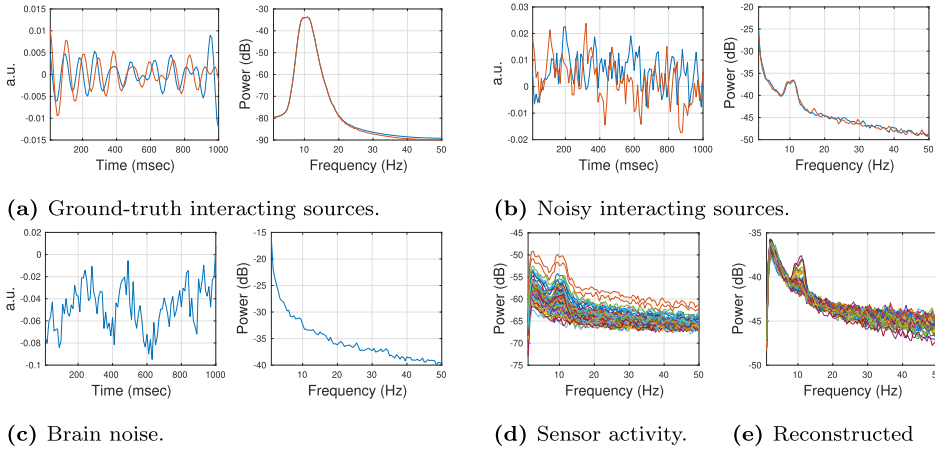


Fig. 1. Example of simulated data in time and frequency domain. (a) Ground-truth activity at two interacting sources was generated as random white noise filtered in the alpha band (8 to 12 Hz). Left: the one-second window of data in the time domain. Right: power spectral density (PSD). (b) Two interacting signals, generated as a mixture of the ground-truth activity and pink background noise ($\text{SNR}_\theta = 3.5 \text{ dB}$). Left: one-second window of data in the time domain. Right: PSD. (c) Brain noise, generated as random pink noise without additional activity in the alpha band (shown is the activity of an exemplary non-interacting source). Left: one-second window of data in time domain. Right: PSD. (d) PSD of activity at the sensor level is generated by mixing white sensor noise, and the interacting signal, and the brain noise at the sensor level ($\text{SNR} = 3.5 \text{ dB}$). (e) PSD of reconstructed source-level activity. Shown are PSDs of the first principal component of all 68 regions.

We use a surface-based source model with $N_v = 1895$ dipolar sources placed in the cortical gray matter. Regions are defined according to the Desikan-Killiany atlas (Desikan et al., 2006), which is a surface-based atlas with $R = 68$ cortical regions. Depending on the number of interacting voxels (see Experiment 6, Section 3), one or two time series per region are generated. Every ground-truth time series is placed in a randomly selected source location within a region, so that every region contains the same number of ground-truth time series. The N_I region pairs containing the $2N_I$ interacting signals are chosen randomly, and all other regions contain time series with brain noise.

In the next step, source activity is projected to sensor space by using a physical forward model of the electrical current flow in the head, summarized by a leadfield matrix. The leadfield describes the signal measured at the sensors for a given source current density. It is a function of the head geometry and the electrical conductivities of different tissues in the head. The template leadfield is obtained from a boundary element method (BEM) head model of the ICBM152 anatomical head template, which is a non-linear average of the magnetic resonance (MR) images of 152 healthy subjects (Mazziotta et al., 1995). We use Brainstorm (Tadel et al., 2011) and openMEEG (Gramfort et al., 2010) software to generate the headmodel and leadfield. $N_s = 97$ sensors are placed on the scalp following the standard BrainProducts ActiCap97 channel setup. Note that the spatial orientation of all simulated dipolar sources is chosen to be perpendicular to the cortex surface, so the three spatial orientations that define the dipole orientation of the source activity orientations are summarized into one. This assumption implies a scalar leadfield $\mathbf{L}_s \in \mathbb{R}^{N_s \times N_v}$. We denote the columns of \mathbf{L}_s that correspond to the interacting sources by $\mathbf{L}_I \in \mathbb{R}^{N_s \times 2N_I}$ and those corresponding to the brain noise sources by $\mathbf{L}_b \in \mathbb{R}^{N_s \times R-2N_I}$. Signal sources $\tilde{\mathbf{J}}_I$ and brain noise sources $\tilde{\mathbf{J}}_b$ are then separately projected to sensor space:

$$\tilde{\mathbf{Q}}_I = \mathbf{L}_I * \tilde{\mathbf{J}}_I \quad (2)$$

$$\tilde{\mathbf{Q}}_b = \mathbf{L}_b * \tilde{\mathbf{J}}_b, \quad (3)$$

with $\tilde{\mathbf{Q}}_I$ and $\tilde{\mathbf{Q}}_b \in \mathbb{R}^{N_s \times N_t}$.

At sensor level, we mix the different signal and noise components. We generate white sensor noise $\tilde{\mathbf{Q}}_s \in \mathbb{R}^{N_s \times N_t}$ with equal variance at all sensors. The multivariate sensor-space time series corresponding to all three signal components—brain noise, interacting signals, and sensor noise—are divided by their Frobenius norms with respect to the interacting frequency band (8–12 Hz):

$$\tilde{\mathbf{Q}}_{In} = \frac{\tilde{\mathbf{Q}}_I}{\|\tilde{\mathbf{Q}}_{I8-12Hz}\|_{\ell^2}}, \quad (4)$$

$$\tilde{\mathbf{Q}}_{bn} = \frac{\tilde{\mathbf{Q}}_b}{\|\tilde{\mathbf{Q}}_{b8-12Hz}\|_{\ell^2}}, \quad (5)$$

$$\tilde{\mathbf{Q}}_{sn} = \frac{\tilde{\mathbf{Q}}_s}{\|\tilde{\mathbf{Q}}_{s8-12Hz}\|_{\ell^2}}, \quad (6)$$

with $\tilde{\mathbf{Q}}_{I8-12Hz}$, $\tilde{\mathbf{Q}}_{b8-12Hz}$ and $\tilde{\mathbf{Q}}_{s8-12Hz} \in \mathbb{R}^{N_s \times N_t}$. Then the three components are combined as follows: first, we add brain noise and sensor noise with a specific brain noise-to-sensor noise-ratio (BSR) to obtain the total noise $\tilde{\mathbf{Q}}_n$ and normalize it with respect to the interacting frequency band:

$$\tilde{\mathbf{Q}}_n = \theta_{bsr} \tilde{\mathbf{Q}}_{bn} + (1 - \theta_{bsr}) \tilde{\mathbf{Q}}_{sn} \quad (7)$$

$$\tilde{\mathbf{Q}}_{nn} = \frac{\tilde{\mathbf{Q}}_n}{\|\tilde{\mathbf{Q}}_{n8-12Hz}\|_{\ell^2}}. \quad (8)$$

The default BSR value is set to 0 dB, i.e., $\theta_{bsr} = 0.5$. Second, we sum up signal and total noise with a specific global (sensor-level) SNR:

$$\tilde{\mathbf{Q}} = \theta_{snr} \tilde{\mathbf{Q}}_{In} + (1 - \theta_{snr}) \tilde{\mathbf{Q}}_{nn} \quad (9)$$

$$\tilde{\mathbf{Q}}_n = \frac{\tilde{\mathbf{Q}}}{\|\tilde{\mathbf{Q}}_{8-12Hz}\|_{\ell^2}} \quad (10)$$

The default SNR value is set to 3.5 dB, i.e., $\theta_{snr} = 0.6$. An example of the power-spectral density of the resulting activity on sensor level is illustrated in Fig. 1d. As a last step, we high-pass filter the generated sensor data with a cutoff of 1 Hz.

2.2. Source reconstruction

We test four different inverse solutions for source reconstruction: ‘exact’ low-resolution electromagnetic tomography (eLORETA), linearly-constrained minimum variance beamforming (LCMV), dynamic imaging of coherent sources (DICS), and Champagne. Inverse source reconstructions are based on the same leadfield used to simulate the signals. Full 3D currents are estimated for each source dipole. That is, prior information about the dipoles’ orientation is not used. A normal direction could in principle be estimated from the reconstructed cortical surface mesh (which we used here for signal generation); however, such estimation is considered to be rather unstable, since we do not have a good estimate of the cortical surface orientation in practice. The aggregation of the three spatial dimensions is discussed in Section 2.3.

‘Exact’ low-resolution electromagnetic tomography

The starting point to solve the source localization problem is the linear forward model $\tilde{\mathbf{Q}} = \mathbf{L}_v \tilde{\mathbf{J}}$, where $\tilde{\mathbf{Q}} \in \mathbb{R}^{N_s \times N_t}$ stands for the sensor measurements, $\tilde{\mathbf{J}} \in \mathbb{R}^{3N_v \times N_t}$ is the vector-valued activity of the dipolar brain sources to be recovered, and $\mathbf{L}_v \in \mathbb{R}^{N_s \times 3N_v}$ is the vector-valued linear leadfield matrix that maps the electrical activity from sources

to sensor level. Here, $3N_v$ stand for the three spatial dimensions that together define the dipole orientation of the source activity. The solution of this equation is ill-posed since the number of brain sources N_v is much smaller than the number of measurement sensors N_s . Therefore eLORETA imposes the constraint of spatially smooth current density distributions (Pascual-Marqui, 2007; Pascual-Marqui et al., 2011). Briefly, eLORETA uses a weighted minimum norm criterion to estimate the source distribution:

$$\hat{\mathbf{J}} = \arg \min_{\tilde{\mathbf{J}}} [||\tilde{\mathbf{Q}} - \mathbf{L}_v \tilde{\mathbf{J}}||^2 + a \tilde{\mathbf{J}}^\top \mathbf{W} \tilde{\mathbf{J}}], \quad (11)$$

where $a \geq 0$ denotes a regularization parameter, and \mathbf{W} is a block-diagonal symmetric weight matrix:

$$\mathbf{W} = \begin{bmatrix} \mathbf{W}_1 & \mathbf{0} & \dots & \mathbf{0} \\ \mathbf{0} & \mathbf{W}_2 & \dots & \mathbf{0} \\ \vdots & \vdots & \ddots & \vdots \\ \mathbf{0} & \mathbf{0} & \dots & \mathbf{W}_{N_v} \end{bmatrix} \in \mathbb{R}^{3N_v \times 3N_v}, \quad (12)$$

where $\mathbf{0}$ is the 3×3 zero matrix and \mathbf{W}_v the 3×3 weight matrix at the v -th voxel defined in Equation (15). The solution of Equation (11) is given by:

$$\hat{\mathbf{J}} = \mathbf{W}^{-1} \mathbf{L}_v^\top (\mathbf{L} \mathbf{W}^{-1} \mathbf{L}_v^\top + a \mathbf{K})^\dagger \tilde{\mathbf{Q}} = \mathbf{P}^E \tilde{\mathbf{Q}}, \quad (13)$$

where $\mathbf{K} \in \mathbb{R}^{N_s \times N_s}$ is a centering matrix re-referencing the leadfield and sensor measurements to the common-average reference, A^\dagger is the Moore-Penrose pseudo-inverse of a matrix A , and $\mathbf{P}^E \in \mathbb{R}^{N_s \times 3N_v}$ is the eLORETA inverse filter. eLORETA then first computes

$$\mathbf{M} = (\mathbf{L}_v \mathbf{W}^{-1} \mathbf{L}_v^\top + a \mathbf{K})^\dagger \quad (14)$$

and then for $v = 1, \dots, N_v$, calculates weights

$$\mathbf{W}_v = [\mathbf{L}_{v,v}^\top \mathbf{M} \mathbf{L}_{v,v}]^{1/2}, \quad (15)$$

with $\mathbf{L}_{v,v} \in \mathbb{R}^{N_s \times 3}$ denoting the leadfield for a single source location. It then iterates Equation (14) and (15) until convergence and use the final weights to calculate $\hat{\mathbf{J}}$. eLORETA has been shown to outperform other linear solutions in localization precision (Allouch et al., 2022; Halder et al., 2019; Pascual-Marqui, 2007).

In this study, we choose the regularization parameter based on the best result in a five-fold spatial cross-validation (Hashemi et al., 2021) with fifteen candidate parameters taken from a logarithmically spaced range between $0.01 * \text{Tr}(\text{Cov}_{\tilde{\mathbf{Q}}})$ and $\text{Tr}(\text{Cov}_{\tilde{\mathbf{Q}}})$, where $\text{Tr}(A)$ denotes the trace of a matrix A and $\text{Cov}_{\tilde{\mathbf{Q}}} \in \mathbb{C}^{N_s \times N_s}$ denotes the sample covariance matrix of the sensor-space data.

Linearly-constrained minimum variance beamforming

The LCMV (Van Veen et al., 1997) filter $\mathbf{P}^L \in \mathbb{R}^{N_s \times 3N_v}$ belongs to the class of beamformers. It estimates source activity separately for every source location. While LCMV maximizes source activity originating from the target location, it suppresses noise and other source contributions. Let $\mathbf{L}_{v,v} \in \mathbb{R}^{N_s \times 3}$ and $\mathbf{P}_v^L \in \mathbb{R}^{N_s \times 3}$ denote the leadfield and projection matrix for a single source location, respectively. The LCMV projection filter minimizes the total variance of the source-projected signal across the three dipole dimensions:

$$\mathbf{P}_v^L = \underset{\mathbf{P}_v}{\text{argmin}} \text{Tr} \left(\mathbf{P}_v^\top \text{Cov}_{\tilde{\mathbf{Q}}} \mathbf{P}_v \right) \quad (16)$$

under the unit-gain constraint

$$\mathbf{P}_v^\top \mathbf{L}_{v,v} = \mathbf{I}_{3 \times 3}. \quad (17)$$

The source estimate $\hat{\mathbf{J}}_v \in \mathbb{R}^{3 \times N_t}$ at the v -th voxel is given by

$$\hat{\mathbf{J}}_v = \left[(\mathbf{L}_{v,v}^\top \text{Cov}_{\tilde{\mathbf{Q}}}^{-1} \mathbf{L}_{v,v})^{-1} \mathbf{L}_{v,v}^\top \text{Cov}_{\tilde{\mathbf{Q}}}^{-1} \right] \tilde{\mathbf{Q}} = \mathbf{P}_v^L \tilde{\mathbf{Q}}. \quad (18)$$

Previous simulations indicated that LCMV overall shows a higher connectivity reconstruction accuracy than eLORETA but is more strongly affected by low SNR (Anzolin et al., 2019). We show a power spectrum of exemplary LCMV-reconstructed source activity in Fig. 1e.

Dynamic imaging of coherent sources

DICS (Gross et al., 2001) is the frequency-domain equivalent of LCMV. In contrast to LCMV, DICS estimates spatial filters separately for each spectral frequency. The DICS filter \mathbf{P}^D is evaluated for a given frequency f using the real part of the sensor-level cross-spectral density matrix \mathbf{S}_Q :

$$\mathbf{P}_v^D(f) = (\mathbf{L}_{v,v}^\top \mathbf{S}_Q(f)^{-1} \mathbf{L}_{v,v})^{-1} \mathbf{L}_{v,v}^\top \mathbf{S}_Q(f)^{-1} \quad (19)$$

with

$$\mathbf{S}_Q(f) = \left\langle \mathbf{q}(f, e) \mathbf{q}^*(f, e) \right\rangle_e \in \mathbb{C}^{N_s \times N_s}, \quad (20)$$

where $(\cdot)^*$ denotes complex conjugation and $\mathbf{q}(f, e)$ denotes the Fourier transform of the sensor measurements $\tilde{\mathbf{q}}(t, e)$. That is, the time-domain sensor signal $\tilde{\mathbf{Q}}$ is cut into N_c epochs of T time samples to derive $\tilde{\mathbf{q}}(t, e)$, then multiplied with a Hanning window of length T , and Fourier-transformed epoch by epoch to derive $\mathbf{q}(f, e)$.

The beamformer filter $\mathbf{P}^D(f) = [\mathbf{P}_1^D(f), \dots, \mathbf{P}_{N_v}^D(f)]$ can then be used to project the sensor cross-spectrum to source space:

$$\mathbf{S}_J(f) = \mathbf{P}^D(f) \mathbf{S}_Q(f) \mathbf{P}^D(f) \in (\mathbb{C})^{3N_v \times 3N_v}. \quad (21)$$

Based on previous literature described above, we hypothesize that the beamformer solutions (LCMV and DICS) perform better than eLORETA when used in combination with undirected FC measures. However, since directed FC measures need to aggregate information across frequencies, we hypothesize that the estimation of such measures might be negatively affected by DICS source reconstruction. Concretely, we expect that DICS' ability to optimize SNR per frequency and, thereby, to reconstruct different sources for each frequency can be counterproductive in cases where in fact the same pairs of sources are interacting at multiple frequencies. In contrast, we expect that LCMV, which reconstructs a single set of sources by optimizing the SNR across the whole frequency spectrum, would yield more consistent source cross-spectra and, therefore, better directed FC estimates than DICS.

Champagne

Champagne (Wipf et al., 2010) uses hierarchical sparse Bayesian inference for inverse modelling. Specifically, it imposes a zero-mean Gaussian prior independently for each source voxel. The prior source covariance is given by

$$\boldsymbol{\Gamma} = \begin{bmatrix} \boldsymbol{\Gamma}_1 & \mathbf{0} & \dots & \mathbf{0} \\ \mathbf{0} & \boldsymbol{\Gamma}_2 & \dots & \mathbf{0} \\ \vdots & \vdots & \ddots & \vdots \\ \mathbf{0} & \mathbf{0} & \dots & \boldsymbol{\Gamma}_{N_v} \end{bmatrix} \in (\mathbb{R})^{3N_v \times 3N_v}, \quad (22)$$

where $\boldsymbol{\Gamma}_v$ is the 3×3 covariance of the v -th voxel. Here we use a Champagne variant that models each $\boldsymbol{\Gamma}_v$ as a full positive-definite matrix

$$\boldsymbol{\Gamma}_v = \begin{bmatrix} \gamma_{v,1} & \gamma_{v,4} & \gamma_{v,5} \\ \gamma_{v,4} & \gamma_{v,2} & \gamma_{v,6} \\ \gamma_{v,5} & \gamma_{v,6} & \gamma_{v,3} \end{bmatrix} \quad (23)$$

with six parameters. The prior source variances and covariances in $\boldsymbol{\Gamma}$ are treated as model hyperparameters and are optimized in an iterative way. For any given choice of $\boldsymbol{\Gamma}$, the posterior distribution of the source activity is given by (Wipf et al., 2010):

$$p(\tilde{\mathbf{J}} | \tilde{\mathbf{Q}}, \gamma) = \prod_{t=1}^{N_t} \mathcal{N}(\hat{\mathbf{j}}(t), \boldsymbol{\Sigma}_j), \quad \text{where} \quad (24)$$

$$\hat{\mathbf{j}}(t) = \boldsymbol{\Gamma} \mathbf{L}_v^\top (\boldsymbol{\Sigma}_q)^{-1} \tilde{\mathbf{q}}(t) = \mathbf{P}^C \tilde{\mathbf{q}}(t) \quad (25)$$

$$\boldsymbol{\Sigma}_j = \boldsymbol{\Gamma} - \boldsymbol{\Gamma} \mathbf{L}_v^\top (\boldsymbol{\Sigma}_q)^{-1} \mathbf{L}_v \boldsymbol{\Gamma} \quad (26)$$

$$\Sigma_q = \sigma^2 \mathbf{I} + \mathbf{L}_v \Gamma \mathbf{L}_v^\top, \quad (27)$$

and where σ^2 denotes a homoscedastic sensor noise variance parameter. The posterior parameters $\hat{\mathbf{j}}(t)$ and Σ_j are then used to obtain the next estimate of γ by minimizing the negative log model evidence (Bayesian Type-II likelihood):

$$\mathcal{L}^H(\gamma) = -\log p(\tilde{\mathbf{Q}}|\gamma) = \frac{1}{N_t} \sum_{t=1}^{N_t} \tilde{\mathbf{q}}(t)^\top \Sigma_q^{-1} \tilde{\mathbf{q}}(t) + \log \|\Sigma_q\|. \quad (28)$$

This process is repeated until convergence. Importantly, the majority of source variance parameters converges to zero in the course of the optimization, so that the reconstructed source distribution becomes sparse.

In the original Champagne version, a baseline or control measurement is used to estimate noise covariance in sensor data. Since baseline data are not available in our study, we use a homoscedastic noise model in which all sensors are assumed to be perturbed by uncorrelated Gaussian white noise with equal variance, and estimate the shared variance parameter using five-fold spatial cross-validation (Hashemi et al., 2021). Again, fifteen candidate parameters are taken from a logarithmically spaced range between $0.01 * \text{Tr}(\text{Cov}_{\tilde{\mathbf{Q}}})$ and $\text{Tr}(\text{Cov}_{\tilde{\mathbf{Q}}})$.

2.3. Dimensionality reduction

To aggregate time series of multiple sources within a region, an intuitive approach would be to take the mean across sources within each spatial dimension. However, this approach has two disadvantages: First, it assumes a high homogeneity within all voxels of a pre-defined region, which is not always given. Second, it does not offer a solution for aggregating the three spatial dimensions, since averaging across these might lead to cancellations due to different polarities.

Principal component analysis

An alternative approach is to reduce the dimensionality of multiple time series by employing a singular value decomposition (SVD) or, equivalently, principal component analysis (PCA), and to subsequently only select the C strongest PCs accounting for most of the variance within a region for further processing. Let $\tilde{\mathbf{J}}_r \in \mathbb{R}^{N_t \times 3R}$ denote the reconstructed broad-band source time courses of R dipolar sources within a single region r after mean subtraction. The covariance matrix $\text{Cov}_r = \frac{\tilde{\mathbf{J}}_r^\top \tilde{\mathbf{J}}_r}{N_t - 1} \in \mathbb{R}^{3R \times 3R}$ is a symmetric matrix that can be diagonalized as

$$\text{Cov}_r = \mathbf{B}\mathbf{V}\mathbf{B}^\top, \quad (29)$$

where $\mathbf{B} \in \mathbb{R}^{3R \times 3R}$ is a diagonal matrix containing the eigenvalues λ_v (variances) of the PCs, which are, without loss of generality, assumed to be given in descending order, and $\mathbf{V} \in \mathbb{R}^{3R \times 3R}$ is a matrix of corresponding eigenvectors in which each column contains one eigenvector. The j^{th} PC can then be found in the j^{th} column of $\tilde{\mathbf{J}}_r \mathbf{V}$.

In practice, the PCs are calculated using an SVD of the zero-mean data matrix $\tilde{\mathbf{J}}_r$ as

$$\tilde{\mathbf{J}}_r = \mathbf{U}\mathbf{D}\mathbf{V}^\top. \quad (30)$$

Using the ‘economy version’ of the SVD, $\mathbf{U} \in \mathbb{R}^{N_t \times 3R}$ is a matrix of orthonormal PC time courses, $\mathbf{D} \in \mathbb{R}^{3R \times 3R}$ is a matrix of corresponding singular values, and $\mathbf{V} \in \mathbb{R}^{3R \times 3R}$ is the matrix of eigenvectors (or, equivalently, singular vectors) defined above. Note that the square of the elements of \mathbf{D} , divided by $N_t - 1$, are identical to the variances of the corresponding PCs (eigenvalues of Cov_r). Each squared singular vector, normalized by the sum of all singular vectors, thus corresponds to the variance explained by the corresponding singular vector. We will use this property for the two VARPC pipelines (Section 2.5).

Comparing PCA and SVD, one can easily see that

$$\text{Cov}_r = \mathbf{V}\mathbf{D}\mathbf{U}^\top \mathbf{U}\mathbf{D}\mathbf{V}^\top = \mathbf{V} \frac{\mathbf{D}^2}{N_t - 1} \mathbf{V}^\top, \quad (31)$$

and $\lambda_v = \frac{d_v^2}{N_t - 1}$. Thus, the PCs can also be calculated with SVD:

$$\tilde{\mathbf{J}}_r \mathbf{V} = \mathbf{U}\mathbf{D}\mathbf{V}^\top \mathbf{V} = \mathbf{U}\mathbf{D}. \quad (32)$$

To reduce the dimensionality of the voxel data within one region, we keep only the strongest C PCs, i.e., the columns of \mathbf{UD} that correspond to the largest eigenvalues. For a more extensive overview of the relationship between SVD and PCA, we refer to Wall et al. (2003). Note that in this study, we applied SVD on the time-domain source signals $\tilde{\mathbf{J}}_r$ for most of the pipelines. However, we applied PCA on the real part of the source-level cross-spectrum, summed across frequencies, in case of DICS. For the ease of reading, we will stick to PCA terminology for all pipelines in the following.

It has been popular in the literature (Basti et al., 2020; Friston et al., 2006) to select only the first PC for every region and subsequently employ a univariate FC measure for further processing. We describe this approach further in Section 2.5, pipeline FIXPC1.

2.4. Connectivity metrics

There are numerous approaches to estimate FC (Schoffelen and Gross, 2019). One key distinction can be made between FC metrics that measure undirected (symmetric) interactions between signals and those that also measure the direction of FC.

It has been shown that the estimation of both undirected and directed FC from M/EEG recordings is complicated by the presence of mixed noise and signal sources (Bastos and Schoffelen, 2016; Haufe et al., 2013; Nolte et al., 2004; Schawronkow and Nikulin, 2021; Wang et al., 2018). Due to volume conduction in the brain, signal sources from all parts of the brain superimpose at each M/EEG sensor. Projecting the sensor signals to source space can help disentangling separate signal sources. However, a signal reconstructed at a specific source voxel may still contain contributions from other sources in its vicinity. This phenomenon is called source leakage (Schoffelen and Gross, 2009).

Volume conduction and source leakage can lead to spurious FC despite the absence of genuine interactions (Haufe et al., 2013; Nolte et al., 2004). To overcome this problem, robust FC metrics have been developed (Haufe et al., 2013; Nolte et al., 2004; 2008; Winkler et al., 2016). Robustness is here referred to as the property of an FC measure to converge to zero in the limit of infinite data when the observed data are just instantaneous mixtures of independent sources (Nolte et al., 2004). Robust FC metrics use that spurious interactions due to signal mixing are instantaneous, while physiological interactions impose a small time delay. Robust FC metrics are therefore only sensitive to statistical dependencies with a non-zero time delay while eliminating zero-delay contributions.

We here test six different FC measures, four to detect undirected FC (coherence, iCOH, MIC, and MIM), and two measures that estimate the direction of interaction between two sources (multivariate GC and TRGC). This selection includes four robust FC metrics (c.f. Section 1) and two non-robust ones (coherence and GC). Based on the literature described above, we hypothesize that robust metrics will perform better than non-robust metrics. Please note that all tested FC metrics are frequency-resolved. That is, all metrics output an $N_{roi} \times N_{roi} \times N_{freq}$ tensor that contains the estimated FC for all region pairs at all frequencies. However, since we expect the interaction to be located in the interacting frequency band between 8 and 12 Hz (see Section 2.1), we select only those frequency bins within this band and average the FC scores across them. As a result, we obtain an $N_{roi} \times N_{roi}$ matrix.

All tested FC metrics are derived from the cross-spectrum. Let $\tilde{\mathbf{x}}(t, e) \in \mathbb{R}^K$ and $\tilde{\mathbf{y}}(t, e) \in \mathbb{R}^L$ be two multivariate time series where $t \in \{1, \dots, T\}$ indexes samples within epochs of 2 seconds length and e indexes epochs. Often, $K = L = 3$ represents the three dipole orientations of two reconstructed current sources. In other cases, K and L denotes the number of retained data dimensions of two brain regions after (e.g., PCA) dimensionality reduction. These time-domain data are then multiplied with a Hanning window and Fourier transformed into $\mathbf{x}(f, e)$ and

$y(f, e)$, where $f \in \{0, 0.5, \dots, 50\}$ indexes frequencies. The joint cross-spectrum is then computed from the Fourier-transformed data as

$$\mathbf{S}_{[\mathbf{x}\mathbf{y}]}(f) = \begin{bmatrix} \mathbf{S}_{\mathbf{xx}}(f) & \mathbf{S}_{\mathbf{xy}}(f) \\ \mathbf{S}_{\mathbf{yx}}(f) & \mathbf{S}_{\mathbf{yy}}(f) \end{bmatrix} \in (\mathbb{C})^{(K+L) \times (K+L)}, \quad (33)$$

where $\mathbf{S}_{\mathbf{xy}} = \langle \mathbf{x}(f, e)\mathbf{y}^*(f, e) \rangle_e \in \mathbb{C}^{K \times L}$.

Coherence and imaginary part of coherency

(Absolute) coherence (COH) and iCOH are measures of the synchronicity of two time series. Both coherence and iCOH are derived from the complex-valued coherency, which is a generalization of correlation in the frequency domain. As such, coherency quantifies the linear relationship between two time series at a specific frequency. Its phase expresses the average phase difference between the two time series, whereas its absolute value expresses the stability of the phase difference.

Complex-valued coherency $\mathbf{C}_{\mathbf{xy}} \in \mathbb{C}^{K \times L}$ is the normalized cross spectrum (Nunez et al., 1997):

$$\mathbf{C}_{\mathbf{xy}}(f) = \frac{\mathbf{S}_{\mathbf{xy}}(f)}{(\mathbf{S}_{\mathbf{xx}}(f)\mathbf{S}_{\mathbf{yy}}(f))^{1/2}}. \quad (34)$$

Based on the terminology of Nolte et al. (2004), we define *coherence* as the absolute part of coherency: $\text{COH}_{\mathbf{xy}}(f) = |\mathbf{C}_{\mathbf{xy}}(f)| \in \mathbb{R}^{K \times L}$, where $|\cdot|$ denotes the absolute value. Coherence captures both zero-delay and non-zero-delay synchronization between two time series. This can be problematic in the context of M/EEG measurements, where substantial zero-delay synchronization can be introduced by signal spread due to volume conduction or source leakage in absence of genuine interactions between distinct brain areas (Nolte et al., 2004). In contrast, the imaginary part of coherency is a robust FC measure since it is only non-zero for interactions with a phase delay different from multiples of π (Nolte et al., 2004). Here, we use the absolute value of the imaginary part of coherency, $\text{iCOH}_{\mathbf{xy}}(f) = |\mathbf{C}_{\mathbf{xy}}^{\Im}(f)| \in \mathbb{C}^{K \times L}$, as a measure of synchronization strength, where \mathbf{C}^{\Im} denotes the imaginary part of \mathbf{C} .

Note that both coherence and iCOH are not designed to aggregate FC between two multivariate time series into one FC score. A single FC score can be obtained by taking the average across all elements of $\text{COH}_{\mathbf{xy}}$ or $\text{iCOH}_{\mathbf{xy}}$, respectively.

Multivariate interaction measure and maximized imaginary coherency

The multivariate interaction measure (MIM) and maximized imaginary coherency (MIC, Ewald et al., 2012) are multivariate generalizations of iCOH and are therefore also robust against source leakage.

MIM is defined as follows:

$$\text{MIM}_{\mathbf{xy}}(f) = \text{Tr} \left[\left(\mathbf{C}_{\mathbf{xx}}^{\Re}(f) \right)^{-1} \mathbf{C}_{\mathbf{xy}}^{\Im}(f) \left(\mathbf{C}_{\mathbf{yy}}^{\Re}(f) \right)^{-1} \left(\mathbf{C}_{\mathbf{xy}}^{\Im}(f) \right)^{\top} \right], \quad (35)$$

where \mathbf{C}^{\Re} denotes the real part of \mathbf{C} . In contrast, MIC aims at maximizing iCOH between the two multivariate time series. That is, MIC finds projections from two multi-dimensional spaces to two one-dimensional spaces such that iCOH between the projected signals becomes maximal:

$$\text{MIC}_{\mathbf{xy}}(f) = \max_{\mathbf{a}, \mathbf{b}} \left(\frac{\mathbf{a}^{\top} \tilde{\mathbf{S}}_{\mathbf{xy}}^{\Im}(f) \mathbf{b}}{|\mathbf{a}| |\mathbf{b}|} \right), \quad (36)$$

where $\tilde{\mathbf{S}}$ is a whitened version of the cross-spectrum \mathbf{S} (Ewald et al., 2012), and where $\mathbf{a} \in \mathbb{R}^{K \times 1}$ and $\mathbf{b} \in \mathbb{R}^{L \times 1}$ are projection weight vectors corresponding to the subspaces, or regions, of \mathbf{x} and \mathbf{y} , respectively. Note that, while the imaginary part itself can be positive or negative, flipping the sign of either \mathbf{a} or \mathbf{b} will also flip the sign of the imaginary part. Thus, without loss of generality, maximization of Eq. (36) will find the imaginary part with strongest magnitude.

All undirected FC metrics (COH, iCOH, MIC, and MIM) are bounded between 0 and 1.

Multivariate Granger causality and time-reversed Granger causality

Granger Causality (GC) defines directed interactions between time series using a predictability argument (Bressler and Seth, 2011; Granger, 1969). Considering two univariate time series $\tilde{\mathbf{x}}(t)$ and $\tilde{\mathbf{y}}(t)$, we say that $\tilde{\mathbf{y}}$ Granger-causes $\tilde{\mathbf{x}}$ if the past information of $\tilde{\mathbf{y}}$ improves the prediction of the presence of $\tilde{\mathbf{x}}$ above and beyond what we could predict by the past of $\tilde{\mathbf{x}}$ alone. That is, GC does not only assess the existence of a connection but also estimates the direction of that connection. We here use a spectrally resolved multivariate extension of GC (Barnett and Seth, 2014; Barrett et al., 2010; Geweke, 1982), which allows us to estimate Granger-causal influences between groups of variables at individual frequencies. There are multiple strategies to arrive at spectral Granger causality estimates. Here, we follow recommendations made in Barnett et al. (2018); Barnett and Seth (2014, 2015); Faes et al. (2017) that ensure stable and unbiased estimates, and use Matlab code provided by the respective authors.

We first transform the joint cross-spectrum into an autocovariance sequence $\mathbf{G}_{[\mathbf{x}\mathbf{y}]}(p) \in \mathbb{R}^{(K+L) \times (K+L)}$ with lags $p \in \{0, 1, \dots, N_p\}$, $N_p = 20$, using the inverse Fourier transform. The autocovariance spectrum is further used to estimate the parameters $\mathbf{A}(p) \in \mathbb{R}^{(K+L) \times (K+L)}$, $p \in \{1, \dots, N_p\}$ and $\Sigma = \text{Cov}_t[\epsilon(t)] \in \mathbb{R}^{(K+L) \times (K+L)}$ of a linear autoregressive model

$$\begin{bmatrix} \mathbf{x}(t) \\ \mathbf{y}(t) \end{bmatrix} = \sum_{p=1}^{N_p} \mathbf{A}(p) \begin{bmatrix} \mathbf{x}(t-p) \\ \mathbf{y}(t-p) \end{bmatrix} + \epsilon(t) \quad (37)$$

of order N_p using Whittle's algorithm (Barnett and Seth, 2014; Whittle, 1963). Autoregressive model parameters are next converted into a state-space representation $(\mathbf{A}, \bar{\mathbf{C}}, \bar{\mathbf{K}}, \bar{\Sigma})$ corresponding to the model

$$\mathbf{z}(t) = \bar{\mathbf{A}}\mathbf{z}(t) + \bar{\mathbf{K}}\epsilon(t) \quad (38)$$

$$\begin{bmatrix} \tilde{\mathbf{x}}(t) \\ \tilde{\mathbf{y}}(t) \end{bmatrix} = \bar{\mathbf{C}}\mathbf{z}(t) + \epsilon(t), \quad (39)$$

using the method of Aoki and Havenner (1991), where $\tilde{\mathbf{x}}(t) = [\tilde{\mathbf{x}}^{\top}(t), \tilde{\mathbf{x}}^{\top}(t-1), \dots, \tilde{\mathbf{x}}^{\top}(t-N_p)]^{\top}$ and $\tilde{\mathbf{y}}(t) = [\tilde{\mathbf{y}}^{\top}(t), \tilde{\mathbf{y}}^{\top}(t-1), \dots, \tilde{\mathbf{y}}^{\top}(t-N_p)]^{\top}$ are temporal embeddings of order N_p , $\mathbf{z}(t) \in \mathbb{R}^{(K+L)N_p}$ and $\epsilon(t) \in \mathbb{R}^{(K+L)N_p}$ are unobserved variables, and all parameters are $(K+L)N_p \times (K+L)N_p$ matrices. Subsequently, the transfer function $\mathbf{H}(z) \equiv \mathbf{I} - \bar{\mathbf{C}}(\mathbf{I} - \bar{\mathbf{A}}z)^{-1}\bar{\mathbf{K}}z \in \mathbb{C}^{(K+L)N_p \times (K+L)N_p}$ of a moving-average representation

$$\begin{bmatrix} \mathbf{x}(t) \\ \mathbf{y}(t) \end{bmatrix} = \mathbf{H}(z) \cdot \epsilon(t) \quad (40)$$

of the observations is derived, where $\mathbf{I} \in \mathbb{R}^{(K+L)N_p \times (K+L)N_p}$ denotes the identity matrix and where $z = e^{-i4\pi f/T}$ for a vector of frequencies $f \in \{0 \text{ Hz}, 0.5 \text{ Hz}, \dots, 50 \text{ Hz}\}$, $T = 200$, and a factorization of the joint cross-spectrum is obtained as $\mathbf{S}_{[\mathbf{x}\mathbf{y}]}(f) = \mathbf{H}(f)\bar{\Sigma}\mathbf{H}^*(f)$ (Barnett and Seth, 2015). Frequency-dependent *Granger scores*

$$\mathcal{F}_{\mathbf{x} \rightarrow \mathbf{y}}(f) = \log \frac{\|\mathbf{S}_{\mathbf{yy}}(f)\|}{\|\mathbf{S}_{\mathbf{yy}}(f) - \mathbf{H}_{\mathbf{yx}}(f)\bar{\Sigma}_{\mathbf{xx}|\mathbf{y}}\mathbf{H}_{\mathbf{yx}}^*(f)\|} \quad (41)$$

and (analogously) $\mathcal{F}_{\mathbf{y} \rightarrow \mathbf{x}}(f)$ are then calculated, where $\mathbf{H}(f)$ and $\bar{\Sigma}$ are partitioned in the same way as $\mathbf{S}(f)$, where $\bar{\Sigma}_{\mathbf{xx}|\mathbf{y}} \equiv \bar{\Sigma}_{\mathbf{xx}} - \bar{\Sigma}_{\mathbf{xy}}\bar{\Sigma}_{\mathbf{yy}}^{-1}\bar{\Sigma}_{\mathbf{yx}}$ denotes a partial covariance matrix, and where $\|\cdot\|$ denotes matrix determinant (Barnett and Seth, 2015). Finally, differences

$$\mathcal{F}_{\mathbf{x} \rightarrow \mathbf{y}}^{\text{net}}(f) \equiv \mathcal{F}_{\mathbf{x} \rightarrow \mathbf{y}}(f) - \mathcal{F}_{\mathbf{y} \rightarrow \mathbf{x}}(f) \quad (42)$$

and $\mathcal{F}_{\mathbf{y} \rightarrow \mathbf{x}}^{\text{net}}(f) = -\mathcal{F}_{\mathbf{x} \rightarrow \mathbf{y}}^{\text{net}}(f)$ summarizing the net information flow between the multivariate time series $\tilde{\mathbf{x}}(t)$ and $\tilde{\mathbf{y}}(t)$ are calculated (Winkler et al., 2016).

Just like coherence, GC is not robust, i.e. can deliver spurious results for mixtures of independent sources as a result of volume conduction or source leakage (e.g., Haufe et al., 2013; 2012). This can be easily acknowledged by considering a single source that spreads into two measurement channels, which are superimposed by distinct noise

terms. In that case, both channels will mutually improve each other's prediction in the sense of GC (Haufe and Ewald, 2019). This problem is overcome by a robust version of GC, time-reversed GC (TRGC), which introduces a test on the temporal order of the time series. That is, TRGC estimates the directed information flow once on the original time series and once on a time-reversed version of the time series. If GC is reduced or even reversed when the temporal order of the time series is reversed, it is likely that the effect is not an artifact coming from volume conduction (Haufe et al., 2013; 2012; Vinck et al., 2015; Winkler et al., 2016). Formally, multivariate spectral GC as introduced above can be evaluated on the time-reversed data by fitting the autoregressive model in Eq. (37) on the transposed autocovariance sequence $\mathbf{G}_{[xy]}^{\text{TR}}(p) = \mathbf{G}_{[xy]}^{\top}(p)$, $p \in \{0, 1, \dots, N_p\}$. This yields net GC scores $F_{x-y}^{\text{TR net}}(f)$ for the time-reversed data, which are subtracted from the net scores obtained for the original (forward) data to yield the final time-reversed GC scores:

$$F_{x-y}^{\text{TRGC}}(f) \equiv F_{x-y}^{\text{net}}(f) - F_{x-y}^{\text{TR net}}(f) \quad (43)$$

and (analogously) $F_{y-x}^{\text{TRGC}}(f) \equiv F_{y-x}^{\text{net}}(f) - F_{y-x}^{\text{TR net}}(f) = -F_{x-y}^{\text{TRGC}}(f)$.

2.5. Pipelines

In the following section, we describe the processing pipelines that were tested. All pipelines take the sensor measurements $\bar{\mathbf{Q}}$ as input. Then all pipelines calculate and apply an inverse model \mathbf{P} to project sensor data to source level. From there, we aggregate voxel activity within regions by employing PCA and estimate inter-regional FC with various FC metrics described above. We describe several strategies of combining PCA with the calculation of FC in the following subsections. This step results in a $N_{roi} \times N_{roi} \times N_{freq}$ FC matrix which is then averaged across the frequency bins within the interaction frequency band (8–12 Hz). The output of all pipelines is one connectivity score for every region combination. We describe the processing exemplarily for the calculation of FC between two regions X and Y.

Pipelines FIXPC1 to FIXPC6: Fixed number of principal components

The first six pipelines use PCA dimensionality reduction. Afterwards, depending on the pipeline, a fixed number C of either one, two, three, four, five, or six strongest PCs are selected for further processing. Then, FC is calculated: in case of univariate measures (i.e., coherence and iCOH), we first calculate FC scores between all PC combinations of the two regions X and Y and then average across all pairwise FC scores. In case of multivariate FC measures, we directly calculate a single FC score between the PCs of region X and those of region Y. This approach has been used previously (e.g. Schöffelen et al., 2017).

Pipelines VARPC90 and VARPC99: Variable numbers of principal components

Pipelines VARPC90 and VARPC99 are equivalent to the FIXPC pipelines, with the difference that we do not select the same fixed number of PCs for every region. Instead, we select the number of PCs such that at least 90% (VARPC90) or 99% (VARPC99) of the variance in each ROI is preserved (c.f. Section 2.3). Thus, an individual number of PCs is chosen for each region. FC is then calculated analogously to pipelines FIXPC1 to FIXPC6. The idea of selecting the number of PCs such that a pre-defined fraction of the variance is retained has been used in previous literature (e.g. Gómez-Herrero et al., 2008).

Pipeline MEANFC: Mean first FC second

In this pipeline, the time series of all voxels within one region are averaged separately for the three orthogonal dipole orientations. Then, for univariate FC measures, FC is calculated between all 3×3 dimension combinations of the 3D-time series of region X and region Y. Afterwards, the average of these nine FC scores is taken. Multivariate FC measures are directly calculated between the 3D time series.

Pipeline CENTRAL: Central voxel pick

In this pipeline, we select only the central voxel of each region for further processing. The central voxel of a region is defined as the voxel whose average Euclidean distance to all other voxels in the region is minimal. To calculate the FC score between the 3D time series of the central voxel of region X and the 3D time series of the central voxel of region Y, we proceed analogous to pipeline MEANFC: in case of univariate FC measures, the FC score for all combinations of dipole orientations is calculated and then averaged. In case of multivariate FC measures, only one FC score is calculated between the two 3D time series. Selecting the time series of the central voxel as the representative time series for the region is an idea that has been used in previous studies already (Perinelli et al., 2022).

Pipeline FCMEAN: FC first mean second

In pipeline FCMEAN, the multivariate FC between each 3D voxel time series of region X with each voxel time series of region Y is calculated first. That is, if R_X is the number of voxels of region X and R_Y is the number of voxels in region Y, $R_X * R_Y$ FC scores for all voxel combinations are calculated. To obtain a single FC score between region X and region Y, we then average all $R_X * R_Y$ FC scores. Due to computational and time constraints, we test this pipeline only for MIM and MIC. This approach has also been used in the literature before (Babiloni et al., 2018).

Pipeline TRUEVOX: True voxel pick

This pipeline is used as a baseline. Here we select the voxel for further processing that indeed contains the activity of the given ROI—i.e. the ground-truth voxel (see Section 2.1). All further processing is analogous to pipeline CENTRAL. In configurations with two active voxels per region (see Section 3, Experiment 6), FC scores are calculated for $2 * 3 * 3$ voxel- and dipole orientation combinations.

2.6. Performance evaluation

We use a rank-based evaluation metric to assess the performance of the pipelines. All processing pipelines result in one FC score for every region-region combination. To evaluate the performance of a pipeline, we first sort all FC scores in a descending order and retrieve the rank $r \in \mathbb{R}^{N_I}$, with $N_I \in \{1, 2, 3, 4, 5\}$ denoting the number of ground-truth interactions. Based on this rank vector, we calculate the percentile rank (PR):

$$PR' = \frac{\sum_i^{N_I} \left(1 - \frac{r_i}{F}\right)}{N_I}, \quad (44)$$

with F denoting the total number of FC scores. The PR' is then normalized to the perfect-skill PR_{ps} and no-skill PR_{ns} cases, and is therefore defined between 0 and 1:

$$PR_{ps} = \frac{\sum_i^{N_I} \left(1 - \frac{i}{F}\right)}{N_I} \quad (45)$$

$$PR_{ns} = \frac{\sum_i^{N_I} \left(1 - \frac{F-i+1}{F}\right)}{N_I} \quad (46)$$

$$PR = \frac{PR' - PR_{ns}}{PR_{ps} - PR_{ns}}. \quad (47)$$

We report all PR values rounded to the second decimal. In case of the phase-based FC metrics, the PR is calculated on the original FC scores. In case of GC and TRGC, we separately evaluate each pipeline's interaction detection ability, and its ability to determine the direction of the interaction. For evaluating the detection, we calculate the PR on the absolute values of the FC scores, whereas for evaluating the directionality determination performance, we calculate the PR only on the positive FC scores. Note that this is sufficient for the anti-symmetric directed FC measures used here.

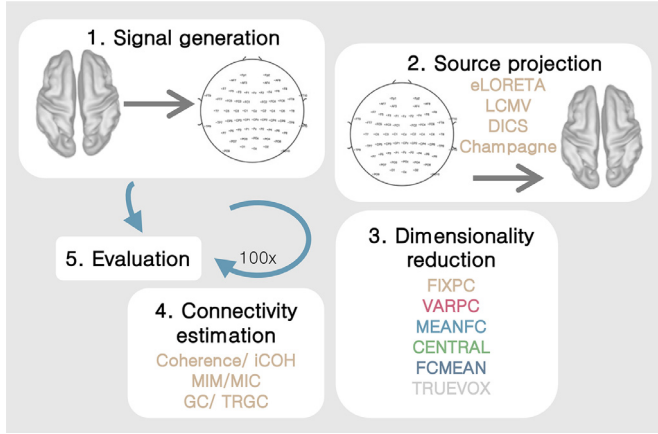


Fig. 2. Experimental setup. Every experiment consisted of five consecutive steps: (1) Signal generation. (2) Source projection. (3) Dimensionality reduction within regions. (4) Functional connectivity estimation. (5) Performance evaluation. Every experiment was carried out 100 times.

2.7. Statistical assessment

In Experiment 1C, we provide a suggestion on how to statistically assess the presence of FC. Here, we obtain p-values by testing against a surrogate distribution consistent with the null hypothesis of zero interaction between all region pairs. The 10,000 samples of the surrogate distribution are drawn by shuffling epochs relative to each other when computing the cross-spectrum. More specifically, we calculate the cross-spectrum between the time series of one region and the shuffled time series of another region with the Welch method, where the diagonal entries of the cross-spectrum (spectral powers) are obtained without shuffling. From the shuffled cross-spectrum, MIM is calculated. We obtain p-values by counting the number of shuffled MIM-samples that are higher than the true MIM score and dividing this number by the total number of samples in the null distribution. FDR-correction (α -level = 0.05) is used on the upper triangle of the region–region p-value matrix to set a significance threshold.

2.8. ROIconnect Toolbox

Based on our experimental results (see Section 3), we identified a set of recommended methods and pipelines. These have been implemented in a Matlab toolbox and are made available as a plugin to the free EEGLab package². This toolbox also contains code for analyzing spectral power in EEG source space, and for visualizing power and FC results in source space. A comprehensive description of the functionality and usage of the toolbox is provided in Appendix A. Moreover, an exemplary application of the toolbox to the analysis of a real EEG dataset is provided in Section 4.

3. Experiments and results

We conducted a set of experiments to assess the influence of the different pipeline parameters on the reconstruction of ground-truth region-to-region FC. We describe the general experimental setting in Fig. 2. Each experiment consisted of the following steps: (1) Signal generation. (2) Source projection. (3) Dimensionality reduction within regions. (4) Functional connectivity estimation. (5) Performance evaluation. Each experiment was carried out 100 times (= iterations). If not indicated otherwise, all experiments had the following default setting:

- LCMV inverse solution

- SNR = 3.5 dB
- BSR = 0 dB
- number of interactions = 2
- time delay of the interaction = 50 to 200 ms
- number of generated sources per region = 1

If not stated otherwise, the following parameters were drawn randomly in each iteration: ground-truth interacting (seed and target) regions (two distinct regions uniformly drawn between 1 and N_{roi}), ground-truth active voxel(s) within regions (uniformly drawn between 1 and R_{roi}), time delay (uniformly drawn between 50 and 200 ms). Furthermore, brain noise and sensor noise, as well as the signal were generated based on (filtered) random white noise processes as described above.

Fig. 3 to Fig. 11 show the results of experiments 1–6. In addition, all main results are summarized in Table 1. All figures (plotting code adapted from Allen et al., 2019) follow the same scheme: in every subplot, the 100 dots on the right side mark the performance, i.e. the PR, measured in each of the 100 iterations. On the left, a smooth kernel estimate of the data density is shown. The red and black lines represent the mean and median PR of the experiment, respectively, and the boxcar marks the 2.5th and 97.5th percentiles. Please note that the Y-axis is scaled logarithmically in all plots. We tested differences between pipeline performances with a one-sided Wilcoxon signed-rank test. Please note that a p-value $p_{A,B}$ corresponds to a one-sided test for $B > A$.

Matlab code to reproduce all experiments is provided under³.

3.1. Experiment 1

Experiment 1A

In Experiment 1A, we evaluated the performance of different FC metrics in detecting the ground-truth interactions. The ability to detect FC was tested for coherence, iCOH, MIC, MIM, GC, and TRGC. The ability to detect the correct direction of the interaction was tested for GC and TRGC (see Section 2.4).

In Fig. 3, we show the performances of different FC metrics. We see that MIM, MIC and TRGC (detection) all have a mean PR of over 0.97 and clearly outperform the other measures in detecting the ground-truth FC. The non-robust metrics coherence (mean PR = 0.59) and GC (mean PR = 0.95) detect the ground-truth interactions less reliably ($p_{\text{coherence}, \text{MIM}} < 10^{-4}$;

$p_{\text{GC}, \text{MIM}} = 0.0040$). When comparing GC and TRGC in their ability to infer the direction of the interaction, TRGC (mean PR = 0.98) outperforms GC (mean PR = 0.96; $p_{\text{GC}, \text{TRGC}} < 10^{-4}$).

Experiment 1B

In Experiment 1B, we tested the influence of different strategies of dimensionality reduction within regions. In Fig. 4, we show the comparison for MIM (interaction detection) and TRGC (directionality determination). For MIM, we observe that the FIXPC pipelines show a better performance than most of the other pipelines. Within the FIXPC pipelines, the pipelines with two, three, or four PCs perform best (all mean PR = 0.99, $p_{\text{FIXPC}2, \text{FIXPC}3} < 10^{-4}$). Only the TRUEVOX (baseline) pipeline using ground-truth information on voxel locations expectantly shows a higher performance (mean PR = 1.00; $p_{\text{FIXPC}3, \text{TRUEVOX}} < 10^{-4}$). The two VARPC pipelines show a substantially reduced performance (mean PR = 0.96 and mean PR = 0.73, respectively; both $p_{\text{VARPC}, \text{FIXPC}3} < 10^{-4}$). The MEANFC and CENTRAL pipelines (mean PR = 0.98 and mean PR = 0.96, respectively) also show reduced performance in comparison to the FIXPC3 pipeline (both $p < 10^{-4}$). The FCMEAN pipeline (mean PR = 0.97) also did not perform as well as the FIXPC3 pipeline ($p < 10^{-4}$) while taking much longer to compute (FIXPC3 < 1 h, FCMEAN = 32 h, single core, allocated memory: 16 GB).

² <https://github.com/sccn/roiconnect>

³ <https://github.com/fpellegrini/FCsim>

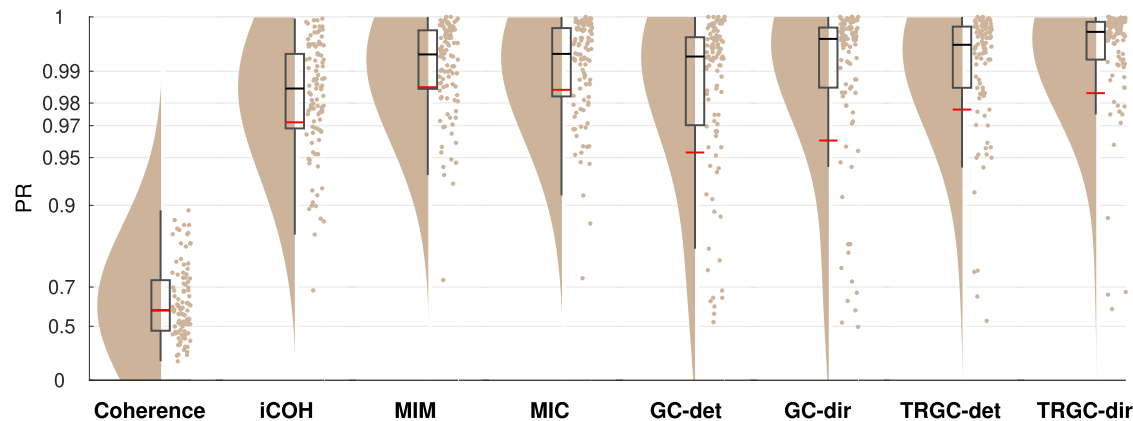
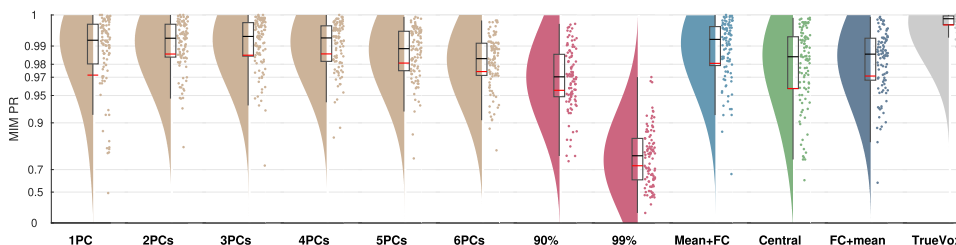


Fig. 3. Comparison of different functional connectivity metrics (Experiment 1A). Red and black lines indicate the mean and median percentile rank (PR), respectively. The boxcar marks the 2.5th and 97.5th percentiles.

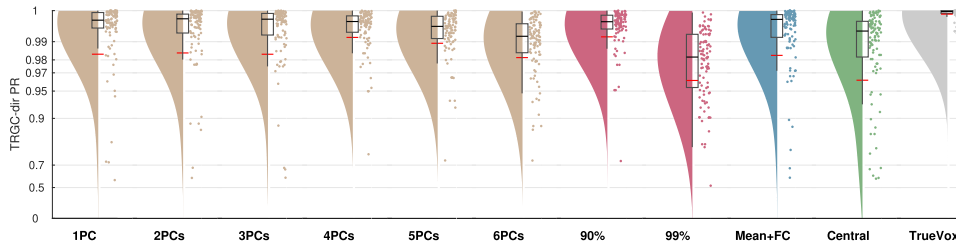
Table 1

Summary of the results of experiment one to six. A pipeline including robust multivariate FC metrics like MIM or TRGC, a PCA with fixed number of selected components, and LCMV source reconstruction yields the best performance.

#Exp.	Tested parameter	Result
1A	FC metric	MIM/TRGC yield best performance.
1B	pipelines	Fixed PC+FC yield best performance.
2	Inverse solution	LCMV yields best performance.
3A	SNR	The higher the better.
3B	BSR	The less sensor noise the better.
4	#Interactions	The lower the better.
5	Short interaction delays	Longer delays yield better performance.
6	Two active sources	Overall lower performance. Peak performance at three to four PCs.



(a) Undirected FC reconstruction performance using MIM.



(b) Directed FC reconstruction performance using TRGC.

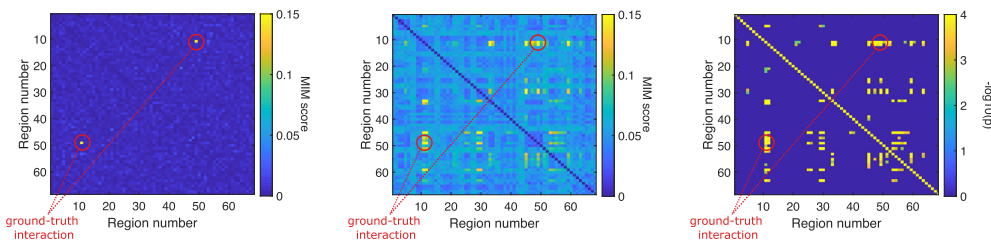
In terms of directionality estimation using TRGC, the outcome is similar. Again, the TRUEVOX pipeline shows perfect performance (mean PR = 1.00). The FIXPC pipelines also exhibit very high performances (FIXPC4: mean PR = 0.99). Notably, in contrast to the results obtained with MIM, the VARPC90 also achieves competitive performance (mean PR = 0.99, $p_{VARPC90, FIXPC3} = 0.0235$). Please see Figure S1 to compare computation times of all pipelines.

We show the full matrix of all combinations of FC metrics and dimensionality reduction pipelines in Supplementary Figure S2. However, for all further experiments, we report performances only for MIM (in-

teraction detection) and TRGC (directionality determination) since they performed best in Experiment 1A, and we focus on the FIXPC3 pipeline due to the high performance observed in Experiment 1B.

Experiment 1C

To explore how to statistically assess the presence of FC, we performed an additional experiment for a specific setting (SNR = 3.5 dB, one interaction between region 11 and region 49, BSR = 0 dB, LCMV filter, dimensionality reduction to 3PCs, FC metric = MIM). Here, we obtained p-values by testing against a surrogate distribution consistent



(a) Ground truth source-level connectome measured by MIM.
(b) Reconstructed source-level connectome measured by MIM.

(c) Statistical significance.
P-values masked with FDR correction.

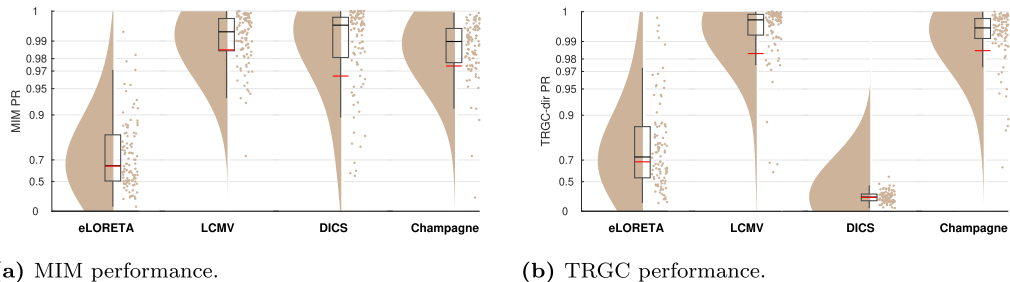


Fig. 6. Comparison of different inverse solutions (Experiment 2). (a) Undirected FC reconstruction performance achieved using the multivariate interaction measure (MIM). (b) Directed FC reconstruction performance achieved using time-reversed Granger causality. Red and black lines indicate the mean and median percentile rank (PR), respectively. The boxcar marks the 2.5th and 97.5th percentile.

with the null hypothesis of zero interaction between all region pairs. In Fig. 5, we contrast the ground-truth ROI-to-ROI connectome with the estimated FC per region combination as well as the $-\log_{10}(p)$ values “surviving” the FDR-correction for this experiment. While in the ground-truth connectome only the ground-truth region combination shows a high MIM score, there are also some high MIM scores in other region combinations than the ground truth in the reconstructed source-level connectome. Still, the ground-truth region combination in this setting achieves the second-highest MIM score (PR = 0.9996). However, in Fig. 5c, we see that testing the statistical significance with a shuffling test results in a substantial number of significant false positive interactions in the vicinity of the simulated interacting region pair. We discuss this result in Section 5.

3.2. Experiment 2

Experiment 2A

In Experiment 2, we tested the influence of the type of inverse solution on the pipelines performances. In Figure 6, we show the comparison between eLORETA, LCMV, DICS, and Champagne. We observe that the two beamformer solutions and Champagne clearly outperform eLORETA (mean PR = 0.65; Figure 6a) in detecting undirected connectivity (all $p < 10^{-4}$). While DICS, LCMV and Champagne all show very good performances, we see a slight advantage of LCMV (mean PR = 0.99) in comparison to Champagne (mean PR = 0.97, $p_{\text{Champagne}, \text{LCMV}} = 0.0013$). We do not observe a significant difference between DICS and LCMV ($p_{\text{DICS}, \text{LCMV}} = 0.2805$).

In terms of directionality determination (Figure 6b), the picture is different: while LCMV (mean PR = 0.98) leads to accurate directionality estimates, DICS fails to detect the direction of the ground-truth interaction in a high number of experiments (mean PR = 0.28, $p_{\text{DICS}, \text{LCMV}} < 10^{-4}$). eLORETA also shows a reduced overall performance (mean PR = 0.69, $p_{\text{eLORETA}, \text{LCMV}} < 10^{-4}$). Champagne shows decent performance (mean PR = 0.99), which is, however, lower than that of LCMV ($p_{\text{Champagne}, \text{LCMV}} < 10^{-4}$).

The differences in computation times of the different inverse solutions are also remarkable. While LCMV (2 sec) and DICS (178 sec) are fast to compute, eLORETA (388 sec) and Champagne (3747 sec) take much longer to compute as a cross-validation scheme to set the regularization parameter is implemented for both. Setting the regularization parameter to a default value would drastically reduce computation time for eLORETA and Champagne, but would also decrease performance (results not shown).

Experiment 2B

To investigate further why eLORETA performs considerably less well than LCMV in our experiments, we generated ground-truth activity with an interaction between one seed voxel in the left frontal cortex and one target voxel in the left precentral cortex. We then again generated sensor data as described in Section 2.1 and applied pipeline FIXPC1 to calculate regional MIM scores. In Supplementary Figure S3, we show the resulting power maps, as well as seed MIM scores and target MIM scores for data projected with eLORETA and MIM, respectively. We see clearly the advantage of LCMV: while both power and MIM in the eLORETA condition are spread out to other regions, LCMV is able to localize the ground-truth power and connectivity very precisely.

Experiment 2C

Does LCMV only perform so well in our experiment because our experimental setup artificially favors it? In the following additional analysis, we investigated whether LCMV still has an advantage over eLORETA when multiple pairs of correlated sources are present. More specifically, we here simulated two pairs of interacting sources where the time courses of the second source pair were identical to those of the first source pair. Results are presented in Figure 7. Please note that in this case, also the cross-interactions between the seed and target regions were evaluated as ground-truth interactions. We see that, while eLORETA is not much affected by the correlated sources setup, LCMV has a decreased reconstruction performance according to both MIM and TRGC. However, LCMV still performs better than eLORETA even in this setup ($p_{\text{eLORETA}, \text{LCMV}} < 10^{-4}$).

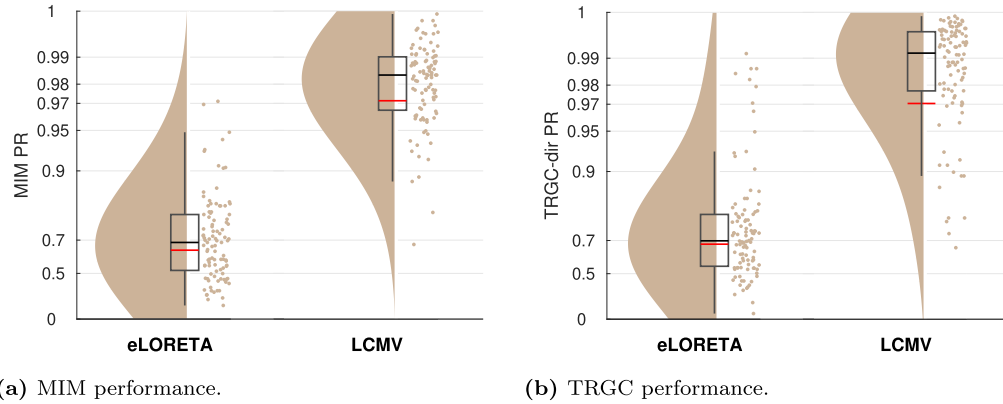


Fig. 7. Performance observed for two perfectly correlated source pairs. (a) Undirected FC reconstruction performance achieved using the multivariate interaction measure (MIM). (b) Directed FC reconstruction performance achieved using time-reversed Granger causality. Red and black lines indicate the mean and median, respectively. The boxcar marks the 2.5th and 97.5th percentile.

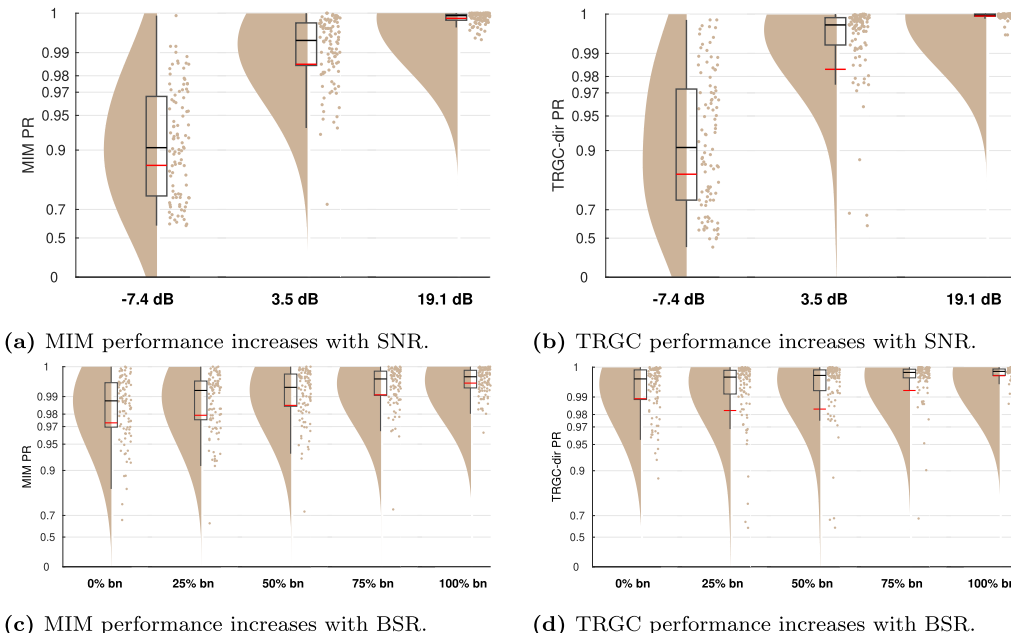


Fig. 8. FC estimation performance depends on the signal-to-noise ratio and brain noise-to-sensor noise ratio (Experiment 3). (a/c) Undirected FC reconstruction performance achieved using the multivariate interaction measure (MIM). (b/d) Directed FC reconstruction performance achieved using time-reversed Granger causality. Red and black lines indicate the mean and median percentile rank (PR), respectively. The boxcar marks the 2.5th and 97.5th percentile.

3.3. Experiment 3

In real-world EEG measurements, data are to a certain extent corrupted by noise, e.g. from irrelevant brain sources, or by noise sources from the outside. In Experiment 3, we investigated the effect of SNR and BSR on FC estimation performance. In Fig. 8a and 8 b, we show the performance of the FIXPC3 pipeline for SNRs of -7.4 dB, 3.5 dB and 19.1 dB. For both MIM (Fig. 8a) and TRGC (Fig. 8b), we observe decreased performances for decreased SNRs, as expected. For an SNR of 19.1 dB, nearly all experiments show a perfect detection of ground-truth interactions (mean PR > 0.99).

Is FC detection more impaired by pink brain noise or white sensor noise? In Experiment 3B, we tested the performance for BSR environments of 100% sensor noise, 25% brain noise, 50% brain noise, 75% brain noise, and 100% brain noise. In Fig. 8c and 8 d, we show the performances for different BSRs. We observe a slightly better performance for signals more strongly contaminated by correlated brain noise than white sensor noise (mean MIM PR 100% brain noise > 0.99) compared to the opposite case (mean MIM PR 0% brain noise = 0.97).

Note that in Experiments 1 to 3, for better comparison between the experimental conditions and to avoid variation due to random factors besides the experimental variation, we used the same generated data within an iteration in every experiment and only varied the tested condition.

3.4. Experiment 4

While we focused on a very simple scenario with only two interacting region pairs so far, real brain activity likely involves multiple interacting sources. To increase the complexity in our setup, we compared performances for different numbers of interacting region pairs in Experiment 4. As expected, Fig. 9 clearly shows that more simultaneous true interactions lead to decreased ability to reliably detect them. While the detection is nearly perfect for one interaction (mean MIM PR > 0.99; mean TRGC PR > 0.99), the performance is much reduced for 5 interactions (mean MIM PR = 0.91; mean TRGC PR = 0.93). This applies for both MIM and TRGC. Please note however, that despite using a normalized version of the PR (see Section 2.6), the PR metric is not

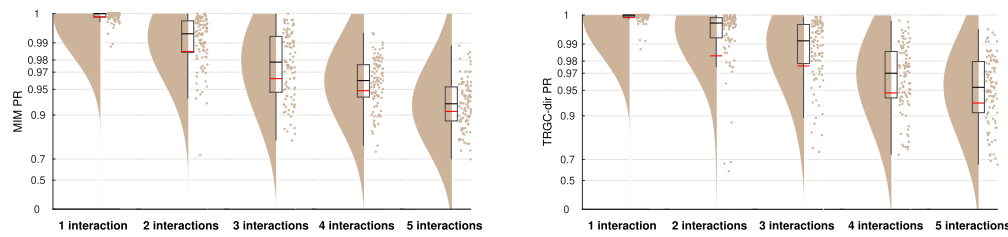


Fig. 9. FC reconstruction performance depends on the number of true interactions (Experiment 4). (a) Undirected FC reconstruction performance achieved using the multivariate interaction measure (MIM). (b) Directed FC reconstruction performance achieved using time-reversed Granger causality. Red and black lines indicate the mean and median percentile rank (PR), respectively. The boxcar marks the 2.5th and 97.5th percentile.

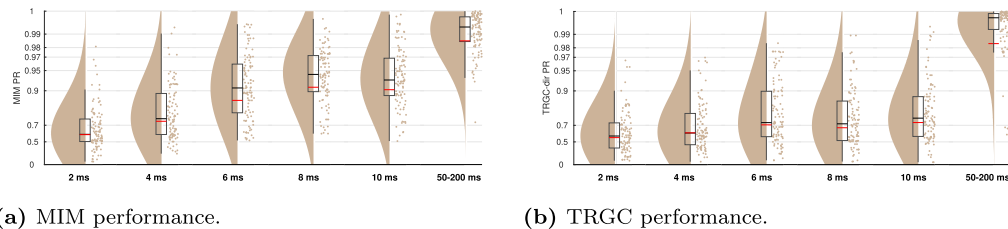


Fig. 10. Performance for very small interaction delays and the default delay (Experiment 5). (a) Undirected FC reconstruction performance achieved using the multivariate interaction measure (MIM). (b) Directed FC reconstruction performance achieved using time-reversed Granger causality. Red and black lines indicate the mean and median percentile rank (PR), respectively. The boxcar marks the 2.5th and 97.5th percentile.

perfectly comparable for different numbers of true interactions. That is, when calculating the PR on randomly drawn data, the PR distribution is close to uniform when only one interaction is assumed, but shows a normal distribution with increasing kurtosis for higher numbers of interactions. However, the mean of the distribution equals to 0.5 for all assumed interactions.

3.5. Experiment 5

While it is not entirely clear how large interaction delays in the brain can be, they likely range between 2 and 100 ms, depending not only on physical wiring, but also on cognitive factors (see Section 5). In Experiment 5, we evaluated to which degree the performance drops when regions interact with shorter time delays of 2, 4, 6, 8, and 10 ms. While the performance for the MIM metric is already quite impaired for a delay of 10 ms (mean PR = 0.90), performance drops drastically for 4 ms (mean PR = 0.73) and 2 ms (mean PR = 0.60) (Fig. 10a). Detecting the direction of the interaction with TRGC is already much more difficult at a true delay of 10 ms (mean PR = 0.73) and is further reduced for a delay of 2 ms (mean PR = 0.56; Fig. 10b).

3.6. Experiment 6

In our previous experiments, the FIXPC pipelines with two to four PCs showed the best performance. But the ‘optimal’ number of PCs likely

depends on the number of (interacting and non-interacting) signals in the brain as well as their relative strengths. To verify that the optimal number of PCs depends on the number of true sources, we increased the number of active voxels per region to two in Experiment 6. We then simulated two bivariate interactions between two different source pairs originating from the same regions. We show the results for pipelines FIXPC1 to FIXPC6 in Fig. 11. Interestingly, we here see that pipelines FIXPC3 (mean MIM PR = 0.99; mean TRGC PR = 0.99) and FIXPC4 (mean MIM PR = 0.99; mean TRGC PR = 0.99) perform clearly better than FIXPC1 (mean MIM PR = 0.89; mean TRGC PR = 0.93) or FIXPC6 (mean MIM PR = 0.98; mean TRGC PR = 0.98). Based on these results, we confirm that the choice of the optimal number of fixed PCs increases with the number of independently active processes within one region (see Section 5 for further discussion).

4. Exploratory analysis of functional connectivity in left vs. right motor imagery

To illustrate how the recommended analysis pipeline can be used to analyse real EEG data, we show an exploratory analysis of power and FC in left and right motor imagery. In the Berlin arm of the so-called VitalBCI study (Blankertz et al., 2010; Sannelli et al., 2019), 39 subjects conducted an experiment in which they imagined a movement with either the left or the right hand (Motor Imagery Calibration set; MI-Cb 1–3). Each trial consisted of a visual stimulus showing a fixation cross

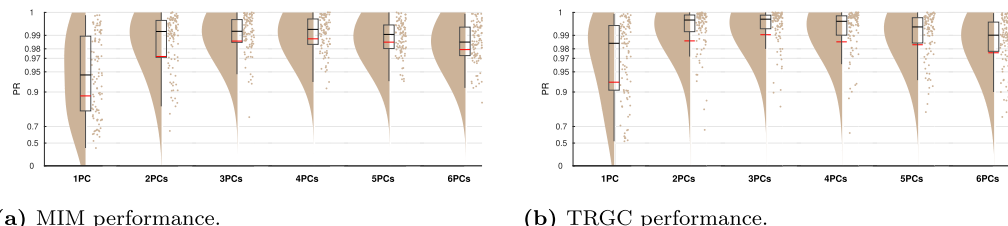


Fig. 11. Performance when two active sources per region are simulated (Experiment 6). (a) Undirected FC reconstruction performance achieved using the multivariate interaction measure (MIM). (b) Directed FC reconstruction performance achieved using time-reversed Granger causality. Red and black lines indicate the mean and median, respectively. The boxcar marks the 2.5th and 97.5th percentile.

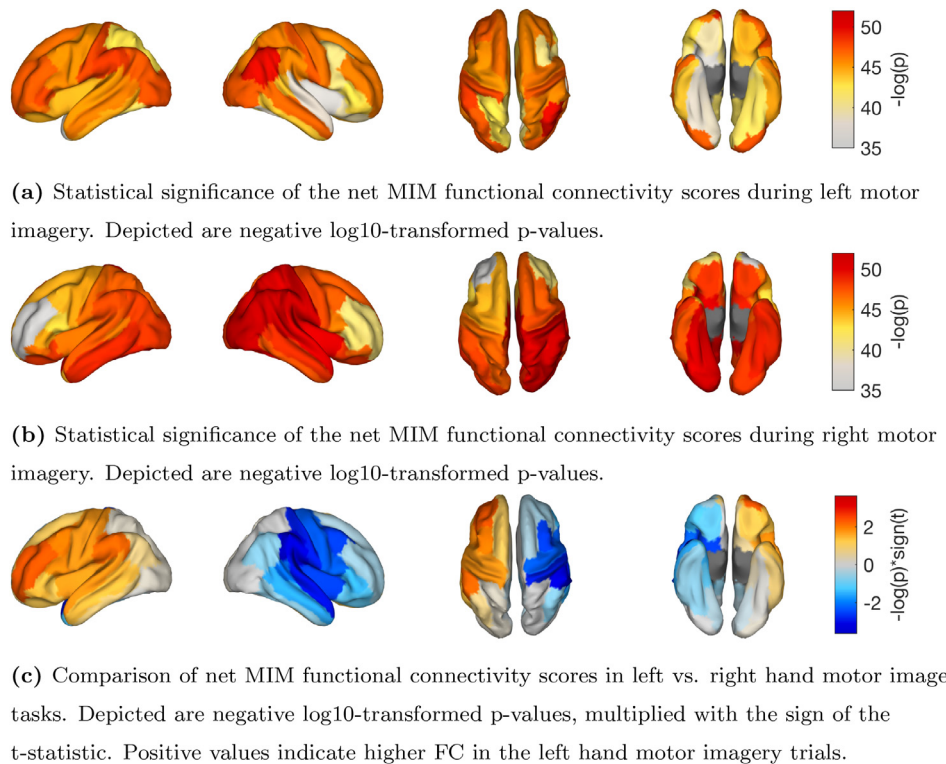


Fig. 12. Results of the exploratory analysis of functional connectivity in left and right hand motor imagery tasks.

imposed with an arrow indicating the task for the trial (i.e., left or right motor imagery). After 4 sec, the stimulus disappeared, and the screen stayed black for 2 sec. Every subject conducted 75 left and 75 right motor imagery trials. During the experiment, EEG data were recorded with a 119-channel whole-head EEG system with a sampling rate of 1000 Hz. For this study, we used a 90-channel whole head standard subset of them. For our analysis, we selected only the 26 subjects for which previous studies have reported that the left vs. right motor imagery conditions could be well separated using statistical and machine learning techniques ('Category I' in Sannelli et al., 2019). Further experimental details are provided in Blankertz et al. (2010); Sannelli et al. (2019).

We filtered the data (1 Hz high-pass filter, 48–52 Hz notch filter, and 45 Hz low-pass filter, all zero-phase forward and reverse second-order digital high-pass Butterworth filters), and then sub-sampled them to 100 Hz. We then rejected artifactual channels based on visual inspection of the power spectrum and the topographical distribution of alpha power (between zero and five per participant, mean 1.19 channels) and interpolated them (spherical scalp spline interpolation). A leadfield was computed using the template head model Colin27_5003_Standard-10-5-Cap339 that is already part of the EEGLAB toolbox. We then epoched the data from 1 to 3 sec post-stimulus presentation start and separated left from right motor imagery trials.

We used the `pop_roi_activity` function of the newly developed ROIconnect plugin for EEGLAB to calculate an LCMV source projection filter, apply it to the sensor data, and calculate region-wise power (see Appendix A for a more detailed description). We then normalized the power with respect to the total power between 3 and 7 Hz as well as 15 and 40 Hz, and averaged it across frequencies between 8 and 13 Hz. The statistical significance of the differences between right- and left-hand motor imagery power was assessed with a paired t-test in every region. In Supplementary Figure S4, we show the negative log₁₀-transformed p-values, multiplied with the sign of the t-statistic. As expected, the results show a clear lateralization for the activation of the motor areas.

To estimate inter-regional FC, we used the `pop_roi_connect` function to calculate MIM based on the three strongest PCs of every region. Again, MIM was averaged across frequencies between 8 and

13 Hz. To reduce the region-by-region MIM matrix to a vector of net MIM scores, we summed up all MIM estimates across one region dimension.

Analogous to our statistical evaluation of simulated data, described in Experiment 1C, we assessed the statistical significance of the net FC of each region against the null hypothesis of zero net interaction separately for each of the two motor imagery conditions. Specifically, we first calculated the true MIM score between all region pairs in all subjects. Then, we generated a null distribution of 1000 shuffled MIM scores for every region combination in every subject. Subsequently, the true and shuffled net MIM scores were calculated by averaging across one of the region dimensions. To obtain p-values, we compared the true MIM of every region and subject to the respective null distribution. To aggregate the p-values across subjects, we applied Stouffer's method (see, e.g., Dowding and Haufe, 2018). Finally, FDR-correction (α -level = 0.05) was used to correct for multiple comparisons. We show the negative log₁₀-transformed p-values in Figs. 12a and 12b.

Additionally, we assessed the statistical difference between the net MIM scores of the left- vs. right-hand motor imagery condition by again using a paired t-test for every region. In Fig. 12c, we show the negative log₁₀-transformed p-values, multiplied with the sign of the t-statistic. Again, as expected, the results show a lateralization for the undirected net FC of the motor areas.

Matlab code of the analyses presented in this section is provided under⁴.

5. Discussion

Estimating functional connectivity between brain regions from reconstructed EEG sources is a promising research area that has generated a number of important results (e.g. Babiloni et al., 2018; Hipp et al., 2011; Schoffelen et al., 2017). However, respective analysis pipelines consist of a number of subsequent steps for which multiple modeling

⁴ <https://github.com/fpellegrini/MotorImag>

choices exist and can typically be justified. In order to identify accurate and reliable analysis pipelines, simulation studies with ground-truth data can be highly informative. However, most existing simulation studies do not evaluate complete pipelines but focus on single steps. In particular, various published studies assume the locations of the interacting sources to be known a-priori, while, in practice, they have to be estimated as well. To this end, it has become widespread to aggregate voxel-level source activity within regions of an atlas before conducting FC analyses across regions. Multiple ways to conduct this dimensionality reduction step have been proposed, which have not yet been systematically compared using simulations. The main focus of our study was thus to identify those EEG processing pipelines from a set of common approaches that can detect ground-truth inter-regional FC most accurately. For the scenario modelled in this study, we observe that a pipeline consisting of an LCMV source projection, PCA dimensionality reduction, the selection of a fixed number of principal components for each ROI, and a robust FC metric like MIM or TRGC results in the most reliable detection of ground-truth FC (see Table 1). Consistent with results reported in Anzolin et al. (2019), LCMV consistently yielded higher FC reconstruction performance than eLORETA. Thus, we here answer the question that Mahjoory et al. (2017) left open, namely which source reconstruction technique is most suitable for EEG FC estimation. Our results are also in line with a larger body of studies that highlighted the advantages of robust FC metrics compared to non-robust ones (e.g. Haufe et al., 2013; Nolte et al., 2004; Schoffelen and Gross, 2019; Vinck et al., 2015; Winkler et al., 2016).

Inverse solutions

For some inverse solutions, the choice of the regularization parameter has been shown to influence the accuracy of source reconstruction (Hashemi et al., 2021; Hincapié et al., 2016). While the parameter is of little importance for methods like LCMV and DICS, which are fitted separately to each source and thus solve low-dimensional optimization problems, it should be carefully chosen for full inverse solutions like Champagne and eLORETA, which estimate the activity at each source voxel within a single model. To avoid a performance drop due to unsuitable regularization parameter choice in eLORETA and Champagne, we used the spatial cross-validation method described in (Habermehl et al., 2014; Hashemi et al., 2021). This method automatically sets the parameter based on the data at hand and has been shown to improve the source reconstruction (Hashemi et al., 2021).

As hypothesized, DICS resulted in poor directionality determination performance, while LCMV and TRGC performed well. This can be explained by the difference between LCMV and DICS: while LCMV estimates the inverse solution in the time domain, DICS estimates the source projection for every frequency separately (Gross et al., 2001). This can lead to inconsistencies across frequencies. Since directionality estimation requires the aggregation of phase information across multiple frequencies, such inconsistencies may lead to failure of detecting true interactions and their directionalities. Therefore, we recommend to avoid using DICS source reconstruction when analysing directed FC. For undirected FC measures, this seems to be less of a problem. Still, in our simulation, LCMV consistently performed (even if only slightly) better than DICS. This can be explained by the lower effective number of data samples that are available to DICS at each individual frequency compared to LCMV, which uses data from the entire frequency spectrum. However, there may be cases when using DICS could result in more accurate localization. For example, this could be the case when the noise has a dominant frequency that is different from the signal.

Robust functional connectivity metrics

In this study, we observed a strong benefit of using robust FC metrics over non-robust metrics in detecting genuine neuronal interactions. Overall, the performance of coherence is highly impaired by the volume

conduction effect (see Figure 3, c.f. Nolte et al., 2004). The TRGC metric performed well for the investigation of the interaction direction, but also satisfactorily well for the interaction detection. However, the computation time for calculating TRGC exceeds that of MIM by far. Thus, we recommend using MIM to detect undirected FC in case the direction of the effect is not of relevance. If TRGC is calculated for estimating the direction of interactions, the absolute value of TRGC can be used to detect interactions as well.

Interestingly, GC without time reversal did not perform much worse than TRGC. This is in line with previous results (Winkler et al., 2016) demonstrating that the calculation of net GC values already provides a certain robustification against volume conduction artifacts. Concretely, it has been shown that net GC is more robust to mixed noise than the standard GC; however not as robust as TRGC (Winkler et al., 2016). We generally recommend using robust FC connectivity metrics like iCOH, MIM/MIC, or TRGC.

Aggregation within regions

When comparing different processing pipelines, we found that employing an SVD/PCA and selecting a fixed number of components for further processing performs better than selecting a variable number of components in every ROI. When further investigating this effect, we found that, for MIM and MIC, the final connectivity score of the VARPC pipelines was positively correlated with the number of voxels of the two concerning ROIs (90%: MIM: $r = 0.50$, MIC: $r = 0.32$; 99%: MIM: $r = 0.70$, MIC: $r = 0.41$). This indicates that the flexible number of PCs leads to a bias in MIM and MIC depending on the size of the two involved ROIs. This could be expected, as the degrees of freedom for fitting MIM and MIC scale linearly with the number of voxels within a pair of regions. These in- or explicit model parameters can be tuned to maximize the FC of the projected data, which may lead to overfitting. For finite data, this leads to a systematic overestimation of FC, to the degree of which it correlates with the number of voxels. Although representing a multivariate technique as well, similar behavior was not observed for TRGC. Here it is likely that a potential bias of the signal dimensionalities would cancel out when taking differences between the two interaction directions as well as between original and time-reversed data.

An interesting and so far unsolved question is how many fixed components should be chosen for further processing. In Experiment 6, we observed a clear performance peak around three to four components (Fig. 11). In the default version with only one active source per ROI, we saw a similar pattern, but not as pronounced as in Experiment 6. This points towards a data-dependent optimal number of components. Future work should investigate how this parameter can be optimized based on the data at hand.

Short time delays

In Experiment 5, we investigated to what extent the performance drops when the true interaction occurs with a very small time delay of 2 to 10 msec, which might be a realistic range for a number of neural interaction phenomena in the brain. Precise data on the typical order of the times within which macroscopic neural ensembles exchange information are, however, hard to obtain, as these transmission times depend not only on the physical wiring but also on cognitive factors that are not straightforward to model. Previous work has shown that delays can range from 2 to 100 msec, depending on the distance and number of synapses between two nodes (e.g. Fries, 2005; Miocinovic et al., 2018; Oswal et al., 2016; Shouno et al., 2017). For example, Oswal et al. (2016) studied interaction delays between the subthalamic nucleus and the motor cortex and found interaction delays of 20 to 46 msec. The satisfactory performance observed in our study for undirected FC at delays of 8 and 10 msec may therefore be of particular importance for clinical scientists that aim at investigating such long-range

interactions. Note that the range of delays that can be detected with robust connectivity metrics strongly depends on the frequency band in which the interaction takes place. If the delay is very short compared to the base frequency of the interaction, then the phase difference it induces is close to either 0 or $\pm\pi$, making it less and less distinguishable from a pure volume conduction effect as it approaches these limits. In addition, the directionality of an interaction can only be resolved by analyzing multiple frequencies. Here, wider interaction bands lead to better reconstructions of the directionality of interactions with shorter delays, whereas higher frequency resolutions (that is, longer data segments) lead to better reconstructions of the directionality of interactions with longer delays. Here, we have demonstrated that alpha-band interactions with physiologically plausible transmission delays can be detected at 0.5 Hz frequency resolution, depending on the underlying SNR as well as additional modeling assumptions (see Limitations below).

Statistical assessment

The goal of this study was to evaluate data analysis pipelines to assess FC. However, we excluded the assessment of any subsequent statistical evaluation of FC, which is not straightforward to investigate in simulation studies. In a simulation setting, we are free to choose the two factors that influence the statistical power of a test—SNR and sample size. Determining realistic ranges for both in the context of EEG FC estimation is challenging but critical. Second, due to source leakage, we must expect (tiny) spill-over effects from interacting to non-interacting region pairs, an effect termed “ghost interactions” (Palva et al., 2018). As a result, these ghost interactions will inevitably become statistically significant for any source pair at high enough SNRs and sample sizes—an effect that can also be seen in Fig. 5c. For these reasons, we here assessed the effect sizes of FC metrics instead of their statistical significance, and focused on evaluating the performance of different FC estimation pipelines relative to one another rather than on their absolute performance. However, future studies should go one step further by systematically assessing statistical maps derived from connectomes using our results as building blocks.

Limitations

While this study investigates a large range of processing pipelines, phase-to-phase FC metrics, and data parameters, it is far from being exhaustive. Other works have shown that many other parameters like channel density (Song et al., 2015), the location of interacting sources (Anzolin et al., 2019), data length (Astolfi et al., 2007; Liuzzi et al., 2017; Sommariva et al., 2019; Van Diessen et al., 2015), referencing (Chella et al., 2016; Huang et al., 2017; Van Diessen et al., 2015), and co-registration (Liuzzi et al., 2017) can influence FC detection. Besides, we here used the same head model for generating the sensor data and estimating the inverse solution. However, we expect worse performance when the head model has to be estimated, and previous work has shown that the quality of head model estimation also influences FC detection (Mahjoory et al., 2017). Likewise, there exist many other inverse solutions, like MNE, wMNE, LORETA, sLORETA, and MSP, just to name a few. Further, there also exist other types of dimensionality reduction techniques. For example, some works selected the source with the highest power within a region or the source that showed the highest correlation to the time series of other sources in the ROI to be representative for all time series of the ROI (Ghumare et al., 2018; Hillebrand et al., 2012). Others have presented a procedure of optimizing a weighting scheme before averaging all time series within a ROI (Palva et al., 2010; 2011).

We also did not investigate the effect of the number of epochs and the epoch length in this study. It has been shown that the number of epochs can introduce a bias for certain connectivity metrics (Vinck et al., 2010). This is the case for connectivity metrics that yield positive values only, like (absolute) coherence, the absolute value of the imaginary part of coherency, MIM, or MIC. For these metrics, for a fixed epoch length,

a lower number of epochs will systematically lead to higher values of estimated connectivity, even under the null hypothesis of no interaction. This is due to the higher variance of the estimates for lower samples sizes, which turns into a positive bias when the absolute value is taken. Further, Fraschini et al. (2016) argued that also the epoch length may have an influence on FC estimation, where shorter epochs were found to introduce a positive bias on FC when the number of epochs was held constant. As a result, we recommend to use fixed numbers and length of epochs throughout a single experiment. This is of particular importance when the goal is to compare different groups or experimental conditions.

As the set of coupling mechanism and corresponding FC metrics that have been proposed is huge, we deliberately constrained our analysis here to phase-phase coupling using a selection of metrics that have previously been shown to be robust to mixing artifacts (Ewald et al., 2012; Haufe et al., 2013; Nolte et al., 2004). In contrast, non-robust metrics have been shown to be prone to the spurious discovery of interactions (Bastos and Schoffelen, 2016; Brunner et al., 2016; Haufe et al., 2013; Nolte et al., 2004; Van de Steen et al., 2019). This was confirmed here again for absolute coherence and GC. For a detailed overview of the taxonomy of FC metrics we refer to the works of Bastos and Schoffelen (2016); Marzetti et al. (2019); Schoffelen and Gross (2019). Our results are obtained for intra-frequency phase–phase coupling, and make no claims about non-linear interaction metrics quantifying phase-amplitude or amplitude–amplitude coupling within or across frequencies (Colclough et al., 2015; De Pasquale et al., 2010; Hipp et al., 2012). Nevertheless, we expect that robust-to-volume conduction measures for these FC types would be required to obtain optimal performance.

A further limitation of simulation studies in general is that assumptions need to be made that are hard, if not impossible, to confirm. Here, our goal was to generate pseudo-EEG data comprising realistic effects of volume conduction using a physical model of a human head. In terms of the generated time series, we focused on alpha-band oscillations as carriers of the modeled interactions. By adding pink brain noise, uniformly distributed across the entire brain, as well as white sensor noise, we obtained simulated sensor-space EEG data that resemble real data in crucial aspects such as spectral peaks and the general 1/f shape of the power spectrum. On the other hand, numerous additional assumptions were made regarding the linear dynamics of the interacting sources, the conception of the interaction as a pure and fixed time delay, the focus on an interaction in the alpha band, the number of interactions, the signal-to-noise ratio, and the stationarity of all signal and noise sources. Several of these experimental variables were systematically varied to provide a comprehensive picture of the performance of each pipeline in a wide range of scenarios. The ranking of the pipelines’ performances was robust in all tested scenarios. However, a remaining question is how realistic the individual studied parameter choices are. Our simulated environment resembles a setting of task-related (ongoing) activity with few dominant active and interacting sources, as opposed to a resting-state setting with numerous equally active and interacting sources. Hincapié et al. (2017) showed that connectivity estimation pipelines including beamformers perform well for point-like sources, whereas for extended cortical patches, MNE source estimation was found to be more accurate. In this study, we simulated point-like sources, which could lead to an overestimation of beamformer performance. Considering that FC analyses are predominantly performed on ongoing (including resting-state) activity, the assumption of having only a few interacting source pairs standing out against non-interacting background sources may be challenged. However, this assumption was made here for the practical purpose of enabling a comparison between approaches. Considering that FC analyses are predominantly performed on ongoing (e.g., resting-state) activity rather than averaged data, the assumptions of only few interacting source pairs standing out against non-interacting background sources with relatively high SNR can certainly be questioned. However, these assumptions were made here for the practical purpose of enabling a comparison between approaches rather than with the ambition of claiming real-world validity.

Future simulation studies should nevertheless strive to further increase the realism of the generated pseudo-EEG signals. In this regard, Anzolin et al. (2021) presented a toolbox that mimics typical EEG artifacts like eye blinks. We restricted ourselves here to using artificial time series designed to exhibit the specific properties assessed by the studied FC metrics; that is, time-delayed linear dynamics. In contrast, biologically inspired models such as the models implemented within the virtual brain toolbox (TVB; Sanz Leon et al., 2013) provide a richer portfolio of non-linear dynamics and thus are alternative ground-truth models specifically when the goal is to validate non-linear FC metrics. The COALIA model (Bensaid et al., 2019), for example, has been used to mimick network activity in epilepsy for the purpose of validating FC estimates (Allouch et al., 2022). Further studies used the same model family to study the effect of parameters such as electrode density on FC estimates (Allouch et al., 2023; Tabbal et al., 2022). Similarly, Jirsa and Müller (2013) have used TVB to evaluate metrics of cross-frequency coupling. Overall, these studies provide complementary evidence that is largely aligned with our results, for example with respect to the superiority of robust connectivity metrics. The plausibility of several assumptions made by neural mass models has also recently been questioned (Pathak et al., 2022). Nevertheless, such models hold great promise as validation tools in the future.

Note in this respect that it was not our intention to propose a realistic model of EEG data or even the whole brain but simply to generate data that would allow us to test how well ROI-level FC can be reconstructed in the presence of volume conduction/source leakage. The types of FC we are interested here (directed and undirected linear FC) have been widely studied and popular metrics to infer these types of FC are known to be heavily affected by volume conduction (Haufe et al., 2013; Nolte et al., 2004). Hence, it was our intention to identify metrics and pipelines that have a high chance of reconstructing FC on the ROI level when signals are mapped to the EEG and back by realistic forward and inverse models. We deliberately do not address the question whether networks estimated using FC metrics provide a correct depiction of actual brain networks.

As a further limitation, our simulations are to some extent restricted to EEG data. However, it can be expected that, qualitatively, the results of this paper could be transferred to MEG data. MEG analyses also suffer from the source leakage problem (Colclough et al., 2016; Pizzella et al., 2014) and benefit from disentangling signal sources with source reconstruction (Marzetti et al., 2019; Schoffelen and Gross, 2019). Moreover, the same FC metrics are typically used in EEG and MEG analyses (Schoffelen and Gross, 2009; 2019). Nevertheless, differences exist, which would be worth studying. In contrast to EEG, which records secondary neuronal return currents, MEG records the magnetic field that is induced by electrical activity and arises in a circular field around an electric current (Hämäläinen et al., 1993). Therefore, MEG cannot record radial neuronal currents (Huang et al., 2007). This must be taken into account when estimating the inverse solution from the leadfield, i.e. it is advised to reduce the rank of the forward model from three to two by applying an SVD at each source location (Westner et al., 2021).

We here provide a simulation framework that is openly accessible by the community. Individual pipeline steps, but also simulated data can easily be replaced by other variants, following a plug-and-play principle. A such, we encourage readers to test aspects of the pipelines, other data, and other FC metrics not considered here.

6. Conclusion

This work compared an extensive set of data analysis pipelines for the purpose of extracting directed and undirected functional connectivity between predefined brain regions from simulated EEG data. While several individual steps of such pipelines have been benchmarked in previous studies, we focused specifically on the problem of aggregating source-reconstructed data into region-level time courses and, ultimately, region-to-region connectivity matrices. Thereby, we close a gap in the current literature evaluating FC estimation approaches. We show that

using non-robust FC metrics greatly reduces the ability to correctly detect ground-truth FC. Further, in our simulated pseudo-EEG data, the use of the eLORETA inverse solution also leads to worse FC detection performance than beamformers. Moreover, the use of inverse solutions that are frequency-specific, such as DICS, may hamper the correct identification of the directionality of interactions. Finally, unequal dimensionalities of signals at different ROIs may bias certain connectivity measures, such as MIC and MIM, degrading their ability to identify true interactions from a noise floor. Thus, dimensionality reduction techniques should be applied such that the number of retained signal components is the same for all regions. We expect that avoiding these pitfalls may enhance the correct interpretation and comparability of results of future connectivity investigations. FC pipelines that show promising results with our simulated pseudo-EEG data consist of beamformer or champagne source reconstruction, aggregation of time series within ROIs using a fixed number of strongest PCs, and using a robust FC metric like MIM or TRGC. To which scenarios these results can be generalized remains to be shown in further studies. In practice, low SNR, high numbers of interactions, and small interaction delays may, however, reduce the performance even of the best performing pipelines.

Data and code availability

The code for the simulation can be found here: <https://github.com/fpellegrini/FCsim>. The code for the ROIconnect plugin can be found here: <https://github.com/sccn/roiconnect>. And the code for the minimal real data example here: <https://github.com/fpellegrini/MotorImag>. Data of the real data example are available upon request.

Declaration of Competing Interest

The authors declare that they have no known competing financial interests or personal relationships that could have appeared to influence the work reported in this paper.

Credit authorship contribution statement

Franziska Pellegrini: Methodology, Software, Investigation, Writing – original draft, Visualization. **Arnaud Delorme:** Validation, Software, Writing – review & editing. **Vadim Nikulin:** Methodology, Writing – review & editing, Supervision. **Stefan Haufe:** Conceptualization, Methodology, Validation, Investigation, Resources, Writing – review & editing, Supervision, Project administration, Funding acquisition.

Data availability

Data will be made available on request.

Acknowledgements

This project was supported by the European Research Council (ERC) under the European Union's Horizon 2020 research and innovation programme (Grant agreement No. 758985) and through Deutsche Forschungsgemeinschaft (DFG, German Research Foundation) Project-ID 424778381 TRR 295. We thank Tien Dung Nguyen for contributing to the development of the ROIconnect plugin. The computations for this work were partly run on the open Neuroscience Gateway cluster (Sivagnanam et al., 2013).

Appendix A. ROIconnect toolbox

ROIconnect is a freely available open-source plugin to the popular MATLAB-based open-source toolbox EEGLAB for EEG data analysis. It adds the functionality of calculating region-wise power and inter-regional FC on the source level. Moreover, it provides functions to visualize power and FC. All functions can be accessed by the EEGLAB GUI

or the command line. ROIconnect uses core EEGLAB functions for importing and preprocessing EEG data, and calculating the leadfield and source model: we refer users to other EEGLAB functions to preprocess data before applying ROIconnect functions. The ROIconnect plugin can be downloaded through github⁵ or installed via the EEGLAB GUI extension manager.

Key features

The features of ROIconnect are implemented in three main functions: `pop_roi_activity`, `pop_roi_connect`, and `pop_roi_connectplot`.

`pop_roi_activity` takes an EEG struct containing EEG sensor activity, a pointer to a headmodel and a source model, the atlas name, and the number of PCs for dimensionality reduction as input. It then calculates a source projection filter (default: LCMV) and applies it to the sensor data. Power is then calculated with the Welch method for every frequency on the voxel time series and then summed across voxels within regions. The result is saved in `EEG.roi.source_roi_power`. To estimate region-wise FC, the `pop_roi_activity` function reduces the dimensionality of the time series of every region by employing a PCA and selecting the strongest PCs (as defined in the input) for every region. The resulting time series are then stored in `EEG.roi.source_roi_data`.

`pop_roi_connect` calculates FC between regions. It builds on the output of `pop_roi_activity`. That is, it takes the EEG struct as input, as well as the name of the FC metrics that should be calculated. The function calculates all FC metrics in a frequency-resolved way. That is, the output contains FC scores for every region-region-frequency combination. To avoid biases due to different data lengths, `pop_roi_connect` estimates FC for time windows ('snippets') of 60 sec length (default), which subsequently can be averaged (default) or used as input for later statistical analyses. The snippet length can be flexibly adjusted by the user. The output of this function is stored under the name of the respective FC metric under `EEG.roi`.

The `pop_roi_connectplot` function enables visualizing power and FC in the following modes:

- Power as region-wise bar plot.
- Power as source-level cortical surface topography.
- FC as region-by-region matrix.
- Net FC, that is, the mean FC from all regions to all regions, as cortical surface topography.
- Seed FC, that is, the FC of a seed region to all other regions, as cortical surface topography.

For plotting, a specific frequency or frequency band can be chosen by the user. For matrix representations, it is also possible to just plot one of the hemispheres or only regions belonging to specific brain lobes.

Supplementary material

Supplementary material associated with this article can be found, in the online version, at [10.1016/j.neuroimage.2023.120218](https://doi.org/10.1016/j.neuroimage.2023.120218)

References

- Allen, M., Poggiali, D., Whitaker, K., Marshall, T.R., Kievit, R.A., 2019. Raincloud plots: a multi-platform tool for robust data visualization. *Wellcome Open Res.* 4.
- Allouch, S., Kabbara, A., Duprez, J., Khalil, M., Modolo, J., Hassan, M., 2023. Effect of channel density, inverse solutions and connectivity measures on EEG resting-state networks reconstruction: a simulation study. *Neuroimage* 271, 120006.
- Allouch, S., Yochum, M., Kabbara, A., Duprez, J., Khalil, M., Wendling, F., Hassan, M., Modolo, J., 2022. Mean-field modeling of brain-scale dynamics for the evaluation of EEG source-space networks. *Brain Topogr.* 35 (1), 54–65.
- Anzolin, A., Presti, P., Van De Steen, F., Astolfi, L., Haufe, S., Marinazzo, D., 2019. Quantifying the effect of demixing approaches on directed connectivity estimated between reconstructed EEG sources. *Brain Topogr.* 32 (4), 655–674.
- Anzolin, A., Toppi, J., Pettit, M., Cincotti, F., Astolfi, L., 2021. SEED-G: Simulated EEG data generator for testing connectivity algorithms. *Sensors* 21 (11), 3632.
- Aoki, M., Havenner, A., 1991. State space modeling of multiple time series. *Econom. Rev.* 10 (1), 1–59.
- Astolfi, L., Cincotti, F., Mattia, D., Marziani, M.G., Baccala, L.A., de Vico Fallani, F., Salinari, S., Ursino, M., Zavaglia, M., Ding, L., et al., 2007. Comparison of different cortical connectivity estimators for high-resolution EEG recordings. *Hum. Brain Mapp.* 28 (2), 143–157.
- Babiloni, C., Del Percio, C., Lizio, R., Noce, G., Lopez, S., Soricelli, A., Ferri, R., Nobili, F., Arnaldi, D., Famà, F., et al., 2018. Abnormalities of resting-state functional cortical connectivity in patients with dementia due to Alzheimer's and Lewy body diseases: an EEG study. *Neurobiol. Aging* 65, 18–40.
- Barnett, L., Barrett, A.B., Seth, A.K., 2018. Solved problems for granger causality in neuroscience: a response to Stokes and Purdon. *Neuroimage* 178, 744–748.
- Barnett, L., Seth, A.K., 2014. The MVGC multivariate granger causality toolbox: a new approach to granger-causal inference. *J. Neurosci. Methods* 223, 50–68.
- Barnett, L., Seth, A.K., 2015. Granger causality for state-space models. *Phys. Rev. E* 91 (4), 040101.
- Barrett, A.B., Barnett, L., Seth, A.K., 2010. Multivariate granger causality and generalized variance. *Phys. Rev. E* 81 (4), 041907.
- Basti, A., Nili, H., Hauk, O., Marzetti, L., Henson, R.N., 2020. Multi-dimensional connectivity: a conceptual and mathematical review. *Neuroimage* 117179.
- Bastos, A.M., Schafele, J.-M., 2016. A tutorial review of functional connectivity analysis methods and their interpretation pitfalls. *Front. Syst. Neurosci.* 9, 175.
- Bensaid, S., Modolo, J., Merlet, I., Wendling, F., Benquet, P., 2019. Coalia: a computational model of human EEG for consciousness research. *Front. Syst. Neurosci.* 13, 59.
- Blankertz, B., Sannelli, C., Halder, S., Hammer, E.M., Kübler, A., Müller, K.-R., Curio, G., Dickhaus, T., 2010. Neurophysiological predictor of SMR-based BCI performance. *Neuroimage* 51 (4), 1303–1309.
- Bradley, A., Yao, J., Dewald, J., Richter, C.-P., 2016. Evaluation of electroencephalography source localization algorithms with multiple cortical sources. *PLoS ONE* 11 (1), e0147266.
- Bressler, S.L., Seth, A.K., 2011. Wiener-granger causality: a well established methodology. *Neuroimage* 58 (2), 323–329.
- Brunner, C., Billinger, M., Seeger, M., Mullen, T.R., Makeig, S., 2016. Volume conduction influences scalp-based connectivity estimates. *Front. Comput. Neurosci.* 10, 121.
- Castaña Candamil, S., Höhne, J., Martínez-Vargas, J.-D., An, X.-W., Castellanos-Domínguez, G., Haufe, S., 2015. Solving the EEG inverse problem based on space-time-frequency structured sparsity constraints. *Neuroimage* 118, 598–612.
- Chella, F., Pizzella, V., Zappasodi, F., Marzetti, L., 2016. Impact of the reference choice on scalp EEG connectivity estimation. *J. Neural Eng.* 13 (3), 036016.
- Colclough, G.L., Brookes, M.J., Smith, S.M., Woolrich, M.W., 2015. A symmetric multivariate leakage correction for MEG connectomes. *Neuroimage* 117, 439–448.
- Colclough, G.L., Woolrich, M.W., Tewarie, P.K., Brookes, M.J., Quinn, A.J., Smith, S.M., 2016. How reliable are MEG resting-state connectivity metrics? *Neuroimage* 138, 284–293.
- D'Andrea, A., Chella, F., Marshall, T.R., Pizzella, V., Romani, G.L., Jensen, O., Marzetti, L., 2019. Alpha and alpha-beta phase synchronization mediate the recruitment of the visuospatial attention network through the superior longitudinal fasciculus. *Neuroimage* 188, 722–732.
- De Pasquale, F., Della Penna, S., Snyder, A.Z., Lewis, C., Mantini, D., Marzetti, L., Belardinelli, P., Ciancetta, L., Pizzella, V., Romani, G.L., et al., 2010. Temporal dynamics of spontaneous MEG activity in brain networks. *Proc. Natl. Acad. Sci.* 107 (13), 6040–6045.
- Desikan, R.S., Ségonne, F., Fischl, B., Quinn, B.T., Dickerson, B.C., Blacker, D., Buckner, R.L., Dale, A.M., Maguire, R.P., Hyman, B.T., et al., 2006. An automated labeling system for subdividing the human cerebral cortex on MRI scans into gyral based regions of interest. *Neuroimage* 31 (3), 968–980.
- Dowding, I., Haufe, S., 2018. Powerful statistical inference for nested data using sufficient summary statistics. *Front. Hum. Neurosci.* 12, 103.
- Ewald, A., Marzetti, L., Zappasodi, F., Meinecke, F.C., Nolte, G., 2012. Estimating true brain connectivity from EEG/MEG data invariant to linear and static transformations in sensor space. *Neuroimage* 60 (1), 476–488.
- Faes, L., Stramaglia, S., Marinazzo, D., 2017. On the interpretability and computational reliability of frequency-domain granger causality. *F1000Res* 6.
- Fraschini, M., Demuru, M., Crobe, A., Marrosu, F., Stam, C.J., Hillebrand, A., 2016. The effect of epoch length on estimated EEG functional connectivity and brain network organisation. *J. Neural Eng.* 13 (3), 036015.
- Fries, P., 2005. A mechanism for cognitive dynamics: neuronal communication through neuronal coherence. *Trends Cogn. Sci. (Regul. Ed.)* 9 (10), 474–480.
- Fries, P., 2015. Rhythms for cognition: communication through coherence. *Neuron* 88 (1), 220–235.
- Friston, K.J., 2011. Functional and effective connectivity: a review. *Brain Connect.* 1 (1), 13–36.
- Friston, K.J., Rotshtein, P., Geng, J.J., Sterzer, P., Henson, R.N., 2006. A critique of functional localisers. *Neuroimage* 30 (4), 1077–1087.
- Geweke, J., 1982. Measurement of linear dependence and feedback between multiple time series. *J. Am. Stat. Assoc.* 77 (378), 304–313.
- Ghumare, E.G., Schroten, M., Vandenberghe, R., Dupont, P., 2018. A time-varying connectivity analysis from distributed EEG sources: a simulation study. *Brain Topogr.* 31 (5), 721–737.
- Gómez-Herrero, G., Atienza, M., Egiazarian, K., Cantero, J.L., 2008. Measuring directional coupling between EEG sources. *Neuroimage* 43 (3), 497–508.
- Gramfort, A., Papadopoulou, T., Olivi, E., Clerc, M., 2010. OpenMEEG: open-source software for quasistatic bioelectromagnetics. *Biomed. Eng. Online* 9 (1), 1–20.

⁵ <https://github.com/sccn/roiconnec>

- Granger, C.W.J., 1969. Investigating causal relations by econometric models and cross-spectral methods. *Econometrica: J. Econom. Soc.* 424–438.
- Gross, J., Kujala, J., Hämäläinen, M., Timmermann, L., Schnitzler, A., Salmelin, R., 2001. Dynamic imaging of coherent sources: studying neural interactions in the human brain. *Proc. Natl. Acad. Sci.* 98 (2), 694–699.
- Grova, C., Daunizeau, J., Lina, J.-M., Bénar, C.G., Benali, H., Gotman, J., 2006. Evaluation of EEG localization methods using realistic simulations of interictal spikes. *Neuroimage* 29 (3), 734–753.
- Habermehl, C., Steinbrink, J.M., Müller, K.-R., Haufe, S., 2014. Optimizing the regularization for image reconstruction of cerebral diffuse optical tomography. *J. Biomed. Opt.* 19 (9), 096006.
- Halder, T., Talwar, S., Jaiswal, A.K., Banerjee, A., 2019. Quantitative evaluation in estimating sources underlying brain oscillations using current source density methods and beamformer approaches. *eNeuro* 6 (4).
- Hämäläinen, M., Hari, R., Ilmoniemi, R.J., Knuttila, J., Lounasmaa, O.V., 1993. Magnetoencephalography theory, instrumentation, and applications to noninvasive studies of the working human brain. *Rev. Mod. Phys.* 65 (2), 413.
- Hashemi, A., Cai, C., Kutyniok, G., Müller, K.-R., Nagarajan, S.S., Haufe, S., 2021. Unification of sparse bayesian learning algorithms for electromagnetic brain imaging with the majorization minimization framework. *bioRxiv*. 2020–08.
- Haufe, S., Ewald, A., 2019. A simulation framework for benchmarking EEG-based brain connectivity estimation methodologies. *Brain Topogr.* 32 (4), 625–642.
- Haufe, S., Nikulin, V.V., Müller, K.-R., Nolte, G., 2013. A critical assessment of connectivity measures for EEG data: a simulation study. *Neuroimage* 64, 120–133.
- Haufe, S., Nikulin, V.V., Nolte, G., 2012. Alleviating the influence of weak data asymmetries on granger-causal analyses. In: International Conference on Latent Variable Analysis and Signal Separation. Springer, pp. 25–33.
- Haufe, S., Nikulin, V.V., Ziehe, A., Müller, K.-R., Nolte, G., 2008. Combining sparsity and rotational invariance in EEG/MEG source reconstruction. *Neuroimage* 42 (2), 726–738.
- Haufe, S., Tomioka, R., Dickhaus, T., Sannelli, C., Blankertz, B., Nolte, G., Müller, K.-R., 2011. Large-scale EEG/MEG source localization with spatial flexibility. *Neuroimage* 54 (2), 851–859.
- Hillebrand, A., Barnes, G.R., Bosboom, J.L., Berendse, H.W., Stam, C.J., 2012. Frequency-dependent functional connectivity within resting-state networks: an atlas-based MEG beamformer solution. *Neuroimage* 59 (4), 3909–3921.
- Hincapié, A.-S., Kujala, J., Mattout, J., Dalgault, S., Delpuech, C., Mery, D., Cosmelli, D., Jerbi, K., 2016. MEG Connectivity and power detections with minimum norm estimates require different regularization parameters. *Comput. Intell. Neurosci.* 2016.
- Hincapié, A.-S., Kujala, J., Mattout, J., Pasquarella, A., Dalgault, S., Delpuech, C., Mery, D., Cosmelli, D., Jerbi, K., 2017. The impact of MEG source reconstruction method on source-space connectivity estimation: a comparison between minimum-norm solution and beamforming. *Neuroimage* 156, 29–42.
- Hipp, J.F., Engel, A.K., Siegel, M., 2011. Oscillatory synchronization in large-scale cortical networks predicts perception. *Neuron* 69 (2), 387–396.
- Hipp, J.F., Hawellek, D.J., Corbetta, M., Siegel, M., Engel, A.K., 2012. Large-scale cortical correlation structure of spontaneous oscillatory activity. *Nat. Neurosci.* 15 (6), 884–890.
- Huang, M.-X., Song, T., Hagler Jr, D.J., Podgorny, I., Jousmaki, V., Cui, L., Gao, K., Harrington, D.L., Dale, A.M., Lee, R.R., et al., 2007. A novel integrated MEG and EEG analysis method for dipolar sources. *Neuroimage* 37 (3), 731–748.
- Huang, Y., Zhang, J., Cui, Y., Yang, G., He, L., Liu, Q., Yin, G., 2017. How different EEG references influence sensor level functional connectivity graphs. *Front. Neurosci.* 11, 368.
- Idjadi, M.J., Zhang, J., Stephani, T., Nolte, G., Mueller, K.-R., Villringer, A., Nikulin, V., 2021. Harmoni: a method for eliminating spurious interactions due to the harmonic components in neuronal data. *bioRxiv*.
- Jaiswal, A., Nenonen, J., Stenroos, M., Gramfort, A., Dalal, S.S., Westner, B.U., Litvak, V., Mosher, J.C., Schöfelen, J.-M., Witton, C., et al., 2020. Comparison of beamformer implementations for MEG source localization. *Neuroimage* 216, 116797.
- Jirsa, V., Müller, V., 2013. Cross-frequency coupling in real and virtual brain networks. *Front. Comput. Neurosci.* 7, 78.
- Korhonen, O., Palva, S., Palva, J.M., 2014. Sparse weightings for collapsing inverse solutions to cortical parcellations optimize m/EEG source reconstruction accuracy. *J. Neurosci. Methods* 226, 147–160.
- Liuuzzi, L., Gascoyne, L.E., Tewarie, P.K., Barratt, E.L., Boto, E., Brookes, M.J., 2017. Optimising experimental design for MEG resting state functional connectivity measurement. *Neuroimage* 155, 565–576.
- Mahjoory, K., Nikulin, V.V., Botrel, L., Linkenkaer-Hansen, K., Fato, M.M., Haufe, S., 2017. Consistency of EEG source localization and connectivity estimates. *Neuroimage* 152, 590–601.
- Marzetti, L., Basti, A., Chella, F., D'Andrea, A., Syrjälä, J., Pizzella, V., 2019. Brain functional connectivity through phase coupling of neuronal oscillations: a perspective from magnetoencephalography. *Front. Neurosci.* 13, 964.
- Mazzotta, J.C., Toga, A.W., Evans, A., Fox, P., Lancaster, J., et al., 1995. A probabilistic atlas of the human brain: theory and rationale for its development. *Neuroimage* 2 (2), 89–101.
- Miocinovic, S., de Hemptinne, C., Chen, W., Isbaine, F., Willie, J.T., Ostrem, J.L., Starr, P.A., 2018. Cortical potentials evoked by subthalamic stimulation demonstrate a short latency hyperdirect pathway in humans. *J. Neurosci.* 38 (43), 9129–9141.
- Nolte, G., Bai, O., Wheaton, L., Mari, Z., Vorbach, S., Hallett, M., 2004. Identifying true brain interaction from EEG data using the imaginary part of coherency. *Clin. Neurophysiol.* 115 (10), 2292–2307.
- Nolte, G., Ziehe, A., Nikulin, V.V., Schlögl, A., Krämer, N., Brismar, T., Müller, K.-R., 2008. Robustly estimating the flow direction of information in complex physical systems. *Phys. Rev. Lett.* 100 (23), 234101.
- Nunez, P.L., Srinivasan, R., Westdorp, A.F., Wijesinghe, R.S., Tucker, D.M., Silberstein, R.B., Cadusch, P.J., 1997. EEG Coherency: i: statistics, reference electrode, volume conduction, laplacians, cortical imaging, and interpretation at multiple scales. *Electroencephalogr. Clin. Neurophysiol.* 103 (5), 499–515.
- Oswal, A., Beudel, M., Zrinzo, L., Limousin, P., Hariz, M., Foltyne, T., Litvak, V., Brown, P., 2016. Deep brain stimulation modulates synchrony within spatially and spectrally distinct resting state networks in parkinsons disease. *Brain* 139 (5), 1482–1496.
- Palva, J.M., Monto, S., Kulashekhar, S., Palva, S., 2010. Neuronal synchrony reveals working memory networks and predicts individual memory capacity. *Proceed. Natl. Acad. Sci.* 107 (16), 7580–7585.
- Palva, J.M., Wang, S.H., Palva, S., Zhigalov, A., Monto, S., Brookes, M.J., Schöfelen, J.-M., Jerbi, K., 2018. Ghost interactions in MEG/EEG source space: anote of caution on inter-area coupling measures. *Neuroimage* 173, 632–643.
- Palva, S., Kulashekhar, S., Hämäläinen, M., Palva, J.M., 2011. Localization of cortical phase and amplitude dynamics during visual working memory encoding and retention. *J. Neurosci.* 31 (13), 5013–5025.
- Pascual-Marqui, R.D., 2007. Discrete, 3d distributed, linear imaging methods of electric neuronal activity. part 1: exact, zero error localization. *arXiv preprint arXiv:0710.3341*.
- Pascual-Marqui, R.D., Lehmann, D., Koukkou, M., Kochi, K., Anderer, P., Saletu, B., Tanaka, H., Hirata, K., John, E.R., Prichet, L., Biscay-Lirio, R., Kinoshita, T., 2011. Assessing interactions in the brain with exact low-resolution electromagnetic tomography. *Philos. Trans. A Math. Phys. Eng. Sci.* 369, 3768–3784.
- Pathak, A., Roy, D., Banerjee, A., 2022. Whole-brain network models: from physics to bedside. *Front. Comput. Neurosci.* 16.
- Perinelli, A., Asseconti, S., Tagliabue, C.F., Mazza, V., 2022. Power shift and connectivity changes in healthy aging during resting-state EEG. *Neuroimage* 119247.
- Pizzella, V., Marzetti, L., Della Penna, S., de Pasquale, F., Zappasodi, F., Romani, G.L., 2014. Magnetoencephalography in the study of brain dynamics. *Funct. Neurol.* 29 (4), 241.
- Rubega, M., Carboni, M., Seeber, M., Pascucci, D., Tourbier, S., Toscano, G., Van Mierlo, P., Hagmann, P., Plomp, G., Vulliemoz, S., et al., 2019. Estimating EEG source dipole orientation based on singular-value decomposition for connectivity analysis. *Brain Topogr.* 32 (4), 704–719.
- Sannelli, C., Vidaurre, C., Müller, K.-R., Blankertz, B., 2019. A large scale screening study with a SMR-based BCI: categorization of BCI users and differences in their SMR activity. *PLoS ONE* 14 (1), e0207351.
- Sanz Leon, P., Knock, S.A., Woodman, M.M., Domide, L., Mersmann, J., McIntosh, A.R., Jirsa, V., 2013. The virtual brain: a simulator of primate brain network dynamics. *Front. Neuroinform.* 7, 10.
- Schaworonkow, N., Nikulin, V.V., 2021. Is sensor space analysis good enough? spatial patterns as a tool for assessing spatial mixing of EEG/MEG rhythms. *bioRxiv*.
- Schöfelen, J.-M., Gross, J., 2009. Source connectivity analysis with MEG and EEG. *Hum. Brain Mapp.* 30 (6), 1857–1865.
- Schöfelen, J.-M., Gross, J., 2019. Studying dynamic neural interactions with MEG. Magnetoencephalography: from signals to dynamic cortical networks 519–541.
- Schöfelen, J.-M., Hultén, A., Lam, N., Marquand, A.F., Uddén, J., Hagoort, P., 2017. Frequency-specific directed interactions in the human brain network for language. *Proc. Natl. Acad. Sci.* 114 (30), 8083–8088.
- Shoumo, O., Tachibana, Y., Nambu, A., Doya, K., 2017. Computational model of recurrent subthalamo-pallidal circuit for generation of parkinsonian oscillations. *Front. Neuroanat.* 11, 21.
- Silfverhult, M.J., Hintsala, H., Kortelainen, J., Seppänen, T., 2012. Experimental comparison of connectivity measures with simulated EEG signals. *Med. Biol. Eng. Comput.* 50 (7), 683–688.
- Sivagnanam, S., Majumdar, A., Yoshimoto, K., Astakhov, V., Bandrowski, A.E., Martone, M.E., Carnevale, N.T., et al., 2013. Introducing the neuroscience gateway. *IWSG* 993, 0.
- Sommariva, S., Sorrentino, A., Piana, M., Pizzella, V., Marzetti, L., 2019. A comparative study of the robustness of frequency-domain connectivity measures to finite data length. *Brain Topogr.* 32 (4), 675–695.
- Song, J., Davey, C., Poulsen, C., Luu, P., Turovets, S., Anderson, E., Li, K., Tucker, D., 2015. EEG Source localization: sensor density and head surface coverage. *J. Neurosci. Methods* 256, 9–21.
- Van de Steen, F., Faes, L., Karahan, E., Songsiri, J., Valdes-Sosa, P.A., Marinazzo, D., 2019. Critical comments on EEG sensor space dynamical connectivity analysis. *Brain Topogr.* 32, 643–654.
- Supp, G.G., Schlögl, A., Trujillo-Barreto, N., Müller, M.M., Gruber, T., 2007. Directed cortical information flow during human object recognition: analyzing induced EEG gamma-band responses in brain's source space. *PLoS ONE* 2 (8), e684.
- Tabbal, J., Kabbara, A., Yochum, M., Khalil, M., Hassan, M., Benquet, P., 2022. Assessing HD-EEG functional connectivity states using a human brain computational model. *J. Neural Eng.* 19 (5), 056032.
- Tadel, F., Baillet, S., Mosher, J.C., Pantazis, D., Leahy, R.M., 2011. Brainstorm: a user-friendly application for MEG/EEG analysis. *Comput. Intell. Neurosci.* 2011.
- Van Diesen, E., Numan, T., Van Dellen, E., Van Der Kooi, A.W., Boersma, M., Hofman, D., Van Lutterveld, R., Van Dijk, B.W., Van Straaten, E., Hillebrand, A., et al., 2015. Opportunities and methodological challenges in EEG and MEG resting state functional brain network research. *Clin. Neurophysiol.* 126 (8), 1468–1481.
- Van Veen, B.D., Van Drongelen, W., Yuchtman, M., Suzuki, A., 1997. Localization of brain electrical activity via linearly constrained minimum variance spatial filtering. *IEEE Trans. Biomed. Eng.* 44 (9), 867–880.
- Vinck, M., Huerdeman, L., Bosman, C.A., Fries, P., Battaglia, F.P., Pennartz, C.M.A., Tiesinga, P.H., 2015. How to detect the granger-causal flow direction in the presence of additive noise? *Neuroimage* 108, 301–318.

- Vinck, M., van Wingerden, M., Womelsdorf, T., Fries, P., Pennartz, C.M.A., 2010. The pairwise phase consistency: a bias-free measure of rhythmic neuronal synchronization. *Neuroimage* 51 (1), 112–122.
- Wall, M.E., Rechtsteiner, A., Rocha, L.M., 2003. Singular Value Decomposition and Principal Component Analysis. In: A practical approach to microarray data analysis. Springer, pp. 91–109.
- Wang, H.E., Bénar, C.G., Quilichini, P.P., Friston, K.J., Jirsa, V.K., Bernard, C., 2014. A systematic framework for functional connectivity measures. *Front. Neurosci.* 8, 405.
- Wang, S.H., Lobier, M., Siebenhüner, F., Puoliväli, T., Palva, S., Palva, J.M., 2018. Hyperedge bundling: a practical solution to spurious interactions in MEG/EEG source connectivity analyses. *Neuroimage* 173, 610–622.
- Westner, B.U., Dalal, S.S., Gramfort, A., Litvak, V., Mosher, J.C., Oostenveld, R., Schafelen, J.-M., 2021. A unified view on beamformers for m/EEG source reconstruction. *Neuroimage* 118789.
- Whittle, P., 1963. On the fitting of multivariate autoregressions, and the approximate canonical factorization of a spectral density matrix. *Biometrika* 50 (1–2), 129–134.
- Winkler, I., Panknin, D., Bartz, D., Müller, K.-R., Haufe, S., 2016. Validity of time reversal for testing granger causality. *IEEE Trans. Signal Process.* 64 (11), 2746–2760.
- Wipf, D.P., Owen, J.P., Attias, H.T., Sekihara, K., Nagarajan, S.S., 2010. Robust bayesian estimation of the location, orientation, and time course of multiple correlated neural sources using MEG. *Neuroimage* 49 (1), 641–655.

Distinguishing between- from within-site phase-amplitude coupling using antisymmetrized bispectra

Franziska Pellegrini^{a,b}, Tien Dung Nguyen^{a,1}, Taliana Herrera^a, Vadim Nikulin^f, Guido Nolte^e, Stefan Haufe^{c,d,a,b,*}

^a*Charité-Universitätsmedizin Berlin, Charitéplatz 1, Berlin, 10117, Germany*

^b*Bernstein Center for Computational Neuroscience, Philippstraße 13, Berlin, 10117, Germany*

^c*Technische Universität Berlin, Straße des 17. Juni 135, Berlin, 10623, Germany*

^d*Physikalisch-Technische Bundesanstalt Braunschweig und Berlin, Abbestraße 2–12, Berlin, 10587, Germany*

^e*UKE,*

^f*Max Planck Institute for Human Cognitive and Brain Sciences Leipzig, Stephanstraße 1a, Leipzig, 04103, Germany*

Abstract

Phase-amplitude coupling (PAC) is a form of cross-frequency coupling in which the amplitude of a fast oscillation is locked to the phase of a slow oscillation. PAC has been proposed as a mechanism for integrating slow large-scale networks with fast-oscillating local processes in the brain. On a signal level, PAC can be observed in single time series, reflecting local dynamics, or between two time series, potentially reflecting a functional interaction between distinct brain sites. To investigate the role of PAC as a mechanism of brain signalling, it is important to distinguish these two cases. However, when mixtures of underlying signals are observed, between-site PAC can spuriously emerge even if the true interaction is only local

*Corresponding author: haufe@tu-berlin.de

(within-site). This problem arises in electrophysiological recordings where mixing occurs due to volume conduction or the presence of a shared electrical reference. To address this problem, we propose to estimate PAC using the anti-symmetrized bispectrum (ASB-PAC). It has previously been shown that the cross-bispectrum can be used to measure PAC while efficiently suppressing Gaussian noise, and that the anti-symmetrized bispectra vanish for mixtures of independent sources. However, ASB-PAC has so far not been used to assess the presence of genuine between-site PAC. Using simulations, we here investigate the performance of different algorithms to detect PAC in a mixed signal setting as well as the performance of the same methods to distinguish genuine between-site PAC from within-site PAC. This is done in a minimal two-channel setup as well as in a more complex setting that assesses PAC on reconstructions of simulated EEG sources. We observe that bispectral PAC methods are considerably better at detecting simulated PAC in the volume conduction setting than three conventional PAC estimators. ASB-PAC achieves the highest performance in detecting genuine between-site PAC interactions while detecting the fewest spurious interactions. Using the ASB-PAC could therefore greatly facilitate the interpretation of future PAC studies when discriminating local from remote effects.

We demonstrate the application of ASB-PAC on EEG data from a motor imagery experiment. Additionally, we present an upgraded version of the free ROIconnect plugin for the EEGLAB toolbox, which includes PAC and ASB-PAC metrics based on bispectra.

Keywords: Electroencephalography, Simulation, Phase-amplitude coupling, Bispectrum, Anti-symmetrization, Motor Imagery

1. Introduction

Phase-amplitude coupling (PAC) is a form of cross-frequency coupling in which the amplitude of a fast oscillation is correlated with the phase of a slow oscillation (e.g., Canolty et al., 2006; Tort et al., 2010; Hyafil et al., 2015). It has been suggested that PAC facilitates the coordination of neural activity across various spatial and temporal scales by decomposing neural computations into discrete units of activity for cognitive processes like memory, attention, and learning (Canolty and Knight, 2010; Hyafil et al., 2015). These units are aligned with rhythmic external sensory and motor activities (Canolty and Knight, 2010). Further, it has been suggested that functional PAC may be pathologically increased in patients with movement disorders (De Hemptinne et al., 2013; Yin et al., 2022).

Historically, research focused on the detection of PAC within a single signal (e.g., Osipova et al., 2008; Cohen et al., 2009; Voytek et al., 2010; Florin and Baillet, 2015; Watrous et al., 2015; Yin et al., 2022). However, other studies also aimed to investigate the coupling between the phase of a slow oscillation (SO) in one signal and the fast oscillation (FO) of another signal, originating from two spatially different locations (e.g., Voytek et al., 2015; Daitch et al., 2016; Nandi et al., 2019). Tort et al. (2008) report a coupling between the phase of striatal theta and the amplitude of high-frequency oscillations in the hippocampus, and vice versa, in local field potential (LFP) recordings. Maris et al. (2011) showed the presence of PAC between different intracranial electroencephalography (EEG) electrodes. Others have reported functional PAC between different channels of scalp EEG (Schack et al., 2002; Isler et al., 2008; Jirsa and Müller, 2013). In addition, an EEG study (Gong

et al., 2021) reported that only PAC between different ICA components was clinically relevant compared to PAC from the same ICA component. These studies suggest that between-site PAC could serve as a mechanism for the integration of spatially distributed neuronal activity (Jirsa and Müller, 2013; Hyafil et al., 2015). Further, it has been suggested that between-site PAC could serve as a gating mechanism that enables spatially distributed networks to coordinate and operate in parallel (van der Meij et al., 2012).

There have been multiple suggestions on how to measure PAC (e.g., Canolty et al., 2006; Penny et al., 2008; Tort et al., 2010; Özkurt and Schnitzler, 2011; Canolty and Knight, 2010; Kovach et al., 2018; Zandvoort and Nolte, 2021). Traditional metrics are based on a process that first extracts the slow and fast oscillation by bandpass-filtering the original signal in the respective low and high frequency bands. Then, the amplitude of the fast oscillation is extracted, e.g., by calculating its envelope with the Hilbert transform. The relation between the phase of the slow oscillation and the envelope of the fast oscillation is then assessed by calculating either the coherence (Colgin et al., 2009), phase-locking value (Lachaux et al., 1999), or correlation (Bruns and Eckhorn, 2004) between the slow oscillation and the amplitude of the fast oscillation. Alternatively, dependencies between phase and amplitudes can be assessed non-parametrically by either calculating the mean vector length modulation index (MI Canolty et al., 2006), or by comparing their joint distribution to a uniform distribution using the Kullback-Leibler Modulation Index (Tort et al., 2010). A downside of all of these metrics is that they heavily depend on filtering parameters in the pre-processing step (Aru et al., 2015; Kovach et al., 2018; Zandvoort and Nolte,

2021). More recent studies have pointed out that the cross-bispectrum or cross-bicoherence can also be employed to assess PAC (e.g., Hyafil, 2015; Kovach et al., 2018; Zandvoort and Nolte, 2021). Indeed, Hyafil (2015) clarified that bicoherence represents phase–phase coupling between three phases and thus essentially corresponds to PAC. Zandvoort and Nolte (2021) further showed theoretically that bispectra closely correspond to conventional PAC metrics for specific filter settings. These studies highlight that metrics based on the bispectrum have two advantages: First, unlike most other PAC metrics, they do not depend of filter settings. And second, the cross-bispectrum efficiently suppresses Gaussian noise (e.g., Nikias and Pan, 1988).

Electrophysiological recordings like intracranial or scalp electroencephalography (EEG), as well as Magnetoencephalography (MEG), are well suited to study PAC because of their high temporal resolution. However, EEG/MEG recordings are often corrupted by noise and signal mixing (Nolte et al., 2004; Haufe et al., 2013; Bastos and Schoffelen, 2016; Schaworonkow and Nikulin, 2021). In case of sensor-level MEG and scalp EEG, mixing arises due to volume conduction, i.e., the superposition of underlying brain sources on the sensors (e.g., Schaworonkow and Nikulin, 2021). To reconstruct the underlying neuronal sources, it is common practice to use inverse models that project sensor-level activity to source locations in the brain (e.g., Baillet et al., 2001). However, since inverse algorithms are in general unable to reconstruct sources perfectly, signal mixing is not entirely eliminated. This phenomenon is called source leakage (Schoffelen and Gross, 2009). Source mixing can also occur in intracranial EEG recordings, like local field potentials (LFP), e.g., due to volume conduction and a shared electrical reference being used for different

recording sites (Bastos and Schoffelen, 2016).

Signal mixing can degrade the statistical power for detecting PAC within a single channel of measured or reconstructed activity but it cannot lead to spurious PAC. However, when the goal is to study genuine between-site PAC, i.e., coupling between the phase of a slow oscillation coming from one brain location, and the amplitude of a fast oscillation coming from a different brain location, signal mixing can be a confounding factor. In this case, one may erroneously interpret within-site PAC as between-site PAC when slow and fast oscillation signal components leak into both studied channels (Figure 2). This raises the question: how can we distinguish genuine between-site PAC from spurious between-site PAC arising from signal leakage of sources exhibiting within-site PAC? Note that we use the term ‘between-site’ here to refer to the presence of two anatomically distinct neural current sources projecting to M/EEG sensors with different topographies. This would entail cases where sources are physically close to another but currents have distinct spatial orientations either due to a sharp folding of the cortical mantle in the vicinity of the sources or due to recruitment of different neural subpopulations.

There have been various suggestions on how to solve the problem of signal leakage in the context of functional connectivity (FC). For example, Colclough et al. (2015) proposed a symmetric orthogonalization of the time-domain signals before estimating FC metrics. Shahbazi et al. (2010) suggested to compare FC metrics against a null distribution, generated from permuted independent components (IC surrogate approach). And Chella et al. (2014) suggested to use an anti-symmetrization of the cross-bispectrum

to eliminate the effects of mixing artifacts on the bispectrum and illustrated that the anti-symmetrized bispectrum (ASB) vanishes for mixtures of independent sources. To date, however, anti-symmetrized bispectra have not been used to define metrics for genuine between-site PAC (ASB-PAC).

Previous research has established that PAC can be quantified using traditional measures like the MI or through third-order cumulants, such as the bispectrum. However, it remains unclear if these methods can also be used to identify the presence of genuine between-site PAC. Moreover, these metrics are vulnerable to signal mixing (e.g., Chella et al., 2014). In this study, we test three strategies aimed at enhancing the robustness of PAC metrics to signal mixing. These strategies include ASB-PAC, MI based PAC calculated on orthogonalized time series, and the IC surrogate approach. We address the following main questions:

- Are the bispectrum and the MI suitable methods to identify genuine between-site as opposed to within-site PAC?
- Is ASB-PAC a valid measure of between-site PAC?
- Can orthogonalization or the IC surrogate approach be used to make MI basec PAC robust against signal mixing?

In addition to these questions, we are interested in the impact of the signal-to-noise ratio and the number of underlying ground-truth interactions on the accuracy of detection. By answering these questions, we aim at finding an analysis approach that ensures a reliable detection of between-site PAC, even in the presence of mixed noise.

To this end, we first quantify the performance of different algorithms with respect to their ability to detect PAC in a mixed signal setting. Second, we investigate the performance of these methods to distinguish genuine between-site PAC from within-site PAC in the mixed signal setting. We first conduct a set of simple experiments involving only two channels in different signal-and noise settings. These experiments resemble a recording setup of two, potentially invasive, single electrodes. Next, we translate the simulation to an advanced whole-brain setup, reflecting a scalp EEG recording. Finally, we investigate the presence of robust between-site PAC during motor imagery using real scalp-EEG data (Sannelli et al., 2019).

2. Methods

2.1. Univariate PAC

PAC refers to the coupling between a slow and a fast oscillation. For a given univariate time series $x(t) \in \mathbb{R}, t = 1, \dots, N_t$, with N_t denoting the number of time points, the goal is to determine whether there is PAC between the two frequency bands l and h . If $x_l(t) = a_l(t) * \exp^{i\psi_l(t)}$ and $x_h(t) = a_h(t) * \exp^{i\psi_h(t)}$ denote the low and high-frequency parts of the univariate signal, with $a(t) \in \mathbb{R}$ denoting the amplitude and $\psi(t) \in \mathbb{R}$ denoting the phase of the complex-valued signal, PAC refers to the relation between the phase of in the low frequency band $\psi_l(t)$ and the amplitude envelope of the high frequency band $a_h(t)$.

2.2. Within-site and between-site PAC

PAC can occur either between two oscillations within the same signal $x(t)$ (*within-site* PAC), or between two oscillations coming from two different

signals or sites $x(t)$ and $y(t) \in \mathbb{R}$ (*between-site* PAC). In the latter case, PAC is defined as a relation between the phase of signal $x_l(t)$ in the low frequency band $\psi_{lx}(t)$ and the amplitude envelope of signal $y_h(t)$ in the high frequency band $a_{hy}(t)$.

When measuring PAC between sites in a setting with source mixing, we need to distinguish between three scenarios: Scenario I): There is no PAC between $\psi_{lx}(t)$ and $a_{hy}(t)$. Scenario II): There is PAC between $\psi_{lx}(t)$ and $a_{hy}(t)$ that arises from signal mixing, e.g., $x(t) = c * s(t) + n_1(t)$ and $y(t) = b * s(t) + n_2(t)$, with c and $b \in \mathbb{R}$ representing two scaling factors, $s(t) \in \mathbb{R}$ denoting a time series containing univariate PAC, and $n_1(t)$ and $n_2(t) \in \mathbb{R}$ representing two noise time series. Scenario III): There is genuine PAC between $x(t)$ and $y(t)$, i.e., PAC that cannot be explained by signal mixing: $x(t) = c * s_{low}(t) + n_1(t)$ and $y(t) = b * s_{high}(t) + n_2(t)$, with $s_{low}(t)$ and $s_{high}(t) \in \mathbb{R}$ representing two signals that are phase–amplitude coupled.

2.3. Methods that estimate PAC

2.3.1. Conventional metrics

Modulation Index. The idea behind conventional PAC metrics (Canolty et al., 2006; Tort et al., 2010; Özkurt and Schnitzler, 2011) is to assess the statistical dependence between a phase and an amplitude time series. First, they estimate the distributions of the phase of a time series $x_s(t)$ and the amplitude of a second time series $x_f(t)$, which are hypothesized to contain PA-coupled slow and fast oscillations, respectively. In practice, it might not be known a-priori at what frequencies a given pair of time series exhibits PAC. Therefore, exploratory analyses might sweep through a range of sensible frequency combinations, thereby also swapping the roles of the two time series as slow

or fast oscillations. The slow and fast signal components $x_s(t)$ and $x_f(t)$ are extracted by filtering $x(t)$ in the low and high frequency bands, respectively. In the next step, the time-dependent phase of the slow signal $\psi_s(t)$ is obtained through a Hilbert transform of $x_s(t) = a_s(t) * \exp^{i\psi_s(t)}$. Likewise, the amplitude (envelope) time course of the fast signal, $a_f(t)$, is obtained through a Hilbert transform of $x_f(t) = a_f(t) * \exp^{i\psi_f(t)}$.

To obtain the mean vector length MI (Canolty et al., 2006), the two time series are combined into a composite complex-valued signal:

$$z(t) = a_f(t) e^{i\psi_s(t)} \quad (1)$$

Finally, the MI is obtained as the mean of the absolute value of z across time.

$$\text{MI}_{k,m}(f_{\text{slow}}, f_{\text{fast}}) = \left| \frac{1}{N_t} \sum_t^{N_t} z_t \right|. \quad (2)$$

Note that other versions of the MI have been introduced (Tort et al., 2010; Özkurt and Schnitzler, 2011). In brief, the metric proposed by Tort et al. (2010) assesses the degree of the coupling by calculating the Kullback-Leibler distance of the observed phase-amplitude distribution from a uniform distribution. The metric proposed by Özkurt and Schnitzler (2011) extends the original MI by a normalization with the power of the amplitude vector.

Variants of the MI have been used to investigate both within- and between-site PAC; however, it is unclear whether they can distinguish genuine between-site PAC from PAC arising from mixtures of signals exhibiting within-site PAC.

Bispectral PAC estimation. The cross-bispectrum belongs to the class of higher-order poly-spectra. Precisely, it is the two-dimensional third-order

statistical moment in frequency domain. To estimate the bispectrum, the time series are cut into epochs $e \in 1, \dots, N_e$, and Fourier-transformed. In its most general form, it is calculated for a combination of three channels \tilde{x}_k , \tilde{x}_m , and \tilde{x}_n , and between two frequencies f_1 and f_2 :

$$B_{k,m,n}(f_1, f_2) = \frac{1}{N_e} \sum_e^{N_e} \tilde{x}_{k,e}(f_1) \tilde{x}_{m,e}(f_2) \tilde{x}_{n,e}^*(f_1 + f_2) \in \mathbb{C}, \quad (3)$$

where $.^*$ denotes the complex conjugation.

Recent works have pointed out that PAC can also be estimated from the bispectrum (Kovach et al., 2018; Zandvoort and Nolte, 2021). To this end, the bispectrum B is calculated between channel k at frequency f_1 and channel m at frequencies f_2 and $f_1 + f_2$, where $\tilde{x}_{m,e}(f)$ denotes the e -th epoch of the Fourier-transformed data of channel m at frequency f :

$$B_{k,m,m}(f_1, f_2) = \frac{1}{N_e} \sum_e^{N_e} \tilde{x}_{k,e}(f_1) \tilde{x}_{m,e}(f_2) \tilde{x}_{m,e}^*(f_1 + f_2) \in \mathbb{C}. \quad (4)$$

While some works (Kovach et al., 2018; Zandvoort and Nolte, 2021) have shown analytically that the bispectrum is a suitable measure for PAC, it has not been extensively and systematically tested. Moreover, it has not been tested yet whether bispectra can be used to assess genuine between-site PAC not explained by within-site PAC.

Filter settings. As discussed by Zandvoort and Nolte (2021), PAC between a slow and a fast oscillation with respective peak frequencies f_{slow} and f_{fast} corresponds to bispectral interactions at frequency triples ($f_1 = f_{\text{slow}}, f_2^a = f_{\text{fast}} - f_{\text{slow}}, f_3^a = f_1^a + f_2^a = f_{\text{fast}}$) and ($f_1 = f_{\text{slow}}, f_2^b = f_{\text{fast}}, f_3^b = f_1^b + f_2^b = f_{\text{fast}} + f_{\text{slow}}$) (see Figure 2). Note that the relevance of the “sidelobe” frequencies $f_2^a = f_{\text{fast}} - f_{\text{slow}}$ and $f_3^b = f_{\text{fast}} + f_{\text{slow}}$ in PAC arises from the

multiplicative modulation of the fast signal by the amplitude of the slow signal, which amounts to a convolution in frequency domain. As a result, f_2^a and f_3^b are visible also as additional peaks of spectral power (sidelobes) around the peak of the fast oscillation.

For conventional metrics such as the MI, there have been discussions about how to correctly set the filter parameters, and especially the band width to obtain the fast oscillation (e.g., Berman et al., 2012; Aru et al., 2015; Zandvoort and Nolte, 2021). For example, some works have recommended to set the filter broad enough to include both side lobes f_2^a and f_3^b . However, Zandvoort and Nolte (2021) pointed out that this leads to a smeared estimation of PAC and instead recommend to include only f_{fast} and one of the two side lobes. Here we propose a third alternative—analogous to the bispectral estimate—namely to estimate PAC twice, once with filter settings that include f_2^a and f_{fast} , and with filter settings that include f_{fast} and f_3^b .

Note, however, that the notations typically used for bispectral and conventional PAC metrics are not consistent (Zandvoort and Nolte, 2021): while the bispectrum is written as a function of two frequencies f_1 and f_2 , implying that the third frequency is fixed at $f_1 + f_2$, the MI is typically written as a function of the slow frequency and the *center* frequency of the fast oscillation, assuming a symmetrical filter around it. Thus, bispectral PAC at $[f_{\text{slow}}, f_{\text{fast}}]$ corresponds to MI-PAC at $[f_{\text{slow}}, f_{\text{fast}} + 0.5f_{\text{slow}}]$.

Based on these considerations, and following the conventional notation, the final bispectral PAC estimates in this study are obtained as

$$\text{PAC}_{k,m}^B(f_{\text{slow}}, f_{\text{fast}}) = 0.5 \cdot |B_{k,m,m}(f_1, f_2^a)| + 0.5 \cdot |B_{k,m,m}(f_1, f_3^b)| \quad (5)$$

and the final MI-PAC estimates are obtained as

$$\text{PAC}_{k,m}^{\text{MI}}(f_{\text{slow}}, f_{\text{fast}}) = 0.5 \cdot |\text{MI}_{k,m}(f_1, f_2^a + 0.5f_1)| + 0.5 \cdot |\text{MI}_{k,m}(f_1, f_2^b + 0.5f_1)|, \quad (6)$$

where the band width of the fast-frequency filter is not much larger than $f_{\text{fast}} - f_{\text{slow}}$ (see Section 3).

2.4. Statistical testing

To statistically assess whether an observed MI is statistically significant, the true MI can be compared against an empirical null distribution. Samples consistent with the null hypothesis of no PAC being present can be obtained by randomly permuting the order of the epochs of one of the time series and subsequently recalculating PAC on the permuted epochs:

$$\text{MI}_{k,m}^{p_i}(f_{\text{slow}}, f_{\text{fast}}) = \left| \frac{1}{N_t} \sum_t^{N_t} a_{f,p_i(e)}(t) e^{i\psi_{s,e}(t)} \right|. \quad (7)$$

for the i th iteration with $i = 1, \dots, S$, where $p_i(e)$ is a random permutation of the epochs $e = 1, \dots, N_e$.

Analogously, for the bispectral method, the epochs of the Fourier-domain data $\tilde{x}_{m,e}$ can be permuted to obtain a null distribution for statistical testing:

$$B_{k,m,m}^{p_i}(f_1, f_2) = \frac{1}{N_e} \sum_e^{N_e} \tilde{x}_{k,e}(f_1) \tilde{x}_{m,p_i(e)}(f_2) \tilde{x}_{m,p_i(e)}^*(f_1 + f_2) \in \mathbb{C} \quad (8)$$

This procedure is repeated S times to obtain the desired surrogate distribution. P-values are then calculated as follows:

$$p = \frac{\sum_{s=1}^S c_s}{S}, \text{ with } c_s = \begin{cases} 1, & \text{if } \text{PAC}_{\text{surr}} > \text{PAC} \\ 0, & \text{otherwise} \end{cases} \quad (9)$$

2.5. Conventional metrics and between-site PAC

Neither the bispectrum nor the MI are not able to distinguish genuine between-site PAC from spurious PAC arising from signal mixing (Scenario II vs. Scenario III described in Section 2.2). That is, neither metric is able to identify whether observed PAC originates from a single underlying source that has leaked into the two time series, or from two different underlying sources. Similarly, the permutation-based statistical assessment that we propose to test whether the MI or bispectrum is significant is unable to differentiate between within-site PAC and between-site PAC. This is because permutations disrupt all data interactions, including those caused by mixed sources. As a consequence also interactions from the type of Scenario II are tested significant. To address this limitation, alternative methods are essential. In the following, we summarize three approaches that are candidates to solve this problem.

2.6. Anti-symmetrization

For the bispectrum, anti-symmetrization has been proposed to correct for effects that arise from signal mixing (Chella et al., 2014). Based on anti-symmetrized bispectra, we can define the following PAC metric whose expected value for mixtures of independent (potentially within-site PAC coupled) signals is zero:

$$\begin{aligned} \text{PAC}_{k,m}^{\text{ASB}}(f_{\text{slow}}, f_{\text{fast}}) &= B_{[k,m,m]}(f_1, f_2) \\ &= 0.5 \cdot (B_{k,m,m}(f_1, f_2^a) - B_{m,k,m}(f_1, f_2^a)) \\ &\quad + 0.5 \cdot (B_{k,m,m}(f_1, f_2^b) - B_{m,k,m}(f_1, f_2^b)) \end{aligned} \quad (10)$$

If the slow and fast oscillations originate from two distinct sites, implying a genuine between-site interaction, then we would expect to observe the slow oscillation solely at one site and the fast oscillation at the other site. Contrarily, if the PAC interaction is derived from a single source that leaks to two sites, then both the slow and fast oscillations should be present at each site. Taking advantage of this fact, we can discern genuine interactions based on their anti-symmetric nature by subtracting the symmetric part of the interaction. However, it is unclear whether this leakage-corrected bispectrum can still be interpreted as PAC. Therefore a systematic evaluation whether the ASB-PAC can be used to estimate between-site PAC is needed.

2.7. Orthogonalization

An equivalent technique to anti-symmetrization for bispectra is not available for the MI. However, several methods have been proposed in the literature as general solutions to remove the effect of source mixing from data or from statistical contrasts against null distributions. First, a multivariate symmetric orthogonalization technique has been proposed by Colclough et al. (2015). This technique removes instantaneous correlations between multivariate time series, which is proposed as a general correction for source leakage effects in functional connectivity analyses. The authors demonstrate its usability in a simulation where partial correlations between power envelopes are analyzed, as well as in a real resting-state MEG data example. Thus, even though symmetric orthogonalization is not specifically designed for PAC problems, it may be suitable to solve the source mixing problem also for between-site PAC.

The advantage of the symmetric orthogonalization over similar decor-

relation schemes (e.g., Hipp et al., 2012; Brookes et al., 2012) is that the result is not dependent on the ordering of the region time series, and that the resulting time series are as close as possible (in the least-squares sense) to the original time series. This orthogonalization scheme is based on the Löwdin method (Löwdin, 1950) and can be implemented using a singular value decomposition (Colclough et al., 2015; Annavarapu, 2013):

$$\mathbf{X} = \mathbf{UDV}^\top \quad (11)$$

$$\tilde{\mathbf{X}} = \mathbf{U}(\mathbf{V}^\top), \quad (12)$$

where $\mathbf{X} \in \mathbb{R}^{N_t \times R}$ contains R time series to be orthogonalized. R indicates the number of time series that are investigated, and \mathbf{V}^\top denotes the transpose of \mathbf{V} . Using the 'economy version' of the SVD, $\mathbf{U} \in \mathbb{R}^{N_t \times R}$ is a matrix of orthonormal time courses, $\mathbf{V} \in \mathbb{R}^{R \times R}$ is a matrix of singular vectors, $\mathbf{D} \in \mathbb{R}^{R \times R}$ is a matrix of singular values, and $\tilde{\mathbf{X}} \in \mathbb{R}^{N_t \times R}$ is the matrix of symmetrically orthogonalized time courses.

To test the statistical significance of the resulting PAC, surrogate data without PAC are constructed. To this end, the epochs of one times series are permuted and concatenated back to form a time series. Then the symmetric orthogonalization is applied to the concatenated time series, and PAC $\text{PAC}_{\text{surr}}^{\text{MI}}$ is estimated on the surrogate data. Finally the p-value is calculated as described above.

2.8. Surrogate data using independent component analysis

Another general approach to account for artifacts of source mixing is to generate a null distribution by permuting the epochs of independent component (IC) time series (Shahbazi et al., 2010). In this study, this method will

be called IC surrogate analysis (IC-surr). The idea of this approach is to construct surrogate data that are statistically as close as possible to the original data, but are still physically realistic mixtures of independent sources rather than being completely independent. The comparison of the observed FC to the distribution of FC obtained from surrogate data can then reveal whether observed FC is a genuine effect that cannot be explained by source mixing alone. The authors demonstrate the usability for the linear measures coherence and imaginary part of coherency, 1:2 phase coupling, and Granger causality in simulated and real EEG data. They show that results obtained with the robust FC measure imaginary coherency cannot be explained by the surrogate data. Further, for Granger Causality, a non-robust measure, they observe that the ground-truth interactions that they simulated were attenuated but not removed in the surrogate data. The authors propose that the IC-surr approach is applicable to other interaction measures as well. Therefore, we also include this approach in our study and test whether it can be used to target the between-site PAC estimation problem.

We here describe the approach exemplarily for a setting with N_s channels. The first step in the IC surrogate analysis is to perform independent component analysis (ICA) of the time series matrix $\mathbf{X} \in \mathbb{R}^{N_t \times N_s}$. In brief, ICA finds a weighting matrix $\mathbf{W} \in \mathbb{R}^{N_s \times N_s}$ that unmixes the sensor data into ICs that are minimally statistically dependent according to some criterion:

$$\mathbf{S} = \mathbf{X}\mathbf{W} \in \mathbb{R}^{N_t \times N_s} . \quad (13)$$

In the present study, we use the Infomax ICA algorithm (Bell and Sejnowski, 1995) as implemented by the `runica.m` function of the EEGLab package (Delorme and Makeig, 2004), but other algorithms are conceivable. Sub-

sequently, the ICs are permuted by temporally shifting them randomly with respect to each other. Finally, the concatenated component time series are projected back to the original space:

$$\mathbf{X}_{\text{shuf}} = \mathbf{S}_{\text{shuf}} \mathbf{A} , \quad (14)$$

with $\mathbf{A} = \mathbf{W}^{-1} \in \mathbb{R}^{N_s \times N_s}$ denoting the ICA mixing matrix. From \mathbf{X}_{shuf} , the MI can be calculated again. The p-value is then calculated by comparing the original MI against the IC-surrogate MI distribution.

3. Experiments

To test whether the various PAC metrics and robustification approaches are able to distinguish genuine between-site PAC while rejecting contributions from within-site PAC, we performed a number of experiments, which are described below.

First, to ensure that performance differences between the MI- and bispectrum-based PAC metrics cannot be attributed to different performances in the detection of univariate PAC, we conducted a small baseline experiment. To this end, we simulated univariate PAC within a single channel, added noise with varying signal-to-noise ratios (SNRs), and measured PAC between the phase of the slow oscillation and the amplitude of the fast oscillation within the single channel.

We then conducted two experiments involving only $N_s = 2$ channels, which allow us to quantify the performance of different analysis pipelines in different SNR settings. In 2CHAN-BI (c.f. Table 1), we simulated true bivariate PAC between the two channels. These experiments allow us to study

the sensitivity of our analysis pipelines with respect to detecting ground-truth between-channel interactions as a function of SNR. In the 2CHAN-UNI experiments, we simulated two univariate phase–amplitude coupled signals mixed into each of the two channels. This setup enables us to assess false-positive rates of the different approaches. Please note that we here use the term *bivariate PAC* to describe ground-truth between-region or between-channel PAC, reflecting a true interaction between a slow oscillation in one brain source and a fast oscillation in another brain source. In contrast, we use the term *univariate PAC* describing ground-truth within-region or within-channel PAC, reflecting PAC between a slow and a fast oscillation within the same source site.

Subsequently, we considered a whole-brain scalp-EEG setting. From this setting, we expect to gain insights beyond the minimal two-channel setup into how well the methods might work on EEG data in practice. Again, we simulated two cases. In Experiment EEG-BI (c.f. 2), three true bivariate PAC interactions between six randomly selected regions of the brain were modeled, while all other regions emitted only independent brain noise activity. This experiment allows us to study the sensitivity of the tested approaches in a setting with realistic signal mixing. In Experiment EEG-UNI, we considered three active regions containing independent univariate within-region PAC, while again all other regions elicit independent brain noise only. This experiment is important to test the suitability of the approaches in eliminating spurious PAC detection in a setting with realistic signal mixing. In the following, we first describe two-channel experiments before moving on to more complex whole-brain EEG experiments. Matlab code to reproduce all

Simulation		Interaction	Evaluation
1CHAN-UNI	Single-channel baseline	Univariate PAC within a single channel.	TPR
2CHAN-BI-IND	Two-channel bivariate, independent	Bivariate PAC between two channels.	TPR
2CHAN-BI-MIX	Mixed		
2CHAN-UNI-IND	Two-channel univariate, independent	Two channels with two univariate PAC time series.	TNR
2CHAN-UNI-MIX	Mixed		

Table 1: Overview of the univariate baseline experiment (1CHAN-UNI) and the differences between the four 2CHAN experimental settings: modeled interaction and performance evaluation (TPR: true positive rate, TNR: true negative rate).

experiments is provided¹. The implementation for the bispectra is based on the open-source METH toolbox².

3.1. Baseline experiment on univariate PAC detection

3.1.1. Data generation

We generated time series at a sampling rate of 200 Hz with a recording length of $N_t = 120\,000$ samples amounting to a duration of 10 minutes. The signal was generated as random white Gaussian noise filtered in the low frequency band (defined here as ranging from 9 to 11 Hz) for the slow

¹<https://github.com/fpellegrom/PAC>

²<https://www.nitrc.org/projects/meth/>

Simulation		Interaction	Evaluation
EEG-BI	Whole-brain EEG bivariate	Three bivariate interactions between six regions. Other regions contain independent brain noise.	PR
EEG-BI-SNR	Varying SNR	Three bivariate interactions between six regions.	
EEG-BI-INT	Varying N_{I-bi}	One, three, or five bivariate interactions.	
EEG-UNI	Whole-brain EEG univariate	One univariate PAC time series. Other regions contain independent brain noise.	gFPR
EEG-UNI-SNR	Varying SNR	One univariate PAC time series.	
EEG-UNI-INT	Varying N_{I-uni}	One, three, or five univariate PAC time series.	

Table 2: Overview of the differences between the six whole-brain EEG experimental settings: modeled interaction and performance evaluation (SNR: signal-to-noise ratio, N_{I-bi} number of bivariate interactions, N_{I-uni} number of univariate interactions, PR: percentile rank, gFPR: global false positive rate).

oscillation, denoted $x_s(t)$ with $t \in \{1, \dots, N_t\}$, and in the high frequency band (ranging from 58 to 62 Hz) for the fast oscillation, $x_{f\text{-raw}}(t)$. Throughout, we used zero-phase forward and reverse second-order digital Butterworth band-pass filters. The PAC interaction was modeled as coupling between the phase of the slow oscillation and the amplitude of the fast oscillation. To achieve this, we extracted the phase of the slow oscillation $\psi_s(t)$ and the phase of the fast oscillation $\psi_f(t)$ by means of the Hilbert transform, from which we calculated the modulated fast oscillating signal x_f :

$$x_f(t) = \Re \left[(1 - \cos(\psi_s(t))) e^{i\psi_f(t)} \right], \quad (15)$$

with $\Re[x]$ denoting the real part of x . We divided both the slow and the fast oscillating signal by their $_2$ -norms for normalization: $\mathbf{x}_{fn} = \frac{\mathbf{x}_f}{\|\mathbf{x}_f\|_2} \in \mathbb{R}^{N_t}$ and $\mathbf{x}_{sn} = \frac{\mathbf{x}_s}{\|\mathbf{x}_s\|_2} \in \mathbb{R}^{N_t}$, where $\mathbf{x}_f = [x_f(1), \dots, x_f(N_t)]^\top \in \mathbb{R}^{N_t}$ and $\mathbf{x}_s = [x_s(1), \dots, x_s(N_t)]^\top \in \mathbb{R}^{N_t}$ are the concatenated values of $x_f(t)$ and $x_s(t)$ at all time points, respectively. Finally, we summed up the slow and the fast oscillation to yield the univariate PAC signal:

$$\mathbf{p}_1 = \mathbf{x}_{fn} + \mathbf{x}_{sn}, \quad (16)$$

and then divided the signal by its Frobenius norm: $\mathbf{p}_{1n} = \frac{\mathbf{p}_1}{\|\mathbf{p}_1\|_2}$.

We generated a time series $\mathbf{c}_1 \in \mathbb{R}^{N_t}$, representing channel noise, as random white noise. The channel noise time series was then also divided by its $_2$ -norm: $\mathbf{c}_{1n} = \frac{\mathbf{c}_1}{\|\mathbf{c}_1\|_2}$. Finally, we formed a weighted sum of signal and channel noise:

$$\mathbf{p}_{1c} = \theta \mathbf{p}_{1n} + (1 - \theta) \mathbf{c}_{1n} \in \mathbb{R}^{N_t}, \quad (17)$$

where the parameter $\theta \in [0, 1]$ defines the signal-to-noise ratio on channel level (SNR_c), which can be expressed in decibel (dB) as: $\text{SNR}_{c\theta} = 20 * \log_{10}(\frac{\theta}{1-\theta})$ dB. We compared the performance of various MI variants and the bispectrum without anti-symmetrization in detecting the univariate PAC for the following SNR_c values: noise only ($\theta = 0$), -19 dB ($\theta = 0.1$), -12 dB ($\theta = 0.2$), -7 dB ($\theta = 0.3$), and -4 dB ($\theta = 0.4$).

3.1.2. PAC analysis

To estimate PAC, we first cut the time series into epochs. PAC estimation based on the MI requires one to cut both signals into long epochs (Tort et al., 2010). That is, for MI-based metrics, we split the data into $N_e = 60$ epochs of length $L_e = 2000 = 10$ sec. For bispectral PAC metrics, we cut the time series into $N_e = 300$ epochs of 2 seconds length (i.e., 400 samples).

To estimate the MI, we filtered the epoched time series in the low and high frequency bands. Since we modelled the ground-truth interaction at $f_{\text{slow}} = 10$ Hz and $f_{\text{fast}} = 60$ Hz, we calculated the MI once between the slow signal $x_s(t)$ filtered between 9 and 11 Hz and the fast signal $x_f(t)$ filtered between 49 and 61 Hz, and once between the slow signal and the fast signal filtered between 59 and 71 Hz (c.f. Section 2.3.1 for a detailed explanation on filter settings). Subsequently, the two MI estimates were averaged.

To estimate the bispectral metrics, we Fourier-transformed every epoch after multiplying it with a 400-point symmetric Hanning window. Afterwards, we estimated the bispectra once at ($f_1 = 10$ Hz, $f_2^a = 50$ Hz, $f_1 + f_2^a = 60$ Hz) and once at ($f_1 = 10$ Hz, $f_2^b = 60$ Hz, $f_1 + f_2^b = 70$ Hz). Subsequently, the two estimates were averaged.

For the baseline experiment, we also assessed the performance of addi-

tional variants of the MI as introduced by Tort et al. (2010) and Özkurt and Schnitzler (2011). Tort et al. (2010) tested their MI metric against other measures of PAC, like, e.g., the phase locking value, and found that it is suitable to measure univariate PAC. Özkurt and Schnitzler (2011) also compared their proposed MI metric to other PAC measures like the general linear model approach and showed that it is superior to them.

To assess the statistical significance of the PAC estimate, we generated a surrogate distribution with $S = 1000$ samples, from which we calculate a p-value as described in Section 2.4.

3.1.3. Performance evaluation

The experiment was repeated $D = 100$ times to obtain 100 p-values p_d . PAC was considered statistically significant for p-values below an α -level of 0.05. To assess whether the studied PAC detection pipelines are able to correctly detect the presence of PAC, we evaluated the true positive rate (TPR):

$$TPR = \frac{1}{D} \sum_{d=1}^D c_d, \text{ with } c_d = \begin{cases} 1, & \text{if } p_d < \alpha \\ 0, & \text{otherwise} \end{cases} \quad (18)$$
(19)

3.2. Two-channel experiments

In the two-channel experiments (Figure 1), we generated either two underlying time series exhibiting a true bivariate PAC interaction (referred to as 2CHAN-BI), or two independent time series each exhibiting univariate PAC (referred to as 2CHAN-UNI, see Section 3.2.1). The underlying signals were

then further linearly mixed into two measurement channels (see Figure 2 for an overview of the generated signals). The objective of the two-channel setup is to provide a simplified context for showcasing the characteristics of the different PAC estimation approaches. We expect that all non-robust metrics are not capable of distinguishing within- from between-site PAC. Conversely, the ASB-PAC should be able to distinguish these. However, it is unclear how the orthogonalization approach (Colclough et al., 2015) and the IC surrogate method (Shahbazi et al., 2010) might perform. The two-channel setup offers a good way to analyze their behavior in a simple controlled setup.

3.2.1. Data generation

As in the baseline experiment, we generated a slow oscillation (9 to 11 Hz) and a fast oscillation (58 to 62 Hz) time series at a sampling rate of 200 Hz with a recording length of $N_t = 120\,000$ samples = 10 minutes. As described above, the amplitude of the fast oscillation was modulated by the phase of the slow oscillation. Afterwards, they were normalized by their $_2$ -norms.

We generated time series \mathbf{c}_1 and $\mathbf{c}_2 \in \mathbb{R}^{N_t}$, representing noise in the two channels, as random white noise. The channel noise time series were then also divided by their $_2$ -norms: $\mathbf{c}_{1n} = \frac{\mathbf{c}_1}{\|\mathbf{c}_1\|_2}$ and $\mathbf{c}_{2n} = \frac{\mathbf{c}_2}{\|\mathbf{c}_2\|_2}$.

In the experimental setting comprising an underlying signal with bivariate PAC (2CHAN-BI), we added the channel noise to the slow and the fast oscillating signals, respectively:

$$\mathbf{x}_{fc} = \theta \mathbf{x}_{fn} + (1 - \theta) \mathbf{c}_{1n} \in \mathbb{R}^{N_t}, \quad (20)$$

$$\mathbf{x}_{sc} = \theta \mathbf{x}_{sn} + (1 - \theta) \mathbf{c}_{2n} \in \mathbb{R}^{N_t}. \quad (21)$$

To simulate signal mixing (MIX), we multiplied the two channel time series

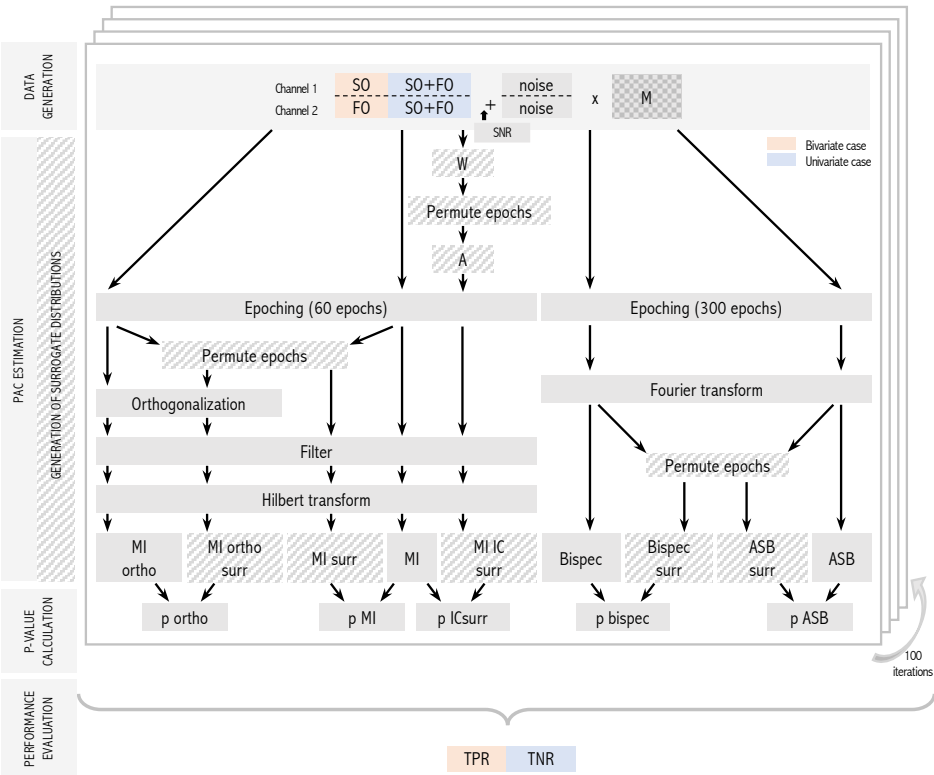


Figure 1: Structure of the two-channel experiments and data analysis consisting of the following steps: data generation, PAC estimation and generation of surrogate distributions, p-value calculation, performance evaluation. SO: slow oscillation, FO: fast oscillation, M: mixing matrix, ICs: components retrieved from an independent component analysis (ICA), W: ICA unmixing matrix, A: ICA mixing matrix, MI: modulation index, ASB-PAC: anti-symmetrized bispectrum, TPR: true positive rate, TNR: true negative rate.

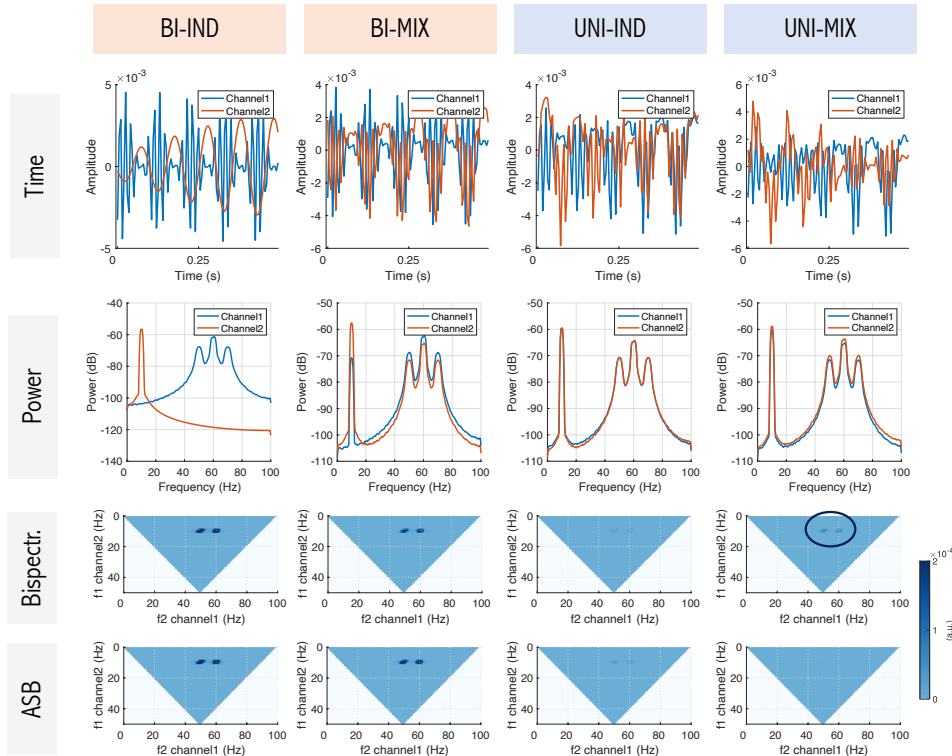


Figure 2: Overview of signals in the 2CHAN experiments. Shown are exemplary signals without the addition of noise. First row: excerpt of signal in time domain. Second row: power spectrum. Third row: full bispectrum. Fourth row: full anti-symmetrized bispectrum. Substantial bispectral energy is observed in the UNI-MIX case despite the absence of between-site PAC interactions (black circle).

by a mixing matrix \mathbf{M} : $\mathbf{d}_{\text{bivar}} = \mathbf{x} * \mathbf{M}$, with $\mathbf{x} = [\mathbf{x}_{\text{fc}}, \mathbf{x}_{\text{sc}}] \in \mathbb{R}^{N_t \times 2}$, and with

$$\mathbf{M} = \begin{bmatrix} 1 & 2(\beta - 0.5) \\ 2(\epsilon - 0.5) & 1 \end{bmatrix} \in \mathbb{R}^{2 \times 2}, \quad (22)$$

with β and ϵ representing two random parameters drawn from a uniform distribution on the open interval $(0, 1)$.

In the setting comprising two underlying signals with univariate PAC (2CHAN-UNI), we generated two independent univariate PAC signals \mathbf{p}_1 and $\mathbf{p}_2 \in \mathbb{R}^{N_t}$, representing the data of the two channels. To generate data of the first channel, we summed up the slow and fast oscillation:

$$\mathbf{p}_1 = \mathbf{x}_{\text{fn}} + \mathbf{x}_{\text{sn}}, \quad (23)$$

then divided the result by its Frobenius norm: $\mathbf{p}_{1n} = \frac{\mathbf{p}_1}{\|\mathbf{p}_1\|_2}$, and finally added channel noise:

$$\mathbf{p}_{1c} = \theta \mathbf{p}_{1n} + (1 - \theta) \mathbf{c}_{1n} \in \mathbb{R}^{N_t}. \quad (24)$$

Data for the second channel were generated analogously. Finally, we again mixed the two channels with the mixing matrix \mathbf{M} : $\mathbf{d}_{\text{univar}} = \mathbf{p} * \mathbf{M}$, with $\mathbf{p} = [\mathbf{p}_{1c}, \mathbf{p}_{2c}] \in \mathbb{R}^{N_t \times 2}$ (MIX).

We conducted experiments for the following SNR_cs: noise only ($\theta = 0$), -12 dB ($\theta = 0.2$), -4 dB ($\theta = 0.4$), 4 dB ($\theta = 0.6$), and 12 dB ($\theta = 0.8$). To quantify the effect of signal leakage on the different PAC metrics, we conducted all experiments once without mixing ($\beta = \epsilon = 0.5$, denoted as 2CHAN-BI-IND, 2CHAN-UNI-IND), and once with the additional random linear mixing of the two source channels (2CHAN-BI-MIX, 2CHAN-UNI-MIX).

The PAC analysis of the two-channel experiments follows the simulation flow described in Section 3.1 (1CHAN-UNI). Note that for both the true PAC score (PAC) and the PAC scores (PAC_{surr}) obtained from surrogate data, we estimated the coupling between the two time series in both directions, but always selected the larger PAC score of the two for further processing.

3.2.2. Performance evaluation

To assess whether the studied PAC detection pipelines are able to correctly detect the presence of bivariate (between-site) PAC in experimental setting 2CHAN-BI, we evaluated the TPR. Conversely, in setting 2CHAN-UNI, in which only univariate (within-site) PAC was simulated, we evaluated the true negative rate (TNR) to assess whether metrics correctly reject the hypothesis that the observed PAC originates from two different sources.

Every experiment was repeated for $D = 100$ times to obtain 100 p-values p_d . PAC is considered statistically significant for p-values below an α -level of 0.05. The TPR (for $\theta > 0$ and TNR (for $\theta = 0$) were calculated as follows:

$$TPR = \frac{1}{D} \sum_{d=1}^D c_d, \text{ with } c_d = \begin{cases} 1, & \text{if } p_d < \alpha \\ 0, & \text{otherwise} \end{cases} \quad (25)$$

$$TNR = \frac{1}{D} \sum_{d=1}^D 1 - c_d. \quad (26)$$

3.3. Whole-brain EEG experiments

To assess the extent to which the considered PAC estimation pipelines are also able to distinguish between- from within-site PAC in a practical setting involving source mixing, we next conducted a set of advanced EEG experiments (Figure 3). This included the presence of noise sources, source mix-

ing through a realistic EEG forward model, realistic preprocessing including source reconstruction, and the application of dimensionality reduction techniques. Further, we here varied the SNR and the number of ground-truth interactions to assess their influence on the sensitivity and specificity of the candidate PAC detection pipelines.

3.3.1. Data generation

We generated time series at a sampling rate of 200 Hz with a recording length of $N_t = 120\,000$ samples, amounting to 10 minutes duration. The slow and fast oscillations x_s and x_f were generated as in the two-channel experimental setup (see Section 3.2.1). Additionally, to make the signal more realistic, we here transformed x_s and x_f to a 1/f-shape before further processing. To this end, the signal was first Fourier-transformed. Subsequently, every value of the Fourier-transformed signal was divided by its corresponding frequency. Afterwards, the signal was transformed back to time domain by using an inverse Fourier transform.

In the *bivariate* PAC Experiments EEG-BI, we generated bivariate interactions between N_{I-bi} pairs of time series, as described in Section 3.2.1. We then added pink (1/f scaled) background noise as follows: For every interaction, we generated time series \mathbf{b}_1 and $\mathbf{b}_2 \in \mathbb{R}^{N_t}$, representing the background noise for the two sources. The background noise time series were then also divided by their 2-norms: $\mathbf{b}_{1n} = \frac{\mathbf{b}_1}{\|\mathbf{b}_1\|_2}$ and $\mathbf{b}_{2n} = \frac{\mathbf{b}_2}{\|\mathbf{b}_2\|_2}$.

We added the background noise to the slow and the fast oscillating signals,

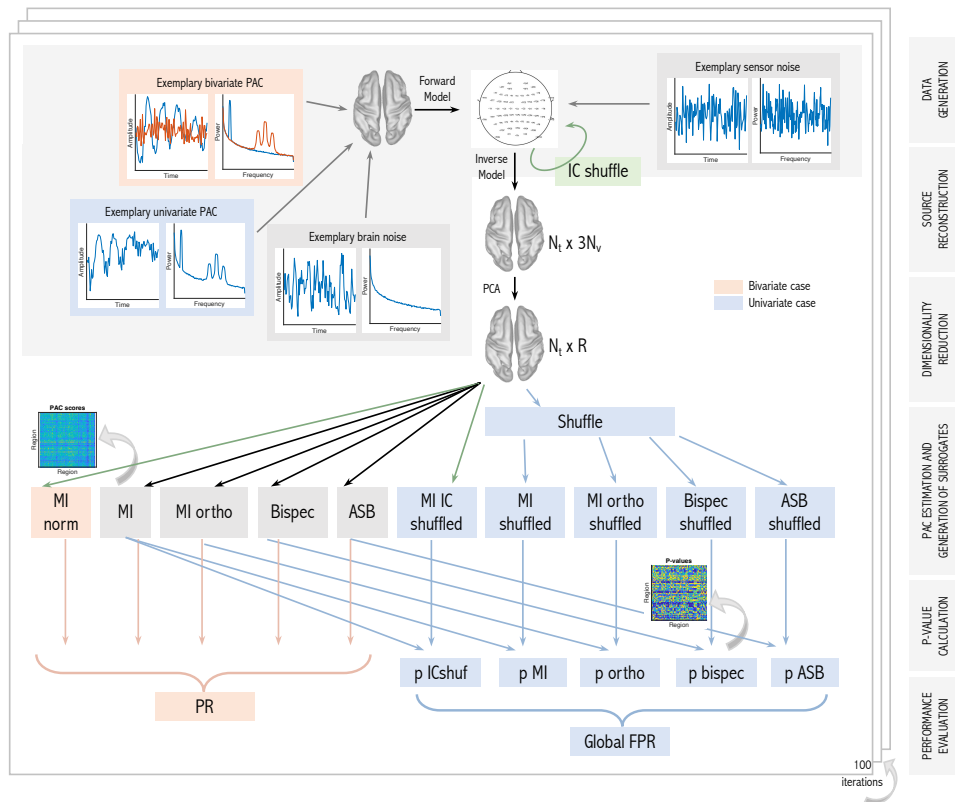


Figure 3: Structure of the whole-brain EEG simulation study consisting of the following steps: data generation, source reconstruction, dimensionality reduction, PAC estimation and generation of surrogates, p-value calculation, and performance evaluation. In case of genuine bivariate (between-site) simulated PAC, detection performance is evaluated with the percentile rank (PR). In the case of solely univariate (within-site) PAC, null distributions are generated and a p-value for every region combination is calculated. From this, we calculate the global false positive rate (global FPR).

respectively:

$$\mathbf{x}_{fb} = \gamma \mathbf{x}_{fn} + (1 - \gamma) \mathbf{b}_{1n} \in \mathbb{R}^{N_t}, \quad (27)$$

$$\mathbf{x}_{sb} = \gamma \mathbf{x}_{sn} + (1 - \gamma) \mathbf{b}_{2n} \in \mathbb{R}^{N_t}, \quad (28)$$

where $\gamma \in [0, 1]$ defines the signal-to-noise ratio on source level (SNR_s) and is fixed here to $\gamma = 0.6$.

In the *univariate* PAC experiments EEG-UNI, we generated N_{I-uni} univariate PAC time series by summing up the PA-coupled slow and fast oscillations to form a single signal, and by adding pink background noise as described above.

In both the bivariate and univariate PAC experiments, we additionally simulated activity of non-interacting sources—referred to as *brain noise*—using mutually independent random pink noise signals only without additional activity in the alpha band or any other specific frequency band.

3.3.2. EEG signal simulation

EEG forward modeling was carried out in Brainstorm (Tadel et al., 2011) using the ICBM152 anatomical head template, which is a non-linear average of the magnetic resonance (MR) images of 152 healthy subjects (Mazziotta et al., 1995). Within the ICBM152 anatomical model, $N_v = 1895$ dipolar sources were placed in the cortical gray matter half-way between the white matter—gray matter and gray matter—cerebro-spinal fluid interfaces. Each dipole thereby models the net primary electrical current elicited by a large population of pyramidal cortical neurons. A cortical parcellation according to the Desikan-Killiany atlas (Desikan et al., 2006) was used to assign each dipole to one of $R = 68$ regions. A set of $N_s = 97$ EEG sensors were placed on

the scalp following the standard BrainProducts ActiCap97 channel montage. The mapping from dipolar sources to EEG sensors was calculated with a three-shell boundary element (BEM) model using the OpenMEEG (Gramfort et al., 2010) package with the three shells representing the brain-skull, skull-skin and skin-air interfaces, respectively. The result is summarized in the *leadfield* matrix $L \in \mathbb{R}^{N_s \times 3N_v}$.

For the purpose of this simulation, a single ground-truth source time series was placed in each of the 68 regions of the DK atlas, where the location within each region was chosen at random. The spatial orientation of all sources was set to be perpendicular to the cortical surface at the given location. In the univariate PAC experiments, the regions in which the univariate PAC sources are placed were chosen randomly. In the bivariate PAC experiments, the region pairs in which the pairs of interacting PAC signals were placed were also chosen randomly, where we ensured that low and high-frequency components were not located within the same region. In all other regions of the DK atlas, a single brain noise source was placed. The following steps were described extensively in (Pellegrini et al., 2023). In brief, signal and brain noise sources were separately projected to the EEG sensor space using the lead field matrix. On sensor level, channel noise was generated as Gaussian white noise (c.f. Section 3.2.1), and mixed with the brain noise (brain noise to sensor noise ratio of 19 dB) to obtain the *total noise*. Afterwards, we summed up signal and noise with a predefined total SNR, denoted_t. We adjusted the default total SNR_t to 12 dB in the univariate PAC experiments, and to 0 dB in the bivariate PAC experiments. These different settings were chosen to create a challenging problem setting in both cases. As a last step,

to make the generated data more realistic, we high-pass filtered the generated sensor data with a cutoff of 1 Hz. The resulting time series on sensor level is here called $\mathbf{Q} \in \mathbb{R}^{N_t \times N_s}$.

If not indicated otherwise, all experiments with ground-truth bivariate PAC interactions had the following default settings:

- $\text{SNR}_t = 0 \text{ dB}$
- Number of PAC interactions: $N_{I-bi} = 3$.

All experiments simulating univariate PAC sources within individual regions had the following default settings:

- $\text{SNR}_t = 12 \text{ dB}$
- Number of PAC seed regions $N_{I-uni} = 1$.

In Experiment EEG-UNI-SNR, we assessed PAC detection performance as a function of SNR, considering SNRs of 0 dB, 7.4 dB, and 12 dB. The SNRs for Experiment EEG-BI-SNR was chosen to be lower to avoid ceiling effects in the results: here, we assessed the metrics' performances for SNRs of -7.4 dB, 0 dB, and 7.4 dB. In Experiment EEG-BI-INT and EEG-UNI-INT, we tested the influence of the number of ground-truth interactions and show results for 1, 3, and 5 interactions.

In the EEG-BI experiments, ground-truth interacting regions (two disjoint sets of region indices were drawn randomly from a uniform distribution between 1 and R in each iteration. In the EEG-UNI experiments, ground-truth seed region(s) containing the univariate PAC signal (seed region index uniformly drawn between 1 and R) were drawn randomly. Furthermore, the

ground-truth active voxel(s) within regions (uniformly drawn between 1 and the number of sources within the ground-truth region), brain noise and sensor noise, as well as the signal were generated based on (filtered) random white noise processes as described above.

3.3.3. EEG source reconstruction

The following steps and parameter choices build on the results of Pellegrini et al. (2023). We estimated the activity of the underlying dipolar electrical current sources by constructing linearly-constrained minimum variance (LCMV, Van Veen et al., 1997) beamformers $\mathbf{P} \in \mathbb{R}^{N_s \times 3N_v}$ and applying them to the sensor time series:

$$\hat{\mathbf{J}}_v = \mathbf{Q}\mathbf{P}, \quad (29)$$

with $\hat{\mathbf{J}}_v \in \mathbb{R}^{N_t \times 3N_v}$ representing the source-level time series. The result is one time series for each of the three spatial orientations of each dipole. To aggregate the reconstructed time series of all dipolar sources within one region, we performed singular value decomposition (SVD), and selected only the strongest SVD component for every region for further processing (c.f. Pellegrini et al., 2023). Let $\mathbf{J}_{v,r} \in \mathbb{R}^{N_t \times 3V}$, $r \in \{1, \dots, R\}$ denote the source time courses of V sources within the r -th single region. These time courses were aggregated into a single time series by projecting $\mathbf{J}_{v,r}$ onto its strongest SVD component using the filter $\mathbf{Y}_r \in \mathbb{R}^{3V \times 1}$:

$$\mathbf{J}_{\text{agg},r} = \mathbf{J}_{v,r}\mathbf{Y}_r \in \mathbb{R}^{N_t \times 1}. \quad (30)$$

Note that beamformers and PCA that were calculated on unfiltered data comprising both slow and fast signal components in each experimental run.

All region time courses $\mathbf{J}_{\text{agg},r}, r \in \{1, \dots, R\}$ were then concatenated into a matrix $\mathbf{J}_R \in \mathbb{R}^{N_t \times R}$, whose columns contain the single time courses $\mathbf{J}_{\text{agg},r}$ of all R regions.

3.3.4. PAC analysis

We included the same PAC metrics as in the two-channel experiments in the comparison. In the following, we describe how PAC metrics are applied in the bivariate and univariate whole-brain EEG experiments.

We calculated PAC scores between all region combinations. Note that for the orthogonalization method, we symmetrically orthogonalized all 68 region time series to each other before calculating the MI. Thus, \mathbf{X} in Eq.(11) now refers to the region time series \mathbf{J}_R and $R = 68$ denotes the number of regions.

Here we focus on the ability of the PAC estimation approaches to discriminate between- from within-site PAC in the current whole-brain *bivariate* PAC experiments. Therefore, we did not perform statistical testing for significant PAC like in the two-channel experimental setting. That is, instead of comparing PAC scores to null distributions obtained on permuted data, we directly evaluated the detection performance of PAC metrics with the percentile rank (PR; see Section 3.3.5). An exception was the surrogate data method of Shahbazi et al. (2010), which relies on statistical testing against a suitable null hypothesis, and whose usage is described in the next paragraph. Only in the EEG-UNI experiments, we did generate null distributions by permuting epochs, analogous to what is described for the two-channel experiments. We use the null distributions to calculate a p-value to assess the false positive rate of each approach (see Section 3.3.5).

Application of ICA-based surrogate data in whole-brain experiments. Rather than defining its own PAC metrics, the surrogate data approach of Shahbazi et al. (2010) is based on a comparison of observed FC scores against a distribution of FC scores obtained under the specific null hypothesis of independent sources. In order to evaluate the percentile rank for this approach, PAC scores were standardized using the estimated mean and standard deviation of the null distribution, and standardized PAC scores instead of ‘raw’ ones were compared to the ground truth. We generated a null distribution by applying Eq. (13) to the sensor time series, epoching the data on the independent component level, randomly permuting the order of the epochs separately for each IC, and projecting the thereby shuffled components back to sensor space by applying Eq. (14). Note that \mathbf{X} in Eq. (13) now refers to the EEG sensor time series \mathbf{Q} . From the surrogate sensor time series, we obtained surrogate source-level PAC scores by applying the same data processing steps as used for the original data including LCMV source projection, within region dimensionality reduction using PCA, and between-region PAC estimation using the MI. We repeated this procedure 100 times to obtain a null distribution of 100 MI scores consistent with a null hypothesis of zero between-site interactions. We used this null distribution in two different ways: in the bivariate PAC experiments, we normalized the obtained true MI scores of every region combination by subtracting the mean of the null distribution and dividing by its standard deviation to obtain MI_{norm} . In contrast, in the univariate PAC experiments, we used the null distribution to obtain a p-value to assess the false positive rate (see Section 3.3.5). PAC scores corresponding to p-values below $\alpha = 0.05$ were considered significant.

3.3.5. Performance evaluation

Each experiment was carried out 100 times. We use different metrics to evaluate the performance of different PAC estimators in the EEG-BI and EEG-UNI experiments, respectively. In the bivariate PAC experiments, we were interested to quantify each PAC metric's ability to detect the simulated ground-truth between-site PAC interactions. In the univariate PAC experiments, no between-site PAC was present. Here we were interested to quantify how prone PAC metrics are to still signal false positive between-site interactions. Please note that in both types of experiments, we only studied across-region PAC detection and do not evaluate the PAC metrics' abilities to detect univariate PAC within regions.

Percentile rank. In the presence of bivariate simulated PAC, we used the percentile rank (PR) to determine how accurately different PAC approaches discriminate regions pairs with ground-truth bivariate PAC from other region pairs. Every region–region combination was assigned a single real-valued FC score from every PAC estimation pipeline. In order to assess a pipeline's success, we first sorted all FC scores in descending order to obtain the rank vector $\mathbf{r} \in \mathbb{R}^{N_{I-bi}}$, where $N_{I-bi} \in \{1, 2, 3, 4, 5\}$ is the number of ground-truth interactions, and where the j th position of \mathbf{r} contains the index of the j th ranked connection. The PR was determined using this rank vector:

$$PR' = \frac{\sum_{i=1}^{N_{I-bi}} (1 - \frac{r_i}{F})}{N_{I-bi}}, \quad (31)$$

with $F = R^2 - R = 4556$ denoting the total number of PAC scores. The PR' was then normalized using the perfect-skill PR, PR_{ps} , and the no-skill PR,

PR_{ns} , and therefore takes values between 0 and 1:

$$PR_{ps} = \frac{\sum_i^{N_{I-bi}} \left(1 - \frac{i}{F}\right)}{N_{I-bi}} \quad (32)$$

$$PR_{ns} = \frac{\sum_i^{N_{I-bi}} \left(1 - \frac{F-i+1}{F}\right)}{N_{I-bi}} \quad (33)$$

$$PR = \frac{PR' - PR_{ns}}{PR_{ps} - PR_{ns}}. \quad (34)$$

We report all PR values rounded to the second decimal.

False positive rate. To define the global FPR, we divided the number of significant PAC interactions (across all region combinations) by the total number of PAC scores F :

$$FPR = \frac{\sum_{f=1}^F q_f}{F}, \text{ with } q_f = \begin{cases} 1, & \text{if } p_f < \alpha \\ 0, & \text{otherwise} \end{cases} \quad (35)$$

$$. \quad (36)$$

We evaluated the FPR separately for regions that are adjacent to the seed regions with the ground-truth univariate PAC signal, and for regions that are not adjacent to the seed regions. Further, we evaluated the two directions of PAC interactions separately. That is, we calculated the FPR both for PAC between the phase of the seed regions and the amplitude of the neighboring regions, and vice versa.

4. Results

4.1. Baseline experiment on univariate PAC detection

The baseline experiment assessed the performance of different PAC metrics and pipelines to detect univariate PAC. With this, we wanted to ensure

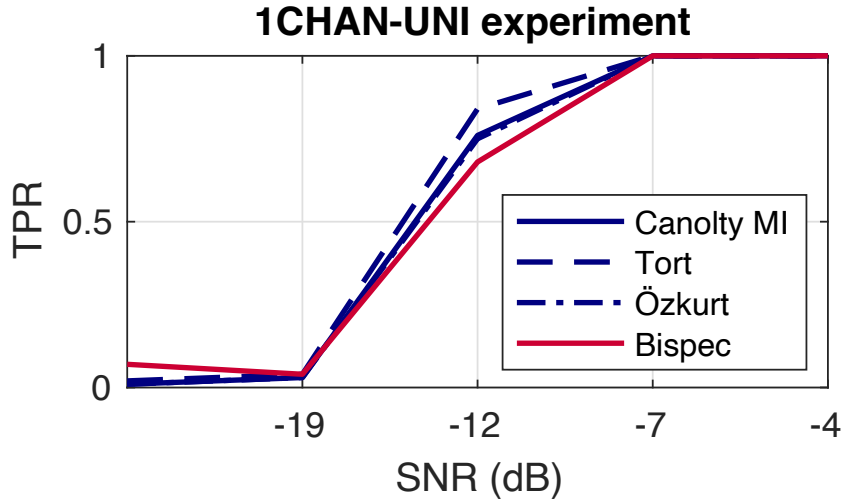


Figure 4: Result of the baseline (1CHAN-UNI) experiment on univariate PAC detection. Sensitivity of mean vector length modulation index Canolty et al. (2006), the two extensions of Tort et al. (2010) and Özkurt and Schnitzler (2011), and bispectrum for the detection of phase-amplitude coupling (PAC) as a function of the signal-to-noise ratio (SNR). PAC is simulated and measured between the slow and fast oscillation within a single channel.

that potential differences in the detection of genuine between-site PAC are not just due to different sensitivities to PAC per se. Figure 4 shows the result of the baseline experiment. We see that all metrics perform similarly well in detecting true within-channel PAC for our chosen filter settings and epoch lengths, with the bispectrum performing slightly worse and the MI by Tort et al. (2010) performing slightly better at -12 dB SNR. To avoid unnecessary high computational cost, we focused on the original MI metric by Canolty et al. (2006) in the following experiments and are not reporting results for the variants proposed by Tort et al. (2010) and Özkurt and Schnitzler (2011).

4.2. Two-channel experiments

We conducted two types of two-channel experiments: the first type involved true bivariate PAC between the two source channels (2CHAN-BI-IND and 2CHAN-BI-MIX) and the other type involved two source channels containing two independent univariate PAC times series 2CHAN-UNI-IND and 2CHAN-UNI-MIX). The ability to correctly detect the presence of PAC was tested for the modulation index (MI), MI calculated on orthogonalized channels (MI+ORTH), MI tested against surrogate data (MI+ICSURR), the bispectrum (BISPEC), and the anti-symmetrized bispectrum (ASB-PAC).

In Figure 5, we observe that all PAC measures perform well in terms of correctly detecting true bivariate PAC between the two channels. This is also true for random mixtures of the same two channels.

As expected, all PAC metrics avoid falsely detecting PAC almost perfectly in the univariate PAC experiment when there is no signal mixing. However, in case of signal mixing, most metrics indicate PAC in sufficiently high SNR environments. This could be erroneously interpreted as genuine between-channel PAC in practice, even though the PAC interaction stems from a single underlying source. Within the MI-based methods, MI+ICSURR performs best with a TNR of 0.30 for an SNR_t of 12 dB (TNR MI = 0.04, TNR BISPEC = 0.04, TNR ORTHO = 0.12 at 12 dB). The only metric that is largely unaffected by signal mixing is the ASB-PAC, which shows a TNR of at least 0.96 throughout all SNRs.

4.3. Whole-brain experiments

To assess the ability of the studied pipelines to distinguish between- from within-site PAC under realistic source mixing, we conducted additional ex-

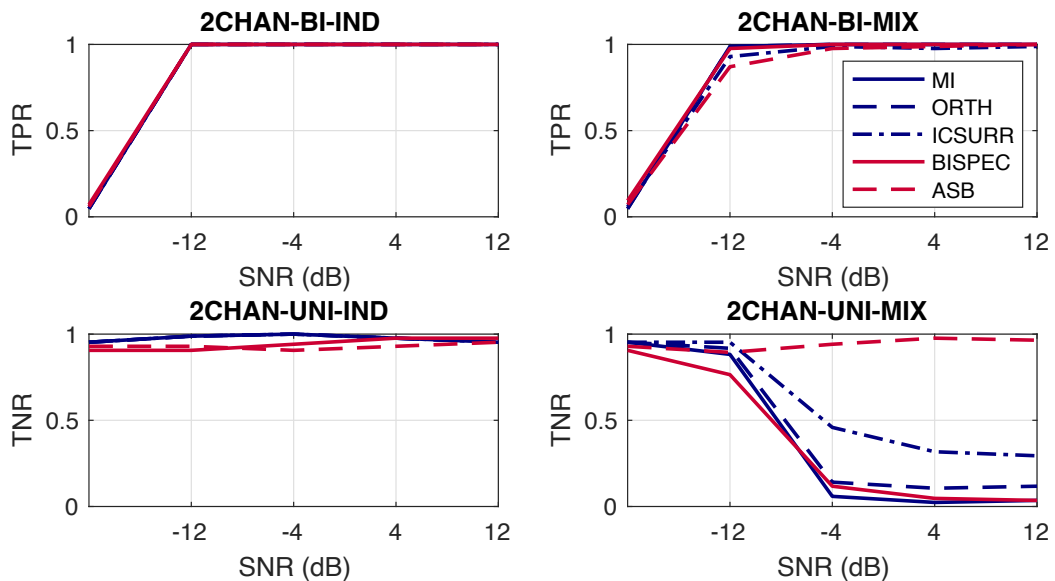


Figure 5: Performance of PAC metrics in two-channel experiments. Top: Simulation of two underlying signals with bivariate PAC without (left) and with (right) additional linear mixing; that is, presence of genuine across-site PAC. Bottom: Simulation of two underlying signals with univariate PAC without (left) and with (right) additional linear mixing; that is absence of genuine between-site PAC. TPR = true positive rate, TNR = true negative rate.

periments on simulated whole-brain EEG data using a realistic volume conductor model.

4.3.1. EEG-BI: detection of true between-site PAC

Experiment EEG-BI. In Experiment EEG-BI, we evaluated the performance of five different PAC metrics in distinguishing genuine ground-truth between-region PAC interactions from within-region PAC as well as the absence of any PAC interactions. Figure 6 shows the results of Experiment EEG-BI. We again see that the bispectral metrics perform slightly better than the MI. Importantly, the ASB-PAC does not perform worse than the bispectrum without anti-symmetrization. However, both MI extensions, MI+ORTHO and overall ICSURR, perform worse than the original MI. We discuss this result in Section 7. In the following experiments with bivariate ground-truth PAC, we focus on the MI and the ASB-PAC.

Experiment EEG-BI-SNR: effect of SNR. In Experiment EEG-BI-SNR, we investigated the effect of the SNR_t on the across-region PAC detection performance in the whole-brain EEG setting. In Figure 7, we show the percentile rank attained by MI, BISPEC and ASB-PAC for SNR_t s of -7.4 dB, 0 dB, and 7.4 dB, respectively. As expected, we see that the performance of all metrics decreases for low SNR_t .

Experiment EEG-BI-INT. How does the complexity of interaction patterns affect between-site PAC detection performance? To investigate this, we varied the number of PAC interactions in the ground-truth data in Experiment EEG-BI-INT. In Figure 8, we see that MI, the conventional bispectrum, and

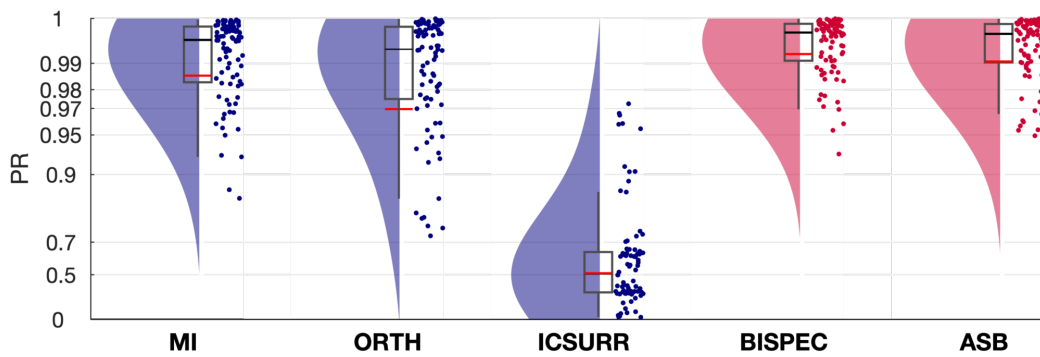


Figure 6: Comparison of different phase–amplitude coupling (PAC) metrics in a whole-brain EEG experiment (Experiment EEG-BI). The dataset encompasses three ground-truth PAC interactions. Pink background noise was introduced to the oscillations, and non-interacting sources were represented using random pink noise signals. EEG signal simulation was conducted using the ICBM152 anatomical head template. Ground-truth sources were allocated in 68 regions of the DK atlas and projected to 97 EEG sensors via a forward model. The synthesized data, comprising signal and noise, had a total SNR of 0 dB and were high-pass filtered at 1 Hz. An LCMV beamformer and principal component analysis were applied to the data, yielding region time courses that underwent PAC metric analysis. Performance was evaluated based on the percentile rank (PR) for the detected bivariate PAC interactions. Red and black lines indicate the mean and median percentile rank (PR), respectively. The boxcar marks the 2.5th and 97.5th percentiles. Note the logarithmically spaced Y-Axis.

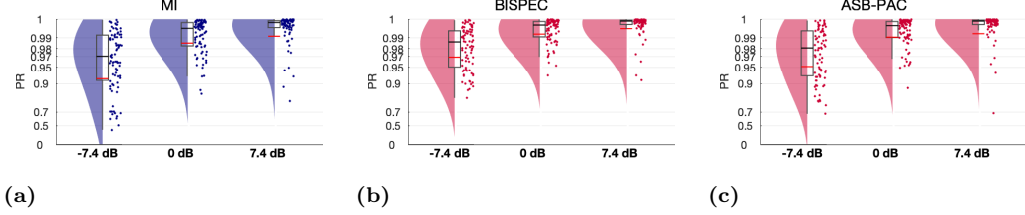


Figure 7: Performance in correctly detecting between-site phase-amplitude coupling as a function of signal-to-noise ratio (Experiment EEG-BI-SNR). Red and black lines indicate the mean and median, respectively. The boxcar marks the 2.5th and 97.5th percentile. Note the logarithmically spaced Y-Axis. It can be seen that the ability to detect true between-site PAC deteriorates in the presence of stronger non-interacting noise signals. MI: Modulation Index, BISPEC: Bispectrum, ASB: Anti-symmetrized bispectrum.

ASB-PAC perform worse for many ground-truth interactions than for few interactions.

Note that, despite using a normalized version of the PR metric, it is not possible to objectively compare PR scores obtained for different numbers of true interactions. While PR distributions are nearly uniform when only one interaction is simulated, they tend to become more concentrated around 0.5 resembling Gaussian and super-Gaussian distributions with increasing kurtosis for increasing numbers of interactions (Pellegrini et al., 2023).

4.3.2. EEG-UNI: univariate within-site PAC

In Experiments EEG-BI, we observed that bispectral methods perform equally as or superior to the MI at detecting ground-truth bivariate between-region PAC. In Experiment EEG-UNI, we assess the same metrics' ability to reject spurious between-region PAC in the univariate PAC setting within

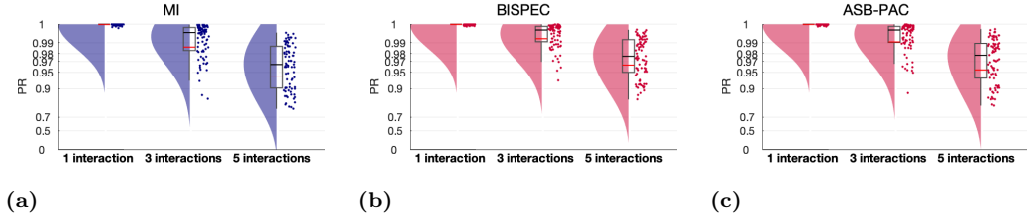


Figure 8: The performance of correctly detecting between-site phase–amplitude coupling depends on the the number of ground-truth PAC interactions (Experiment EEG-BI-INT). Red and black lines indicate the mean and median, respectively. The boxcar marks the 2.5th and 97.5th percentile. Note the logarithmically spaced Y-Axis. MI: Modulation Index, BISPEC: Bispectrum, ASB: Anti-symmetrized bispectrum.

the whole-brain EEG experimental setting.

Two directions of spurious PAC are conceivable: First, there may be PAC between the phase of the seed region, containing the univariate within-region PAC, and the amplitude of another region. Second, there may be spurious PAC between the amplitude of the seed region and the phase of other regions. It may be that the effect of signal mixing depends on the direction of the coupling. Therefore, we here show the results for both directions.

Further, we distinguish between spurious interactions from the seed region to neighbors and to non-neighbors, since we expect a more extreme impairment for interactions between regions that lie close together and are therefore more affected by source leakage. In Figure 9, we show all 2x2 combinations of these parameters (seed = phase vs. seed = amplitude, neighbors vs. non-neighbors).

Experiment EEG-UNI. In Experiment EEG-UNI, we compared the different PAC metrics for the default experimental setting. In Figure 9a, we show the

FPR associated with the spurious detection of between-site coupling between the phase of the ground-truth seed region containing univariate PAC and the amplitude of the neighboring regions. We observe that the ASB-PAC detects by far the fewest false positives. The MI and the bispectrum without anti-symmetrization cannot eliminate the source leakage effect and detects some false positives. While the ICSURR method seems to improve the MI, orthogonalization results in a very high FPR.

Figure 9b shows the FPR for measuring spurious PAC between the amplitude of the ground-truth seed region containing univariate PAC and the phase of neighboring regions. We see a similar pattern as in Figure 9a. However, both the MI and overall the bispectrum without anti-symmetrization perform even worse. The ASB-PAC detects by far the fewest false positives also in this case.

As expected, these effects are far less pronounced for interactions between the ground-truth seed regions and non-neighboring regions (Figures 9c and 9d). This indicates that the observed differences between the robust ASB-PAC, the non-robust MI and the bispectrum without anti-symmetrization indeed arise from the source leakage that is most pronounced in regions that are adjacent to each other.

Experiment EEG-UNI-SNR. In Experiment EEG-UNI-SNR, we investigated how the FPR depends on the SNR, asking: is the ability to reject spurious between-region PAC compromised in low-SNR settings?

In Figure 10, we show the FPR for MI, BISPEC, and ASB-PAC for SNRs of 0 dB, 7.4 dB, and 12 dB. We see that, while the FPR is slightly elevated at 0 dB in case of the MI and bispectrum, the high specificity of the ASB is

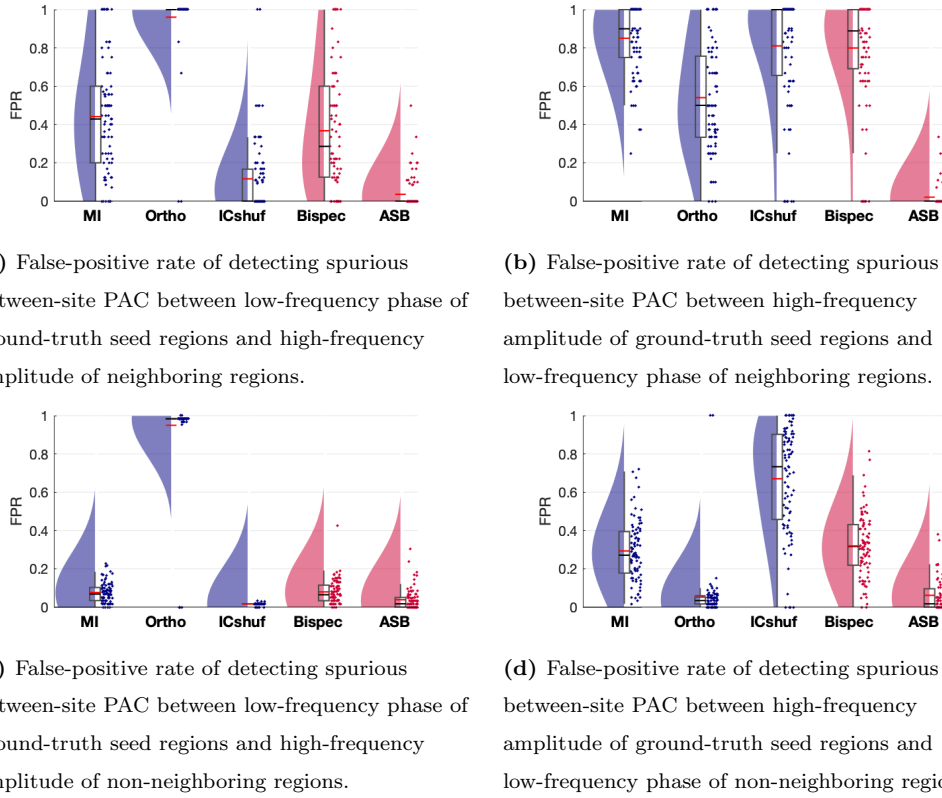


Figure 9: Comparison of different phase–amplitude coupling (PAC) metrics in their ability to avoid detecting spurious between-site PAC (Experiment EEG-UNI). (a/b) Between seed regions and neighboring regions. (c/d) Between seed regions and non-neighboring regions. Red and black lines indicate the mean and median percentile rank (PR), respectively. The boxcar marks the 2.5th and 97.5th percentile.

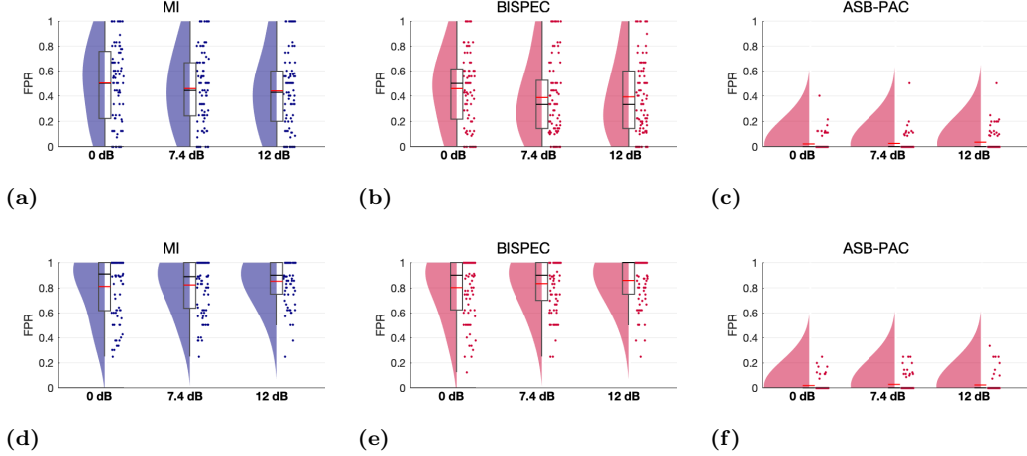


Figure 10: Ability of different PAC estimation pipelines to reject spurious between-site PAC in different signal-to-noise (SNR) settings (Experiment EEG-UNI-SNR). (a) to (c): Rate of false-positive detections of between-site PAC detections between the phase of low-frequency signals at ground-truth seed regions and the amplitude of high-frequency signals at neighboring regions. (d) to (f): Rate of false-positive between-site PAC detections between the amplitude of low-frequency signals at ground-truth seed regions and the phase of high-frequency signals at neighboring regions. Red and black lines indicate the mean and median, respectively. The boxcar marks the 2.5th and 97.5th percentile. MI: Modulation Index, BISPEC: Bispectrum, ASB: Anti-symmetrized bispectrum.

not compromised at low SNR settings.

Experiment EEG-UNI-INT. In Experiment EEG-UNI-INT, we compared the ability to avoid detecting spurious between-region PAC for different numbers of ground-truth univariate within-site interactions. In Figure 11, we see that the performance of the MI and the bispectrum is slightly compromised for multi-interaction settings. Conversely, the high performance of ASB-PAC does not depend on the number of ground-truth interactions.

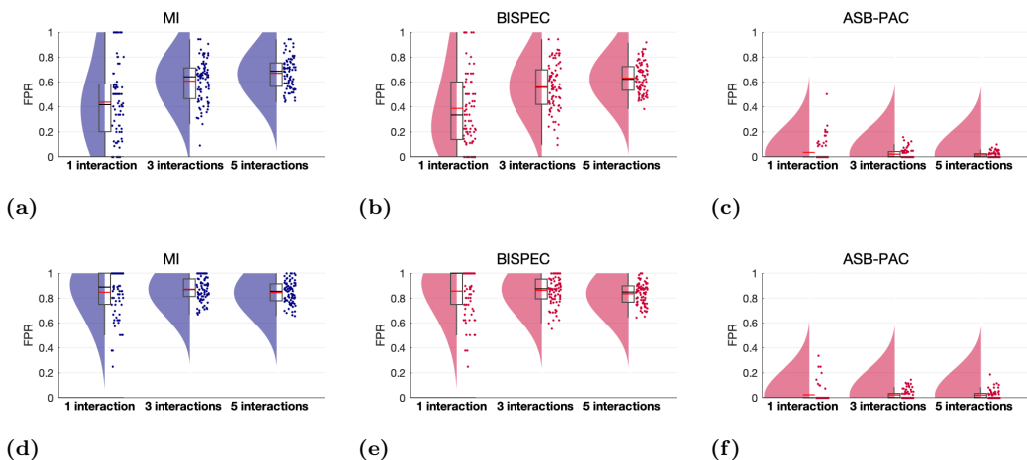


Figure 11: Ability of different PAC estimation pipelines to reject spurious between-site PAC for different number of ground-truth univariate PAC seed regions (Experiment EEG-UNI-INT). (a) to (c): Rate of false-positive detections of between-site PAC between the phase of low-frequency signals at ground-truth seed regions and the amplitude of high-frequency signals at neighboring regions. (d) to (f): Rate of false-positive detections of between-site PAC between the amplitude of low-frequency signals at ground-truth seed regions and the phase of high-frequency signals at neighboring regions. Red and black lines indicate the mean and median, respectively. The boxcar marks the 2.5th and 97.5th percentile. MI: Modulation Index, BISPEC: Bispectrum, ASB: Anti-symmetrized bispectrum.

5. Exploratory analysis of PAC in motor imagery

To demonstrate the utility of the ASB-PAC in real EEG data, we present an exploratory analysis of PAC in motor imagery. The Berlin arm of the VitalBCI study (Blankertz et al., 2010; Sannelli et al., 2019) involved 39 participants who took part in an experiment where, among other tasks, they imagined performing a movement with either their left or right hand (referred to as the Motor Imagery Calibration set; MI-Cb 1-3).

Motor imagery (MI) is a mental simulation of movement (Neuper et al., 2005). It has been shown that it induces neural activity in primary sensory and motor areas that is similar to activity induced by real movements and that can be measured by EEG (Scherer and Vidaurre, 2018). Movement-related EEG responses include event-related potentials (ERPs, e.g., Jongsma et al., 2013) and event-related desynchronization or synchronization (ERD/S Scherer and Vidaurre, 2018) of specific oscillations. For example, it has been shown that motor imagery of hand movements result in an ERD in the μ and β frequency band (Scherer and Vidaurre, 2018). Motor imagery may also be reflected in functional connectivity patterns, as several studies have shown (Vidaurre et al., 2020; Pellegrini et al., 2023).

It is conceivable that also PAC may emerge during motor imagery, reflecting processes of cognitive integration and communication during the planning of the movement. Technically, bivariate, between-site, PAC may also arise from the co-occurrence of both ERP and ERD/S phenomena as a response to the presentation of a stimulus. On the other hand, univariate, within-site, PAC could emerge as an ubiquitous phenomenon that reflects non-linear processes in the data generation, which manifest in specific non-sinusoidal wave

shapes of brain oscillations and non-Gaussian distributions. Such univariate PAC coupling can also occur due to non-zero mean of oscillations where for instance the amplitude modulation of alpha oscillations would mimic PAC (Studenova et al., 2022). Thus, it is an interesting question whether and between which sites PAC occurs during motor imagery. Furthermore, if PAC is observed, one may ask whether the observed phenomenon has an interpretation as an interaction between distinct brain regions (between-region PAC) or could be explained by single individual PAC sources (within-region PAC). Conversely, if PAC is observed due to a co-occurrence of ERP and ERD/S, it is of interest whether these are potentially elicited by the same sources or provably come from distinct generators.

In every trial of the VitalBCI experiment, a visual stimulus displaying a fixation cross accompanied by an arrow indicating the task (i.e., left or right motor imagery) was shown. Four seconds later, the stimulus disappeared, and the screen remained black for 2 seconds. Subjects were asked to perform motor imagery of the respective hand for as long as the arrow was present on the screen. Each subject completed 75 left and 75 right MI trials. EEG data were recorded using a 119-channel whole-head EEG system with a sampling rate of 1000 Hz (see Blankertz et al., 2010; Sannelli et al., 2019, for further details).

For the analysis, we used the ROIconnect plugin³ (Pellegrini et al., 2023) in combination with EEGLAB. We used a standard set of 90 EEG channels covering the whole head. Further, we selected 26 subjects for our analyses.

³<https://github.com/sccn/roiconnect>

The subject inclusion criteria were based on previous studies that demonstrated successful classification between left and right motor imagery conditions using machine learning methods (“Category I” in Sannelli et al., 2019). Prior to the analysis, the data underwent several preprocessing steps, including filtering (1 Hz high-pass filter, 48–52 Hz notch filter, and 45 Hz low-pass filter, all implemented using zero-phase forward and reverse second-order digital Butterworth filters), as well as subsampling to 100 Hz. Artifactual channels were identified through visual inspection of the power spectrum and the topographical distribution of alpha power. On average, 1.19 channels (ranging from zero to five per participant) were found to be artifactual and were subsequently interpolated using spherical scalp spline interpolation. A leadfield was computed using the Colin27 5003 Standard-10-5-Cap339 template head model (5003 voxels, standard 10-5 channel positions), which is a preexisting component of the EEGLAB toolbox. Subsequently, the data were cut into segments ranging from 1 to 3 seconds after the start of each stimulus presentation and separated into left and right motor imagery trials. For further analysis, only the right-hand motor imagery trials were used. To project sensor data to source level, we used an LCMV filter which was constructed on the same sensor data. Finally, we aggregated the multivariate source time series within regions using PCA and selected the strongest PC per region (see Pellegrini et al., 2023).

Previous research suggests that functional connectivity is modulated in motor imagery (Vidaurre et al., 2020; Pellegrini et al., 2023) with especially the sensori- and motor cortices being involved (Scherer and Vidaurre, 2018). However, PAC between the different involved areas has never been inves-

tigated before with robust metrics. In this study, we selected the left and right pre- and post-central cortices as regions of interest, as this is where the sensori- and motor areas are located.

In the following analysis, we addressed the following questions:

1. Is motor imagery characterized by within-site PAC during in the sensori- and motor cortices?
2. Is motor imagery also associated with genuine between-site PAC between sensori- and motor cortices, indicating a role of PAC as a mechanism of distant brain communication in MI?
3. If PAC as detected by the conventional bispectrum is observed, does it vanish when using a robust PAC metric, i.e., the ASB-PAC? We hypothesized that the differences between the between-site PAC estimates obtained by the uncorrected bispectrum and the ASB-PAC are more pronounced for regions that lie close together, in contrast to regions that lie on different hemispheres.

To this end, we estimated PAC in three ways:

- Within-region PAC measured with the conventional bispectrum (BIS-PEC).
- Between-region PAC measured with the conventional bispectrum (BIS-PEC).
- Between-region PAC measured with ASB-PAC.

Since previous research found that motor imagery is mostly reflected in the μ and β bands, we calculated bispectra between slow oscillations of 1 to 12 Hz,

and fast oscillations between 1 and 50 Hz (both with 1 Hz resolution). Since Fourier coefficients can only be evaluated up to the Nyquist frequency in a meaningful way, and the third term of the bispectrum includes the sum of the slow and fast oscillation frequencies, our analyses had to be restricted to frequency combinations whose sum did not exceed the Nyquist frequency. To ensure that the fast oscillation frequency carrying the amplitude envelope is significantly higher than the slow oscillation frequency carrying the phase, and to avoid strong confounds by interactions of the slow oscillation with its second and third harmonic, we constrained our analyses to fast oscillation frequencies whose frequency was at least three times higher than the frequency of the corresponding slow oscillation.

To test whether the observed PAC scores are significantly different from chance levels, we employed the permutation-based statistical approach as in the simulations (see Section 2.4). In brief, for each observed PAC score, we calculated the same bispectral metrics for randomly across epochs permuted Fourier coefficients to obtain samples of a null distribution consistent with the null hypothesis of no PAC interaction (see Eq. 8). We generated 5000 samples of the null distribution and subsequently evaluated for how many of the surrogate samples the estimated PAC value exceeded the PAC value obtained on the original data (see Eq. 9). To aggregate the resulting p-values over subjects, we employed Stouffer's method (Dowding and Haufe, 2018).

Figure 12a shows frequency combinations with significant PAC as estimated with the conventional bispectrum without anti-symmetrization. We observe significant within- as well as between-region PAC between the phase of low-frequent oscillations and the amplitude of beta and gamma oscillations.

tions across many frequency combinations and between all ROIs. This leads to the question to what extent the observed between-region effects indeed reflect underlying coupling between distinct brain areas as opposed to non-linear properties of single brain sources.

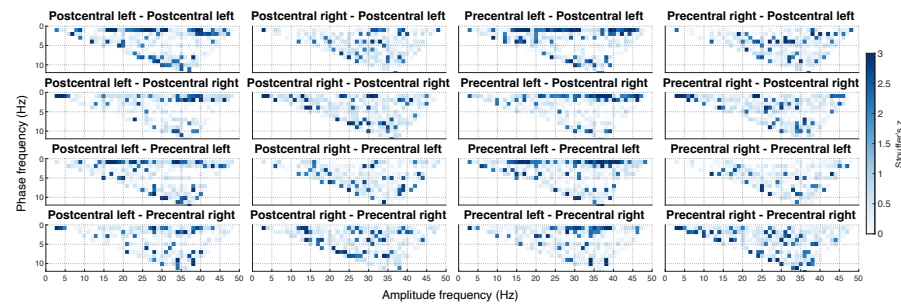
Figure 12b shows corresponding results for ASB-PAC. We clearly see that the observed PAC between regions in the same hemisphere vanishes when employing the anti-symmetrization. This absence in comparison to Figure 12a suggests that part of the between-region PAC implicated by the original bispectral metric in fact cannot be explained by genuine between-site interactions and may instead results from signal spread between the pre- and post-central cortices of the same hemisphere. In contrast, inter-hemispheric PAC effects were even more pronounced when assessed through ASB-PAC as compared to the conventional bispectrum. This may speak to a favourable cleaning effect of the anti-symmetrization by which signal contaminations attributable to signal spread are effectively removed.

Matlab code of the analyses presented in this section is provided under⁴.

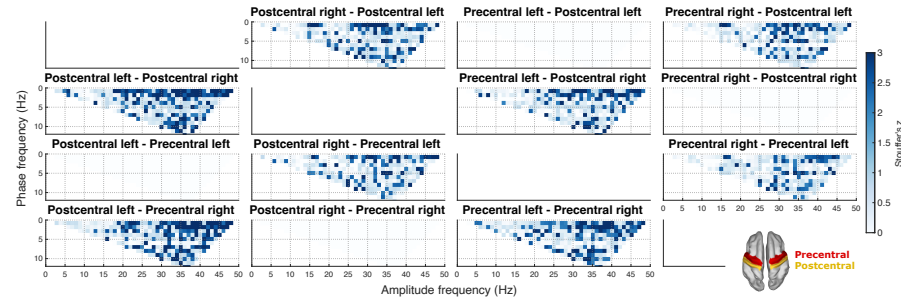
6. EEGlab plugin for bispectral PAC estimation

ROIconnect is a freely available open-source EEGLAB plugin that provides a suite of signal processing methods proposed in the literature to estimate FC between regions of interests (ROIs). We first introduced the toolbox in Pellegrini et al. (2023), describing basic features including source reconstruction techniques, dimensionality reduction within regions, region-based

⁴<https://github.com/fpellegini/MotorImag>



(a) Within- and between-site PAC as assessed by the bispectrum without anti-symmetrization.



(b) Between-site PAC as assessed by the anti-symmetrized bispectrum (ASB-PAC).

Figure 12: Phase-amplitude coupling (PAC) within and between left and right postcentral and precentral cortices during motor imagery of the right hand. Displayed are z-scores resulting from Stouffer's method of combining subject-level p-values. In both figures, only statistically significant ($p < 0.05$) effects are drawn opaque. The thumbnail on the bottom right of (b) shows the cortical localization of the two regions of interest.

power estimation with optional 1/f correction and estimation of region-based 1/f slope, robust inter-regional linear FC estimation, as well as various options to visualize power and FC. All functions can be accessed through the EEGLAB GUI or the command line. As an EEGLAB plugin, ROIconnect has access to core EEGLAB functions for importing and preprocessing EEG data as well as for calculating the leadfield and the source model. The toolbox is available on GitHub under⁵ and is installable through the EEGLAB GUI extension manager. In the following section, we describe advanced features and main updates to the toolbox resulting from the outcomes of this study.

6.1. Phase-amplitude coupling

Our results suggest that the bispectrum is a suitable method to detect PAC. Further, we observed that the ASB robustly detects between-site PAC in the presence of volume conduction considerably better than the conventional bispectrum or methods based on the Modulation Index. To this end, we implemented functions for robust estimation of (within- and between-region) PAC based on the bispectrum, and for between-region PAC based on the ASB.

The `pop_roi_connect` function of ROIconnect allows users to estimate PAC between two frequencies or frequency bands, generating bispectral estimates for the required region-region-frequency-frequency combination. The number of ROIs can be predefined by the user. Beyond PAC, this function can also be utilized for other functional connectivity metrics calculations.

⁵<https://github.com/sccn/roiconnect>

6.2. Statistics

A statistics mode is provided for assessing the statistical significance of the estimated FC metrics using a permutation-based approach. For bispectral connectivity metrics, we implemented the method used in this study, where a surrogate distribution sample is obtained by randomly permuting the epochs of a channel. The cross-bispectrum is then computed on the shuffled time series.

Statistical analysis of FC metrics is available through `pop_roi_connect` by activating the statistics mode. Additionally, the resulting p-values can be visualized as cortical surface topographies for a selected frequency or frequency band.

7. Discussion

In this study, we addressed potential limitations of existing PAC metrics, such as the MI and bispectrum, in assessing genuine between-site PAC and their vulnerability to signal mixing. We evaluated the effectiveness of three strategies, namely the ASB-PAC, MI with orthogonalization, and the IC surrogate approach, to enhance the robustness of the conventional PAC metrics. Furthermore, we explored the influence of the SNR and the number of ground-truth interactions on PAC detection accuracy.

We introduced a minimal two-channel experimental setting, which allowed us to quantify and compare the performance of various PAC metrics in correctly distinguishing the presence of ground-truth between-channel PAC from univariate PAC observed in the same channel pairs but originating from single sources. We identified ASB-PAC to be the only PAC metric that is able

to consistently reject spurious between-channel PAC in a setting with two independent but mixed univariate PAC time series, while also being able to detect genuine ground-truth bivariate (between-site) interactions with high sensitivity. In a more complex whole-brain EEG-like experimental setup, we confirmed the excellent performance of ASB-PAC in both cases: it robustly detected ground-truth inter-regional PAC in low to moderate noise settings. Conversely, in the exclusive presence of univariate PAC sources, ASB-PAC attained a low false-positive rate, whereas other metrics were characterized by the detection of many spurious interactions.

Spurious between-site PAC is a result of local source leakage

False-positive between-site PAC was more frequently detected between neighboring regions in comparison to non-neighboring regions. This is an expected result since so-called source leakage occurs predominantly between regions that lie close together. This can also be seen in Figure S1, which shows that there is a higher correlation between the time courses of a seed region and its neighbors compared to non-adjacent regions. This is then also reflected in higher but spurious PAC (Figure S2).

We found more spurious PAC between the amplitude of the fast oscillation in the seed PAC region and the phase of the slow oscillation in the neighboring regions than vice versa. This can be explained by the comparably higher power or SNR of the univariate PAC signal at low frequencies due to the applied 1/f scaling (see Section 3.3.1). The higher power leads to more source leakage for the slow oscillation than for the fast oscillation. Therefore, false-positive between-region PAC is more likely to be observed between the phase of this leaked slow oscillation and the fast oscillation-amplitude measured in

the seed region. We investigated this in a single whole-brain experiment (univariate PAC, all parameters set to default), where we assessed the correlation between the time courses of the slow and fast oscillation of the seed region and the corresponding slow and fast oscillation of the neighboring regions, respectively (see Figure S1). We found a mean absolute Pearson correlation of $r = 0.42$ for the slow oscillation, but a correlation of only $r = 0.22$ for the fast oscillation, which shows that the slow oscillation leaked more from the seed region into the neighboring regions than the fast oscillation due to its higher SNR_t.

Physiological interpretation of ASB-PAC

Note that, while the bispectral index $\text{PAC}_{k,m}^{\text{B}}(f_{\text{slow}}, f_{\text{fast}}) = 0.5 \cdot |B_{k,m,m}(f_1, f_2^a)| + 0.5 \cdot |B_{k,m,m}(f_1, f_2^b)|$ is a valid characterization of PAC, this is not necessarily the case for the difference measure $\text{PAC}_{k,m}^{\text{ASB}}(f_{\text{slow}}, f_{\text{fast}}) = B_{[k,m,m]}(f_1, f_2) = 0.5 \cdot (B_{k,m,m}(f_1, f_2^a) - B_{m,k,m}(f_1, f_2^a)) + 0.5 \cdot (B_{k,m,m}(f_1, f_2^b) - B_{m,k,m}(f_1, f_2^b))$ meaning that there might in general be no real-world PAC signal whose bispectrum is PAC^{ASB} . Specifically, the correction terms $B_{m,k,m}(f_1, f_2^a)$ and $B_{m,k,m}(f_1, f_2^b)$ correspond to interactions between a signal x_m at frequencies f_1 and $f_1 + f_2^{a/b}$ with another signal x_k at frequencies $f_2^{a/b}$, respectively, which, as such, are not PAC interactions. One may thus wonder what it means to subtract $B_{m,k,m}$ from $B_{k,m,m}$, and whether the subtraction could potentially lead to the removal or cancellation of neurophysiological information of potential interest. Here we argue that this is unlikely, as nonlinear interactions between $B_{m,k,m}(f_1, f_2^a)$ and $B_{m,k,m}(f_1, f_2^b)$ as described above are not expected to occur regularly in the brain. On the other hand, such interactions provably emerge as a result of source mixing in the presence of

a source with within-site PAC. In such cases, it is beneficial to remove the leakage artifact picked up by $B_{m,k,m}(f_1, f_2^a)$ and $B_{m,k,m}(f_1, f_2^b)$, whereas in cases without substantial leakage, both terms are expected to be negligible and thus their removal is not expected to influence the ASB-PAC. This consideration is confirmed by our numerical experiments, where the sensitivity (as measured by the PR) of the ASB-PAC in the bivariate PAC setting is comparable to that of the original bispectrum while a consistently low FPR is attained in the presence of solely univariate ground truth PAC interactions throughout all mixing proportions and SNRs.

A situation in which what we call genuine between-site PAC, as characterized by ASB-PAC, still has ambiguous interpretations is when one signal with univariate PAC is reflected in two channels with different constant time delays. The resulting between-channel PAC cannot be explained by linear mixing as a volume conduction or source leakage artifact. Yet, one may argue that the simplest and thus more likely mechanism of information transfer in this setting is just a mere delayed forwarding of the broad-band signal than an intricate phase-amplitude coupling between distinct frequency bands. To test for such simpler hypotheses, it can be advisable to additionally test for stable non-zero phase delays between channels either in the low frequency band, the high frequency band, or both. This can be achieved using established metrics based on the cross- or bispectrum (Nolte et al., 2004; Haufe et al., 2013; Winkler et al., 2016).

Orthogonalization and ICA-based surrogates cannot distinguish within- from between-site PAC

Both orthogonalization (Colclough et al., 2015; Hipp et al., 2012) and surrogate data approaches perturbing the data at the level of independent components (Shahbazi et al., 2010) have been proposed as general purpose strategies to remove artifacts of volume conduction from M/EEG data and subsequent functional connectivity analyses. Thus, it may seem worthwhile to assess the ability of these approaches to distinguish genuine between-site PAC from PAC that is measured between two different sites but is inherently caused by within-site PAC of a single sources whose signal leaks into both sites. Our experimental results, however, demonstrate that both the orthogonalization approach and the ICA-based surrogates do not improve the performance of the MI in terms of detecting the presence of across-region PAC. Orthogonalization even worsens the performance of the original MI metric in the whole-brain experiments. The use of ICA based surrogates seems to provide an improvement in certain simple setups such as the two-channel experiments with source mixing but not in more complex scenarios with larger numbers of channels.

Here we provide arguments for the suboptimal behavior of both methods for the studied problem. Both approaches decompose the sensor data into components that are orthogonal and (in case of ICA-based surrogates) “maximally” statistically independent from another. Here statistical independence is typically achieved by maximizing non-Gaussianity based on the argument that mixtures of independent signals (e.g. due to volume conduction) are closer to be Gaussian distributed than the unmixed signals. The

idea of the ICA-based surrogate data approach is to remove any residual functional connectivity at the component level by randomly shifting component time course relative to each other. When projecting the shifted components back to sensor space, surrogate data complying with the null hypothesis of zero source-level FC are hoped to be obtained, which can be tested against. However, this reasoning only applies to FC metrics that are strictly bi- or multivariate. Cross-frequency interactions such as PAC, which can emerge within single univariate time series, are likely to be retained in single independent components, and are thus preserved even under random shifts of the components relative to each other. We can easily understand that exactly that happens for univariate PAC sources, whose individual slow and fast-oscillation spectral components are Gaussian distributed by construction, but the summation of which is (by virtue of the higher-order PAC interaction) super-Gaussian. Thus, ICA algorithms aiming to maximize non-Gaussianity have a strong incentive to retain univariate PAC signals in single components rather than splitting them into slow- and fast-oscillation parts. We confirmed this behavior by investigating power spectra of the ICs, calculated from sensor-level activity in the EEG-UNI experiment in one simulation run. We found that a large number of ICs contained both the low-frequency peak and the high-frequency peak with the two side lobes (Figure S3). Consequently, permuting the components does not create an adequate null distribution. Spatio-spectral decomposition (SSD, Nikulin et al., 2011) could be a more suitable approach to overcome this problem. In contrast to ICA, it is designed for maximizing the signal power at specific frequencies while suppressing signal power at other frequencies. The method could be used to force

the slow and fast oscillation into two different components, and permutation could then result in a more appropriate null distribution. The proposition of SSD-based surrogates as a novel methodology is, however, beyond the scope of this study. Using ICA decomposition and PAC estimation, Gong et al. (2021) showed that the strength of cortical PAC between the phase of beta oscillations and the amplitude of high-frequency gamma activity was increased in patients with Parkinson's disease compared to healthy participants. Moreover, PAC also predicted the severity of motor deficits measured with the part 3 of Movement Disorder Society Unified Parkinson's Disease Rating Scale. Importantly, this prediction was only possible when the phase and amplitude of the corresponding PAC oscillations was estimated with spatially distinct independent components but not for the PAC within the same components. A validation of these findings with the methods presented in this paper, would provide further evidence for the existence of such across-site PAC. This in turn would be important for the introduction of novel methods for the multilocus non-invasive brain stimulation (Koponen et al., 2018) aimed at the disruption of pathological PAC.

The orthogonalization approach of Colclough et al. (2015) aims to remove artifacts of volume conduction by finding the set of time series that are closest to the original sensor time series in the mean-squared error sense, yet are uncorrelated. This and similar approaches are often used with the implicit expectation that the removal of first-order correlations between orthogonalized time series would also destroy higher-order interactions introduced by the same source mixing process and enable the analysis of non-linear interactions such as PAC or amplitude envelope correlations (AEC, Hipp et al.,

2012; Colclough et al., 2015) without interference from artifacts of volume conduction. However, this is only guaranteed if the orthogonalization indeed recovers the original unmixed sources, which can be prohibited if the number of underlying sources is larger than the number of sensors and/or if the mixing matrix (in the EEG setting the so-called resolution kernel composed of the leadfield and inverse projection matrix) substantially deviates from diagonality. In addition, slow and fast oscillation spectral components of a PAC interaction are in general linearly uncorrelated. Thus, any orthogonalization algorithm has no incentive to group slow and fast oscillation signal parts into the same component but may just as well assign slow and fast oscillation parts to different components that would be uncorrelated but PAC coupled even if the original PAC interaction was just within site. This would lead to the emergence of spurious between-site PAC even on orthogonalized signals.

These considerations signify that tailored solutions such as antisymmetrized bispectra are needed to distinguish genuine between- from within-site PAC. Similarly, simulations as performed here are advisable to critically assess the aptitude of approaches such as orthogonalization when used to address other novel problems in brain functional connectivity estimation.

Limitations

In this study we observed that PAC metrics based on bispectra are well suited for detecting ground-truth PAC even in challenging SNR regimes, and that anti-symmetrization can further robustify the estimation in the sense that it prevents the detection of between-site PAC that can be more trivially explained by mixtures of univariate PAC sources. However, we did

not investigate the possibility of spurious (within- or between-site) PAC due to other reasons. There are various additional possible pitfalls that warrant further discussion/investigation.

First, while the bispectral indices used here do reflect PAC, they may also be influenced by other types of coupling, like phase–frequency, amplitude–frequency, and amplitude–amplitude interactions (Hyafil et al., 2015; Jirsa and Müller, 2013). These possibilities should be carefully ruled out when investigating PAC with bispectra.

Second, it has been shown that spurious PAC detection may arise from physiological artifacts, like eye movements, muscle activity, or heart beat, which can often be simultaneously observed in multiple channels (Giehl et al., 2021). However, this would not pose a problem for ASB-PAC based PAC estimation, which is invariant to mixtures of non-interacting sources by construction (Chella et al., 2014).

And, third, spurious PAC may arise from a rhythmic non-sinusoidal signal and its higher harmonics (Hyafil, 2017; Giehl et al., 2021; Idaji et al., 2022). Indeed, in a recent resting-state MEG study (Giehl et al., 2021), all within-region PAC could be attributed to the present of higher harmonics or physiological artifacts in the data. To rule out unwanted effects of higher harmonics, a novel method, Harmoni (Idaji et al., 2022), was recently developed. Further research should investigate how Harmoni can be combined with the ASB-PAC approach.

8. Conclusion

Between-site PAC can spuriously emerge when a univariate PAC signal is spread to other locations. Therefore, a robust method to disentangle genuine between-site PAC from within-site PAC is needed. In this study, we tested the use of the anti-symmetrized bispectrum to robustly estimate genuine between-site PAC. Previous studies have demonstrated that anti-symmetrized bispectra vanish for mixtures of independent sources. However, the application of ASB-PAC to assess the presence of genuine between-site PAC has not been explored yet. To investigate the performance of different algorithms in detecting PAC in the context of mixed signals, and, thus, in distinguishing between genuine between-site PAC and within-site PAC, we conducted two experiments: one using a minimal two-channel setup and one involving a more complex EEG-like setting that mimicked the generation and reconstructions of underlying EEG sources with forward and inverse modeling techniques. Our findings reveal that the ASB-PAC exhibits superior performance in detecting simulated PAC in the presence of volume conduction, outperforming conventional PAC estimators. Specifically, the ASB-PAC approach demonstrated the highest performance in detecting genuine between-site PAC interactions while detecting the fewest spurious interactions in presence of signal mixing. In light of these results, the use of ASB-PAC-based metrics could significantly enhance the interpretation of future studies investigating PAC as a mechanism of brain communication across macroscopic sites. By effectively addressing the issue of spurious between-site PAC emergence in mixed signal settings, the ASB-PAC approach offers valuable insights into the genuine functional interactions between distinct

brain sites, thereby facilitating a more accurate understanding of PAC's role in brain dynamics and signaling processes.

Data and code availability

The code for the simulation can be found here: <https://github.com/fpellegrini/PAC>. The code for the ROIconnect plugin can be found here: <https://github.com/sccn/roiconnect>. And the code for the minimal real data example here: <https://github.com/fpellegrini/MotorImag>. Data of the real data example are available upon request.

Author Contributions

Franziska Pellegrini: Methodology, Software, Investigation, Writing – original draft, Visualization. **Tien Dung Nguyen:** Software, Writing – original draft, Writing – review & editing. **Taliana Herrera:** Methodology, Investigation. **Vadim Nikulin:** Writing – review & editing, Supervision. **Guido Nolte:** Methodology, Writing – review & editing, Supervision. **Stefan Haufe:** Conceptualization, Methodology, Validation, Investigation, Resources, Writing – review & editing, Supervision, Project administration, Funding acquisition.

Declaration of Competing Interest

The authors declare that they have no known competing financial interests or personal relationships that could have appeared to influence the work reported in this paper.

Acknowledgements

This project was supported by the European Research Council (ERC) under the European Union’s Horizon 2020 research and innovation programme (Grant agreement No. 758985) and through Deutsche Forschungsgemeinschaft (DFG, German Research Foundation) – Project-ID 424778381 – TRR 295(Projects B05 and B02). G.N. was partially funded by the German Research Foundation (DFG, SFB936 Z3 and TRR169, B4). The computations for this work were partly run on the open Neuroscience Gateway cluster (Sivagnanam et al., 2013).

References

- Annavarapu, R. N. (2013). Singular value decomposition and the centrality of löwdin orthogonalizations. *American Journal of Computational and Applied Mathematics*, 3(1):33–35.
- Aru, J., Aru, J., Priesemann, V., Wibral, M., Lana, L., Pipa, G., Singer, W., and Vicente, R. (2015). Untangling cross-frequency coupling in neuroscience. *Current opinion in neurobiology*, 31:51–61.
- Baillet, S., Mosher, J. C., and Leahy, R. M. (2001). Electromagnetic brain mapping. *IEEE Signal processing magazine*, 18(6):14–30.
- Bastos, A. M. and Schoffelen, J.-M. (2016). A tutorial review of functional connectivity analysis methods and their interpretational pitfalls. *Frontiers in systems neuroscience*, 9:175.
- Bell, A. J. and Sejnowski, T. J. (1995). An information-maximization approach to blind separation and blind deconvolution. *Neural computation*, 7(6):1129–1159.
- Berman, J. I., McDaniel, J., Liu, S., Cornew, L., Gaetz, W., Roberts, T. P., and Edgar, J. C. (2012). Variable bandwidth filtering for improved sensitivity of cross-frequency coupling metrics. *Brain connectivity*, 2(3):155–163.
- Blankertz, B., Sannelli, C., Halder, S., Hammer, E. M., Kübler, A., Müller, K.-R., Curio, G., and Dickhaus, T. (2010). Neurophysiological predictor of SMR-based BCI performance. *Neuroimage*, 51(4):1303–1309.

- Brookes, M. J., Woolrich, M. W., and Barnes, G. R. (2012). Measuring functional connectivity in meg: a multivariate approach insensitive to linear source leakage. *Neuroimage*, 63(2):910–920.
- Bruns, A. and Eckhorn, R. (2004). Task-related coupling from high-to low-frequency signals among visual cortical areas in human subdural recordings. *International journal of psychophysiology*, 51(2):97–116.
- Canolty, R. T., Edwards, E., Dalal, S. S., Soltani, M., Nagarajan, S. S., Kirsch, H. E., Berger, M. S., Barbaro, N. M., and Knight, R. T. (2006). High gamma power is phase-locked to theta oscillations in human neocortex. *science*, 313(5793):1626–1628.
- Canolty, R. T. and Knight, R. T. (2010). The functional role of cross-frequency coupling. *Trends in cognitive sciences*, 14(11):506–515.
- Chella, F., Marzetti, L., Pizzella, V., Zappasodi, F., and Nolte, G. (2014). Third order spectral analysis robust to mixing artifacts for mapping cross-frequency interactions in eeg/meg. *Neuroimage*, 91:146–161.
- Cohen, M. X., Axmacher, N., Lenartz, D., Elger, C. E., Sturm, V., and Schlaepfer, T. E. (2009). Good vibrations: cross-frequency coupling in the human nucleus accumbens during reward processing. *Journal of cognitive neuroscience*, 21(5):875–889.
- Colclough, G. L., Brookes, M. J., Smith, S. M., and Woolrich, M. W. (2015). A symmetric multivariate leakage correction for MEG connectomes. *Neuroimage*, 117:439–448.

- Colgin, L. L., Denninger, T., Fyhn, M., Hafting, T., Bonnevie, T., Jensen, O., Moser, M.-B., and Moser, E. I. (2009). Frequency of gamma oscillations routes flow of information in the hippocampus. *Nature*, 462(7271):353–357.
- Daitch, A. L., Foster, B. L., Schrouff, J., Rangarajan, V., Kaşikçi, I., Gattas, S., and Parvizi, J. (2016). Mapping human temporal and parietal neuronal population activity and functional coupling during mathematical cognition. *Proceedings of the National Academy of Sciences*, 113(46):E7277–E7286.
- De Hemptinne, C., Ryapolova-Webb, E. S., Air, E. L., Garcia, P. A., Miller, K. J., Ojemann, J. G., Ostrem, J. L., Galifianakis, N. B., and Starr, P. A. (2013). Exaggerated phase–amplitude coupling in the primary motor cortex in parkinson disease. *Proceedings of the national academy of sciences*, 110(12):4780–4785.
- Delorme, A. and Makeig, S. (2004). Eeglab: an open source toolbox for analysis of single-trial eeg dynamics including independent component analysis. *Journal of neuroscience methods*, 134(1):9–21.
- Desikan, R. S., Ségonne, F., Fischl, B., Quinn, B. T., Dickerson, B. C., Blacker, D., Buckner, R. L., Dale, A. M., Maguire, R. P., Hyman, B. T., et al. (2006). An automated labeling system for subdividing the human cerebral cortex on mri scans into gyral based regions of interest. *Neuroimage*, 31(3):968–980.
- Dowding, I. and Haufe, S. (2018). Powerful statistical inference for nested

data using sufficient summary statistics. *Frontiers in human neuroscience*, 12:103.

Florin, E. and Baillet, S. (2015). The brain's resting-state activity is shaped by synchronized cross-frequency coupling of neural oscillations. *Neuroimage*, 111:26–35.

Giehl, J., Noury, N., and Siegel, M. (2021). Dissociating harmonic and non-harmonic phase-amplitude coupling in the human brain. *NeuroImage*, 227:117648.

Gong, R., Wegscheider, M., Mühlberg, C., Gast, R., Fricke, C., Rumpf, J.-J., Nikulin, V. V., Knösche, T. R., and Classen, J. (2021). Spatiotemporal features of β - γ phase-amplitude coupling in parkinson's disease derived from scalp eeg. *Brain*, 144(2):487–503.

Gramfort, A., Papadopulo, T., Olivi, E., and Clerc, M. (2010). OpenMEEG: opensource software for quasistatic bioelectromagnetics. *Biomedical engineering online*, 9(1):1–20.

Haufe, S., Nikulin, V. V., Müller, K.-R., and Nolte, G. (2013). A critical assessment of connectivity measures for EEG data: a simulation study. *Neuroimage*, 64:120–133.

Hipp, J. F., Hawellek, D. J., Corbetta, M., Siegel, M., and Engel, A. K. (2012). Large-scale cortical correlation structure of spontaneous oscillatory activity. *Nature neuroscience*, 15(6):884–890.

Hyafil, A. (2015). Misidentifications of specific forms of cross-frequency coupling: three warnings. *Frontiers in neuroscience*, 9:370.

- Hyafil, A. (2017). Disharmony in neural oscillations. *Journal of Neurophysiology*, 118(1):1–3.
- Hyafil, A., Giraud, A.-L., Fontolan, L., and Gutkin, B. (2015). Neural cross-frequency coupling: connecting architectures, mechanisms, and functions. *Trends in neurosciences*, 38(11):725–740.
- Idjadi, M. J., Zhang, J., Stephani, T., Nolte, G., Müller, K.-R., Villringer, A., and Nikulin, V. V. (2022). Harmoni: A method for eliminating spurious interactions due to the harmonic components in neuronal data. *NeuroImage*, 252:119053.
- Isler, J. R., Grieve, P. G., Czernochowski, D., Stark, R. I., and Friedman, D. (2008). Cross-frequency phase coupling of brain rhythms during the orienting response. *Brain research*, 1232:163–172.
- Jirsa, V. and Müller, V. (2013). Cross-frequency coupling in real and virtual brain networks. *Frontiers in computational neuroscience*, 7:78.
- Jongsma, M. L., Meulenbroek, R. G., Okely, J., Baas, C. M., Van Der Lubbe, R. H., and Steenbergen, B. (2013). Effects of hand orientation on motor imagery-event related potentials suggest kinesthetic motor imagery to solve the hand laterality judgment task. *PloS one*, 8(9):e76515.
- Koponen, L. M., Nieminen, J. O., and Ilmoniemi, R. J. (2018). Multi-locus transcranial magnetic stimulation—theory and implementation. *Brain Stimulation*, 11(4):849–855.
- Kovach, C. K., Oya, H., and Kawasaki, H. (2018). The bispectrum and its relationship to phase-amplitude coupling. *Neuroimage*, 173:518–539.

- Lachaux, J.-P., Rodriguez, E., Martinerie, J., and Varela, F. J. (1999). Measuring phase synchrony in brain signals. *Human brain mapping*, 8(4):194–208.
- Löwdin, P.-O. (1950). On the non-orthogonality problem connected with the use of atomic wave functions in the theory of molecules and crystals. *The Journal of Chemical Physics*, 18(3):365–375.
- Maris, E., van Vugt, M., and Kahana, M. (2011). Spatially distributed patterns of oscillatory coupling between high-frequency amplitudes and low-frequency phases in human ieeg. *Neuroimage*, 54(2):836–850.
- Mazziotta, J. C., Toga, A. W., Evans, A., Fox, P., Lancaster, J., et al. (1995). A probabilistic atlas of the human brain: theory and rationale for its development. *Neuroimage*, 2(2):89–101.
- Nandi, B., Swiatek, P., Kocsis, B., and Ding, M. (2019). Inferring the direction of rhythmic neural transmission via inter-regional phase-amplitude coupling (ir-pac). *Scientific reports*, 9(1):1–13.
- Neuper, C., Scherer, R., Reiner, M., and Pfurtscheller, G. (2005). Imagery of motor actions: Differential effects of kinesthetic and visual–motor mode of imagery in single-trial eeg. *Cognitive brain research*, 25(3):668–677.
- Nikias, C. L. and Pan, R. (1988). Time delay estimation in unknown gaussian spatially correlated noise. *IEEE Transactions on Acoustics, Speech, and Signal Processing*, 36(11):1706–1714.
- Nikulin, V. V., Nolte, G., and Curio, G. (2011). A novel method for reliable

- and fast extraction of neuronal eeg/meg oscillations on the basis of spatio-spectral decomposition. *NeuroImage*, 55(4):1528–1535.
- Nolte, G., Bai, O., Wheaton, L., Mari, Z., Vorbach, S., and Hallett, M. (2004). Identifying true brain interaction from EEG data using the imaginary part of coherency. *Clinical neurophysiology*, 115(10):2292–2307.
- Osipova, D., Hermes, D., and Jensen, O. (2008). Gamma power is phase-locked to posterior alpha activity. *PloS one*, 3(12):e3990.
- Özkurt, T. E. and Schnitzler, A. (2011). A critical note on the definition of phase-amplitude cross-frequency coupling. *Journal of Neuroscience methods*, 201(2):438–443.
- Pellegrini, F., Delorme, A., Nikulin, V., and Haufe, S. (2023). Identifying good practices for detecting inter-regional linear functional connectivity from eeg. *NeuroImage*, page 120218.
- Penny, W., Duzel, E., Miller, K., and Ojemann, J. (2008). Testing for nested oscillation. *Journal of neuroscience methods*, 174(1):50–61.
- Sannelli, C., Vidaurre, C., Müller, K.-R., and Blankertz, B. (2019). A large scale screening study with a SMR-based BCI: Categorization of BCI users and differences in their SMR activity. *PLoS One*, 14(1):e0207351.
- Schack, B., Vath, N., Petsche, H., Geissler, H.-G., and Möller, E. (2002). Phase-coupling of theta–gamma eeg rhythms during short-term memory processing. *International Journal of Psychophysiology*, 44(2):143–163.

Schaworonkow, N. and Nikulin, V. V. (2021). Is sensor space analysis good enough? spatial patterns as a tool for assessing spatial mixing of EEG/MEG rhythms. *bioRxiv*.

Scherer, R. and Vidaurre, C. (2018). Motor imagery based brain–computer interfaces. In *Smart wheelchairs and brain-computer interfaces*, pages 171–195. Elsevier.

Schoffelen, J.-M. and Gross, J. (2009). Source connectivity analysis with MEG and EEG. *Human brain mapping*, 30(6):1857–1865.

Shahbazi, F., Ewald, A., Ziehe, A., and Nolte, G. (2010). Constructing surrogate data to control for artifacts of volume conduction for functional connectivity measures. In *17th International Conference on Biomagnetism Advances in Biomagnetism–Biomag2010*, pages 207–210. Springer.

Sivagnanam, S., Majumdar, A., Yoshimoto, K., Astakhov, V., Bandrowski, A. E., Martone, M. E., Carnevale, N. T., et al. (2013). Introducing the neuroscience gateway. *IWSG*, 993:0.

Studenova, A. A., Villringer, A., and Nikulin, V. V. (2022). Non-zero mean alpha oscillations revealed with computational model and empirical data. *PLoS computational biology*, 18(7):e1010272.

Tadel, F., Baillet, S., Mosher, J. C., Pantazis, D., and Leahy, R. M. (2011). Brainstorm: a user-friendly application for MEG/EEG analysis. *Computational intelligence and neuroscience*, 2011.

- Tort, A. B., Komorowski, R., Eichenbaum, H., and Kopell, N. (2010). Measuring phase-amplitude coupling between neuronal oscillations of different frequencies. *Journal of neurophysiology*, 104(2):1195–1210.
- Tort, A. B., Kramer, M. A., Thorn, C., Gibson, D. J., Kubota, Y., Graybiel, A. M., and Kopell, N. J. (2008). Dynamic cross-frequency couplings of local field potential oscillations in rat striatum and hippocampus during performance of a t-maze task. *Proceedings of the National Academy of Sciences*, 105(51):20517–20522.
- van der Meij, R., Kahana, M., and Maris, E. (2012). Phase–amplitude coupling in human electrocorticography is spatially distributed and phase diverse. *Journal of Neuroscience*, 32(1):111–123.
- Van Veen, B. D., Van Drongelen, W., Yuchtman, M., and Suzuki, A. (1997). Localization of brain electrical activity via linearly constrained minimum variance spatial filtering. *IEEE Transactions on biomedical engineering*, 44(9):867–880.
- Vidaurre, C., Haufe, S., Jorajuria, T., Müller, K.-R., and Nikulin, V. V. (2020). Sensorimotor functional connectivity: a neurophysiological factor related to bci performance. *Frontiers in Neuroscience*, 14:575081.
- Voytek, B., Canolty, R. T., Shestyuk, A., Crone, N. E., Parvizi, J., and Knight, R. T. (2010). Shifts in gamma phase–amplitude coupling frequency from theta to alpha over posterior cortex during visual tasks. *Frontiers in human neuroscience*, 4:191.

- Voytek, B., Kayser, A. S., Badre, D., Fegen, D., Chang, E. F., Crone, N. E., Parvizi, J., Knight, R. T., and D'esposito, M. (2015). Oscillatory dynamics coordinating human frontal networks in support of goal maintenance. *Nature neuroscience*, 18(9):1318–1324.
- Watrous, A. J., Deuker, L., Fell, J., and Axmacher, N. (2015). Phase-amplitude coupling supports phase coding in human ecog. *Elife*, 4:e07886.
- Winkler, I., Panknin, D., Bartz, D., Müller, K.-R., and Haufe, S. (2016). Validity of time reversal for testing granger causality. *IEEE Transactions on Signal Processing*, 64(11):2746–2760.
- Yin, Z., Zhu, G., Liu, Y., Zhao, B., Liu, D., Bai, Y., Zhang, Q., Shi, L., Feng, T., Yang, A., et al. (2022). Cortical phase-amplitude coupling is key to the occurrence and treatment of freezing of gait. *Brain*, 145(7):2407–2421.
- Zandvoort, C. S. and Nolte, G. (2021). Defining the filter parameters for phase-amplitude coupling from a bispectral point of view. *Journal of Neuroscience Methods*, 350:109032.

Cortical networks of parkinsonian gait: a metabolic and functional connectivity study

Franziska Pellegrini, PhD^{1,2}; Nicoló G. Pozzi, MD, PhD^{3 ¶}; Chiara Palmisano, PhD^{1,4 ¶}; Giorgio Marotta, MD⁵;
Andreas Buck, MD⁶; Stefan Haufe, PhD^{1,2,7,8} and Ioannis U. Isaias, MD, PhD^{3,4*}

1. Charité - Universitätsmedizin Berlin, corporate member of Freie Universität Berlin and Humboldt-Universität zu Berlin, and Berlin Institute of Health, Berlin Center for Advanced Neuroimaging (BCAN), Berlin, Germany
2. Bernstein Center for Computational Neuroscience, Berlin, Germany
3. Department of Neurology, University Hospital of Würzburg and The Julius Maximilian University of Würzburg, Würzburg, Germany
4. Parkinson Institute Milan, ASST G. Pini-CTO, Milano, Italy
5. Department of Nuclear Medicine, Fondazione IRCCS Ca' Granda Ospedale Maggiore Policlinico, Milano, Italy
6. Department of Nuclear Medicine, University Hospital of Würzburg, Würzburg, Germany
7. Uncertainty, Inverse Modeling and Machine Learning Group, Faculty IV Electrical Engineering and Computer Science, Technical University of Berlin, Berlin, Germany
8. Physikalisch-Technische Bundesanstalt Braunschweig und Berlin

¶ Contributed equally

* Correspondence

Isaias_I@ukw.de

Abstract

Objective: Locomotion is an automated voluntary movement sustained by coordinated neural synchronization across a distributed brain network. The cerebral cortex is central for adapting the locomotion pattern to the environment and alterations of cortical network dynamics can lead to gait impairments. Gait problems are a common symptom with a still unclear pathophysiology and represent an unmet therapeutical need in Parkinson's disease. Little is known about the cortical network dynamics of locomotor control in these patients.

Methods: We studied the cortical basis of parkinsonian gait by combining metabolic brain imaging with high-density EEG recordings and kinematic measurements performed at rest and during unperturbed overground walking.

Results: We found significant changes in functional connectivity between frontal, sensorimotor and visuomotor cortical areas during walking as compared to resting. Specifically, hypokinetic gait was associated with poor information flow from the supplementary motor area (SMA) to precuneus and from calcarine to lingual gyrus as well as high information flow from calcarine to cuneus.

Interpretation: Our findings support a role for visuomotor integration processes in PD-related hypokinetic gait and suggest that reinforcing visual information may act as a compensatory strategy to allow SMA-related feedforward locomotor control in PD.

Introduction

In human locomotion, the synergistic movement of different body parts ensure forward motion while maintaining postural balance under changing environmental conditions. Despite being often considered a highly automated movement, human walking requires a fine integration of multiple brain and spinal processes with converging evidence pointing to a leading role of the brain cortex. In particular, dynamic interaction of distributed cortical areas may be essential for the integration of frontal, sensorimotor and visuomotor information,^{1,2} which would adapt the stereotypical activity of the spinal central pattern generators to meet the environmental needs^{3,4}. This remarkable motor control can be achieved with synchronous neuronal oscillations, a mean to coordinate the information flow within functionally specialized neural networks (for review⁴⁻⁶). Alterations of these finely tuned dynamics would hamper locomotor control and result in gait impairments.

Gait impairments are a common phenomenon in Parkinson's disease (PD) and can encompass a wide range of gait disturbances, ranging from hypokinetic gait to episodic gait freezing. In many cases, gait impairments lead to falls, injuries and fear of falling, which can severely affect patient's quality of life⁷. While several studies assessed the role of subcortical nuclei^{5,8-10} in the pathophysiology of gait impairment in PD, recent findings have expanded beyond basal ganglia dysfunctions^{10,11} and suggested a primary role for the brain cortex^{4,12}. Both functional and molecular imaging studies showed that deficits in the integration between frontal and sensorimotor areas might contribute to the disruption of gait automation and favor the development of gait impairments^{4,12}. More recently, studies on cortical visual processing showed that gait impairment correlate with visual perceptual deficits, thus supporting a role for visuomotor processing in the pathophysiology of gait impairment in PD^{4,12}. Yet, a direct assessment of cortical network dynamics during actual locomotion in subjects with PD is still lacking. In particular, it is still unknown how the locomotor information flows within the cortical network in unmedicated PD patients and which integration processes are most relevant for gait under striatal dopamine depletion.

Here, we directly tackle this issue by combining sequential brain metabolic investigations during resting and walking with high-density EEG recordings and kinematic assessments of gait performances in unmedicated PD patients. We leveraged this multimodal approach to describe the cortical network dynamics of locomotion control in PD, detailing the functional roadblocks and rerouting of cortical locomotor information in PD.

Materials and methods

Subjects

We studied ten individuals (five females) with idiopathic PD as assessed by means of the UK Brain Bank Criteria. To be included in the study, patients had to be able to walk independently for at least three minutes straight, after pausing all dopaminergic medications for 12 h (meds-off). The presence of any other neurological disease, including cognitive decline (i.e., Mini-Mental State Examination score <27), vestibular disorders or orthopedic impairments were considered exclusion criteria. Two patients were implanted for bilateral subthalamic deep brain stimulation (Medtronic 3389 and Activa PC+S, Medtronic, PLC). Stimulation was turned off two hours prior to the recordings and remained off for all duration of the experiment.

We assessed the motor condition with the Unified Parkinson's Disease Rating Scale motor part (UPDRS-III) in meds-off and meds-on (i.e., one hour after the intake of the levodopa equivalent daily dose, LEDD) and disease stage with the Hoehn and Yahr (H&Y) scale. We computed the percentage of improvement in the UPDRS-III score due to dopaminergic medication intake, as follows¹⁰:

$$[(a - b)/a] \times 100$$

where a is the UPDRS-III meds-off score and b is the UPDRS-III meds-on score. Demographic and clinical information is listed in Table 1.

The study was approved by the Ethical Committee of the University of Würzburg (n. 36/17 and 103/20) and conformed to the declaration of Helsinki. All participants gave their written informed consent to participation.

Experimental setup

We investigated brain metabolism and brain functional connectivity at rest and during unperturbed, overground walking (Figure 1). All evaluations were performed in meds-off and took place on two nonconsecutive days in the morning after fasting and pausing all dopaminergic medications for at least 12 h (overnight). Each participant was first investigated at rest. In this condition, participants were asked to comfortably sit on a chair with their eyes open looking at a target on a wall, in a quiet and well illuminated room (i.e., the same used for the forthcoming walking investigation) for 10 minutes before (preconditioning) and for 20 minutes after the injection of [18F]fluorodeoxyglucose (FDG). We recorded cortical electrophysiological activity and monitored body kinematics for 5 minutes before and for 20 minutes after the injection. The PET scan took place 30 minutes after the FDG injection. The same workflow was applied for the studying of gait. Participants walked barefoot at their self-selected speed following a large ellipsoidal path of about 60 m length without perturbations. This setting was chosen to let the subjects walk freely without interruption of the gait pattern. The clinical condition of the

participants was monitored by a neurologist trained in movement disorders (I.U.I. and N.G.P.) during the whole period of the study acquisitions. No patient had overt and continuous tremor or other symptoms that might act as a potential confounder of cerebral FDG uptake.

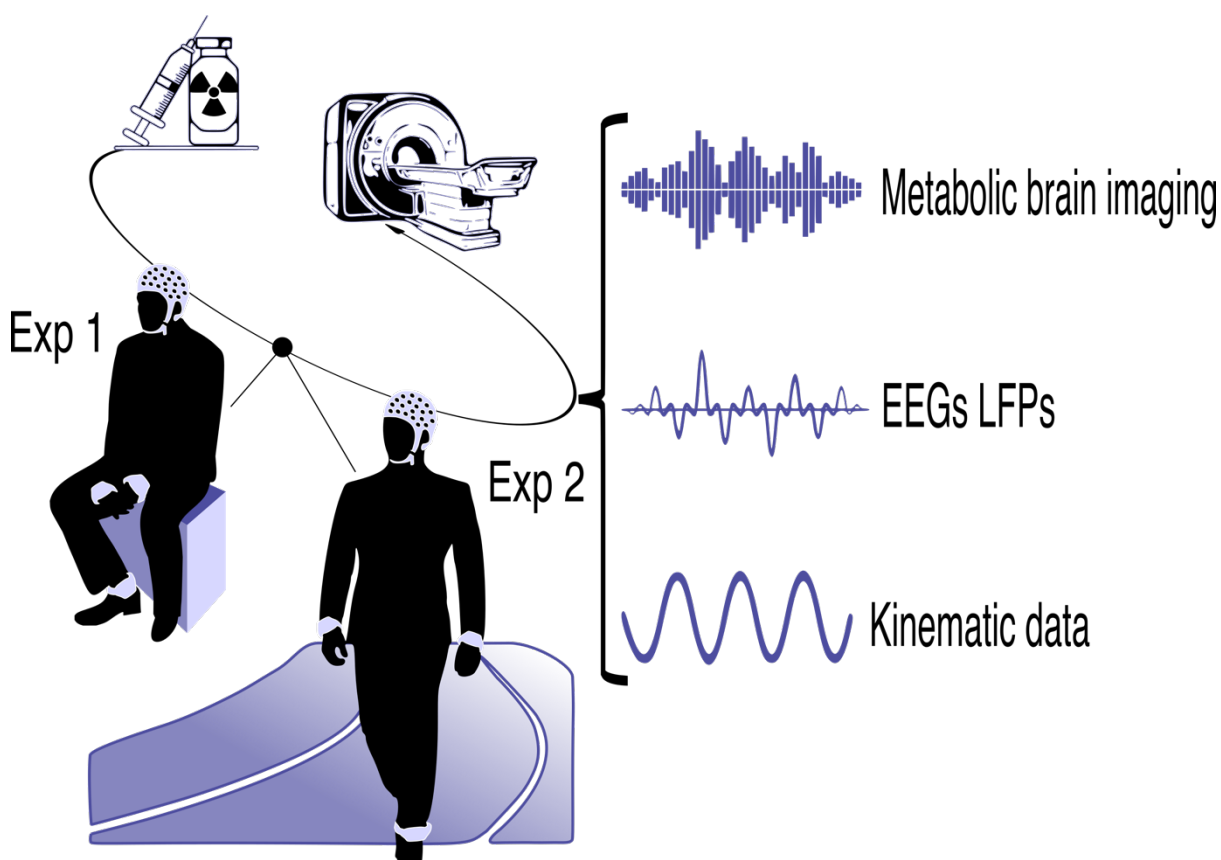


Figure 1: Experimental setup. The simultaneously recorded signals are schematically represented here. Every participant underwent one resting and one walking assessment in two nonconsecutive days in stim-off and meds-off condition (i.e., without subthalamic stimulation and after >12h withdrawal of all dopaminergic medication). Experiments took place always in the morning, participants were fasting >12h. Brain activity (i.e., EEG) and metabolism, and kinematic measurements were assessed simultaneously. Imaging scan took place 30 min after i.v. injection of [¹⁸F]fluorodeoxyglucose (FDG). Recordings took place before (preconditioning) and after FDG injection.

Gait kinematics

Throughout the entire walking period, we recorded gait kinematics using three inertial measurement units (IMU, sampling rate of 128 Hz, Opal, APDM, USA) placed on the outer part of the ankles and on the sternum (xiphoid process). In three subjects, we could not acquire IMU recordings due to technical issues. In two of them, we defined gait events with surface electromyography (EMG) as described in ¹³. The second patient (N2) showed artifacts in the EMG signals and was discarded for kinematic analyses. EMG activity was recorded bilaterally from tibialis anterior, soleus, gastrocnemius medialis, gastrocnemius lateralis, and vastus lateralis at a sampling rate of 1000 Hz (FREEEMG, BTS, Italy). IMU, EMG and EEG recordings were synchronized with a transistor-transistor logic (TTL) reference signal and an electrical artifact provided by a transcutaneous electrical nerve stimulation (TENS) device at the beginning and end of each recording session¹⁰. We detected heel strike and toe-off events from the angular velocity profiles measured with respect to the IMU medio-lateral axis as previously described¹³ and computed: i) swing duration (as the duration between successive toe-off and heel strike events), ii) stride duration (as the time difference between two successive heel strikes), and the swing/stride duration (as ratio of the swing and stride duration).

We further correlate kinematic measurements with clinical scores (i.e., UPDRS-III meds-off) with Pearson correlation.

Brain metabolic imaging

The execution and analysis of PET scans have been previously described in detail^{14,15}. In brief, all PET/CT scans were performed with a Biograph mCT 64 (Siemens Medical Solutions). For both resting and walking investigations, the PET scan was started 30 min after the injection of 208±16.5 MBq of FDG. PET was performed in 3D mode for 10 min/one bed position using a 400 × 400 matrix with an axial resolution of 2 mm full-width at half-maximum and an in-plane resolution of 4.7 mm. CT scans for attenuation correction were acquired using a low-dose protocol. PET data were reconstructed iteratively (24 subsets, three iterations, Gaussian filtering) using HD reconstruction mode. FDG data processing was performed with statistical parametric mapping software SPM12 (Wellcome Department of Cognitive Neurology, London) implemented in Matlab (MathWorks, Natick, MA, USA). PET images were spatially normalized into the Montreal Neurological Institute standard template (MNI, McGill University, Montreal QC, Canada) using the affine transformation (12 parameters for rigid transformations) of SPM12. Spatially normalized images were then smoothed with a Gaussian filter (FWHM 12 mm) to increase signal-to-noise ratio. Based also on the body weight of each patient, we calculated the standardized uptake value (SUV) of brain regions as defined by the AAL Atlas (PickAtlas Tool, Version 3.0.5 software). After calculating the SUV mean of the white matter in the individual PET, we normalized the SUV of each brain region by the SUV whole mean to remove the effects of the differences in the overall counts. We then computed the change of brain metabolic activity between resting and walking conditions by comparing the relative metabolic changes in a voxel-wise manner. To this aim, we used SPM12 for between-group analysis (i.e., conducting a pairwise t-test for every region). Both metabolism increases and decreases were considered significant for p<0.05 (uncorrected). Significant regions were used as regions of interest (ROIs) in all further analyses (Figure 3).

EEG recordings and preprocessing

Neurophysiological recordings were performed using a 64-channel EEG (MOVE, Brain Products) with a sampling rate of 500 Hz. EEG data were resampled to a sampling rate of 125 Hz, zero-phase lowpass-filtered at 45 Hz, and highpass-filtered at 1 Hz (zero-phase forward and reverse second-order digital band-pass Butterworth filter). Line noise was eliminated using a zero-phase bandstop filter with stop band between 47 and 53 Hz. For the walking trials, we discarded the EEG activity in the time-period before the first heel strike and after the last toe-off event as not related to walking. Artifactual channels and segments were identified using automated artifact rejection¹⁶. We manually detected remaining channels with artifacts by inspecting topographic plots of the alpha power (8-13 Hz). Artifactual channels were replaced with spherical spline interpolation on the scalp. Artifactual segments were removed for independent component analysis (ICA) but were preserved for subsequent analyses to grant for the continuity of the data. To remove eye movements from the data, we regressed out the time series of the two electrodes closest to the eyes (FP1 and FP2) from the time series of all other electrodes. As a further cleaning step, we applied artifact subspace reconstruction¹⁶. Then we conducted ICA using runica¹⁷ and visually detected and rejected eye, heart, and muscle components. The EEG data were then re-referenced to a common-average reference. Due to severe artefact contamination, we excluded one subject from the cortical analysis (N3).

Head modeling and source localization

For all but one participant (N9), we constructed individual volume conductor models based on structural MRI data to account for their different head anatomies. In N9, we applied the ICBM-152 template¹⁸, as the MRI was unavailable. Where available, lead fields were constructed based on exact channel positions. First, the MRI data were segmented into white matter and grey matter (WM and GM). To this end, we used the recon-all command of the freesurfer software (version 1.0)^{19,20} to obtain triangularized surface meshes for the WM-GM and GM-CSF interfaces. Based on these segmentations, we reconstructed the outline of the brain. We constructed personalized head models with the boundary element method (BEM)^{21,22} with three layers (scalp, outer skull, inner skull) using OpenMEEG²¹ and Brainstorm²³. MRI and EEG channel positions were co-registered using fiducial points at the nasion, left ear and right ear. The source model consisted of 2000 locations evenly spaced and placed in the center of the gray matter (half-way between the GM-cerebrospinal fluid and WM-GM interfaces). From the individual head model and the cleaned EEG data, we calculated a personalized linear inverse filter (linearly-constrained minimum variance spatial filtering, LCMV)²⁴ to project the EEG channel time series to the source locations. Note that we constructed LCMV filters on the cleaned and filtered times series of every session separately. The LCMV projection yields an estimate of the 3D primary current of an assumed dipolar electrical source, representing the combined activity of a large group of neurons, separately for each source location. On the source level, we labelled every source as being part of one of the regions of the AAL atlas (PickAtlas Tool, Version 3.0.5 software)²⁵.

Spectral power and directed functional connectivity estimation

We assessed spectral power and directed functional connectivity (FC) within and between AAL regions using a recently validated pipeline²⁶. To avoid a bias due to different trial lengths in the FC measures²⁷, we cut every trial into intervals of one minute length. After cutting, data intervals of under one minute length were discarded from further analysis. Power and FC were then calculated for every interval individually and treated as different samples for linear mixed-effects modeling (LMEs; see also Statistical Analysis Section). To calculate power at every source location, we used the Welch method (2 s non-overlapping epochs, resulting in a 0.5 Hz frequency resolution), and averaged power across sources and 3D dipole orientations within the AAL regions to obtain one power estimate per region. FC was calculated in three steps²⁶. First, we applied dimensionality reduction to the time series of all voxels of each ROI. To this end, we performed a principal component analysis (PCA) and kept the first principal component of every ROI for further processing. Second, we calculated time-reversed spectral Granger causality (TRGC)²⁸ as measure for directed FC between all ROI pairs. Compared to conventional measures of directed FC, TRGC offers empirically and theoretically proven robustness to artifacts of source mixing due to volume conduction in the head or spatial leakage in inverse solutions²⁸⁻³⁰. Finally, power and FC scores were averaged within two personalized frequency bands of interest (BOIs): a broad low-frequency band containing both theta and alpha and the individual beta band. To derive the borders of the individual frequency bands, we first estimated the individual alpha frequency (IAF) as the alpha peak location on the 1/f-corrected power spectra³¹. According to³², we defined the theta/alpha band to be between $0.4 * IAF$ and $1.2 * IAF$, and the beta band to be between $1.2 * IAF$ and 30 Hz. Averaged powers were log-transformed prior to subsequent statistical analysis. Subsequently reported results thus always refer to log power.

Comparison of spectral power and functional connectivity between resting and walking

To compare power and FC between the resting and walking condition, we calculated an LME for every BOI and ROI or, in case of FC, ROI pair. Specifically, power and FC were calculated for 1min-intervals (see above). These intervals were then presented as samples in the LME. To control for subject- and hemisphere-related biases, subject ID and hemisphere were included as a random and fixed factor, respectively. To correct for multiple comparisons, we used the false discovery rate (FDR) method³³. FDR correction was done separately for the analysis of changes between resting and walking, and for the analysis of the relationship between gait kinematics and EEG. Note that we only calculated FC for the lower triangular matrix (see Figure 4 and Figure 5), since the values of the upper triangular matrix are redundant: $TRGC_{A \rightarrow B} = -TRGC_{B \rightarrow A}$ (i.e., due to the anti-symmetry of the TRGC measure, any increases in the information flow from a region A to a region B can also be interpreted as a decreased in flow from region B to region A). FDR correction was also applied only on one direction of information flow due to the anti-symmetry.

Table 1
Demographic and clinical data.

Patient	Sex	Age	Age at onset	LEDD	H&Y	UPDRS-III meds-off	UPDRS-III meds-on	% Improvement
1	F	60-64	50-54	680	2	34	24	29
2	F	60-64	45-49	715	2	20	4	80
3	M	65-69	55-59	300	1	13	6	54
4	M	60-64	50-54	610	2	12	5	58
5	M	65-69	55-59	610	2	30	21	30
6	F	55-60	45-49	640	1	9	5	44
7	M	55-59	50-54	900	2	28	5	82
8	M	45-49	35-39	1167	3	50	15	70
9	F	65-69	60-64	440	2	14	4	70
10	F	55-59	50-54	362	1	18	11	39

Age is expressed in years. F = female and M = male; H&Y = Hoehn and Yahr stage; LEDD = Levodopa Equivalent Daily Dose (expressed in mg); UPDRS-III = Unified Parkinson's Disease Rating Scale motor examination after overnight (>12 h) suspension of all dopaminergic drugs (meds-off) and at 60 min upon receiving 1 to 1.5 times (range 200-300 mg) the levodopa-equivalent of the morning dose (meds-on). % Improvement indicates the percentual amelioration of UPDRS-III score normalized to the UPDRS-III score in meds-off¹⁰.

Results

Clinical and kinematic data

Detailed demographic and clinical data are listed in Table 1. The average age of the participants was 60 ± 7 years and the average disease duration was 9 ± 7 years. The average LEDD at the time of the experiment was 642 ± 256 mg/day. The average UPDRS-III score in meds-off state was 23 ± 13 points and 10 ± 7 points in meds-on (at 60 min upon receiving 1 to 1.5 times the levodopa-equivalent of the morning dose). The average improvement was 56% (range 29% to 71%).

Kinematic measurements of the lower limbs are listed in Table 2. We showed a positive Pearson correlation between UPDRS-III score and stride duration ($p_{\text{stride-UPDRS}} = 0.017$, $\text{coeff}_{\text{stride-UPDRS}} = 0.80$, Figure 2), but not with swing duration and swing/stride duration ($p_{\text{swing-UPDRS}} = 0.091$, $p_{\text{swing/stride-UPDRS}} = 0.98$). Therefore, we focused only on stride duration for subsequent analysis.

Table 2

Kinematic data.

Patient	Swing duration seconds	Stride duration seconds	Swing duration/Stride duration
1	0.56	1.17	0.48
4	0.46	1.01	0.45
5	0.54	1.10	0.49
6	0.49	1.09	0.46
7	0.50	1.05	0.47
8	0.52	1.18	0.45
9	0.50	1.00	0.50
10	0.45	1.04	0.43

The swing duration represent the duration between successive toe-off and heel strike events and the stride duration the time difference between two successive heel strikes; both are expressed in seconds. We calculated also the swing/stride duration, which is the ratio of the swing and stride duration.

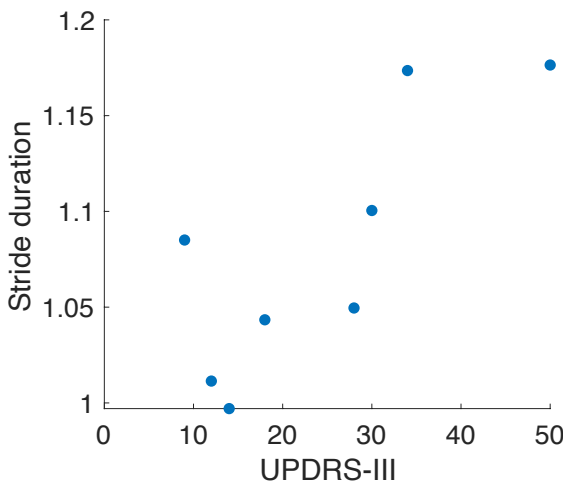


Figure 2: Clinic-Kinematic correlation. Correlation between stride duration and UPDRS-III score ($p = 0.017$, Pearson's correlation coefficient = 0.80). Dots represent single subjects.

Gait-related metabolic brain changes

We showed a gait-related brain metabolic activation pattern comprising the frontal, parietal and occipital cortical areas. Specifically, the following cortical areas showed an increased FDG uptake during walking as compared to resting: supplementary motor area (SMA), paracentral lobule, postcentral gyrus, superior parietal lobule, precuneus, superior occipital gyrus, middle occipital gyrus, cuneus, calcarine fissure and surrounding cortex, lingual gyrus. At subcortical level, we observed activation of the thalamus and cerebellum during walking. These two areas have not been studied further because it is still debated whether they can be reliably recorded with EEG. Of relevance, we did not find any brain region with reduced FDG uptake during walking as compared to resting. The metabolic brain imaging patterns are shown in Figure 3.

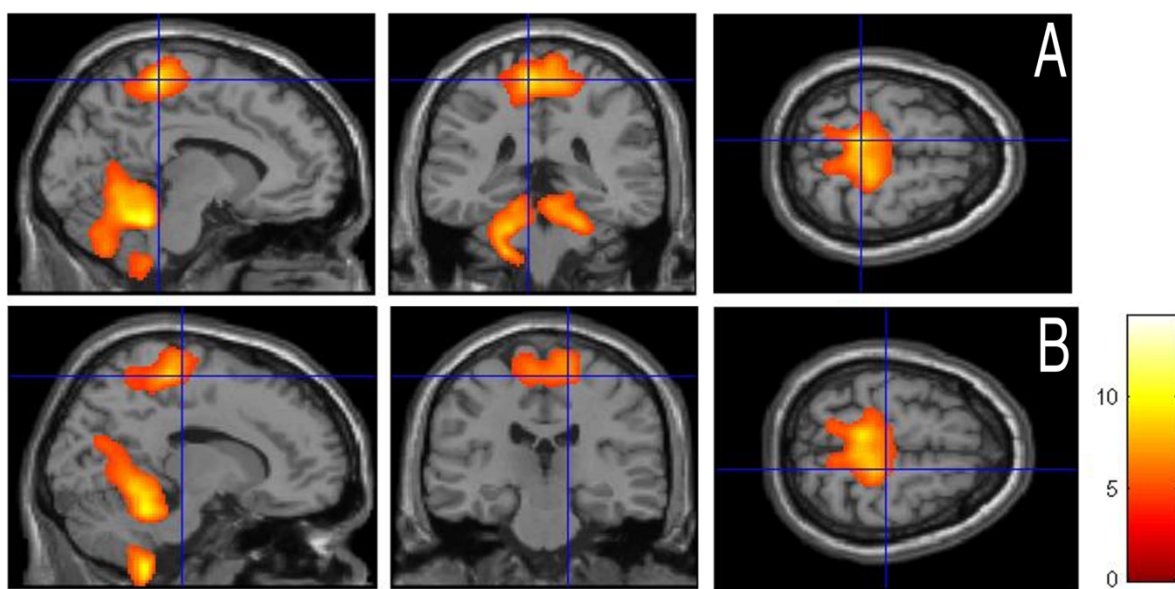


Figure 3: Gait-related metabolic changes (gait vs. resting). The activation clusters are projected onto a standard template provided by SPM in three different views (i.e., sagittal, coronal and axial view from left to right). Top raw (A), crossed blue lines correspond to location (-8, -36, 64), bottom raw (B) crossed blue lines correspond to location (14, -24, 62). Brighter colors reflect significantly increased metabolism in the supplementary motor area (SMA), paracentral lobule (BA 4), postcentral gyrus (BA 1-3), superior parietal lobule (BA 5-7), precuneus (BA 7), superior occipital gyrus (BA 19), middle occipital gyrus (BA 18), cuneus (BA 17), calcarine fissure and surrounding cortex (BA 17), lingual gyrus (BA 19). At subcortical level, the thalamus and cerebellum were more active during walking as respect to resting. Pairwise t-test comparison (SPM 12, $p < 0.001$, uncorrected).

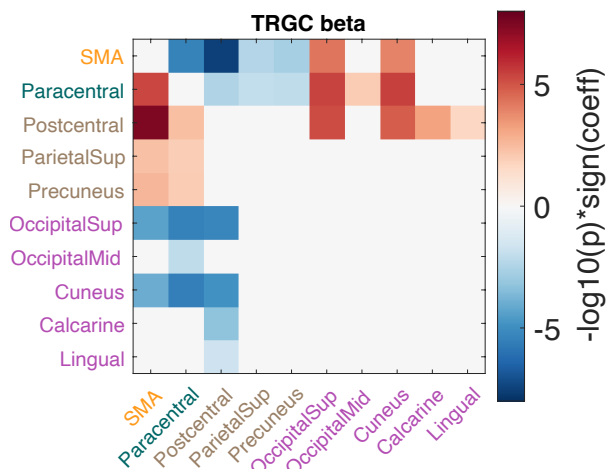


Figure 4. Comparison of EEG markers between resting and walking conditions in the beta band. Changes in directed functional connectivity were estimated by time-reversed Granger causality (TRGC). Red colors either indicate more information flow from the ROI on the Y-axis to the ROI on the X-axis in walking compared to resting, or less information flow from the ROI shown on the X-axis to the ROI shown on the Y-axis. We show $\log_{10} p$ -values, thus values below -2 and above 2 would indicate significance at alpha level 0.01. Signed $\log_{10} p$ -values that did not survive FDR correction are set to zero.

EEG power and functional connectivity during walking

We observed an increase in power for both frequency bands (i.e., theta-alpha and beta) and over all ROIs in walking as compared to resting, thus matching the brain metabolic changes (supplementary figure S1). Then, we estimated directed functional connectivity (i.e., TRGC) and showed changes between frontal, parietal and occipital areas in PD patients during walking with respect to resting (Figure 4). In the beta band, during walking we showed reduced information flow from the SMA to motor areas corresponding to the lower limb representation in the motor and sensory homunculus (i.e., paracentral) and sensory areas (i.e., postcentral, parietal

sup. and precuneus). In contrast, functional connectivity from SMA to visuomotor areas (i.e., cuneus and superior occipital gyrus) was increased during walking compared to resting. The paracentral lobule showed an increased information flow to the SMA and to visuomotor areas, but a reduced connectivity to sensory areas. Sensory areas showed increased functional connectivity with SMA, motor (i.e., the paracentral lobule) and the visuomotor areas during walking with respect to resting. Finally, the visuomotor areas presented a marked reduction in functional connectivity with SMA, motor and sensory areas. Of note, the medial occipital lobule and the lingual gyrus showed the poorest connectivity reduction. The same pattern of functional connectivity changes described for the beta band was shown overall also for the theta-alpha bands (supplementary figure S2).

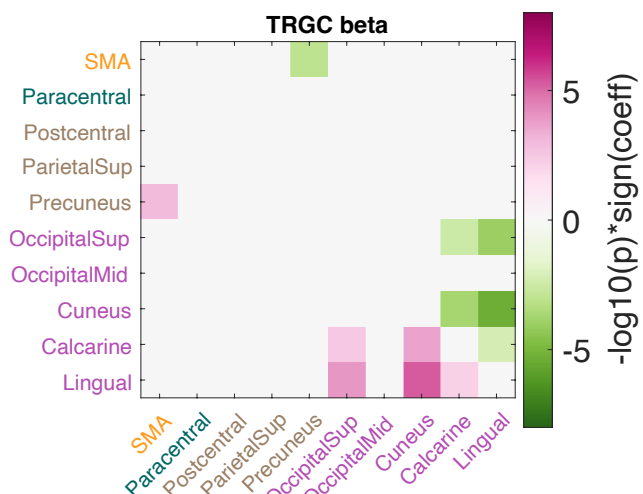


Figure 5. Correlation between stride duration and directed functional connectivity during walking. Pink colors indicate a positive correlation between stride duration and the net information flow from a region plotted on the Y-axis to a region plotted on the X-axis, while green colors indicate a negative correlation. We show $\log_{10} p$ -values, thus values below -2 and above 2 would indicate significance at alpha level 0.01. Signed $\log_{10} p$ -values that were not significant after FDR correction are set to zero.

Correlation of cortical network dynamics changes and gait kinematics

To test the relevance of the changes in cortical network dynamics, we investigated their correlation with gait performances as assessed by means of kinematic measurements.

We observed an overall negative relationship between stride duration and EEG power, thus supporting a functional role for the selected areas in gait control.

We then observed that only changes in the beta frequency band correlated with the motor performance. Furthermore, we observed that only the connectivity of SMA, precuneus and visuomotor areas was related to gait kinematics. Specifically, we found that the lower the information flow from SMA to precuneus, the higher the stride duration, and thus, the slowest was the gait (hypokinetic gait) (Figure 5). Interestingly, despite not having shown changes in connectivity within visuomotor areas between walking and resting, we noticed that hypokinetic gait was related to poor information flow from visuomotor areas (i.e., occipital superior and cuneus) to lingual gyrus and high information flow calcarine and lingual gyrus to cuneus.

Discussion

Understanding the neural network dynamics underpinning human locomotion is among the greatest challenges in neuroscience and can lay the foundation for novel therapeutic approaches for PD gait impairments¹². Recent evidence points to a central role for a distributed network of cortical areas in the locomotor control in subjects with PD^{5,10,34}. In particular, dynamic synchronization of neural oscillations across functionally connected cortical areas would support motor, sensorimotor and visuomotor processes that sustain an active control of locomotion^{4,6}. We leveraged brain metabolic investigation during gait to assess locomotor networks dynamics and estimated the cortical functional connectivity changes that are relevant for gait in subjects with PD (Figure 4). We show a predominant involvement of the SMA, sensory and visuomotor brain areas. We further identified three main functional connectivity patterns that correlate with gait performance (Figure 5) and suggest a putative roadmap for the flow of locomotor information in PD (Figure 6).

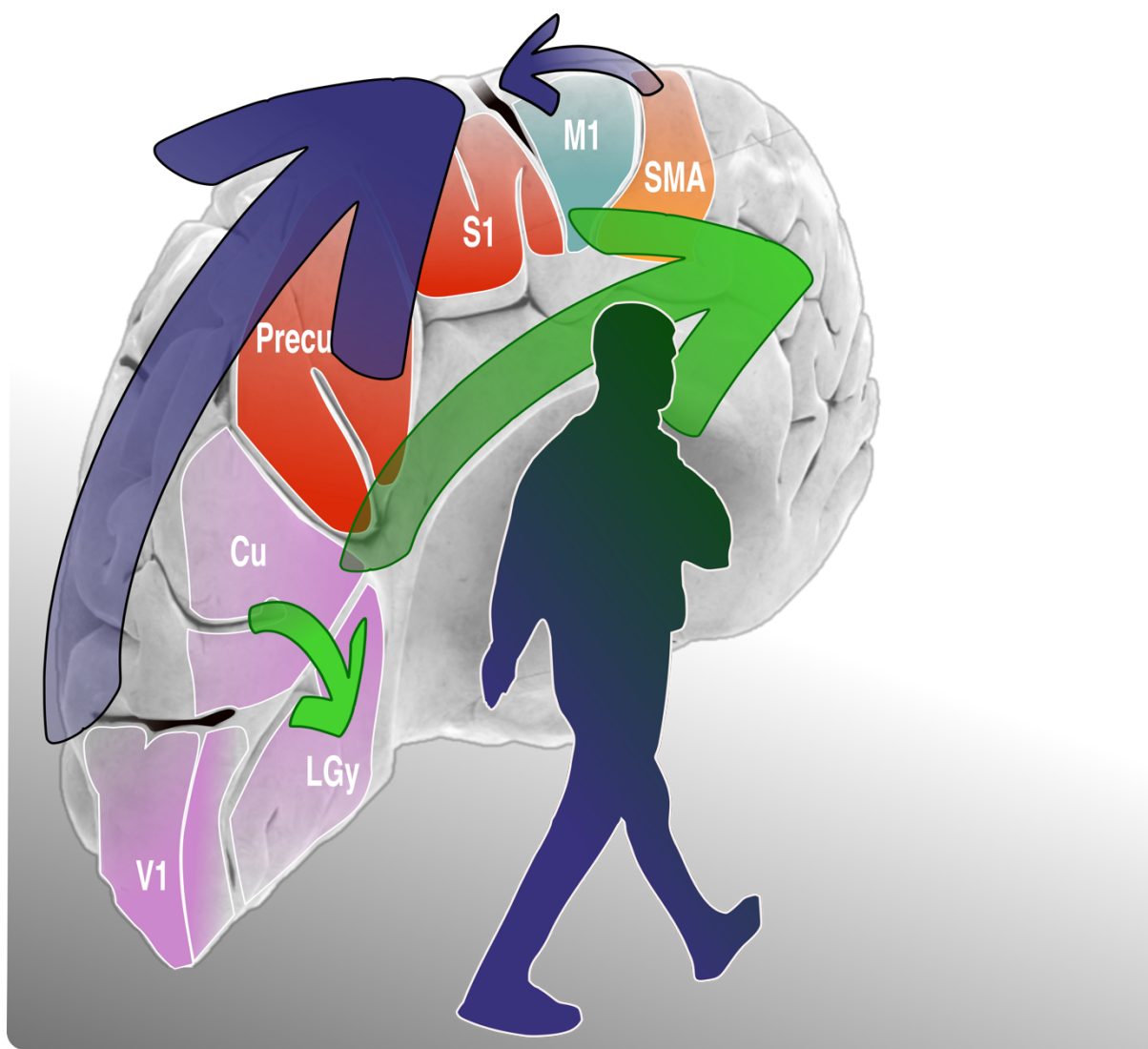


Figure 6. Scheme of the roadblocks and rerouting of locomotion information in PD. In PD, the information flow from visuomotor areas to SMA and from the SMA to sensory areas is impaired (blue arrows), so that a (likely compensatory) rerouting of the locomotor information through the lingual gyrus via the inferior fronto-occipital fasciculus is needed to push forward the locomotor information to sensorimotor brain areas (green arrows). SMA: supplementary motor area; M1: primary motor area (i.e., paracentral gyrus); S1: primary sensory cortex (i.e., postcentral and parietal superior gyrus); Precu: precuneus; Cu: cuneus; LGy: lingual gyrus; V1: calcarine cortex.

Deficient SMA functional connectivity impairs locomotor control

We found a strong reduction of SMA functional connectivity to the main sensory areas (i.e., paracentral lobule, postcentral lobules and precuneus) during walking as compared to resting in unmedicated PD patients (Figure 4). Reduced information flow between SMA and precuneus lead to hypokinetic gait (Figure 5). An interaction between these areas is essential as feedforward locomotor control originating from the SMA needs to be integrated with somatosensory information to update the body schema and to maintain postural control^{35,36}. Several studies reported abnormalities in sensorimotor integration in subjects with PD^{10/9/23 2:40:00 PM} with evidence for a primary SMA dysfunction in parkinsonian patients with gait disturbances^{37,38}. In particular, functional imaging studies showed that the SMA is hypoactive in PD and this correlates with bradykinesia³⁹ impaired generation of anticipatory postural adjustments (APAs)⁴⁰ and episodes of gait freezing⁴¹. Our findings expand on this topic and highlight a primarily functional impairment of the SMA in locomotion with a decoupling with motor and sensory areas during unperturbed, overground walking in unmedicated PD patients.

Visuomotor processing is critical for gait control

Studies in PD showed that gait performances strongly rely on visual inputs⁴² and that alterations of visuomotor processing are associated with gait disturbances⁴³. In our work, walking was associated with a primary

involvement of visuomotor cortex, but with a reduced information flow from these areas to both SMA, motor and sensory cortices (Figure 4). The correlation of functional connectivity patterns of visuomotor areas with gait performances yielded opposing results. Specifically, hypokinetic gait was related to poor information flow from calcarine to lingual gyrus and high information from calcarine to cuneus (Figure 5). Functional imaging studies showed that the lingual gyrus is preferentially involved in direction and discrimination of motion^{44,45}, whereas the cuneus is primarily engaged in basic visual processing (i.e., spatial orientation, frequency, and speed). While a direct engagement in locomotion control of these two areas still need to be proven, preliminary evidence showed that functional connectivity across the bilateral lingual gyrus, calcarine, cuneus, precuneus, and SMA is reduced in PD patients with *freezing of gait* as compared to patients without gait impairment⁴⁶. Furthermore, PD-related degeneration of neurons in the lingual gyrus and the cuneus have been associated with the occurrence of gait disturbances⁴⁷.

Roadblocks and rerouting: the long journey of locomotor information

Altogether our findings detail a roadmap of locomotor information processing in PD and highlight negative functional connectivity changes that may act as roadblock for sensory and visuomotor information processes leading to hypokinetic gait.

The framework of cortical locomotor control starts with sensory inputs (i.e., visual, sensory and proprioceptive information) that generate an internal schema of body and space, which is transmitted to the SMA to be integrated into feedforward locomotor programs. We showed that this process is altered in subjects with PD and highlighted two main functional roadblocks. The first is the impaired information flow from visuomotor areas to SMA that hampers visual integration processing relevant for the construction of APAs (Figure 6). The second roadblock lays in reduced information flow from the SMA to sensory areas that further impairs APAs actualization (Figure 6).

In this scenario, we suggest that an information flow reinforced by the lingual gyrus may act as compensatory strategy to allow the forward processing of visual and locomotor information. This functional rerouting is supported by the articulated anatomical connections of visuomotor areas with frontal areas known as inferior fronto-occipital fasciculus (IFOF)⁴⁵. The IFOF connects the cuneus and lingual gyrus to the frontal cortex with fibers from the lingual gyrus terminating mostly in the inferior frontal gyrus and fibers from the cuneus terminating mostly in the superior frontal gyrus. This wide distribution of cortical terminations would provide additional multimodal information processing fostering locomotion^{48,49}.

Limitations

This study has limitations. First, the relatively small sample size, which mainly derives from the demanding and multimodal approach with multiple brain molecular imaging studies, neurophysiological and kinematic recordings in meds-off state. This complex assessment is not feasible in advanced stages of PD. However, our sample is comparable with other studies on this topic¹⁰ with the additional advantage of leveraging brain metabolic imaging findings for neurophysiological analyses. With this regard, we applied well-established and validated electrophysiological metrics^{26,50}. Second, we limited our EEG analysis to cortical areas and cannot comment on the impact of basal ganglia, thalamus and cerebellum on our findings. Last, the lack of a control group limits the generalization of the findings of this study, which however specifically targeted PD patients. We also cannot comment on the impact of different therapeutic strategies since we limited for now our recordings to unmedicated patients.

Conclusion

This study investigated the functional activity of the cortical locomotor network in unmedicated PD patients during unperturbed overground walking and support a role for visuomotor integration processes in the rescuing of hypokinetic gait in PD. Further studies are needed to assess the impact of dopaminergic and neuromodulation treatments on these functional connectivity pathways.

Acknowledgements

The authors would like to thank J. Brumberg for his support with molecular imaging data acquisition, Prof. C. Matthies, Dr. P. Fricke and Dr. R. Nickl for the neurosurgical management of the patients and Prof. J. Volkmann for the valuable comments on the results.

Author contribution:

I.U.I. and A.B. contributed with the conception and design of the study, F.P., C.P., N.G.P., G.M., S.H. and I.U.I. contributed with acquisition and analysis of data. F.P., C.P., N.G.P., S.H. and I.U.I. contributed also with drafting a significant portion of the manuscript or figures.

Potential conflict of interest:

F.P., C.P., N.G.P., G.M., A.B. S.H and I.U.I. declare no conflicts of interest related to this study.

Data Availability Statement

Due to strict privacy law, data are available upon personal request. Inquiries can be sent to the corresponding author (Ioannis U. Isaias, University Hospital Würzburg, Department of Neurology, Josef-Schneider-Straße 11, 97080 Würzburg, e-mail: Isaias_I@ukw.de).

Funding

The study was sponsored by the Deutsche Forschungsgemeinschaft (DFG, German Research Foundation) - Project-ID 424778381-TRR 295, by the European Union - Next Generation EU - NRRP M6C2 - Investment 2.1 Enhancement and strengthening of biomedical research in the NHS and by the Fondazione Grigioni per il Morbo di Parkinson.

SH and FP were supported by the European Research Council (ERC) under the European Union's Horizon 2020 research and innovation program (Grant agreement No. 758985).

IUI was supported by the New York University School of Medicine and The Marlene and Paolo Fresco Institute for Parkinson's and Movement Disorders, which was made possible with support from Marlene and Paolo Fresco. CP was supported by a grant from the Fondazione Europea di Ricerca Biomedica (FERB Onlus).

References

1. Mirelman A, Shema S, Maidan I, Hausdorff JM. Gait. In: *Handbook of Clinical Neurology*. Vol 159. Elsevier; 2018:119-134. doi:10.1016/B978-0-444-63916-5.00007-0
2. MacKinnon CD. Sensorimotor anatomy of gait, balance, and falls. In: *Handbook of Clinical Neurology*. Vol 159. Elsevier; 2018:3-26. doi:10.1016/B978-0-444-63916-5.00001-X
3. Clancy KB, Orsolic I, Mrsic-Flogel TD. Locomotion-dependent remapping of distributed cortical networks. *Nat Neurosci*. 2019;22(5):778-786. doi:10.1038/s41593-019-0357-8
4. Takakusaki K. Functional Neuroanatomy for Posture and Gait Control. *J Mov Disord*. 2017;10(1):1-17. doi:10.14802/jmd.16062
5. Wang DD, Choi JT. Brain Network Oscillations During Gait in Parkinson's Disease. *Front Hum Neurosci*. 2020;14:568703. doi:10.3389/fnhum.2020.568703
6. Peterson DS, Horak FB. Neural Control of Walking in People with Parkinsonism. *Physiology*. 2016;31(2):95-107. doi:10.1152/physiol.00034.2015
7. Mirelman A, Bonato P, Camicioni R, et al. Gait impairments in Parkinson's disease. *Lancet Neurol*. 2019;18(7):697-708. doi:10.1016/S1474-4422(19)30044-4
8. Arnulfo G, Pozzi NG, Palmisano C, et al. Phase matters: A role for the subthalamic network during gait. *PloS One*. 2018;13(6):e0198691. doi:10.1371/journal.pone.0198691
9. Thevathasan W, Pogosyan A, Hyam JA, et al. Alpha oscillations in the pedunculopontine nucleus correlate with gait performance in parkinsonism. *Brain*. 2012;135(1):148-160. doi:10.1093/brain/awr315
10. Pozzi NG, Canessa A, Palmisano C, et al. Freezing of gait in Parkinson's disease reflects a sudden derangement of locomotor network dynamics. *Brain*. 2019;142(7):2037-2050. doi:10.1093/brain/awz141
11. Shine JM, Handojoseno AMA, Nguyen TN, et al. Abnormal patterns of theta frequency oscillations during the temporal evolution of freezing of gait in Parkinson's disease. *Clin Neurophysiol Off J Int Fed Clin Neurophysiol*. 2014;125(3):569-576. doi:10.1016/j.clinph.2013.09.006
12. Bohnen NI, Costa RM, Dauer WT, et al. Discussion of Research Priorities for Gait Disorders in Parkinson's Disease. *Mov Disord*. 2022;37(2):253-263. doi:10.1002/mds.28883
13. Haufe S, Isaias IU, Pellegrini F, Palmisano C. *Gait Event Prediction from Surface Electromyography in Parkinsonian Patients*. Rehabilitation Medicine and Physical Therapy; 2023. doi:10.1101/2023.01.13.22282375
14. Reich MM, Brumberg J, Pozzi NG, et al. Progressive gait ataxia following deep brain stimulation for essential tremor: adverse effect or lack of efficacy? *Brain J Neurol*. 2016;139(11):2948-2956. doi:10.1093/brain/aww223
15. Hinton GE, Salakhutdinov RR. Reducing the Dimensionality of Data with Neural Networks. *Science*. 2006;313(5786):504-507. doi:10.1126/science.1127647
16. Kothe CA, Makeig S. BCILAB: a platform for brain-computer interface development. *J Neural Eng*. 2013;10(5):056014. doi:10.1088/1741-2560/10/5/056014
17. Bell AJ, Sejnowski TJ. An information-maximization approach to blind separation and blind deconvolution. *Neural Comput*. 1995;7:1129-1159.
18. Mazziotta JC, Toga AW, Evans A, Fox P, Lancaster J. A probabilistic atlas of the human brain: theory and rationale for its development. The International Consortium for Brain Mapping (ICBM). *NeuroImage*. 1995;2(2):89-101.

19. Dale AM, Fischl B, Sereno MI. Cortical surface-based analysis. I. Segmentation and surface reconstruction. *NeuroImage*. 1999;9(2):179-194. doi:10.1006/nimg.1998.0395
20. Fischl B, Sereno MI, Dale AM. Cortical surface-based analysis: II: inflation, flattening, and a surface-based coordinate system. *Neuroimage*. 1999;9(2):195-207.
21. Gramfort A, Papadopoulou T, Olivi E, Clerc M. OpenMEEG: opensource software for quasistatic bioelectromagnetics. *Biomed Eng OnLine*. 2010;9(1):45. doi:10.1186/1475-925X-9-45
22. Kybic J, Clerc M, Abboud T, Faugeras O, Keriven R, Papadopoulou T. A common formalism for the Integral formulations of the forward EEG problem. *IEEE Trans Med Imaging*. 2005;24(1):12-28. doi:10.1109/TMI.2004.837363
23. Tadel F, Baillet S, Mosher JC, Pantazis D, Leahy RM. Brainstorm: A User-Friendly Application for MEG/EEG Analysis. *Comput Intell Neurosci*. 2011;2011:1-13. doi:10.1155/2011/879716
24. Van Veen BD, Van Drongelen W, Yuchtman M, Suzuki A. Localization of brain electrical activity via linearly constrained minimum variance spatial filtering. *IEEE Trans Biomed Eng*. 1997;44(9):867-880. doi:10.1109/10.623056
25. Tzourio-Mazoyer N, Landau B, Papathanassiou D, et al. Automated Anatomical Labeling of Activations in SPM Using a Macroscopic Anatomical Parcellation of the MNI MRI Single-Subject Brain. *NeuroImage*. 2002;15(1):273-289. doi:10.1006/nimg.2001.0978
26. Pellegrini F, Delorme A, Nikulin V, Haufe S. Identifying good practices for detecting inter-regional linear functional connectivity from EEG. *NeuroImage*. Published online June 2023:120218. doi:10.1016/j.neuroimage.2023.120218
27. Vinck M, van Wingerden M, Womelsdorf T, Fries P, Pennartz CMA. The pairwise phase consistency: A bias-free measure of rhythmic neuronal synchronization. *NeuroImage*. 2010;51(1):112-122. doi:10.1016/j.neuroimage.2010.01.073
28. Haufe S, Nikulin VV, Müller KR, Nolte G. A critical assessment of connectivity measures for EEG data: A simulation study. *NeuroImage*. 2013;64:120-133. doi:10.1016/j.neuroimage.2012.09.036
29. Winkler I, Panknin D, Bartz D, Müller KR, Haufe S. Validity of time reversal for testing Granger causality. *IEEE Trans Signal Process*. 2016;64(11):2746-2760. doi:10.1109/TSP.2016.2531628
30. Anzolin A, Presti P, Van De Steen F, Astolfi L, Haufe S, Marinazzo D. Quantifying the Effect of Demixing Approaches on Directed Connectivity Estimated Between Reconstructed EEG Sources. *Brain Topogr*. Published online April 10, 2019. doi:10.1007/s10548-019-00705-z
31. Donoghue T, Haller M, Peterson EJ, et al. Parameterizing neural power spectra into periodic and aperiodic components. *Nat Neurosci*. 2020;23(12):1655-1665. doi:10.1038/s41593-020-00744-x
32. Doppelmayr M, Klimesch W, Pachinger T, Ripper B. Individual differences in brain dynamics: important implications for the calculation of event-related band power. *Biol Cybern*. 1998;79(1):49-57. doi:10.1007/s004220050457
33. Benjamini Y, Hochberg Y. Controlling the false discovery rate: a practical and powerful approach to multiple testing. *J R Stat Soc Ser B Methodol*. Published online 1995:289-300.
34. Isaias IU, Brumberg J, Pozzi NG, et al. Brain metabolic alterations herald falls in patients with Parkinson's disease. *Ann Clin Transl Neurol*. 2020;7(4):579-583. doi:10.1002/acn3.51013
35. Takakusaki K. Neurophysiology of gait: From the spinal cord to the frontal lobe: Neurophysiology of Gait. *Mov Disord*. 2013;28(11):1483-1491. doi:10.1002/mds.25669

36. Zhang S, Li C shan R. Functional connectivity mapping of the human precuneus by resting state fMRI. *NeuroImage*. 2012;59(4):3548-3562. doi:10.1016/j.neuroimage.2011.11.023
37. Rahimpour S, Rajkumar S, Hallett M. The Supplementary Motor Complex in Parkinson's Disease. *J Mov Disord*. 2022;15(1):21-32. doi:10.14802/jmd.21075
38. Tessitore A, Cirillo M, De Micco R. Functional Connectivity Signatures of Parkinson's Disease. *J Park Dis*. 2019;9(4):637-652. doi:10.3233/JPD-191592
39. Brugger F, Wegener R, Walch J, et al. Altered activation and connectivity of the supplementary motor cortex at motor initiation in Parkinson's disease patients with freezing. *Clin Neurophysiol*. 2020;131(9):2171-2180. doi:10.1016/j.clinph.2020.05.023
40. Jacobs JV, Lou JS, Kraakevik JA, Horak FB. The supplementary motor area contributes to the timing of the anticipatory postural adjustment during step initiation in participants with and without Parkinson's disease. *Neuroscience*. 2009;164(2):877-885. doi:10.1016/j.neuroscience.2009.08.002
41. Peterson DS, Pickett KA, Duncan R, Perlmuter J, Earhart GM. Gait-Related Brain Activity in People with Parkinson Disease with Freezing of Gait. Zhou J, ed. *PLoS ONE*. 2014;9(3):e90634. doi:10.1371/journal.pone.0090634
42. Azulay JP, Mesure S, Amblard B, Blin O, Sangla I, Pouget J. Visual control of locomotion in Parkinson's disease. *Brain*. 1999;122(1):111-120. doi:10.1093/brain/122.1.111
43. Martens KAE, Almeida QJ. Dissociating between sensory and perceptual deficits in PD: More than simply a motor deficit. *Mov Disord*. 2012;27(3):387-392. doi:10.1002/mds.24042
44. Servos P. The Neural Substrates of Biological Motion Perception: an fMRI Study. *Cereb Cortex*. 2002;12(7):772-782. doi:10.1093/cercor/12.7.772
45. Palejwala AH, Dadario NB, Young IM, et al. Anatomy and White Matter Connections of the Lingual Gyrus and Cuneus. *World Neurosurg*. 2021;151:e426-e437. doi:10.1016/j.wneu.2021.04.050
46. Yu Q, Li Q, Fang W, et al. Disorganized resting-state functional connectivity between the dorsal attention network and intrinsic networks in Parkinson's disease with freezing of gait. *Eur J Neurosci*. 2021;54(7):6633-6645. doi:10.1111/ejn.15439
47. Tessitore A, Amboni M, Cirillo G, et al. Regional Gray Matter Atrophy in Patients with Parkinson Disease and Freezing of Gait. *Am J Neuroradiol*. 2012;33(9):1804-1809. doi:10.3174/ajnr.A3066
48. de Benedictis,Alessandro, Marras, Carlo Efisio, Petit, Laurent, Sarubbo, Silvio. The inferior fronto-occipital fascicle: a century of controversies from anatomy theaters to operative neurosurgery. *J Neurosurg Sci*. Published online 2021.
49. Suzuki Y, Iseki C, Igari R, et al. Reduced cerebral blood flow of lingual gyrus associated with both cognitive impairment and gait disturbance in patients with idiopathic normal pressure hydrocephalus. *J Neurol Sci*. 2022;437:120266. doi:10.1016/j.jns.2022.120266
50. Bodda S, Maya S, Em Potti MN, et al. Computational analysis of EEG activity during stance and swing gait phases. *Procedia Comput Sci*. 2020;171:1591-1597. doi:10.1016/j.procs.2020.04.170

Curriculum vitae

Mein Lebenslauf wird aus datenschutzrechtlichen Gründen in der elektronischen Version meiner Arbeit nicht veröffentlicht.

List of publications

1. **Pellegrini, F.**, Hawellek, D. J., Pape, A. A., Hipp, J. F., & Siegel, M. (2021). Motion coherence and luminance contrast interact in driving visual gamma-band activity. *Cerebral Cortex*, 31(3), 1622-1631. IF: 5.357
2. Haumesser, J. K., Beck, M. H., **Pellegrini, F.**, Kühn, J., Neumann, W. J., Altschüler, J., ... & van Riesen, C. (2021). Subthalamic beta oscillations correlate with dopaminergic degeneration in experimental parkinsonism. *Experimental Neurology*, 335, 113513. IF: 5.33
3. Haufe, S., Isaias, I. U., **Pellegrini, F.**, & Palmisano, C. (2023). Gait Event Prediction Using Surface Electromyography in Parkinsonian Patients. *Bioengineering*, 10(2), 212. IF: 4.864
4. **Pellegrini, F.**, Delorme, A., Nikulin, V., & Haufe, S. (2023). Identifying good practices for detecting inter-regional linear functional connectivity from EEG. *NeuroImage*, 120218. IF: 7.400
5. **Pellegrini, F.**, Nguyen, T. D., Herrera, T., Nikulin, V., Nolte, G., & Haufe, S. (2023). Distinguishing between- from within-site phase-amplitude coupling using antisymmetrized bispectra [Preprint]. Neuroscience. <https://doi.org/10.1101/2023.10.26.564193>
6. **Pellegrini, F.**, Pozzi, N. G., Palmisano, C., Marotta, G., Buck, A., Haufe, S., & Isaias, I. U. (2023). Cortical networks of parkinsonian gait: A metabolic and functional connectivity study [Preprint]. Neurology. <https://doi.org/10.1101/2023.10.09.23296653>
7. Binns, T. S., Köhler, R. M., Vanhoecke, J., Chikermane, M., Gerster, M., Merk, T., **Pellegrini, F.**, Busch, J. L., Habets, J. G. V., Cavallo, A., Li, N., Horn, A., Krause, P., Faust, K., Schneider, G.-H., Haufe, S., Kühn, A. A., & Neumann, W. J. (2024). Shared pathway-specific network mechanisms of dopamine and deep brain stimulation for the treatment of Parkinson's disease. *bioRxiv*, 2024-04.

Acknowledgements

First of all, I would like to thank my principal supervisor Prof. Stefan Haufe, from whom I was allowed to learn incredibly much over the past years. I especially remember hours of 1-1 sessions in which you introduced me to the world of simulations, signal processing, and statistics, and answered every little question with precision and patience. Without you I would be a good deal less smart today.

Following this, I would like to thank my other two supervisors Prof. Andrea Kühn and Prof. Vadim Nikulin. You have always been there for me with support and valuable advice.

Many thanks to my super cool work group, especially Mahta, Veronika, and Nikita, who often sweetened my workday. Special thanks to my proofreaders Mahta, Nikita, Tien, and Alex, who provided improvements to this work. Many thanks to the reviewers who helped me with valuable comments on our studies, and to the reviewers of this thesis.

Science is not a job that can be accomplished alone. Therefore, I would like to thank Prof. Arnaud Delorme, Prof. Guido Nolte, Prof. Ioannis Isaias, Prof. Chi Wang Ip, Katharina, Chiara, Nicoló, Friederike, and Martina for our collaboration. Further, I have incredibly enjoyed working with 'my' students Tien, Taliana, Tin, and Ana over the years. I think we have learned a lot from each other, and I wish you all the best for the future.

Thanks to Brigitte and Ilaria for their support in endless bureaucracy, to Lisa who guided me through the confusion of PhD regulations and always had an open ear, and Dominik and Willi who saved me many times from collapsing clusters.

Completing a PhD is like a roller coaster ride with many ups and downs. I am very thankful that I always had a good network that supported me when necessary. I would like to mention the early career community of the Retune network, especially my peer2peer mentoring group with Timon, Dennis and Alexia, as well as my colleagues at the BCCN, and Ombuds woman Mrs. Keydel, who helped me a lot when times were rough.

Last but not least, I would like to thank my family and friends, without whom this work would not have been possible. First and foremost, my wonderful parents, who provided me with the confidence that one needs for completing a PhD. Without you, Jolle, Pelle, Oskar, Ada, and Milo, my life would not be half as vibrant and beautiful. Vici, thank you for our long conversations. And Stella, our agreement that we will conquer the world is valid. The most important person comes at the end: Alex, thank you for your endless support in the last years. You broaden my mind and my heart.